Report on resistivity modelling and comparison with other SHGS

Deliverable 5.2

Report on resistivity modelling and comparison with other SHGS

Deliverable 5.2

Responsible author: Ásdís Benediktsdóttir (ÍSOR)

Responsible SP leader: Gylfi Páll Hersir (ÍSOR)

Responsible WP leader: Gylfi Páll Hersir (ÍSOR)

Contributions by: Ásdís Benediktsdóttir (ÍSOR), Gylfi Páll Hersir (ÍSOR), Arnar Már Vilhjálmsson (ÍSOR), Adele Manzella (CNR), Alessando Santilano (CNR) and Sebastian Held (KIT),

Work package 5.1

March 2019

Website: http://www.gemex-h2020.eu

The GEMex project is supported by the European Union's Horizon 2020 programme for Research and Innovation under grant agreement No 727550

Table of Contents

List of figures

List of tables

Executive summary

Task 5.1: *Resistivity imaging of EGS (Enhanced Geothermal Systems) and SHGS (Superhot Geothermal Systems)* is a part of Work package 5, *Detection of deep structures,* within the GEMex project. The two geothermal systems imaged in Mexico were Los Humeros, a SHGS-site and Acoculco, an EGS-site. A total of 122 MT and 120 co-located TEM soundings were performed in Los Humeros and 68 MT and 65 co-located TEM soundings in Acoculco.

Data acquisition took place from November 2017 to February 2019. The acquisition period was longer than anticipated because of various problems. However, in the end almost all the planned sites were visited. The quality of the data was good for most of the soundings, despite the electromagnetic noise from the power plant in Los Humeros and the associated power lines.

The MT data for both areas were processed and quality controlled. PROCMT was used for quality check during fieldwork and BIRRP for transfer functions robust estimation. The dimensionality of the data and geoelectrical structure of the areas were analysed through phase tensor analysis and strike analysis (Tipper-strike and induction arrows). The results are compared with the geological structure. The Los Humeros survey area is characterized by a three-dimensional structure with considerable horizontal contrasts in the resistivity structure. The resistivity structure appears to be characterized by horizontal layers in the Acoculco survey area, with small variations in the lateral direction.

Resistivity models of the two areas were compiled from the results of 1D joint inversion of the TEM and MT data. Here, it was inverted for the apparent resistivity and phase calculated from the determinant value of the MT impedance tensor. During the inversion process the MT data were static shift corrected using the TEM data – the static shift multiplier was one of the parameters inverted for. In Los Humeros the resistivity structure is complex. One of the most prominent feature of the model is a resistive core that domes up along one of the main faults in the region. In Acoculco the resistivity structure is very close to a horizontally layered structure. A conductive cap is revealed at a shallow depth close to a major fault intersection in the area, an area of probable geothermal utilization.

Resistivity models for the two areas were also calculated through 3D inversion of the static shift corrected MT data. For Los Humeros it was inverted for the full impedance tensor – all 4 complex elements while for Acoculco it was inverted for the off-diagonal elements of the tensor. The WSINV3DMT-code was used in the inversion. Four different initial models were used in the inversion for Los Humeros and three for Acoculco. The results from Los Humeros and Acoculco were in good agreement with the 1D inversion results, although the structure in the model became clearer. The resistivity structure in Los Humeros is controlled by the faults in the area as well as the outlines of the Los Potreros caldera. Two main zones of interest were identified. In Acoculco the results are very similar to the 1D joint inversion results, which is not surprising given the horizontally layered structure in the survey area.

The possibility to apply computational intelligence metaheuristics for the geophysical study of geothermal fields was successfully demonstrated. Different approaches were tested, and the results can assist in understanding complex system such as the Acoculco geothermal field. The main results are: i) the identification of the static shift of MT curves by means of joint optimization of TEM and MT data, ii) the computation of a laterally-constrained resistivity profile by means of Particle Swarm Optimization (PSO) with external information inserted as part of the swarm in the optimization procedure, iii) the computation of 1D resistivity models from the joint optimization of VES and TEM data.

The resistivity models in the superhot geothermal Icelandic systems, Krafla and Reykjanes, were revised with respect IDDP-1 and 2. The resistivity structure in Los Humeros was then compared to that found in Krafla and Reykjanes. They all exhibit the case-example resistivity structure of geothermal systems in volcanic settings but as they are located in tectonically different settings, the shape and size of the structures vary.

1 Introduction

This report is deliverable D5.2 within the GEMex project. In the DoW it says on deliverable D5.2: *Report on resistivity modelling and comparison with other SHGS. Refers to tasks 5.1.5, 5.1.6, and 5.1.7. Report describing processing and modelling of existing and new TEM/MT resistivity data provided by the Mexican partners from SHGS and EGS fields. Comparison with similar fields in Iceland.*

These three tasks are:

- *5.1.5. Data processing and resistivity models (1D and 3D) of the Los Humeros and Acoculco (ÍSOR, CNR, KIT).*
- *5.1.6. Revision of the model of Krafla and Reykjanes (ÍSOR).*
- *5.1.7. Comparison with similar modelling from superhot systems in Iceland and data from IDDP-1 and IDDP-2 (ÍSOR).*

Resistivity data, MT and co-located TEM, were collected during several campaigns in Los Humeros (SHGS site) and Acoculco (EGS site) from early November 2017 until February 2019. The field campaign was run by UNAM (National Autonomous University of Mexico) together with UMSNH (Michoacan University of Saint Nicholas of Hidalgo, Mexico) and CICESE (Ensenada Center for Scientific Research and Higher Education, Mexico). ÍSOR (Iceland GeoSurvey) and KIT (Karlsruhe Institute of Technology, Germany), from the European consortium participated in the campaign in the beginning and were a part of the discussions and decisions taken on appropriate field practices and the resistivity survey in general. The campaign took longer than anticipated due to unforeseeable problems of different kind that came up during the acquisition period. However, we managed to collect almost all the data we originally planned to collect. Most of the data are high quality data. A few sites were not accessible, and we did not manage to collect a few soundings in the Acoculco prospect which was due to the denial of the Cuautelolulco municipality to give permission to work there. Location of soundings in the two areas was discussed back and forth and approved by both consortia and within the relevant WPs through emails, telecons and at meetings. The locations were based on previously collected resistivity data and results from geological mapping. In the end a total of 122 MT and 120 co-located TEM soundings were carried out in Los Humeros and 68 MT and 65 TEM in Acoculco.

A lot of effort was put into processing the MT data which was done by the Mexican consortium and discussed thoroughly simultaneously within the two consortia. They used PROCMT for quality check during fieldwork and BIRRP for transfer functions robust estimation. QC of the processed MT data was done by KIT and described in Chapter 4. Phase tensor analysis of the processed MT data was done by KIT while strike analysis (Tipper-strike and induction arrows) was done by ÍSOR and compared with the tectonics of the two areas. This is discussed in Chapter 5. Two workshops were held during the project period in Mexico City organized by the two consortia, on the acquisition and processing of the data and their analyses and inversion, and how to interpret the resulting resistivity models in conjunction with other geoscientific results from the areas (see, Appendix A; (Hersir and Benediktsdóttir, 2018)). These issues were also discussed at all General assembly meetings in GEMex.

The MT/TEM resistivity data for both areas were 1D jointly inverted at ÍSOR, thereby static shift correcting the MT data by using TEM data. The resulting resistivity models for both areas based on the 1D inversion models were downloaded on the VRE of the GEMex project as soon as they were ready so that the models could be used in other Work packages – the same was done with results from the strike analysis. Preliminary versions of this work were discussed simultaneously as the work proceeded at GEMex´s General assembly meetings. In Chapter 6 the methodology of the 1D joint inversion of TEM and MT data applied here is described and the results presented and discussed in geological terms.

Chapter 7 is written by CNR (National Research Council, Italy) and describes the results of an innovative approach applied to the geophysical study of the Acoculco geothermal field. Computational intelligence (CI) methods are exploited for the quantitative data integration of different datasets, by jointly solving the inverse problem of TEM, vertical electrical sounding (VES) and MT.

The 3D inversion of the MT data is the subject of Chapter 8, written by ÍSOR. The inversion was performed using the WSINV3DMT-code, while the Mexican consortium uses another code, the ModEM-code. This gives a most welcome opportunity to compare the two resulting resistivity models based on the two codes. The comparison will be the subject of deliverable 5.8. The methodology applied here in the 3D inversion is described, and the results presented and discussed in geological terms.

Finally, resistivity models from two similar superhot systems in Iceland where the two IDDP wells have been drilled in Krafla, NE Iceland and Reykjanes, SW-Iceland are discussed and compared with results from the superhot system in Los Humeros.

2 MT and TEM methods

2.1 The magnetotelluric (MT) method

In the MT method, the natural fluctuations of the earth's magnetic field are used as signal source. Those fluctuations induce currents in the ground which are measured in the surface (E_x and E_y). The magnetic field is measured in three orthogonal directions (H_x, H_y and H_z). The setup is shown in Figure 1. It is customary to have the x-direction to the magnetic north and that was done in this survey both in Los Humeros and in Acoculco. For a homogeneous or layered earth, the electrical field is induced by (coherent with) its orthogonal source magnetic field (i.e. E_x correlates with H_y, and E_y with H_x). For more complicated resistivity structures these relations become more complex.

The short-period MT data (high frequency) mainly reflect the shallow structures due to their little depth of penetration, whereas the long period data mainly reflect the deeper structures. The MT method has the greatest exploration depth of all resistivity methods, some tens of kilometers, depending on the recorded periods, and is practically the only method for studying deep resistivity structures. In this survey, the exploration depth of the MT soundings is around 3-10 km but varied considerably depending on resistivity and, in particular, on data quality.

The magnetic field was measured with induction coils and the electrical field by a pair of sealed $PbCl_2$ type electrodes. The electrical dipole length was typically 90 m.

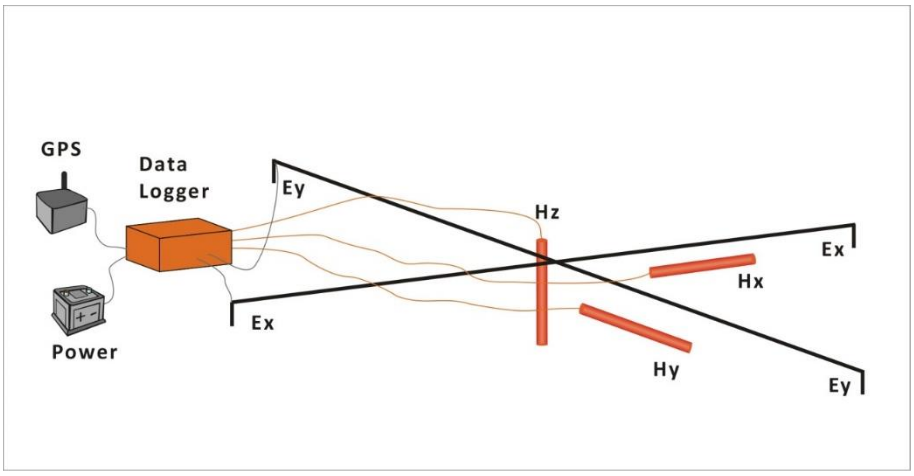

Figure 1: *The setup of an MT sounding*.

The measured MT time series are Fourier transformed into the frequency domain and the "best" solution that describes the relation between the electrical and magnetic field is found by assuming the following equation:

$$\begin{bmatrix} E_x \\ E_y \end{bmatrix} = \begin{bmatrix} Z_{xx} & Z_{xy} \\ Z_{yx} & Z_{yy} \end{bmatrix} \begin{bmatrix} H_x \\ H_y \end{bmatrix} \qquad (1a)$$

Or in matrix notation:

$$\vec{\boldsymbol{E}} = \boldsymbol{Z}\vec{\boldsymbol{H}} \qquad (1b)$$

Where, $\vec{\boldsymbol{E}}$ and $\vec{\boldsymbol{H}}$ are the electrical and magnetic field vectors (in the frequency domain), respectively, and $\boldsymbol{Z}$ is a complex impedance tensor which contains information on the subsurface resistivity structure.

The tensor elements are found by minimizing the absolute square of the difference between the left and the right-hand side of equation 1a with respect to the tensor elements.

For a homogeneous (1D) earth $Z_{xy} = -Z_{yx}$ and $Z_{xx} = Z_{yy} = 0$. For a 2D earth, i.e. resistivity varies with depth and in one of the two principal horizontal directions, it is possible to rotate the coordinate system such that $Z_{xx} = Z_{xx} = 0$, but $Z_{xy} \neq -Z_{yx}$. For a 3D earth all the impedance tensor elements are different.

From the impedances apparent resistivity (ρ) and phases (θ) for each frequency are calculated e.g. as:

$$\rho_{xy} = 0.2T\left|Z_{xy}\right|^2;\ \theta_{xy} = \arg\left(Z_{xy}\right) \qquad (2a)$$

$$\rho_{yx} = 0.2T\left|Z_{yx}\right|^2;\ \theta_{yx} = \arg\left(Z_{yx}\right) \qquad (2b)$$

Processing of the MT data is described and discussed in Chapter 4. The output is saved in standard EDI file format (see SEG, 1991) and serves as input in the inversion of the data.

2.2 The Transient Electromagnetic (TEM) Method

The main purpose of the TEM survey was to correct for the static shift of the MT data. Static shift is caused by near-surface resistivity in-homogeneities at the sounding site and/or topography which distorts the electric field measured in the surface. Static shift introduces an unknown shift multiplier, S, (shift on log-scale) of the apparent resistivity. The shift multiplier is practically independent of frequency (period); therefore, the whole apparent resistivity curve can be shifted up or down when plotted on log-scale (Árnason, 2015).

TEM is based on measuring the decay rate of the vertical component of the magnetic field due to eddy currents induced in the receiver coil after the current in the source loop is turned off. At very early times after the turn-off, the induced currents are at shallow depth, but as time passes, they diffuse downwards and outwards. Therefore, the TEM response is practically independent of shallow resistivity variations and topography at late times, that is, the TEM has no static shift at late times. Therefore, TEM is routinely used to correct for static shifts in MT data and is a practical is practically the only applicable method in volcanic environments. This method has become an industry standard.

To static shift correct the MT data, a TEM sounding was performed at the same place as the MT sounding (within a few tens of meters). For an effective shift correction, the late time gates of the TEM must be probing the same depth interval as the short periods of the MT, i.e. the TEM and MT curves must overlap by several points of good data. The actual correction of the static shift is done by jointly 1D inverting the two data sets. This is done through the TEMTD software, developed at ÍSOR (Árnason, 2006b). In the joint inversion, one extra unknown parameter is added to the set of unknown parameters of the model, namely a shift multiplier, S, which must be divided to the MT apparent resistivity so that both the TEM and MT data curves can be fitted simultaneously by the same model. Prior to the 1D inversion the TEM data were processed using the Linux based TemX program (Árnason, 2006a).

The TEM and MT curves need to have overlap of good data. The MT signal (fluctuations in ambient electromagnetic field) is not controllable. The TEM signal can, on the other hand, be controlled and increased by increasing the size of the source loop and/or its current. Then the TEM signal can be recorded at later times before it is drowned in noise. If the short periods of the MT are noisy, big source loops of the TEM are needed. If, on the other hand, the short periods of the MT have good data, relatively small TEM loops are sufficient.

3 MT and TEM data acquisition

The field work – data acquisition - in Los Humeros and Acoculco was organized by the Mexican consortium: UNAM together with UMSNH and CICESE. From the European consortium, ÍSOR and KIT participated in the campaign in the beginning and were a part of the discussions and decisions taken on appropriate field practices and the resistivity survey in general (see Appendix A).

The survey design in Los Humeros was based on results from previous resistivity data provided by CFE and published in Arzate et al. (2018), and results based on the geological mapping. It should be pointed out here that the survey in Acoculco was not a conventional resistivity survey, its aim was first and foremost to facilitate the application of EGS technologies – results from geological mapping were used for MT/TEM site locations in Acoculco. Location of soundings in the two areas was discussed back and forth and approved by both consortia and within the relevant WPs through emails, telecons and at meetings.

The resistivity campaign began in November 2017 – a remote station was set up in Acoculco to increase the signal to noise ratio of the MT data and collection of TEM and MT data started in Los Humeros. Data collection was done in several campaigns, the last measurements were performed in February 2019. The campaign took longer than anticipated due to unforeseeable problems of different kind that came up during the acquisition period. However, all these problems were solved, thanks to the great effort which our Mexican colleagues put into this work. Almost all the data we originally planned to collect were collected, although a few could not be done because the area was not accessible. A few soundings in the Acoculco prospect could not be carried out because of the denial of the Cuautelolulco municipality to give permission to work there. All the other municipalities in Acoculco (Cruz Colorada, San Francisco Terrerillos and Jonuco Pedernales) gave their permission.

Elements of the field work have been described in a couple of Memos, which are uploaded on GEMex's VRE and published in a report (Hersir and Benediktsdóttir, 2018; attached in Appendix A). Two workshops were held in Mexico City during the acquisition period on the progress of data acquisition, processing work and the upcoming interpretation of the data (see Appendix A).

In Los Humeros 122 MT soundings and 120 co-located TEM soundings were performed, their location is shown in Figure 2. Measurement sites are on a grid with a spacing of 720 m and on a long profile, where gravity was done as well. Three MT sounding sites were not accessible to measure the TEM, because a crop had been planted there. In one site, TEM data were collected in the middle of a lava field, and MT data could not be performed there. In Acoculco the MT soundings were 68 and the TEM soundings 65, their location is shown in Figure 3. The sites are arranged on a grid with 400 m spacing for the fine grid and with 800 m spacing for the coarser grid.

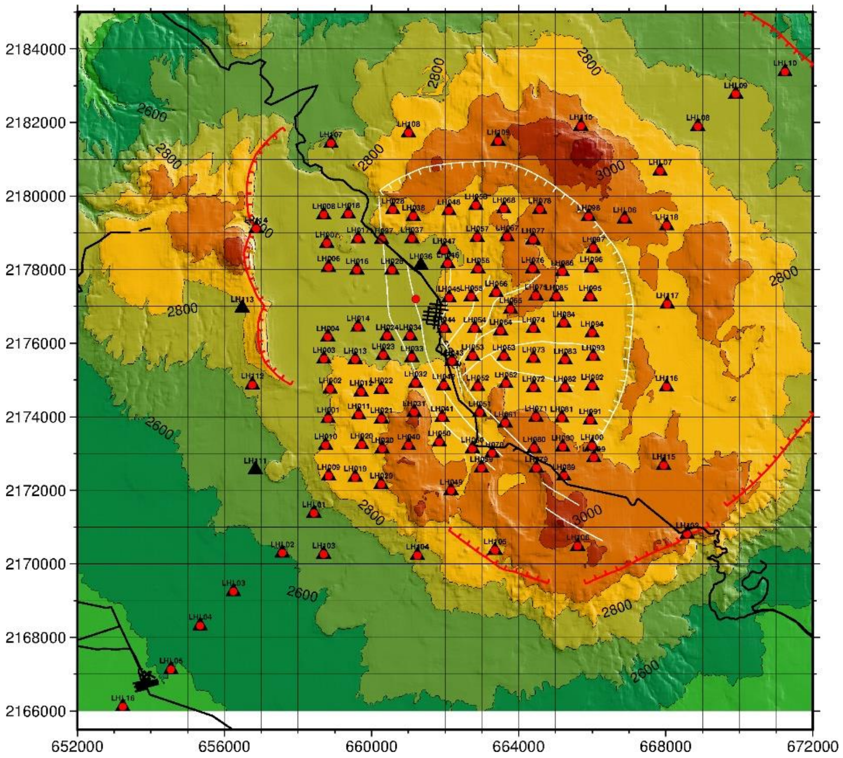

Figure 2: *Location map for the Los Humeros survey area. Black triangles and red circles denote the locations of MT and TEM soundings, respectively. Red and white hatched lines are the Los Humeros and Los Potreros calderas, respectively. White lines are major faults in the area and black lines are roads. Coordinate system is UTM zone 14 WGS84.*

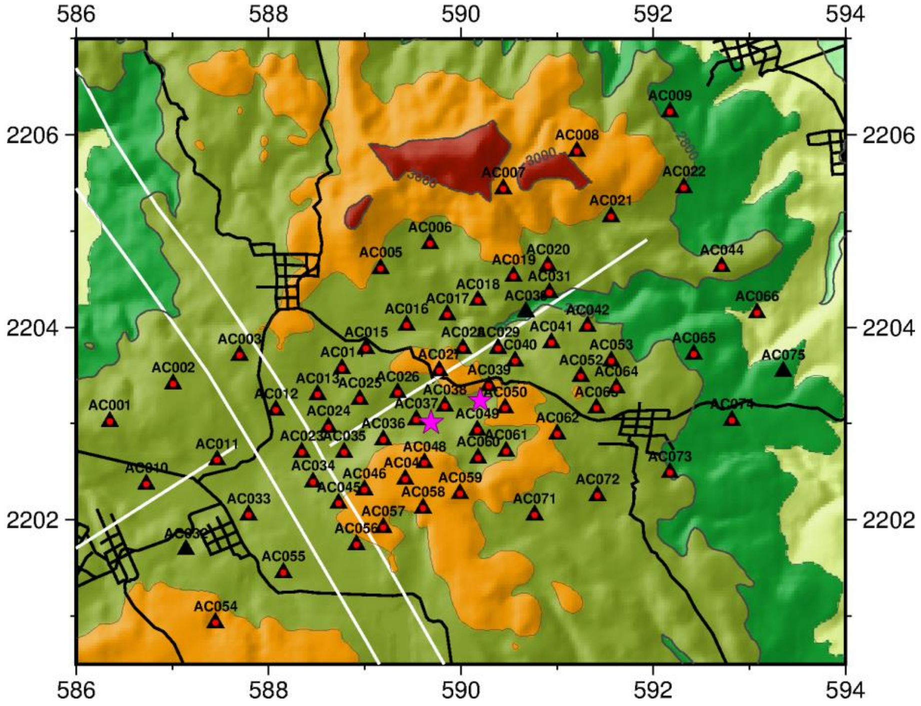

Figure 3: *Location map for the Acoculco survey area. Black triangles and red circles denote the location of MT and TEM soundings, respectively. White lines are major faults in the area and black lines are roads. Coordinate system is UTM zone 14 WGS84.*

In the field work five sets of MT equipment from Metronix, ADU-07 type, was used, collecting data in the frequency range from 0.0001 Hz to 10 kHz. The sampling frequency was 4096 Hz for 30 minutes and 128 Hz for at least 20 hours. One of the MT stations served as a base, or reference station, measuring a continuous MT signal. The reference station was in Acoculco during the Los Humeros survey and vice versa – the two survey areas are some 80 km apart. This recording is used as reference signal to give better data quality (see e.g. Gamble et al., 1979). Some of the MT soundings had bad data, mainly due to noise originating from the proximity of power lines and the power plant in Los Humeros. Each station recorded for approximately 20 hours. Before each station was retrieved and moved to the next location, a preliminary processing of the data was done for quality check. A few soundings were repeated because of poor data quality. In general, the data quality is quite good, but at some locations the longest usable periods are merely 10 seconds.

The equipment used for the TEM measurements was a TerraTEM equipment from Monex GeoScope; single loop, i.e. the same loop was used for transmitting and receiving. The loop size was 100 m x 100 m and the injected current around 8 A. The frequency was 30, 10 and 2.5 Hz.

4 Processing resistivity data

4.1 Processing schemes

Electromagnetic signals are recorded continuously over a certain duration. The five electromagnetic signals (E_x, E_y, H_x, H_y, H_z; see previous section) are recorded using analogue-to-digital (A/D) converter. Conversion of time-varying electromagnetic signals into an interpretable format is known as data processing. In general, processing schemes start with the transformation of data from the time domain into the frequency domain. Electromagnetic waves are dampened during propagation in the subsurface. The damping depends strongly on the wavelength. While short wavelength (high frequencies) have just a small penetration depth, waves of longer wavelength (low frequencies) penetrate deep into the subsurface. Hence, the minimum frequency and, thus, the recording time is a measure of the maximum penetration depth. Thereby, the duration of measurements must be adapted to the target depth. For the exploration of Los Humeros and Acoculco recording times of up to 24 h are selected to reach targets at a few kilometers depth.

Time-to-frequency conversion is carried out by a (Fast) Fourier Transformation (FFT). In plain words the input signal is decomposed and partitioned in participating frequencies. Each frequency contributing to the signal has an amplitude corresponding to the strength of participation of that frequency to original signal. Frequency depended calibration files of induction coils, delivered by the manufacturer of the sampling devices, are considered in the FFT. FFT conversion of a sample side (LH083) is shown in Figure 4. Observations in frequency-domain from discretized time windows are stacked to increase data accuracy.

A priori, data quality can be assessed in the frequency domain. Noise in electromagnetic measurements can be subdivided into geologic and anthropogenic noise. While the source of geologic noise can be studied in detail and evaluated later during interpretation, anthropogenic noise has to be removed from the data during the processing scheme. Szarka (1987) lists sources of anthropogenic noise and found that all objects with free-moving currents effect the measurements, like railway or power lines, anthropogenic vibrations and even moving vehicles or cattle fences. The quality of the data and, hence, the required processing scheme can be evaluated from the data in frequency domain. The shown example (Figure 4) has an elevated quality. The amplitudes of the different frequencies are homogenous with Schumann resonances (at 7.8, 14.1, 20.3, 26.3, and 32.5 Hz), as a result from interaction of EM waves with the ionosphere, clearly visible. At 60 Hz a distinct peak is recorded in all channels originating from the main voltage of the Mexican power grid. Furthermore, smaller presumably anthropogenic noise sources are evident in only some channels (e.g. H_y). A robust processing scheme is selected to eliminate the anthropogenic noise signals to allow an unbiased interpretation.

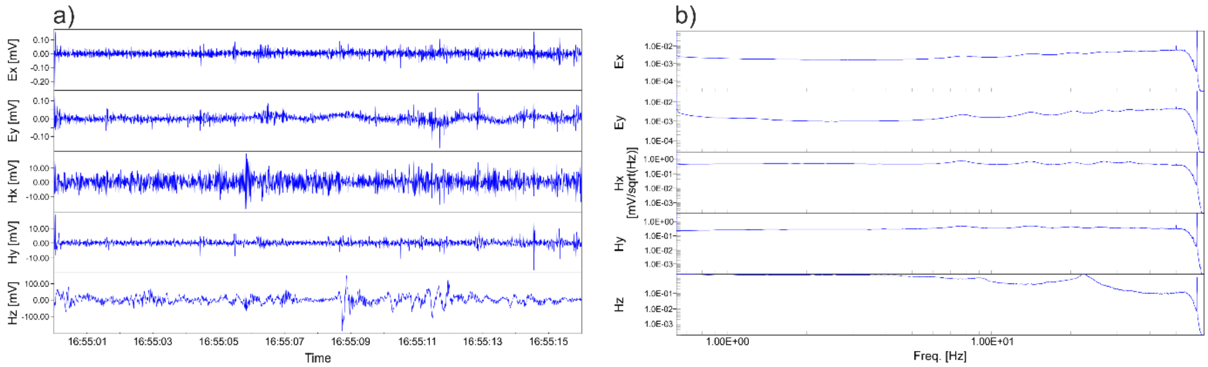

Figure 4: *Fast Fourier Transformation from time-domain (a) to frequency domain (b) for station LH083. Presented data are recording with a frequency of 128 Hz.*

Electromagnetic processing results in the generation of data in an interpretable format. In case of MT these are the apparent resistivity ρ_a and the phase angle Φ. Both parameters are linked (Eq. 1 and Eq. 2) to the measured electric (E_i) and magnetic (H_j) recordings via the impedance tensor ***Z*** (Eq. 3).

$$\rho_{a,ij}(\omega) = \frac{1}{\mu_0 \omega} \left| Z_{ij}(\omega) \right|^2 \qquad \text{(Eq. 1)}$$

$$\text{▯}_{ij} = \tan^{-1}\left(\frac{\Im Z_{ij}}{\Re Z_{ij}}\right) \qquad \text{(Eq. 2)}$$

$$Z_{ij} = \frac{E_i(\omega)}{H_j(\omega)} \qquad \text{(Eq. 3)}$$

To increase the quality of interpretable data the following processing schemes were tested intensively:

- Robust processing scheme after Egbert and Booker (1986)
- Robust processing scheme after Chave and Thomson (2004)
- Processing scheme implemented in WinGLink Software (© Schlumberger) as used e.g. by Held et al. (2016)

WinGLink Software processing yields data of insufficient quality. The results of the processing schemes of Egbert and Booker (1986) and Chave and Thomson (2004) are shown in Figure 5. After quality analysis of a variety of stations considering the whole frequency range, the strongest reduction of uncertainties, the optimal elimination of noise and the generation of smooth curves could be achieved while using Chave's BIRRP code. The bound influence robust processing code was used in advanced mode considering remote referencing. To increase the penetration depth, the processed frequency range was enlarged by decimation of the measured 128 Hz data to 4Hz and subsequent processing of three frequencies bands (4096 Hz, 128 Hz and 4 Hz). A selection of BIRRP processing parameters are listed in Table 1.

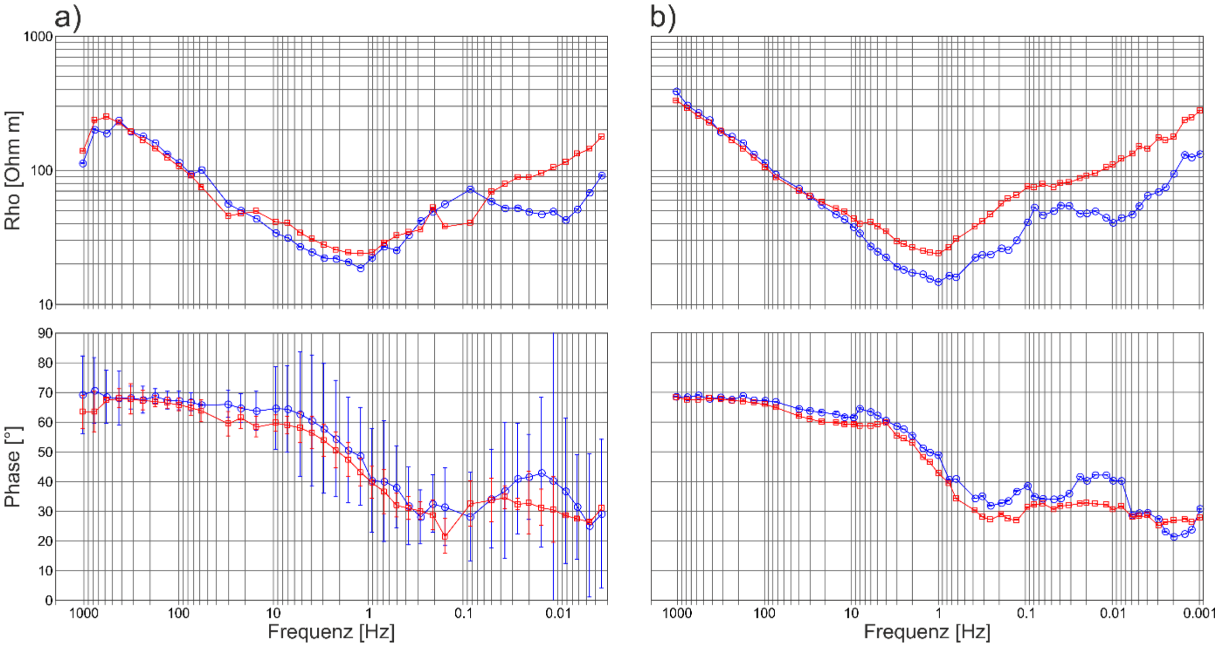

Figure 5: *Robust processing of the LH083 station using the processing scheme of Egbert and Booker (1986) (a) and Chave and Thomson (2004) (b). The uncertainties of the phase angle and also the occurrence of individual outliers is decreased in Chave's BIRRP code.*

Table 1: *Selection of the used BIRRP processing parameters. For a detailed description see BIRRP user manual (http://www.whoi.edu/science/AOPE/people/achave/Site/Next1_files/birrp.5.pdf)*

BIRRP Parameter	4096 Hz	128 Hz	4 Hz	Description
nfft	65536	65536	16384	Maximum window length
nsctmax	13	13	10	Number of reduction steps for each window
mfft	2	1	2	Factor by which nfft is divided while computing the robust AR filter
nf1	150	3 / 6	3	Index of first frequency in each section FFT
nfinc	50	1	1	Increment for subsequent frequencies FFT
nfsect	3			Number of frequencies in each section FFT
c2threshb	0	0.1	0.35	Squared coherence threshold for the initial magnetic field step
c2threshe	0.1	0.1	0.35	Squared coherence threshold for the electric to magnetic field step
nar	15	15	10	Robust autoregressive prewhitening filter
nprej	0			Number of frequencies in FFT section to be rejected

4.2 Quality assessment

The robust processing scheme is optimizing the generation of smooth transfer functions that represent plausible data in respect of the nature of electromagnetic wave propagation. Still after conduction of an optimal processing the interpretable data (apparent resistivity and phase angle) contain scattering and individual outliers. A quality assessment step was introduced to eliminate outliers or highly scattering sections. The following withdrawal criteria were applied:

- Phase angle error: > 5°
- Phase angle difference between adjacent points: > 4°
- Apparent resistivity error: log(error) > ±0.15
- Apparent resistivity scatter: |log (data) – log (polynomial fit)| > 0.08
- Out-of-quadrant phase

After the application of the criteria and withdrawal of outliers and scattering data the measured sites were grouped into three categories: elevated quality (A), intermediate quality (B), insufficient quality (C). An example for each category is shown in Figure 6. For the Los Humeros research area 10 measurement locations belong to category C and 15 measurement locations fall into category B (Figure 6), but the majority of the measurements is of elevated quality. Note that many of the measurements of reduced quality are located next to power plant facilities that might be the origin of the anthropogenic noise decreasing the data quality. For the Acoculco research location only two measurements are of insufficient quality while six belong to category B (Figure 7). The measurement sites of decreased quality are located within an area of high vegetation, where the noise could result from reduced connectivity to the ground or wind induced tree movement.

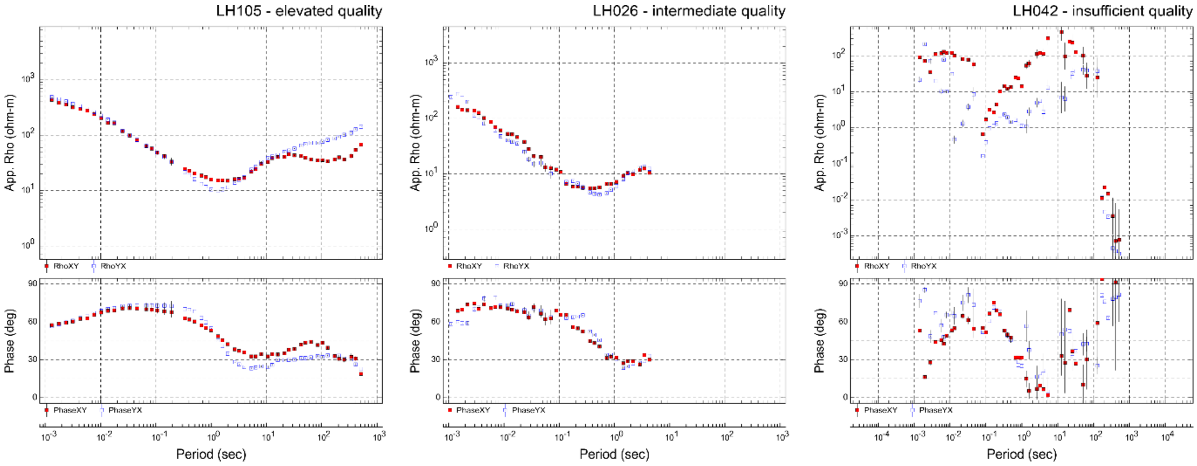

Figure 6: *Examples of the three quality categories of processes MT data from the Los Humeros study area.*

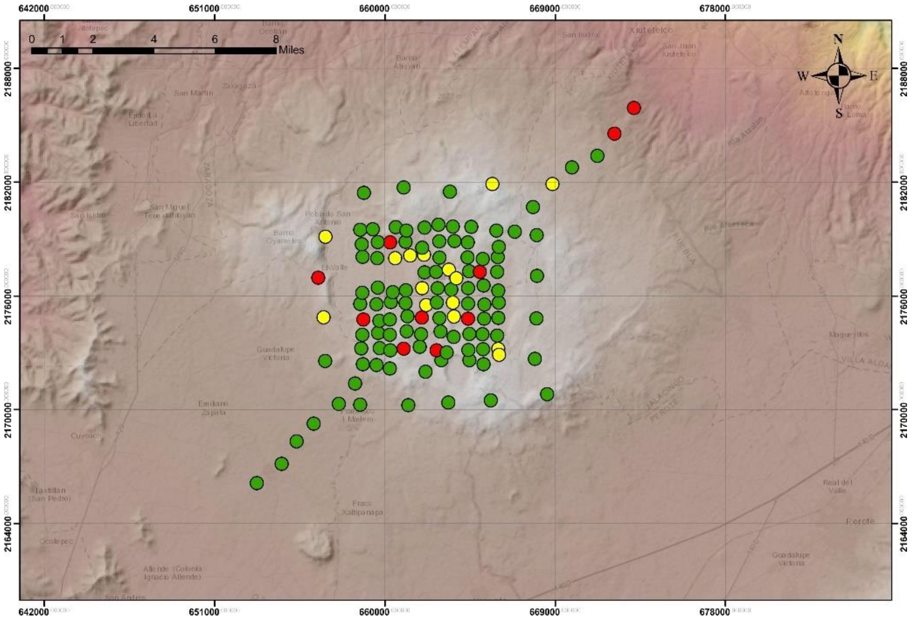

Figure 7: *Data quality of MT measurements from the Los Humeros prospect. Green circles represent measurements of category A, yellow circles belong to category B and red circles to category C.*

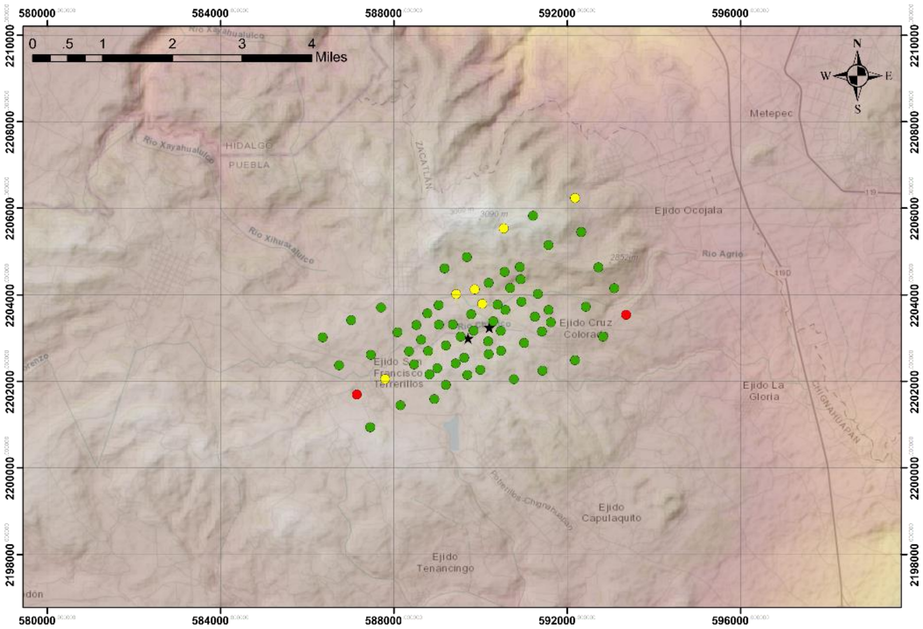

Figure 8: *Data quality of MT measurements from the Acoculco prospect. Green circles represent measurements of category A, yellow circles belong to category B and red circles to category C.*

5 Phase tensor analysis and strike analysis

MT data can give insight into the main electrical orientation of the region. These orientations are usually controlled by some geological phenomena, such as faults or some discontinuities in the subsurface. Here, we use the information from the impedance tensor that can give insight into the main strikes of the area, as a function of period, that can in turn be interpreted as a function of depth.

The parts of the impedance tensor used in each case are briefly presented along with the main results of the analyses.

5.1 Phase tensor analysis

Phase tensor analysis, firstly described by Caldwell et al. (2004), is used to determine the directional behavior of the regional conductivity structures in the study area. The galvanic distortion independent phase tensor Φ can be written as:

$$\begin{bmatrix} \varphi_{11} & \varphi_{12} \\ \varphi_{21} & \varphi_{22} \end{bmatrix} = \frac{1}{\det(X)} \begin{bmatrix} X_{22}Y_{11} - X_{12}Y_{21} & X_{22}Y_{12} - X_{12}Y_{22} \\ X_{11}Y_{21} - X_{21}Y_{11} & X_{11}Y_{22} - X_{11}Y_{12} \end{bmatrix}$$

with X and Y being real and imaginary part of the impedance tensor, respectively. For interpretation the phase tensor can be represented graphically by an ellipse, with its principle axes Φ_{max} and Φ_{min} being the eigenvectors of the complex tensor. The orientation of the axis is affected by the orientation of the main geoelectric strike direction shifting Φ_{max} by the angle α. Galvanic effects (effect of shallow conductivity discontinuities) can distort the EM signal. In those cases, the orientation is biased by the phase tensor skew angle β resulting in an orientation of $\Phi_{max} = \alpha - \beta$ to the observer's coordinate system.

The described parameters are used to deviate the subsurface resistivity structure and its lateral and vertical variations. Angle α, especially in case of consistency, enables the determination of the main geoelectric strike direction, allowing to draw conclusions on geologic or tectonic features yielding this direction. Angle β is a measure, especially in combination with the variability of α, of the dimensionality of the system caused by partly local distortion. If highly variable angles α and high skew angles (β) occur, 3D subsurface resistivity distribution must be considered. The shape of the ellipses contains significant information about the variation of subsurface conductivity distribution. While an elongated ellipse indicated a high lateral conductivity contrast a near circular one points at homogenous nearly 1D conditions. Finally, the size or total area of the ellipses is a measure of the vertical changes of the phase and, hence, conductivity with depth.

5.1.1 Results from Los Humeros

The phase tensor ellipses of the Los Humeros prospect are displayed in a map view in Figure 9. At high to intermediate frequencies (down to a few Hz) large ellipses can be observed. Especially in the western and southern region of the research area enlarged ellipses prevail, hinting at large-scale decreasing resistivities at shallow depth. The NE sector has slightly enlarged phase tensor ellipses at intermediate frequencies (Figure 9 – 6.21 Hz), while the phase tensors in the western and southern sector are already getting smaller. The phase tensors at higher frequencies exhibit homogeneous appearance without a preferred orientation of Φ_{max} and Φ_{min}. The results point towards a layer of a decreased resistivity occurring at variable depth, but these observations need to be confirmed by inversion results. At lower frequencies the phase tensors decrease significantly indicating increased resistivity with depth. A clear anisotropy is observed at low and lowest frequencies (Figure 9 – 20.2429 and 70.4225 sec) with Φ_{max} oriented NE-SW. The anisotropy increases with decreasing frequencies. The phase tensor shape hints towards a body of decreased resistivities located NE or SW of the research area. The almost constant orientation of all ellipses independent of their location indicate a large-scale, regional structure. Considering the slight tendency of anisotropy at intermediate frequencies (Figure 9 – 4.8544) in the NE sector, the origin of anisotropy could be suspected in the NE.

The skew angle β has a higher variance compared to the Acoculco research area. Local clusters of high skew values are observed, but also a general increase of skew angle with decreasing frequencies can be noticed. Consequently, a 3D electromagnetic environment is to be assumed, requiring the application of 3D inversion schemes. A cluster of higher skew values in the northern sector close to the northern caldera rim is identified.

The vertical profiles of the Los Humeros prospect, displayed in two N-S, two E-W and one extended SW-NE profile (Figure 10), underline the findings from horizontal display. Western (NS-1x) and southern (EW-x1) profiles show higher magnitude of average phases than eastern (NS-5x) and northern (EW-x8) profiles. Besides the magnitude of the phases, also the range of increased phases extend over a higher frequency range.

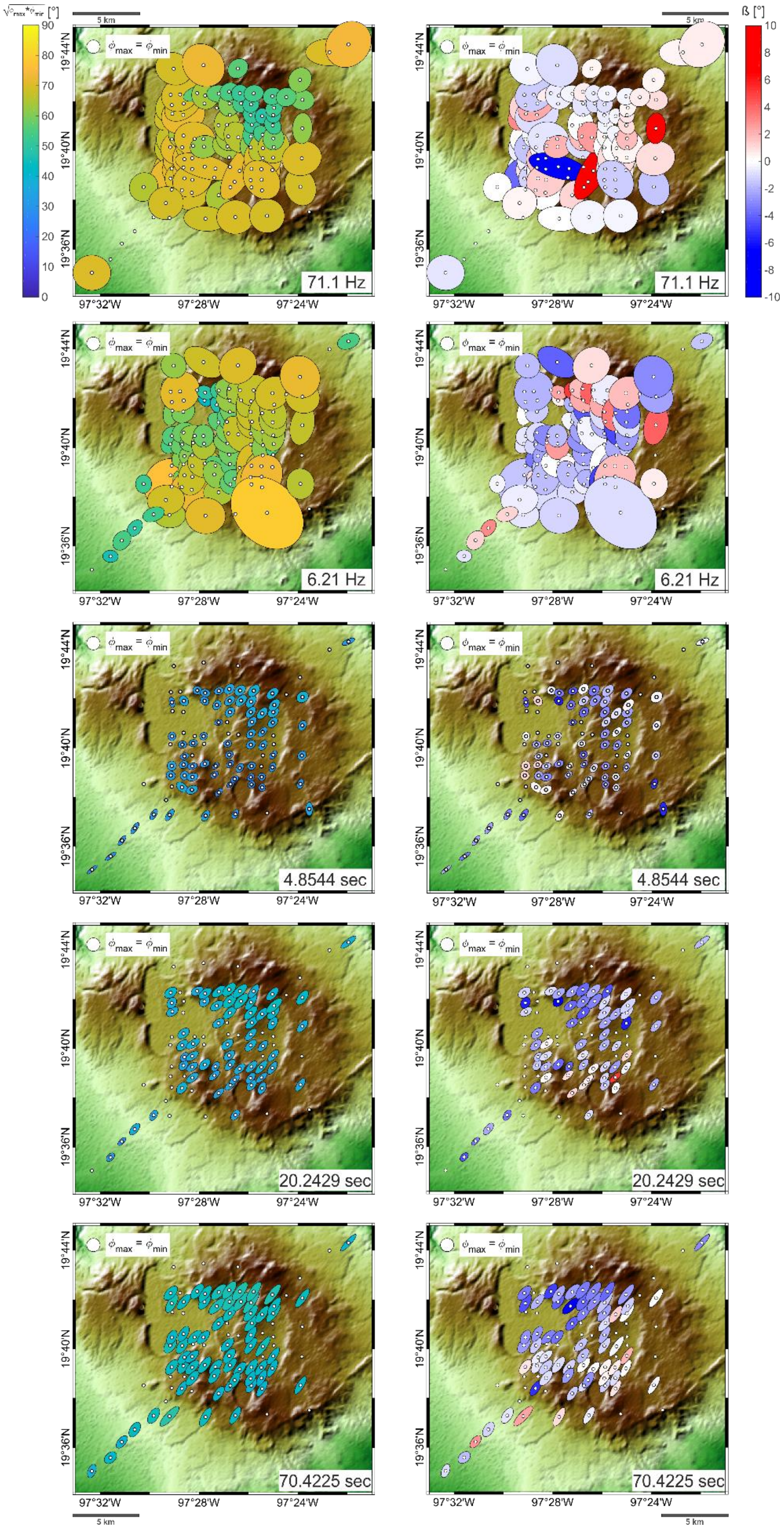

Figure 9: *Horizontal distribution of phase tensor ellipses for different periods displayed for the Los Humeros prospect. The length of the axes is proportional to the principle values (Φ_{max}, Φ_{min}) of the phase tensor. Major axis rotated from E-W direction by angle α – β. Color code at the left side displays the average phase value $\sqrt{\Phi_{max} * \Phi_{min}}$, while the color code at the right side displays skew angle β.*

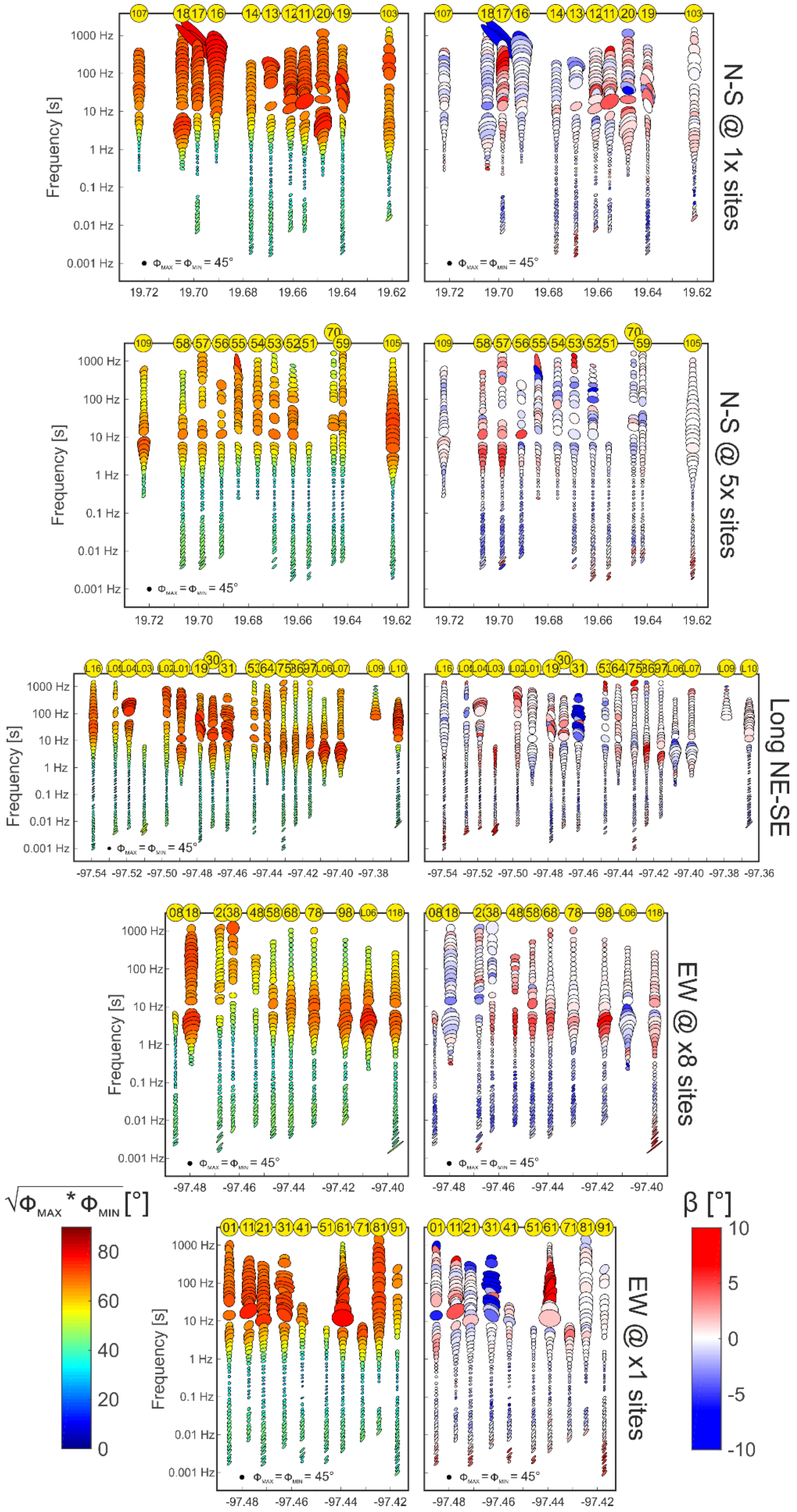

Figure 10: *Vertical plot of phase tensor ellipses for the Los Humeros prospect displayed for two NE-SW profiles. The length of the axes is proportional to principle values (Φ_{max}, Φ_{min}) of the phase tensor. Major axis rotated from E-W direction by angle $\alpha - \beta$. Color code at the left side displays the average phase value $\sqrt{\Phi_{max} * \Phi_{min}}$, while the color code at the right side displays skew angle β.*

5.1.2 Results from Acoculco

Figure 11 displays horizontally the phase tensors of the Acoculco prospect for different frequencies. In general, the skew angle β is low, except for very few local outliers. Just at high periods an increase might be noticed. Yet a complex 3D environment cannot be identified in the data. At higher frequencies (Figure 11 – 284 Hz) the phase tensors show a near-circular shape. A preferential direction cannot be detected. Consequently, a 1D conductivity distribution can be assumed. Like in Los Humeros, the area of the ellipses is big at high frequencies and reduce with decreasing frequency. Yet, compared to Los Humeros, the average phase angle of Acoculco side is smaller in magnitude (Aco: 284 Hz – LH: 71.1 Hz) and occur over a smaller frequency range (Aco: 5 Hz – LH: 4.8sec).

With decreasing frequencies phase tensor ellipses indicate a two-parted subsurface model. West of a line between stations AC019 and AC063 a general reduction of phase angle occurs, while the eastern part is separated of that development maintaining high average phase angles. The existing wells are located west of the separating line in the part of reduced average phase angles. This two-parted appearance remains up to a period of 2 sec. The transition is accompanied by the occurrence of a preferential ellipse orientation in the western, low phase angle area (Figure 11 – 2.5 Hz). At lower frequencies ellipses display a rather homogeneous occurrence of very low phase angles with conservation the preferential orientation (Figure 11 – 2 sec) increasing to low phase angles at highest periods (Figure 11 – 50 sec) without preferential orientation. The origin of the two-parted behavior cannot be assigned from phase tensor analysis alone. To allocate this conductivity, discontinuity to any geological features like a fault or a highly altered zone, additional MT interpretation techniques, like inversion schemes, or other geophysical, geochemical or geological data have to be used.

The vertical phase tensor profiles, displayed in Figure 12, are in good agreement with the previously described results. High phase tensor angles at higher frequencies followed by a two-parted system at intermediate frequencies are consistently observed. Additional information can be derived for the stations 37 and 38 on profile 2 and, noticeable but less obvious, stations 58 – 61 in profile 3. Average phase angle at higher frequencies are significantly lower compared to neighboring stations. Over the whole frequency range phase tensors are more homogeneous having a clear anisotropy at intermediate frequencies. The coincidence of the geothermal surface manifestations and the existing wells as well as the vicinity to the separation between the two parts of different electromagnetic responses is investigated further by application of inversion and especially forward modelling techniques testing different origins (fault zones, local occurrence of cap rocks, etc.) generating that electromagnetic signal.

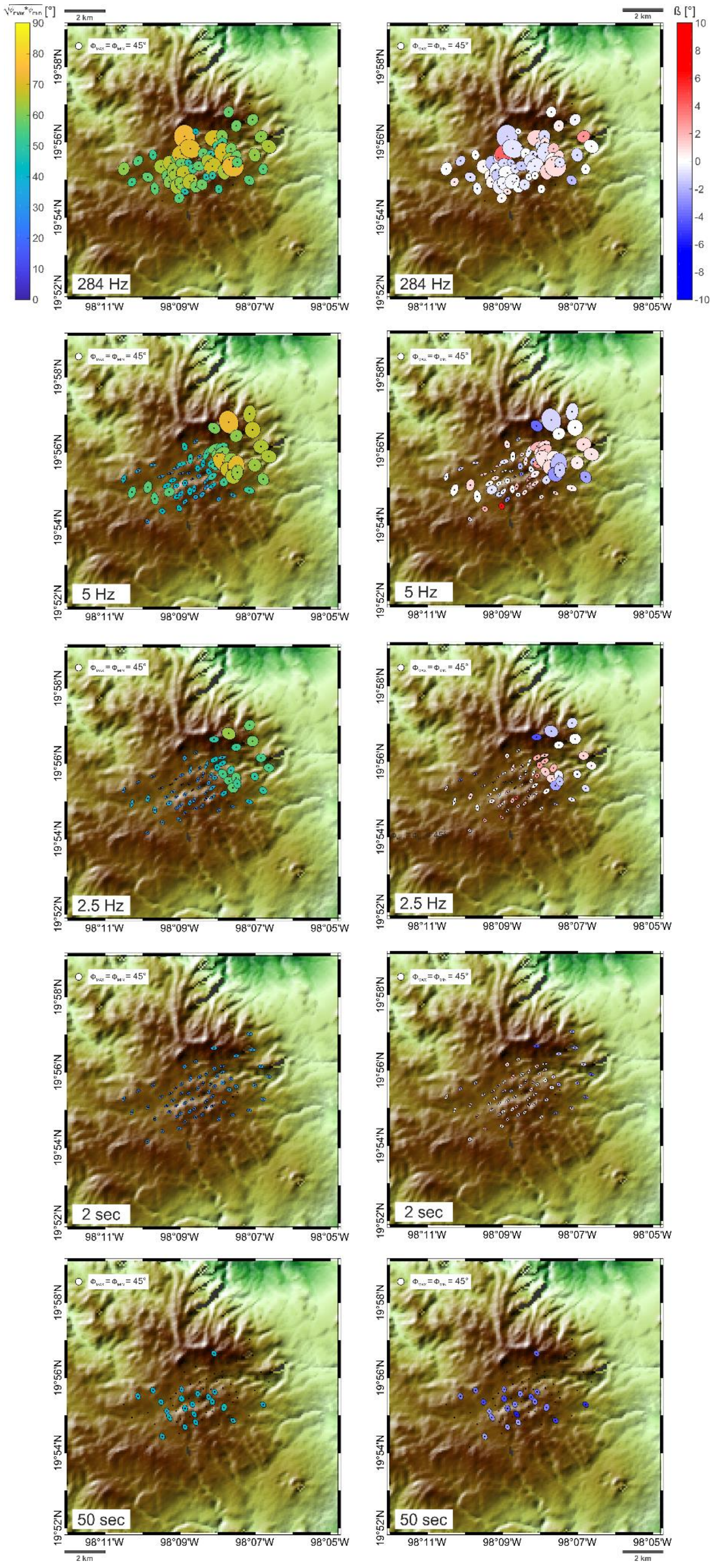

Figure 11: *Horizontal distribution of phase tensor ellipses at different periods displayed for the Acoculco prospect. Lengths of the axes are proportional to principle values (Φ_{max} , Φ_{min}) of the phase tensor. Major axis rotated from E-W direction by angle $\alpha - \beta$. Color code at the left side displays the average phase value $\sqrt{\boldsymbol{\Phi_{max}} * \boldsymbol{\Phi_{min}}}$, while the color code at the right side displays skew angle β.*

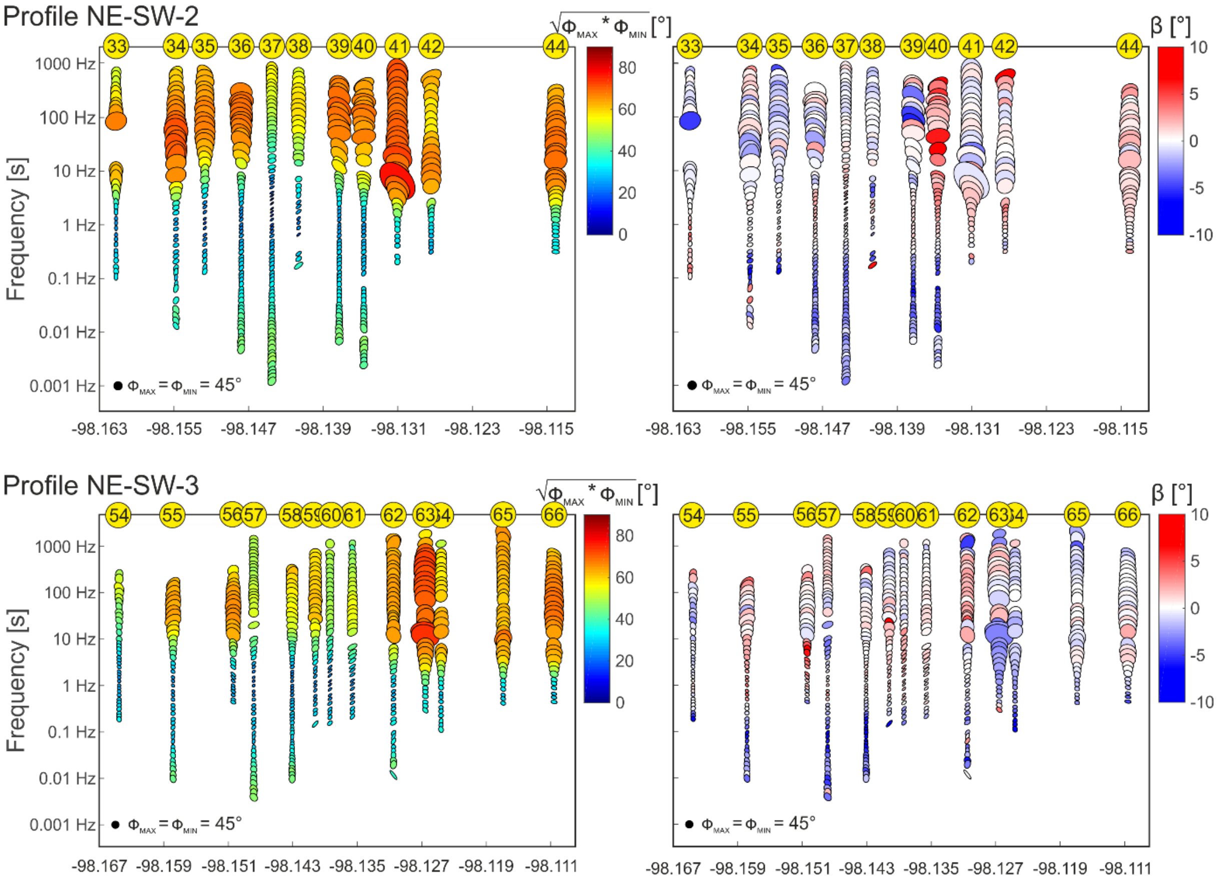

Figure 12: *Vertical plot of phase tensor ellipses for the Acoculco prospect displayed for two NE-SW profiles. Lengths of the axes are proportional to principle values (Φ_{max}, Φ_{min}) of the phase tensor. Major axis rotated from E-W direction by angle $\alpha - \beta$. Color code at the left side displays the average phase value $\sqrt{\Phi_{max} * \Phi_{min}}$, while the color code at the right side displays skew angle β. The two drilled wells are located between stations 37 and 39 at the profile 2 and would reflect positions around station 59 and 61, if display on the southern profile 3.*

5.2 Electrical strike analysis

Electrical strike is often associated with geological faults and fractures, not necessarily seen on the surface. Analysis of the strike can give further information on the subsurface structure and support the resistivity model. In the Los Humeros and Acoculco areas, the electrical strike analysis indicates the directions of lateral resistivity contrasts.

The elements of the MT impedance tensor do, in addition to the resistivity structures below and around the site, depend on the orientation of the x- and y-axis of the field layout. For a 2D Earth, the resistivity varies with depth and in one of the two principal horizontal directions. The horizontal direction perpendicular to that direction is called the geo-electrical strike. The angle the geo-electrical strike, Φ, makes with geographical north is called Swift-angle or Zstrike. It is possible to rotate the coordinate system by mathematical means and recalculate the elements of the impedance tensor for any desired direction. This equals to that the fields, **E** and **H** had been measured in these rotated directions.

If the Earth is 2D and the coordinate system of the field layout has one axis parallel to the geo-electrical strike direction, then: $Z_{xx} = Z_{yy} = 0$, but $Z_{xy} \neq -Z_{yx}$. The geo-electrical strike, Zstrike, can be determined by minimizing the diagonal elements of the impedance tensor: $|Z_{xx}|^2 + |Z_{yy}|^2$ or maximizing the off-diagonal elements: $|Z_{xy}|^2 + |Z_{yx}|^2$ with respect to Φ - the rotation of the coordinate system. There is, however, a 90° ambiguity in the strike angle determined in this way and impossible to distinguish between Φ and $\Phi + 90°$, using calculations based on the impedance tensor alone.

The depth of investigation increases with increasing period. Zstrike depends on the period because the dominant geo-electrical strike can be different at different depths. Vertical magnetic field data, the H_z component, are frequently used for directional analysis through the so-called Tipper, $\boldsymbol{T}$, which relates the vertical component of the magnetic field to its horizontal components:

$$\boldsymbol{H}_z = T_x\boldsymbol{H}_x + T_y\boldsymbol{H}_y \qquad (4)$$

T_x and T_y are the x- and y-component (complex) of the Tipper, respectively. For 1D earth the Tipper is zero, $T_x = T_y = 0$. For a 2D Earth, the coordinate system can be rotated so that the x-axis is in the strike direction, the so-called Tstrike, i.e. $T_x = 0$, but $T_y \neq 0$. This is done by minimizing $|T_x|$. By definition, the Tstrike does not suffer the 90° ambiguity of the Zstrike.

The Tipper can be represented in forms of the real and imaginary parts of the x -and y-components in the form of induction arrows (Figures 13 and 14). According to the sign convention used here (the Wiese convention (Wiese, 1962)), the real arrows point away from a zone of low resistivity at sufficiently low frequencies and towards a zone of higher resistivity (Berdichevsky and Dmitriev, 2002). The length of the arrows indicates the size of the resistivity contrast. For 2D Earth the real and imaginary arrows are collinear and point perpendicular to the geo-electrical strike (Berdichevsky and Dmitriev, 2002).

5.3 Results from Los Humeros

Figures 13 and 14 show the results of the strike analyses in the Los Humeros survey area. Figure 13 and 14 show the induction arrows and T-strike at each survey point in the period range, 0.1 s – 1 s and 1 s – 10 s, respectively. These periods correspond to a depth of a few hundred meters to a few kilometres, respectively.

At 0.5 s the real and imaginary parts of the induction arrows (Figure 13) are collinear pointing roughly NW-SE, suggesting a 2D structure. The T-strike rose diagram for the period range 0.1 s - 1 s has a preferred orientation to the NE-SW, which is in harmony with the induction arrows.

Interestingly, the road that runs through the survey area also splits the direction of the real part of the induction arrows at 0.5 s (Figure 13). It is worth noting that the road runs parallel to the main fault structures in the area. The real part of the induction arrows at soundings, to the west and east of the road, point to the west and northeast, respectively. Therefore, the orientation of the real part of the induction arrows suggests that there is a low-resistivity body along the main faults in the area. We will discover later that this is the low-resistivity cap of the system.

The T-strike in the period range of 0.1 s to 1 s (Figure 13) suggests that the main faults in the area are also a structural boundary. The soundings to the east of the road mostly strike to the NW-SE, whereas the soundings located to the west of the road have a more variable scatter of orientation, going from NNE-SSW to N-S and NNW-SSE, for soundings in the southwest corner and up to the northwest corner.

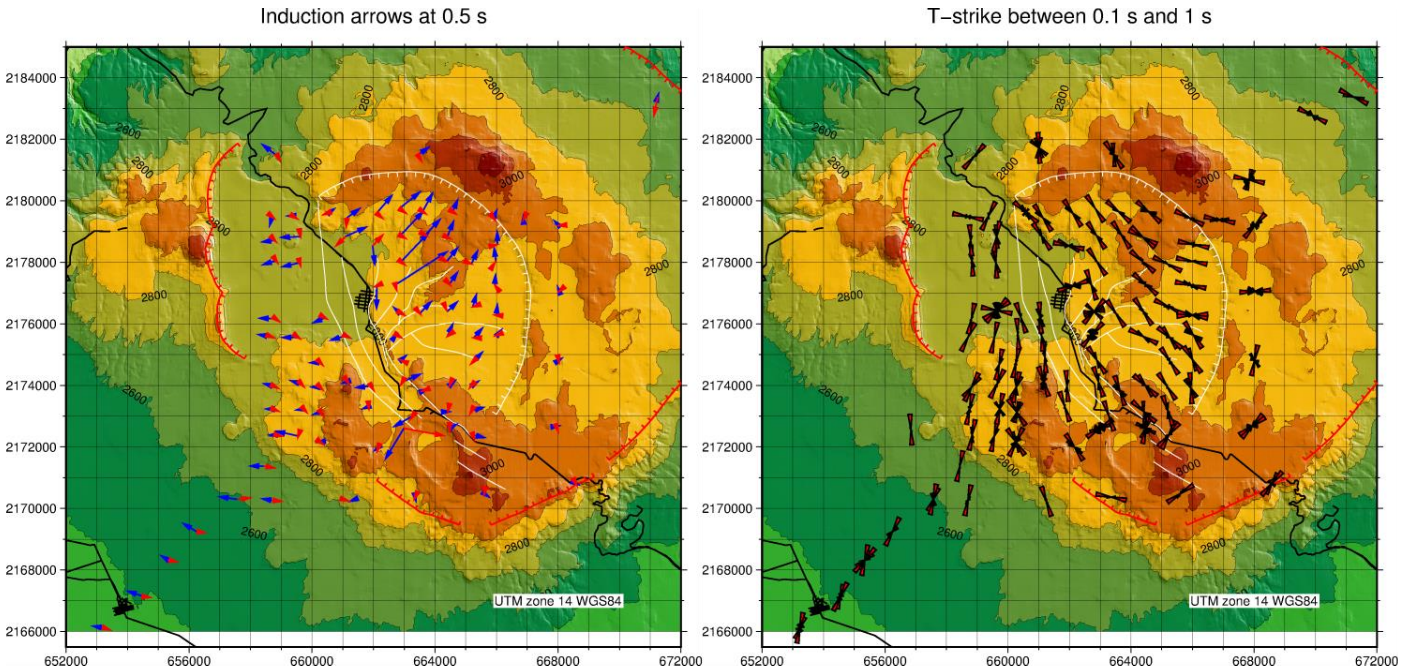

Induction arrows at 0.5 s

T−strike between 0.1 s and 1 s

Figure 13: *Induction arrows at 0.5 s, at each sounding, in the Los Humeros area; blue and red arrows are the real and imaginary components, respectively. (**left panel).** T-strike between 0.1 s – 1 s, at each sounding in the Los Humeros area (**right panel).** Red and white hatched lines are the Los Humeros and Los Potreros calderas, respectively. The white lines are faults in the area and black lines are roads. The coordinate system used is UTM zone 14 WGS84.*

At 5 s the induction arrows exhibit a more variable pattern (Figure 14). The real part of the induction arrows to the west of the road consistently point to the northwest, but are not collinear with the imaginary part, suggesting a 3D resistivity structure. The real part of the induction arrows located to the east of the road point points to directions in the range of N to NNW. Their length increases from south to north, indicating a larger resistivity contrasts in the north. The pattern of the induction arrows is indicative of the presence of an anomalous conductive body close to the southern part of the Los Potreros caldera (white hatched lines in Figure 14).

The T-strike in the range of 1 s to 10 s of the soundings located to the east and west of the road show a dominant strike to the NW-SE and NE-SW, respectively (Figure 14). Again, the barrier along which the distinction between the east and west soundings, can be made, runs along the main NW-SE trending faults in the area, along which the road runs.

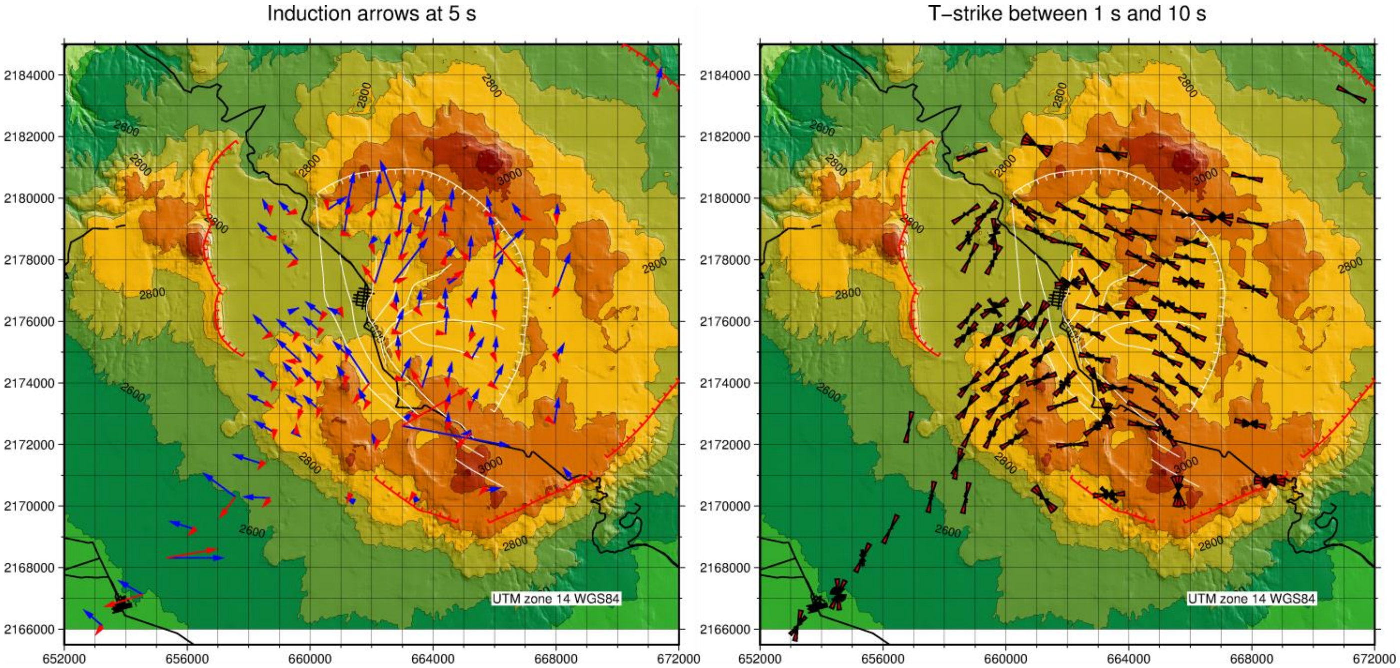

Figure 14: *Induction arrows at 5 s, at each sounding, in the Los Humeros area; blue and red arrows are the real and imaginary components, respectively. (**left panel**). T-strike between 1 s – 10 s, at each sounding in the Los Humeros area (**right panel**). Red and white hatched lines are the Los Humeros and Los Potreros calderas, respectively. The white lines are faults in the area and black lines are roads. The coordinate system used is UTM zone 14 WGS84.*

Figure 15 shows the T-strike for the period range 10 s -100 s and 100 s – 1000 s, reflecting a depth of several km. For the 10 s – 100 s period range, there is still difference between soundings to the east and to the west of the road. The soundings to the west have an E-W orientation while the soundings to the east are oriented NW-SE, like in the 1 s – 10 s period range. The main geo-electrical strike direction in the region at the greatest depth (100 s – 1000 s) is along the main fault orientation in the area, NNW-SSE. The soundings located to the east and west exhibit a similar trend.

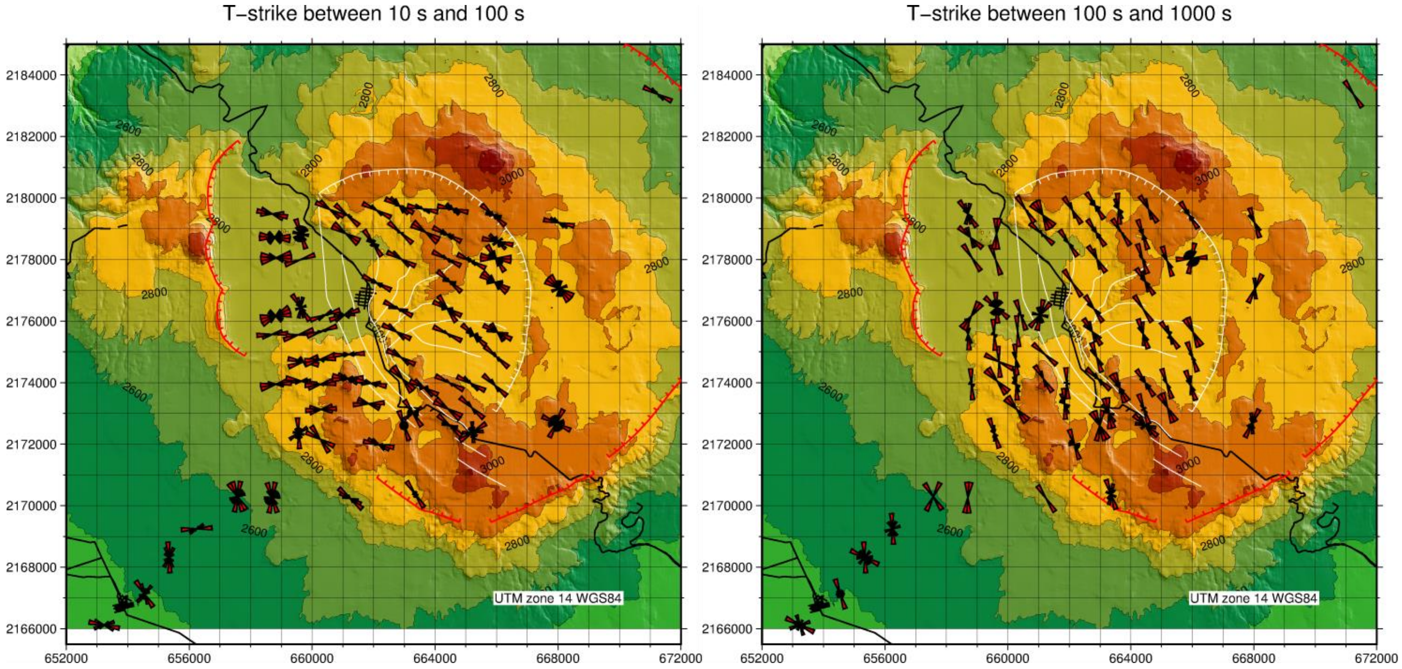

Figure 15: *T-strike between 10 s – 100s (**left panel**) and 100 s and 1000 s (**right panel**). Red and white hatched lines are the Los Humeros and Los Potreros calderas, respectively. The white lines are faults in the area and black lines are roads. The coordinate system used is UTM zone 14 WGS84.*

5.4 Results from Acoculco

Figures 16 - 18 show the results of the strike analyses for the Acoculco survey area. Figures 16 and 17 show the induction arrows and T-strike at each survey point in the period band, 0.1 s – 1 s and 1 s – 10 s, respectively. These period bands correspond to a depth of a few hundred meters to a few kilometres, respectively.

The real part of the induction arrows at 0.5 s (Figure 16) for soundings located in the center of the survey area, show a preferred orientation towards a location near the western well (western magenta star in Figure 3), suggesting a presence of a resistive body at that location.

The T-strike in the period range 0.1 s – 1 s (Figure 16) is scattered, although some patterns can be seen. Many of the soundings exhibit a preferred SW-NE orientation, along one of the main faults in the area while preferred orientation at other soundings seem to fall in line with the other fault trends in the area, SE-NW.

The length of the real part of the induction arrows at 5 s (Figure 17) is small, suggesting a 1D earth. Note that in some cases, for soundings located in the outskirts of the survey area, the length of the real part of the induction arrow is large. This is either due to some local effects in the structure but, more likely, due to noise in the vertical magnetic component (H_z) of the sounding data.

The T-strike in the period range 1 s – 10 s (Figure 17) is very scattered for soundings in the eastern part of the survey area, where no preferred orientation seems to be present. For soundings located to the east of the eastern well (eastern magenta star in Figure 3) the preferred direction seems to be NNW-SSE and NE-SW for soundings located south and north of the SW-NE fault, respectively.

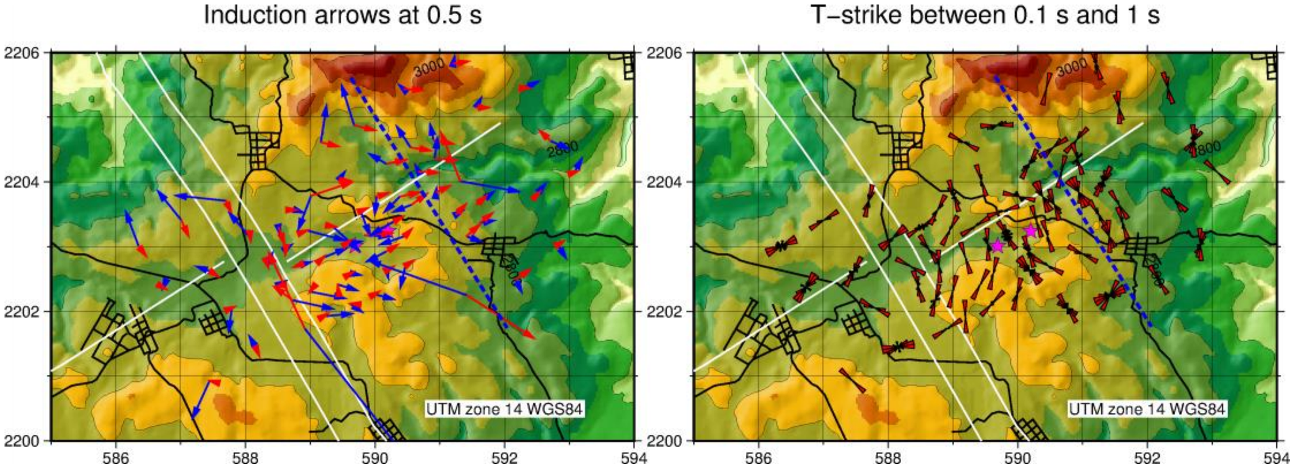
Induction arrows at 0.5 s

T-strike between 0.1 s and 1 s

Figure 16: *Induction arrows at 0.5 s, at each sounding, in the Acoculco area; blue and red arrows are the real and imaginary components, respectively.* ***(left panel).*** *T-strike between 0.1 s – 1 s, at each sounding in the Acoculco area* ***(right panel).*** *The white lines are faults in the area and black lines are roads. Two magenta filled stars are the locations of the two EAC wells. The blue dashed line divides the area into two parts, see text for detail. The coordinate system used is UTM zone 14 WGS84.*

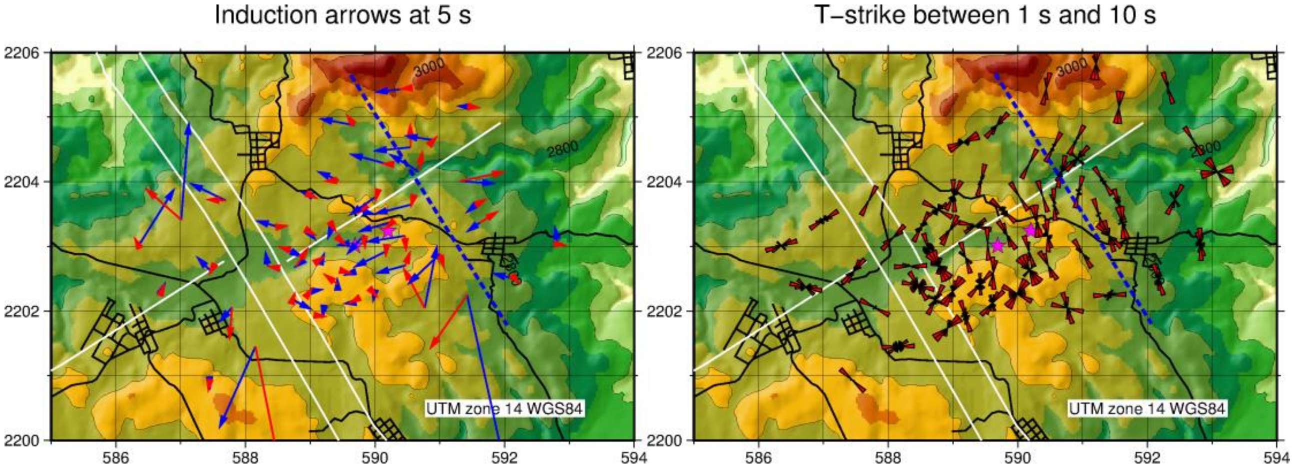
Induction arrows at 5 s

T–strike between 1 s and 10 s

Figure 17: *Induction arrows at 5 s, at each sounding, in the Acoculco area; blue and red arrows are the real and imaginary components, respectively.* ***(left panel).*** *T-strike between 1 s – 10 s, at each sounding in the Acoculco area* ***(right panel).*** *The white lines are faults in the area and black lines are roads. Two magenta filled stars are the locations of the two EAC wells. The blue dashed line divides the area into two parts, see text for detail. The coordinate system used is UTM zone 14 WGS84.*

5.5 Conclusion

The phase tensor and tipper of the MT soundings in the Los Humeros and Acoculco survey areas have been analysed. In Los Humeros there is a clear transition in the behaviour of the data along the main NW-SE trending faults. The soundings to the west exhibit a fairly stable T-strike through the different period ranges, within the range of NW-SE to NNW-SSE. The T-strike for soundings to the east of the main trending faults is from N-S, to SW-NE, to E-W and then, at the greatest depth, NNW-SSE. The phase tensor ellipses at the longest periods agree well with the results of the T-strike analyses. The phase tensor analyses are suggestive that the resistivity structure is highly three-dimensional, where the skew angles range from 10° to -10°.

In Acoculco the phase tensor analyses suggest a one-dimensional resistivity structure. The skew angles scatter around zero and the phase tensor ellipses can be approximated as a circle. The survey area in Acoculco can be divided into two parts (Figures 16-18). In the eastern part the area of the phase tensor ellipses is larger, as compared to the western ellipses, suggesting a more vertical contrast in resistivity structure to the east. The soundings to the east exhibit a N-S preferred orientation according to the T-strike for all frequencies. The real part of the induction arrows at 0.5 s (Figure 16) suggest the presence of circular resistive body just east of the eastern EAC well.

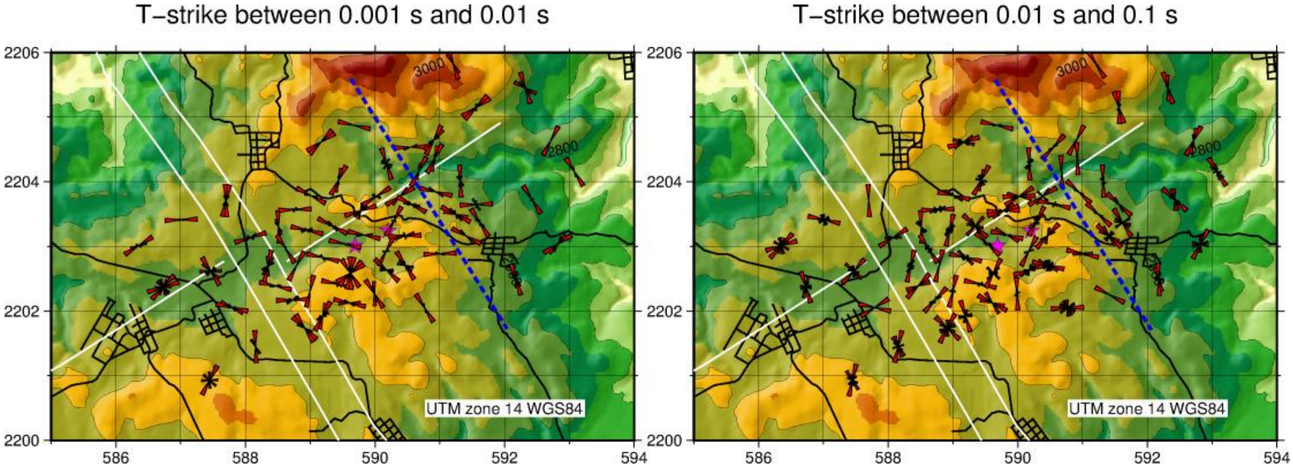

Figure 18: *T-strike between 0.001 s – 0.01 s (**left panel**) and 0.01 s – 0.1 s (**right panel**). The white lines are faults in the area and black lines are roads. Two magenta filled stars are the locations of the two EAC wells. The blue dashed line divides the area into two parts, see text for detail. The coordinate system used is UTM zone 14 WGS84.*

6 1D inversion of the resistivity data

6.1 1D joint inversion using TEMTD

In 1D inversion of MT data it is customary to invert for one of the three rotational invariant parameters:

$$Z_{av} = \frac{Z_{xy} - Z_{yx}}{2}$$

$$Z_{det} = \sqrt{Z_{xx}Z_{yyY} - Z_{xy}Z_{yx}}$$

$$Z_{gm} = \sqrt{-Z_{xy}Z_{yx}}$$

All these parameters give the same values for a 1D earth response, for a 2D earth the *det* (determinant) and the *gm* (geometric mean) reduce to the same value but the *av* (arithmetic mean) is different. For a 3D response, all these parameters are different.

There are different opinions on which of the three invariants, if any, is best suited for a 1D inversion. However, based on the comparison of model responses for 2D and 3D models, it has been suggested that the determinant invariant is the one to use (see e.g. Park and Livelybrook, 1989) and that was done for the data from Mexico presented in this deliverable.

The 1D inversion was done by using the TEMTD code (Árnason, 2006b). Apparent resistivity and phase, calculated from the determinant of the MT impedance tensor were inverted jointly with TEM data. In the joint

TEM/MT inversion, a static shift parameter (Árnason, 2015) is obtained; the TEM data are used to shift the MT apparent resistivity curve up (shift < 1), or down (shift > 1) a described earlier in this deliverable.

Occam's inversion (Constable et al, 1987) was used with 100 horizonal layers. In the Occam's inversion the thicknesses of the layers are kept fixed and they grow exponentially with depth until their reach a homogeneous half-space. With this parametrization the structure is minimized with a smoothly varying resistivity structure with depth. The parameters inverted for are the resistivity values of each layer. Inversion parameters (e.g. the bottom to the homogeneous half-space and initial model) varied from one sounding to another depending on the data. When MT and TEM data were jointly inverted for, one begins by fitting the MT data and then the best fitting model is used as a starting model for the joint inversion.

When a sounding pair has been inverted, the resulting models at all sounding locations are interpolated to form one model. The results are presented in the forms of horizontal and vertical cross-sections.

In Chapter 6.2 and 6.3 we show results of the 1D joint inversion for Los Humeros and Acoculco, respectively.

6.2 Los Humeros: Resistivity model based on joint 1D inversion of TEM and MT data

Figure 19 shows the location of the resistivity soundings in the Los Humeros survey area. A total of 91 MT/TEM sounding pairs were 1D jointly inverted and 13 MT soundings with no co-located TEM data. Some of the TEM soundings are of bad data quality and are therefore, not used in the inversion and in some cases the sounding site was not accessible because of crops which had been planted in the fields where MT sounding data had been acquired. Figure 20 shows examples of inverted MT/TEM pair (Figure 20A) and where only MT data were available (Figure 20B).

Figure 21 shows horizontal cross-sections ((depth-slices) through the 1D model at four different depths. We refer the reader to Appendix B for a complete set of depth-slices through the 1D resistivity model of Los Humeros. At 2600 meters above sea level (Figure 21A) a conductive clay cap is revealed along the main NW-SE trending faults and it is surrounded by zones of higher resistivity. At 2000 meters above sea level (Figure 21B) intermediate to low resistivity values are present. At this depth some parts of the conductive cap are visible (in the south) and areas of slightly higher resistivity values (≈50 Ωm) are seen north and south of the town of Los Humeros, showing the top of the resistive core.

At 1000 meters above sea level (Figure 21C) the NW-SE trending resistive core is seen. The orientation of the resistive core is the same as the orientation of the conductive cap in Figure 21A. A low resistivity zone in the southern end of the survey area is most likely only due to one sounding (sounding LH106). At deeper level, 3000 meters below sea level (Figure 21D), an intermediate NW-SE trending body is seen in a resistive surrounding.

Figures 22 and 23 show two cross-sections through the 1D resistivity model of Los Humeros, reaching down to sea level and 5 km below sea level. For other vertical sections P1, P2 and P3, see Appendix A.

In Figure 22 we see a shallow lying conductive cap extending from below sounding LHL101 to the SW to sounding LH064 in the NE. East of sounding LH064 the conductive cap plunges down. In Figure 23 we see the conductive cap in the middle of the profile and a deep-lying low-resistivity body right below the conductive cap. The deep-seated low-resistivity body is also seen in the vertical cross section at 3000 meters below sea level (Figure 21D).

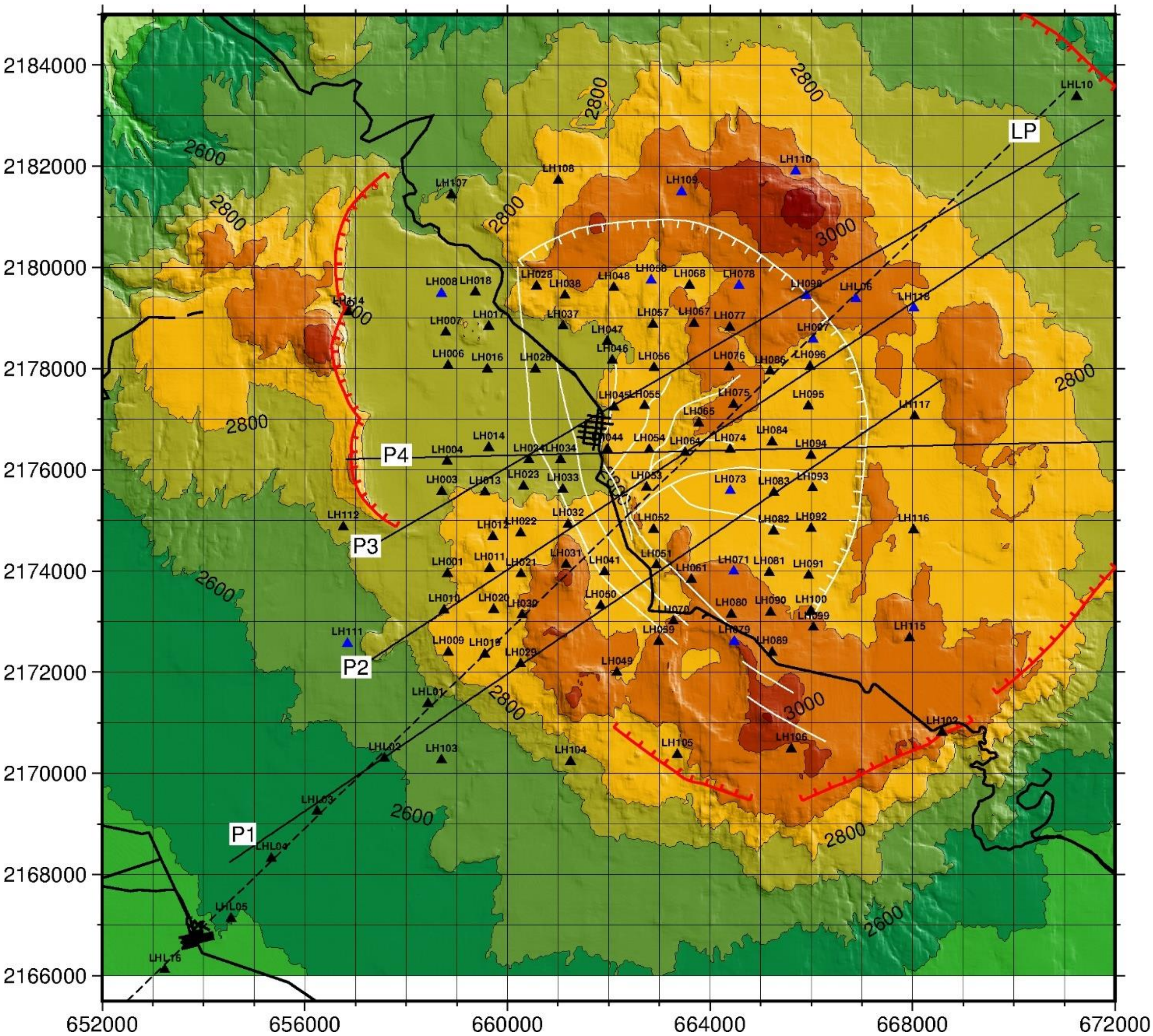

Figure 19: *Location map of the Los Humeros survey area. Triangles are the co-located MT and TEM soundings. Black and blue triangles denote soundings that where static shift corrected, and not static shift corrected, respectively. Names of the soundings are labelled above the triangles. Red and white hatched lines are the Los Humeros and Los Potreros calderas, respectively.* The thick

black lines are roads and white lines are main faults in the region. The location and names of five vertical cross-sections are shown as four black thin lines (P1, P2, P3, P4) and a dashed line (LP)

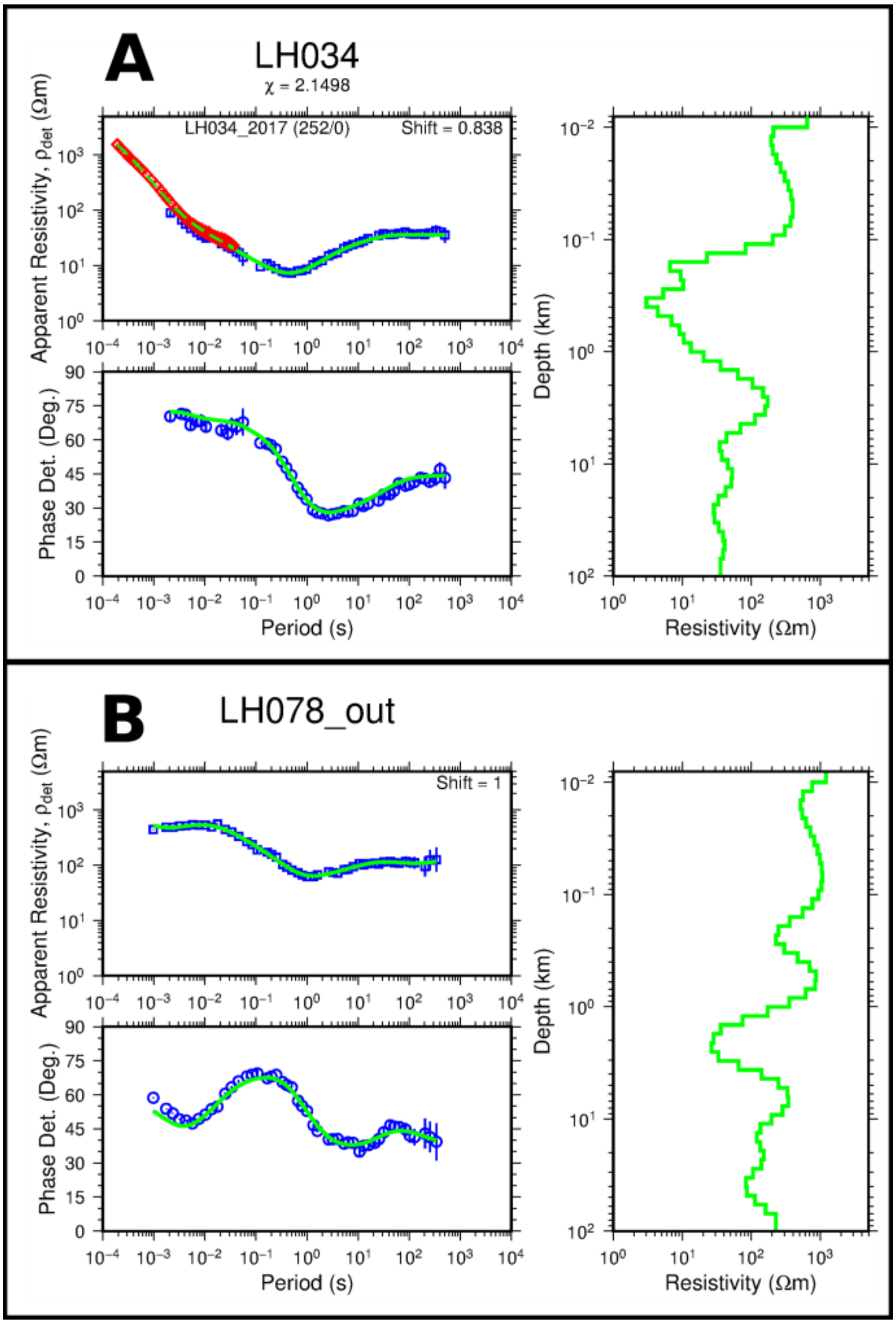

Figure 20: *Examples of 1D inverted resistivity data. In both* ***A*** *and* ***B****: the upper left panel is the apparent resistivity of TEM data transformed to a pseudo curve (red points) and MT data (blue points). The green curve is the apparent resistivity response of the model shown in the right panel. The lower left panel is the phase of the MT data (blue points) and the green curve is the MT phase response of the model.* ***A****. Inversion of sounding LH034 where both MT and TEM data were inverted for jointly. The static shift is shown in the upper right corner of the upper left panel.* ***B.*** *Inversion of sounding LH078 where only MT data were available. For location of the soundings, see Figure 19.*

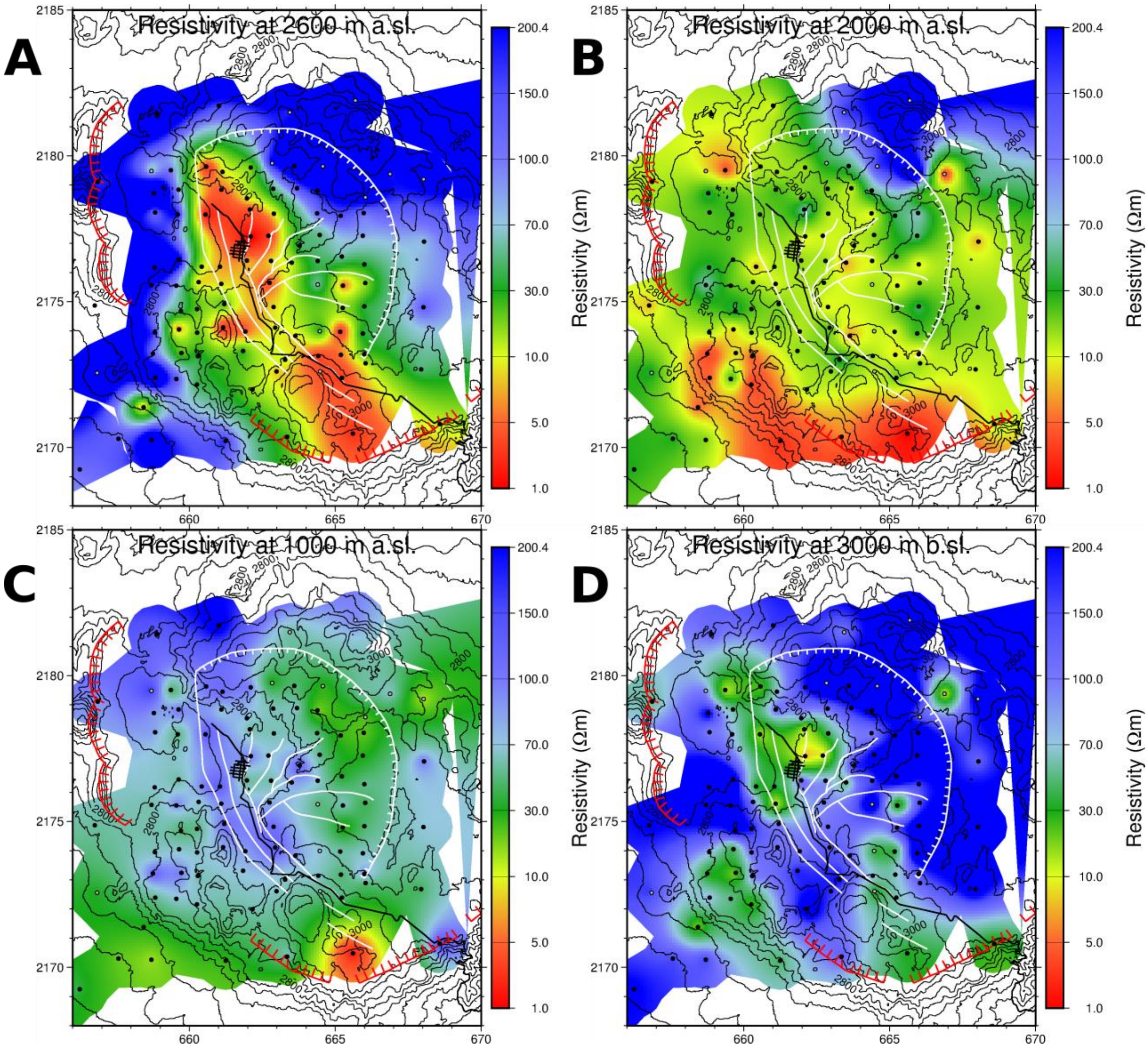

Figure 21 *Horizontal cross-sections (depth-slices) through the 1D model of the Los Humeros prospect at 2600 meters above sea level (**A**), 2000 meters above sea level (**B**), 1000 meters above sea level (**C**) and 3000 meters below sea level (**D**). White and red hatched lines are the Los Potreros and Los Humeros calderas, respectively. Black lines are roads and white lines are main faults in the region. The town of Los Humeros is where the roads form a dense grid. Black circles are MT sounding locations and elevation contour lines are thin black lines, every 100 meters.*

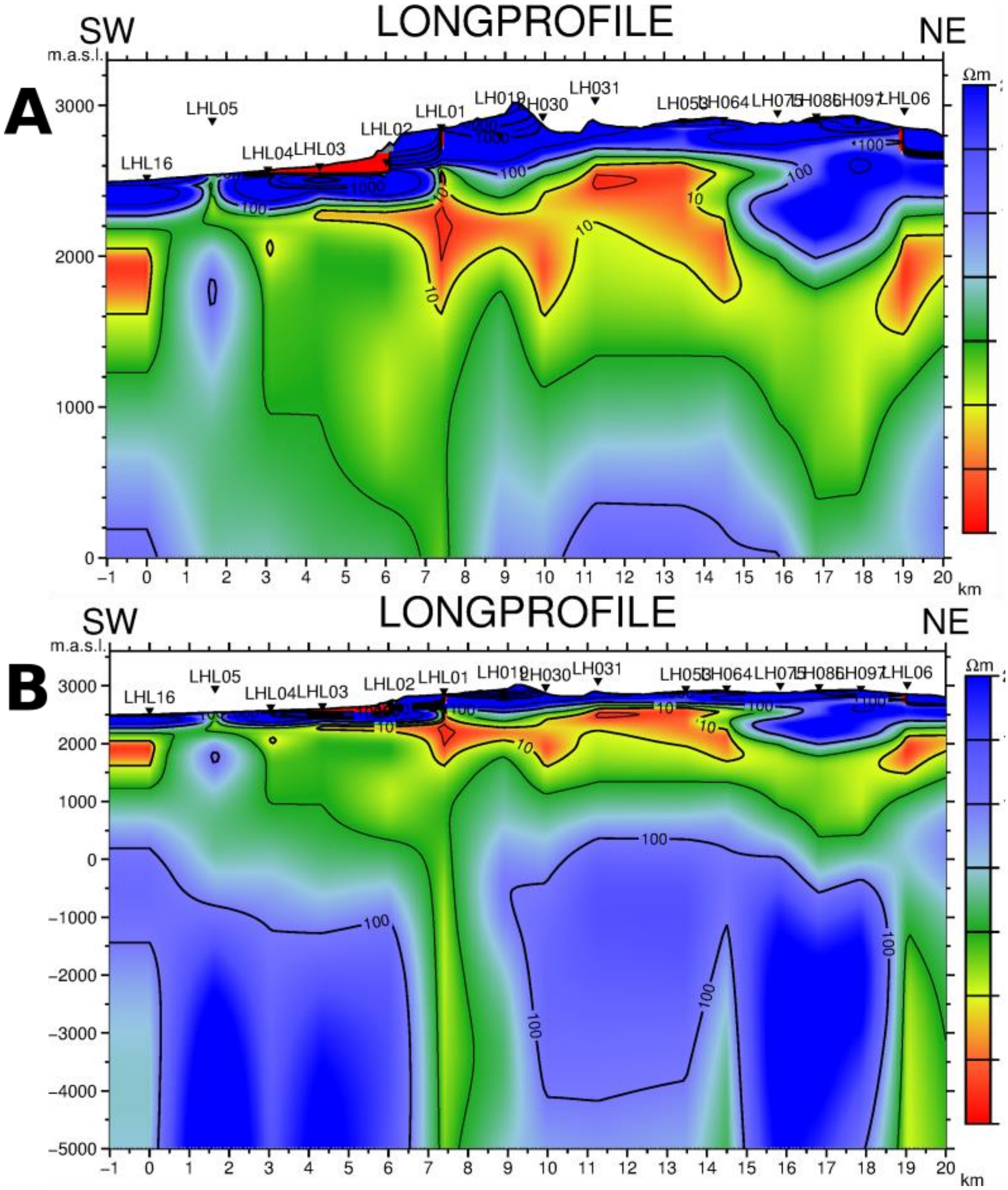

Figure 22: *Vertical cross-section through the 1D resistivity model of Los Humeros, plotted down to sea level (**A**) and 5000 meters below sea level (**B**). Triangles at the surface are the soundings location with their names. The location of the cross-section is marked as LP on Figure 19.*

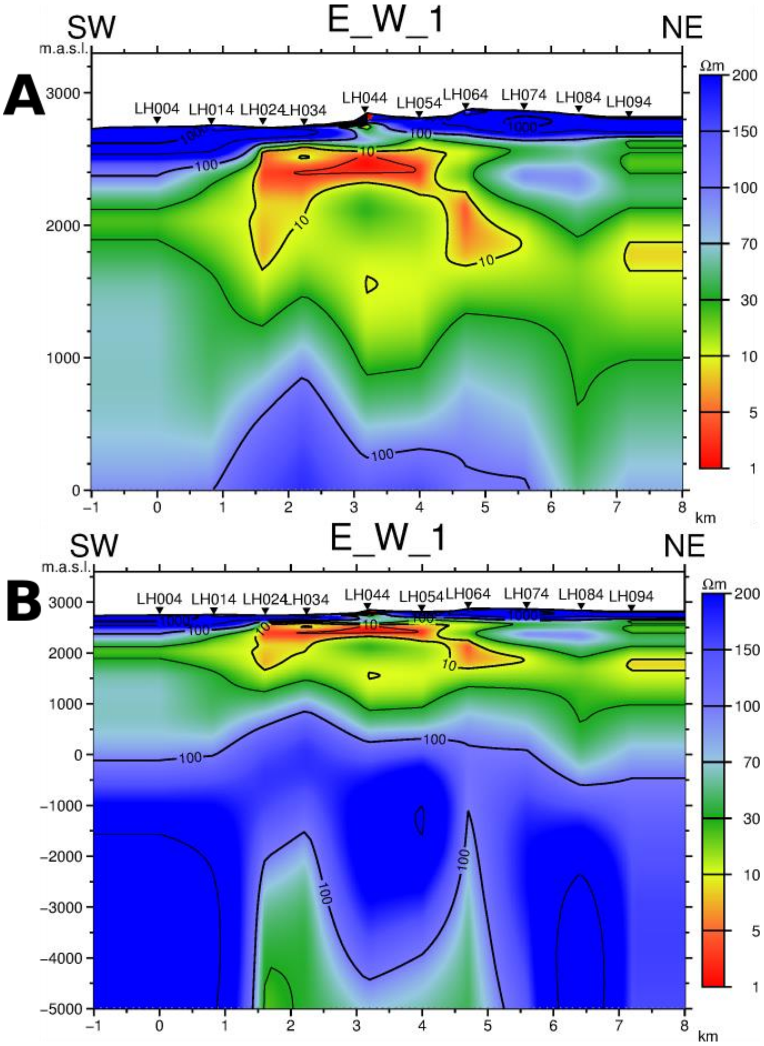

Figure 23: *Vertical cross-section through the 1D resistivity model of Los Humeros, plotted down to sea level (**A**) and 5000 meters below sea level (**B**). Triangles at the surface are the soundings location with their names. Location of the cross-section is marked as P4 in Figure 19.*

6.3 Acoculco: Resistivity model based on 1D joint inversion of TEM and MT data

Figure 24 shows the location of the resistivity soundings in the Acoculco survey area. A total of 65 TEM/MT sounding pairs were jointly inverted and one MT sounding with no co-located TEM data. In that case of bad quality TEM data, the shift was assumed to be 1. Figure 25 shows examples of inverted MT/TEM pair (Figure 25A) and where only MT data were available (Figure 25B).

Figure 26 shows horizontal cross-sections (depth-slices) through the 1D model for four different depths. We refer the reader to Appendix B for a complete set of depth-slices through the 1D resistivity model of the Acoculco survey area. At 2700 meters above sea level (Figure 26A) a conductive clay cap is revealed in most of the survey area, besides the area east of a transition zone, also discussed in Chapter 5.4. At 2500 meters above sea level (Figure 26B) intermediate values are present below the conductive cap at 2700 meters above sea level. The highest resistivity values are below the western EAC well, which is surrounded by zones of lower resistivity, indicating that this is the location of the resistive core. On the east side of the transition zone, low resistivity values are present.

At 1500 meters above sea level (Figure 26C) the area to the west of the transition zone exhibits high resistivity values but the area to the east is characterized by intermediate values. In the area between 1500 meters above sea level down to 3000 meters above sea level (Figure 26D) the resistivity structure remains similar

Figures 27 and 28 show two cross-sections through the 1D resistivity model of Acoculco, reaching down to sea level and 5 km below sea level.

Figure 27, is a NW-SE lying cross-section through the model. The resistivity structure is characterized by a resistive and conductive surface to the NW and SE, respectively. It can therefore, be argued that the conductive cap reaches the surface to the SE. The resistive core domes up below the area, between sounding AC016 and AC061. At greater depth, a layer of intermediate resistivity is present between 1000 – 5000 meters below sea level, which is cut by a column of a higher resistive area located directly under the area between soundings AC027 and AC049.

Figure 28 shows a SW-NE lying cross-section through the model. The conductive cap is thick towards the edges of the profile but becomes thinner towards the center below soundings AC035-AC039. The resistive core clearly domes up, symmetrically, underneath the center of the area under sounding AC037, which is located close to the eastern EAC well.

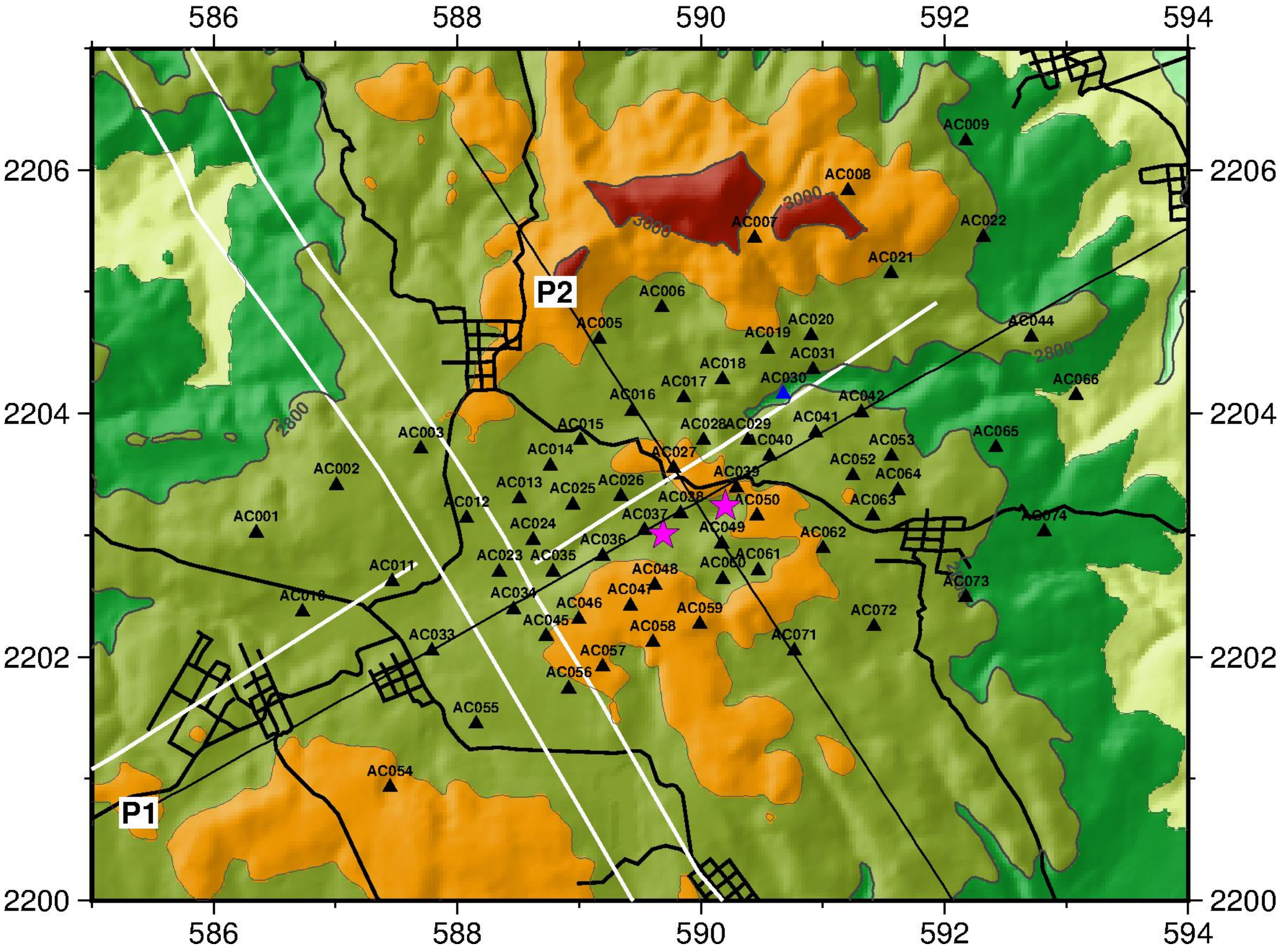

Figure 24: *Location map of the Acoculco area. Triangles are the sounding location with (black) and without (blue) TEM data. Purple stars are the two EAC wells, thick lines are roads and white lines are major faults in the area. The thin black lines are location of vertical sections, P1 and P2 through the resistivity model.*

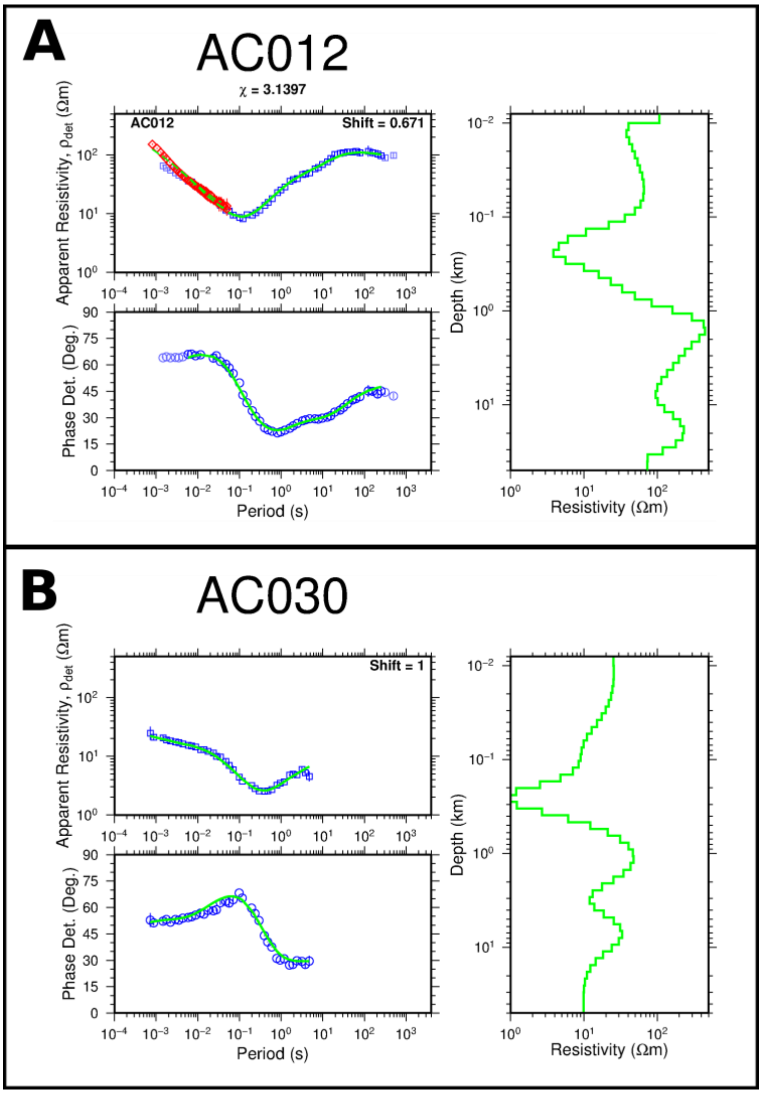

Figure 25: *Examples of 1D inverted resistivity data. In both* ***A*** *and* ***B****: the upper left panel is the apparent resistivity of TEM data transformed to a pseudo curve (red points) and MT data (blue points). The green curve is the apparent resistivity response of the model shown in the right panel. The lower left panel is the phase of the MT data (blue points) and the green curve is the MT phase response of the model.* ***A****. Inversion of sounding AC010 where both MT and TEM data were inverted jointly for. The static shift is shown in the upper right corner of the upper left panel.* ***B.*** *Inversion of sounding AC030 where only MT data were available. For location of the soundings, see Figure 24.*

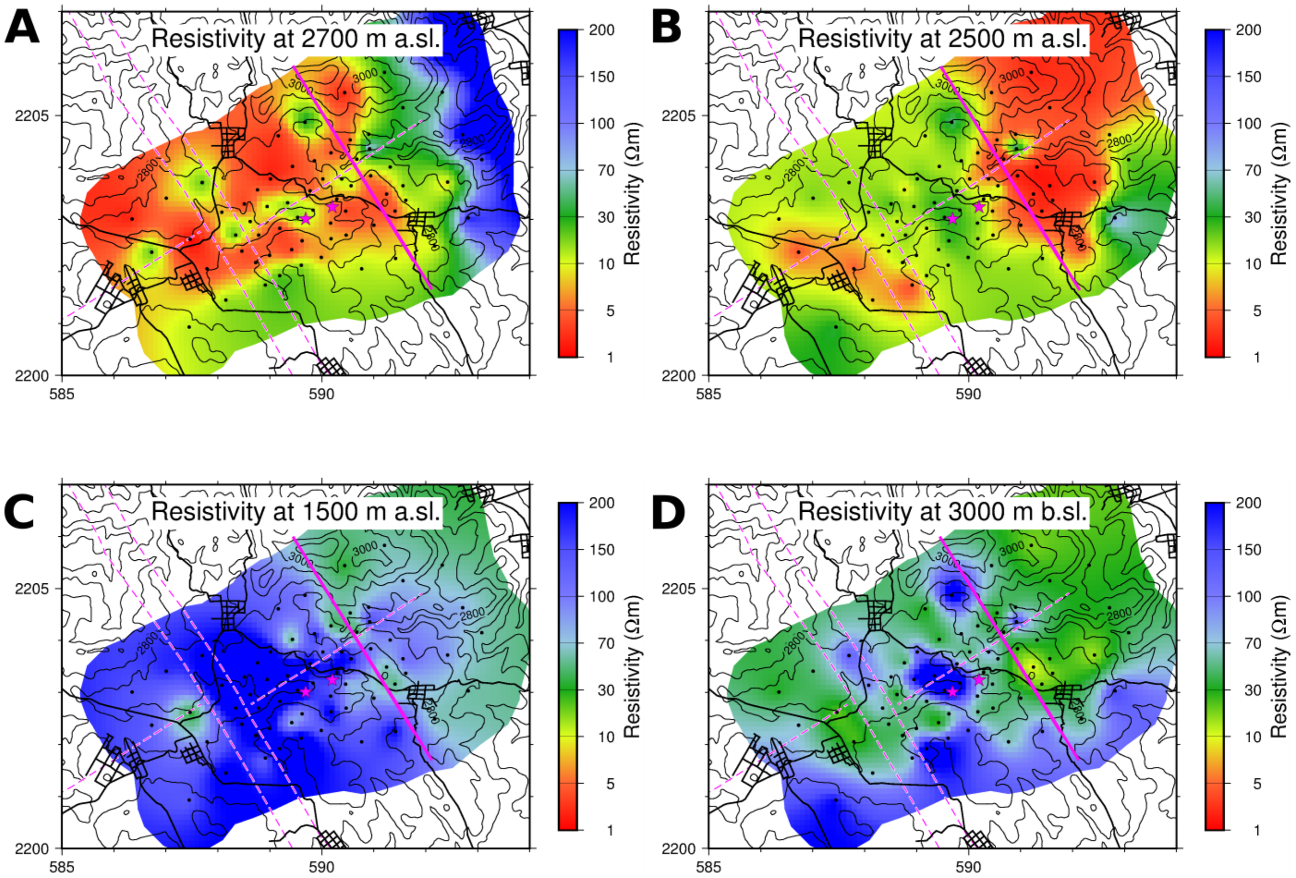

Figure 26: *Horizontal cross-sections through the 1D model of the Acoculco area at 2700 meters above sea level (**A**), 2500 meters above sea level (**B**), 1500 meters above sea level (**C**) and 3000 meters below sea level (**D**). Thick black lines are roads, thin black lines are elevation contours every 50 meters. Pink starts are the locations of the EAC wells, dashed pink lines are major fault lines and thick pink line is the discontinuity as observed from the resistivity data.*

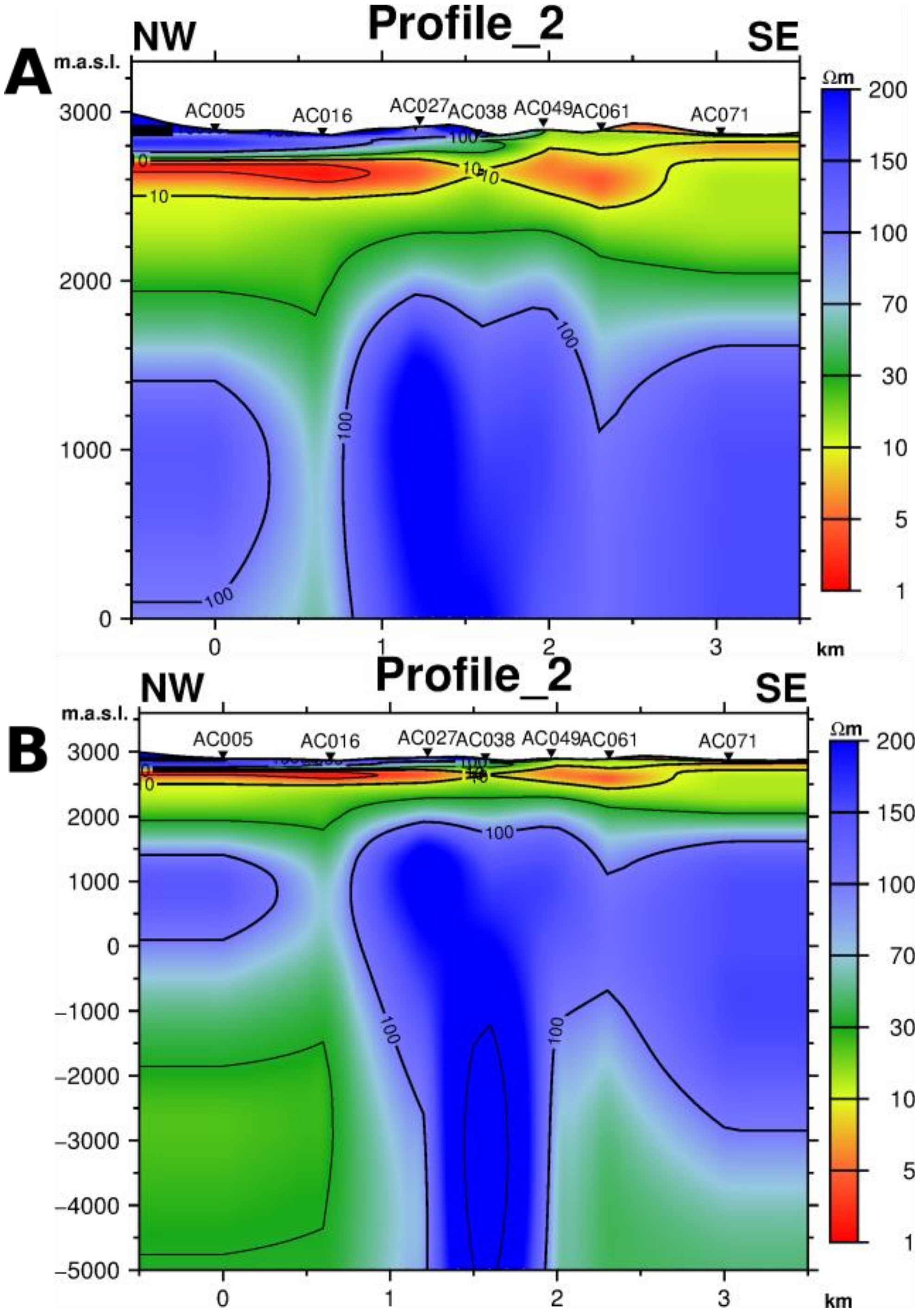

Figure 27: *NW-SE vertical cross-section through the 1D resistivity model of the Acoculco area plotted down to sea level (**A**) and 5000 meters below sea level (**B**). Triangles at the surface are the soundings location with their names. The location of the profile is shown in Figure 24.*

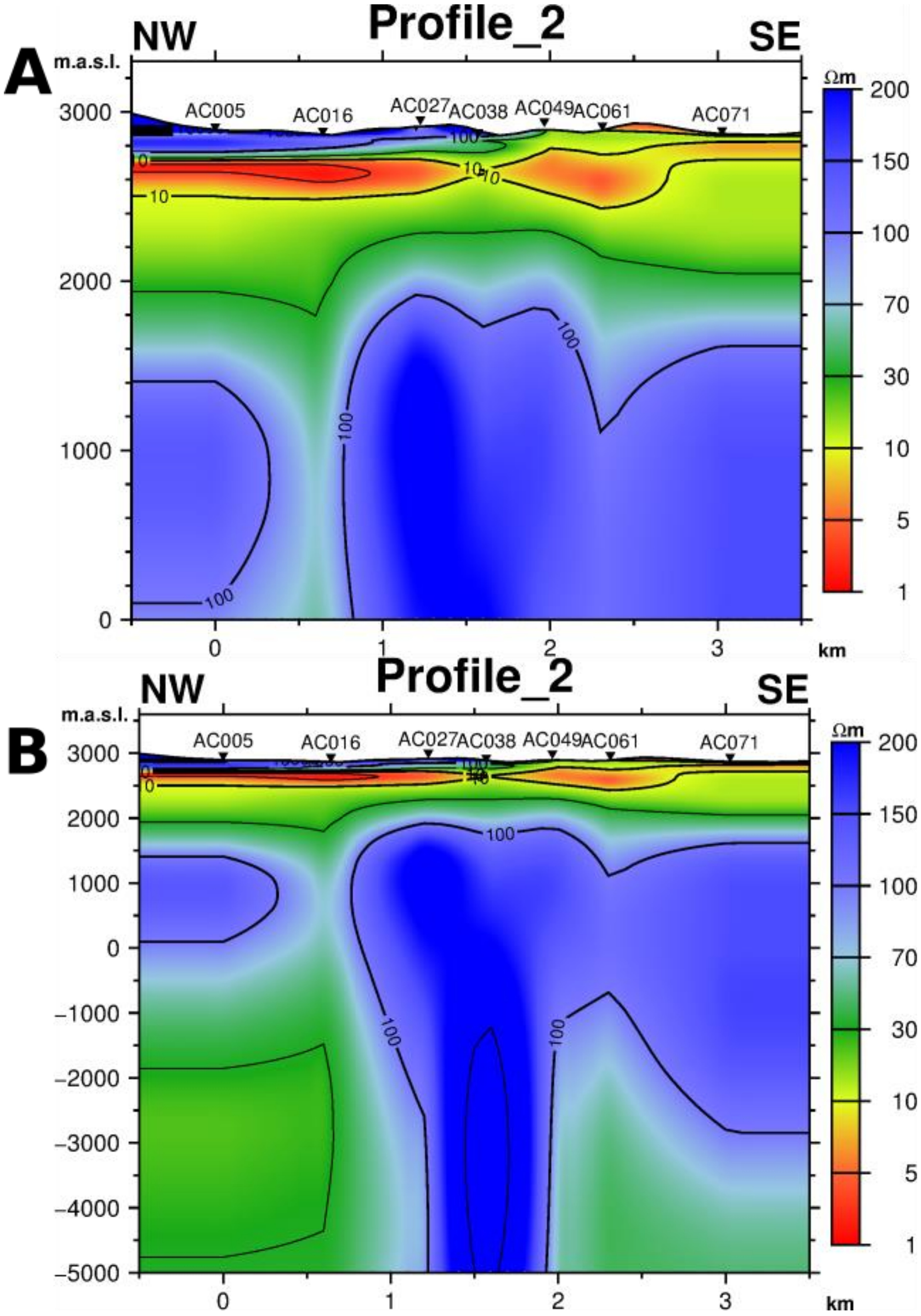

Figure 28: *SW-NE vertical cross-section through the 1D resistivity model of the Acoculco area, plotted down to sea level (**A**) and 5000 meters below sea level (**B**). Triangles at the surface are the soundings location with their names. The location of the profile is shown in Figure 24.*

6.4 Conclusion

The 1D resistivity structure in Los Humeros is three-dimensional, as indicated in the phase tensor and strike analyses and discussed in the previous Chapter. The resistivity structure is aligned with the main NNW-SSE faults in the region. The conductive cap is seen to align with that direction at 2700 meters above sea level. The main up-doming feature in the area lies at the main NNW-SSE faults in the region, which is underlain by an intermediate-resistivity layer at depths greater than 2000 meters.

The resistivity model based on 1D inversion in the Acoculco survey area exhibits a one-dimensional resistivity structure, as predicted by the dimensionality analyses and discussed in the previous Chapter. The area explored is divided into two areas that can be distinguished from one another, maybe the boundary is a buried fault. The conductive cap becomes thinner close to the western EAC well. It is in this area where the resistive core is the shallowest in a very confined area, suggesting the existence of a zone of geothermal interest.

7 Computational intelligence applied to the geophysical study of the Acoculco geothermal system (Mexico)

7.1 Introduction

This chapter is aimed at describing the results of an innovative approach applied to the geophysical study of the Acoculco geothermal field. We exploit computational intelligence (CI) methods for the quantitative data integration of different datasets, by jointly solving the inverse problem of TEM, vertical electrical sounding (VES) and MT.

The methods for solving the inverse problem can be classified into deterministic and probabilistic. Deterministic methods are the conventional means of estimating the resistivity models from TEM, VES and MT data. In general, the model parameters are solved iteratively by minimizing a functional operator according to a derivative approach. The procedure may reach a local minimum of the functional operator depending also on the starting model. In the probabilistic methods, many earth models are proposed, and the theoretical data are compared with the observed data. The minimization function is directly estimated to retrieve the best model. The philosophy of the probabilistic approach, which can be considered as an optimization procedure, is to explore a wider space solution to seek a global solution to the problem.

Monte Carlo methods are based on the concept of random sampling of the model space. Moreover, various schemes, known as global optimization algorithms, are available in the literature (as described, e.g., in Sen and Stoffa, 2013). In recent decades, computational intelligence algorithms based on the concept of adaptive behaviour have been proposed to solve nonlinear problems. The capability of CI allows to implement a metaheuristic suitable for the geophysical joint inversion considering also external information (in this study from wells' stratigraphy).

We adopt the particle swarm optimization (PSO), a metaheuristic that has been successfully tested in the frame of the FP7 IMAGE Project (http://www.image-fp7.eu). We took advantage from the software package already developed for the 1D inversion of MT data by PSO (Godio and Santilano, 2018) and for the joint inversion of TEM and MT data (Santilano et al., 2018). Furthermore, an ongoing collaboration between the Politecnico di Torino (in the frame of a PhD Thesis) and CNR-IGG resulted in the implementation of new modules for the 1D inversion of VES data and the joint inversion of TEM and VES data (Pace et al., under revision).

The need of an accurate integration of geophysical data come from the possibility to overcome specific problems or limits of a single method, such as the static shift effect in MT or the low sensitivity to resistors for TEM or conductors for VES. The importance of integration is particularly high in an area such as the Acoculco Caldera, that has been only partially explored. The limit of an unconstrained starting model for the geophysical inversion is overcome by the use of CI. The few direct subsurface data (wells' stratigraphy) have been used to test an innovative procedure that produce only a slight influence of a-priori information on the optimization.

For this study, we exploited high-performance computational resources with the following features: Intel (R) Xeon (R) CPU E5-2690 v4 @2.60 GHz, 56 CPUs (Dual core), 264 GB of RAM.

7.2 Method: the particle swarm optimization (PSO)

PSO is a heuristic optimization method proposed by Kennedy and Eberhart (1995) and is based on two main concepts: i) simulation of the swarm intelligence and the behaviour of flocks of bird and fish and ii) evolutionary computation.

The elements (or “particles”), that compose the swarm, explore the solution space of the problem; the particle with best fitness value, which corresponds a high quality solution, will be the leader of the group around which other particles will move. The process starts from a population with low fitness and, after successive evolutions, arrives to a solution with higher fitness value according to an adaptive behaviour of the swarm (Figure 29).

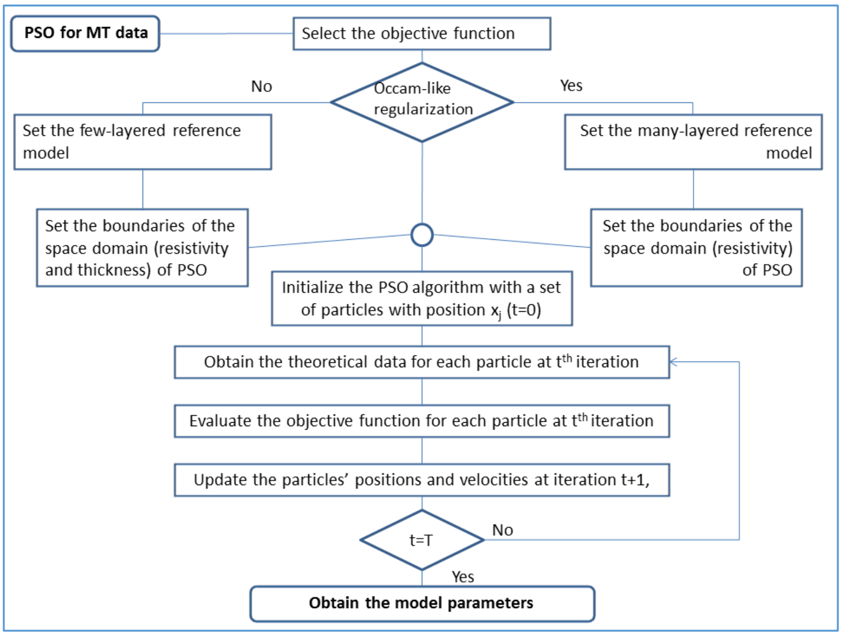

Figure 29: *Flow-chart of the MT data optimization using the PSO scheme (from Godio and Santilano, 2018).*

The swarm represents a population of earth models and it is initialized with random solutions. The particles, i.e. the members of the swarm representing potential models, “fly” through the problem space following the current optimal particles (Sen and Stoffa, 2013). Thus, PSO searches for optima by updating each particle according to certain parameters called position and velocity. Movement of particles is not entirely random; each particle is attracted towards both its own personal best position, in terms of fitness of the solution, and the swarm's best position of particles, which are vectors in the parameter space.

Following Engelbrecht (2007), the velocity consists of three terms: cognitive, social, and inertia. The cognitive component holds the experience of the individual particles, the social component holds shared information about the swarm’s best solution, and the inertia component represents the previous position in the space domain

For the 1D optimization of EM-VES data, the *N*-dimensional space of admissible earth models *j* is defined. For the *k*th parameter of the *j*th model, the lower and upper limits l_k and u_k of the search domain as well as the number of model parameters and particles, are set a priori. Depending on the function to be minimized, the model parameters *k* may be the resistivities ρ and thicknesses, or only the resistivities (with fixed thicknesses) of a layered earth.

The algorithm updates positions, $x_j(t)$, and velocities, $v_j(t)$, of the individuals as follows (Engelbrecht, 2007):

$$\mathbf{v_j}(\mathrm{t}+1) = \varpi \mathbf{v_j}(\mathrm{t}) + c_1 r_1 \left(\mathbf{l_j}(\mathrm{t}) - \mathbf{x_j}(\mathrm{t})\right) + c_2 r_2 \left(\mathbf{g}(\mathrm{t}) - \mathbf{x_j}(\mathrm{t})\right) \quad [1]$$

$$\mathbf{x_j}(\mathrm{t}+1) = \mathbf{v_j}(\mathrm{t}+1) + \mathbf{x_j}(\mathrm{t}) \quad [2]$$

At the *t*th iteration (*t*=0..T, where T is the maximum number of generations), each particle *j* of the swarm samples the search space according to its own misfit history, *lj(t)*, and its companions' search experience, *g(t)*. The coefficients ω, *c1* and *c2,* are the inertia weight, the cognitive attraction and the social attraction, respectively. The random values *r1* and *r2* impose a stochastic influence on the displacement updating.

For every particle of the swarm, the solution of the forward problem is computed according to a non-linear forward functional $F(x_j)$. The PSO optimization process pursues the minimization of an objective function dependent on the computed theoretical response F(x) and observed data (d).

7.2.1 Joint optimization of TEM and MT data

The "static shift" galvanic distortion of MT data is caused by near-surface small-scale heterogeneities or topography. The effect is a frequency-independent shift of the MT apparent resistivity curve for an unknown multiplier (constant on a logarithmic scale) that does not affect the MT phase (Jones, 1988). In a review of the distortion effects in MT, Jones (2012) considers the distortion of regional electric fields by local structures to be the greatest problem. Our work is intended to help overcome this problem by providing a quantitative estimate of the static shift using PSO optimization, considering that the transient EM method is not affected by such galvanic effects and can be used to remove these effects from MT data acquired in the same sites.

We exploit the methodology and the Matlab software package described in Santilano et al. (2018) for the simultaneous optimization of transient EM and magnetotelluric data. The method adopts a joint data set in the frequency domain composed of the MT data and the converted TEM data, as proposed by Sternberg et al. (1988):

$$t = 194/f \; [3]$$

where at a certain site and at the same depth of penetration, the TEM time *t*(s) is assumed to be equivalent to the MT frequency *f* (Hz) according to the equality in equation 3. Further, we have implemented the conversion from TEM signal to TEM apparent resistivity as proposed by Spies and Eggers (1986).

The objective (or minimization) function is of main importance for solving the inverse problem. The method adopts an Occam-like approach (Constable et al., 1987) and applies it to the procedure of optimization by PSO. The aim is to minimize the roughness of the model, in addition to the minimization of the misfit between measured and modelled data. The general minimization function of single MT optimization is slightly modified by considering an additional term to minimize the Euclidean norm of the misfits between the converted TEM apparent resistivity $\rho_{a(TEM);o}$ and the theoretically predicted data $\rho_{a(TEM);p}$ The minimization function for simultaneous optimization is (from Santilano et al., 2018):

$$\Psi(\mathbf{m}) = \left(a\left\|(\mathbf{S}\ \boldsymbol{\rho}_{\mathbf{a,o}}) - \boldsymbol{\rho}_{\mathbf{a,p}}\right\|_2 + b\left\|\boldsymbol{\phi}_{\mathbf{a,o}} - \boldsymbol{\phi}_{\mathbf{a,p}}\right\|_2 + c\left\|\boldsymbol{\rho}_{\mathbf{a(TEM),o}} - \boldsymbol{\rho}_{\mathbf{a(TEM),p}}\right\|_2\right) + \lambda\|\partial \mathrm{m}\|_2 \ [4]$$

An important application of the simultaneous PSO of EM data is the identification and removal of the static shift from the MT data. Basically, the earth resistivity models are evaluated on the basis of the misfit between (1) the predicted MT phase and resistivity and TEM apparent resistivity and (2) the observed TEM apparent resistivity, the MT phase, and the MT apparent resistivity, the latter multiplied by the shift parameter S, which is a parameter to be optimized.

The MT theoretical data are computed in a specific frequency range using a forward modeling based on a recursive formula for computing the surface impedance Z_k at the top of each *k*th layer, as described by Sims and Bostick (1969) and Pethick and Harris (2015).

7.2.2 Single optimization of VES with external information

For the 1D optimization of VES data, the *N*-dimensional space of admissible resistivity earth models *j* is defined. The PSO algorithm is the same used for the optimization of MT data. The resistivity value of the *k*th parameter of the *j*th model is updated, iteration by iteration, according to the adaptive behaviour in order to minimize the misfit between the measured and modelled VES data, in addition to the regularization term, as follows:

$$\Psi\ (\mathbf{m}) = \left(a\left\|\boldsymbol{\rho}_{\mathbf{a,o}} - \boldsymbol{\rho}_{\mathbf{a,p}}\right\|_2\right) + \lambda\ \|\boldsymbol{\partial}\mathbf{m}\|_2 \quad [5]$$

where in this case ρ_a is the apparent resistivity related to the VES method both for measured and modelled data, $\rho_{a,o}$ and $\rho_{a,p}$ respectively. The equation [5] is implemented to provide smooth Occam-like resistivity models. The thickness of the layers is a-priori fixed, whereas the resistivity is optimized.

For the geophysical applications, a-priori or external information of the search space can be introduced to reduce the ambiguities of the solutions. They usually refer to additional information on geological features or on other geophysical values. An innovative approach is here tested: a small part of the swarm particles is initialized with a-priori information in order to influence the oscillation centre and the direction of the swarm. This approach allows to test external information and their compatibility with the measured data. Indeed, the introduction of few known particles is not a strong constrain and the swarm is able to move across the space if the a-priori earth models are not in agreement with data

We have implemented a user-friendly interface to set the a-priori model and the amount of particles to be inserted in the swarm (as its percentage). It should be noted that it is possible to insert more than one a-priori model with a specific percentage of particles for each of them.

For the study of the Acoculco Caldera we have inserted as a-priori information the results of the single optimization of the adjacent VES soundings in order to achieve a laterally-constrained resistivity profile.

7.2.3 Joint optimization of vertical electrical soundings and TEM soundings: the multi objective PSO (MOPSO)

This method is the result of the collaboration between the Politecnico di Torino (in the frame of the PhD Thesis of Francesca Pace) and CNR-IGG. The method is under revision in a peer review journal (Pace et al., under revision) and briefly described in Pace et al. (2018). We apply this method to the study of the Acoculco Caldera.

The joint inversion of multiple datasets can significantly improve their modelling by overcoming the intrinsic limitations of each geophysical method. A multi-objective particle swarm optimization (MOPSO) is implemented to jointly interpret TEM and VES data.

The main difference with the previous two modules (single VES and joint MT/TEM) is that this approach implies the use of two different objective functions; one for each method (VES and TEM). Multi objective optimization aims to find an earth model m that simultaneously minimizes the two components (TEM and VES) of the vector function:

$$\Psi\ (\mathbf{m}) = [\Psi_1\ (\mathbf{m}), \Psi_2\ (\mathbf{m})][6]$$

m is the vector of electrical resistivity to be optimized.

Several solutions are evaluated during the optimization and the identification of the best solution is a key point of the procedure. In this case, the set of solutions is selected as best trade-off according to the Pareto optimality concept (Pareto, 1897). All the non-dominated solutions (for the mathematical definition see Pace et al., 2018) form the Pareto-optimal set. The corresponding objective functions of the non-dominated solutions form the Pareto Front (PF) in the objective space. Among the optimal set of solutions, chose the model with the minimum value of RMS. Furthermore, a time-variant MOPSO was implemented with the coefficients ω, c_1 and c_2 of Eq. 1 changing at each iteration, to provide global exploration of the search space at the beginning of the optimization and local exploitation at the end.

The forward modelling used to compute the theoretical TEM data is from the CR1Dmod package from Ingeman-Nielsen and Baumgartner (2006). The VES forward modelling was adapted from the code VES1dmod by Ekinci and Demirci (2008).

7.3 Dataset

The Acoculco geothermal system is a volcanic super-hot geothermal system located in the Tulancingo–Acoculco Caldera Complex and belonging to the Trans Mexican Volcanic Belt (TMVB). The surface geology of the studied area is the expression of the volcanic evolution of the Tulancingo–Acoculco Caldera. The volcanic rocks are calc-alkaline in composition and range in age from Pliocene to Pleistocene (see López-Hernández et al., 2009 for details)

The dataset we have analysed is composed by TEM and MT data acquired by UNAM and ISOR groups in the frame of the GEMex Project in addition to VES and TEM data acquired by CFE (Comisión Federal de Electricidad) since the late ‘80s. A schematic description of the dataset is provided in Table 1 and Figure 30.

Table 1: *Schematic description of the available datasets.*

Dataset	Number of soundings	Note
AC_MT_GEMex	69	Acquired in the frame of the GEMex Project
AC_TEM_GEMex	69	Acquired in the frame of the GEMex Project
A_TEM_CFE	61	Acquired by CFE in the frame of exploration projects

AC_VES_CFE	61	Acquired by CFE in the frame of exploration projects

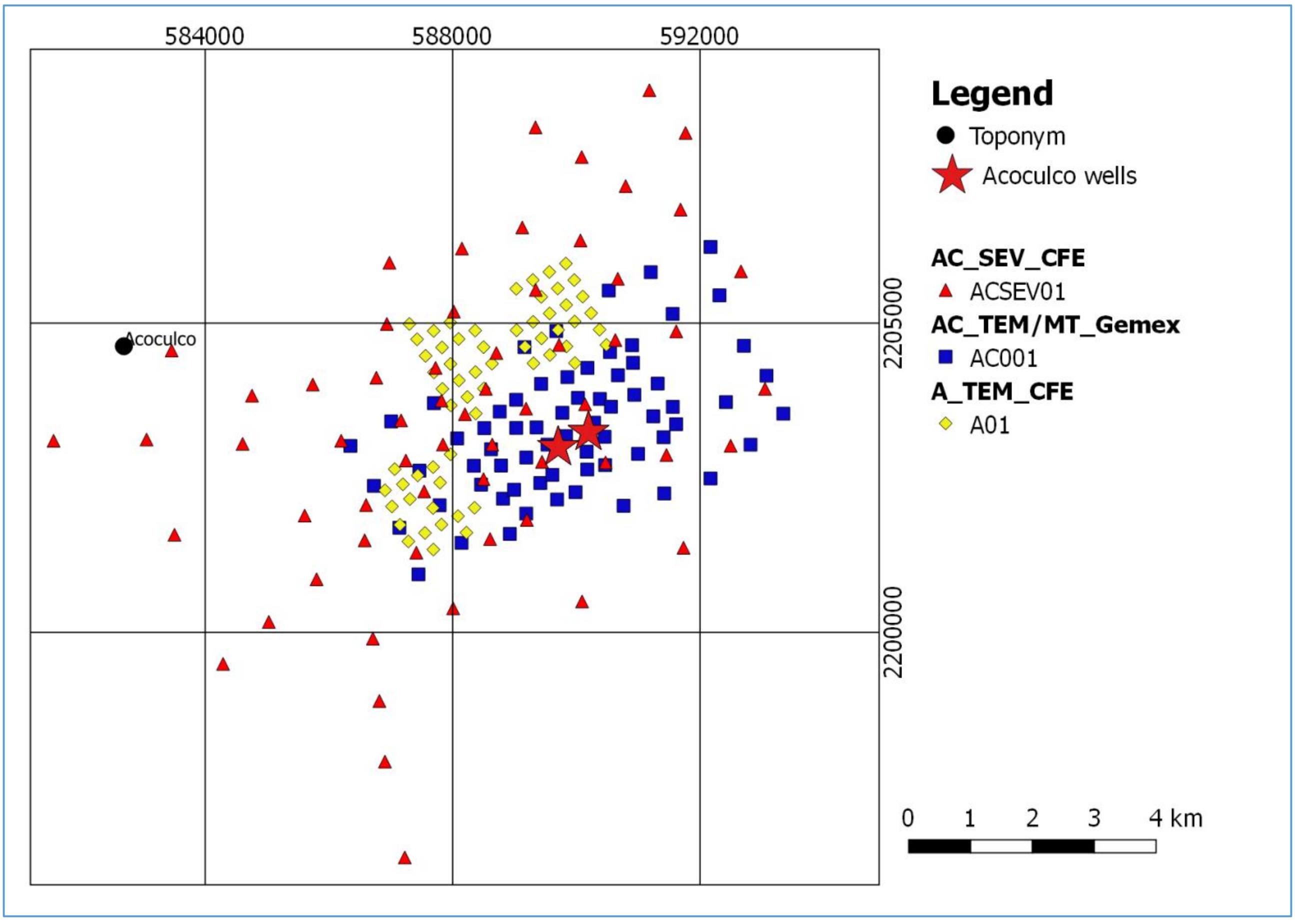

Figure 30: *Map of available geophysical data*

In the frame of the GEMex Project we have implemented a Matlab software package with scripts for reading the measured data and convert them in a suitable format for the optimization procedure. With the developed scripts, TEM soundings's data for each site can be visualised and the best one can be selected for the final conversion from *.usf to *.mat formats. Similar routines have been developed for the VES data, to convert from *.rex to *.mat data format, whereas for MT data the scripts for converting *.edi data to *mat format were already available.

Let us briefly describe the dataset. The TEM soundings from the previous industrial exploration, i.e. the A_TEM_CFE dataset, are usually characterized by low signal to noise ratio. The acquisition layout was a coincident loop with an equivalent area of 90000 m^2; i.e. a length of the square's side of 300 m. The system was set to transmit a current of about 7-8 A with active time gates up to 1.5 $*10^{-01}$ s. Often the voltages measured during the two longest decades were corrupted by noise. We have selected and processed only those TEM soundings of the A_TEM_CFE dataset with an acceptable signal to noise ratio. This dataset was used for the joint optimization with VES data, only if soundings from the AC_TEM_GEMex dataset were not available.

The VES soundings from the previous industrial exploration, i.e. the AC_VES_CFE dataset, appear of good quality. We cannot be sure of the accuracy of the data because of the lack of related errors in the available files. The acquisition was set with a Schlumberger array with AB/2 usually longer than 1000/2000 m up to 5000 m (GEOTEM, 2015). The VES sounding have been used for building a laterally constrained profile and for the joint TEM and VES optimization.

The GEMex datasets we received, both TEM and MT soundings, are of very high quality. Each MT sounding is coupled with a TEM sounding at the same site. Although the MT data were measured in a broad-band frequency interval, in the range of 10^{3}-10^{-3} Hz, only high frequency data (> 0.1 Hz) are available for the analysis in several soundings.

Regarding the GEMex TEM dataset, we have applied the new script for the selection of the best sounding among those acquired at the same site. The acquisition layout was a coincident loop with an equivalent area of 10000 m^{2}; i.e. a length of the square's side of 100 m. The system was set to transmit a current of about 8 A with active time gates up to about 9 $*10^{-02}$ s. Often the voltages measured during the longest decade were corrupted by noise. This dataset was used for running the joint optimization of MT and TEM data with the aim to identify the static shift of MT curves with the help of a computational intelligence metaheuristic. The AC_TEM_GEMex was used also for the joint TEM and VES optimization.

7.4 Results

7.4.1 Results from the joint optimization of transient EM and magnetotelluric data

This part of the study is aimed at providing an accurate esteem of the static shift *S* affecting the MT curve, by means of computational intelligence. A brief description of the method is provided in the sub-subchapter 1.2.1. We stress that for the study of Acoculco site we implemented the conversion from TEM to MT apparent resistivity data following Spies and Eggers (1986) and Sternberg et al. (1988), so to compare TEM and MT data measured at the same site. An example from the site AC053 (XY component) is provided, showing a perfect match between the converted TEM curve and the MT curve, evidently not affected by static shift (Figure 31).

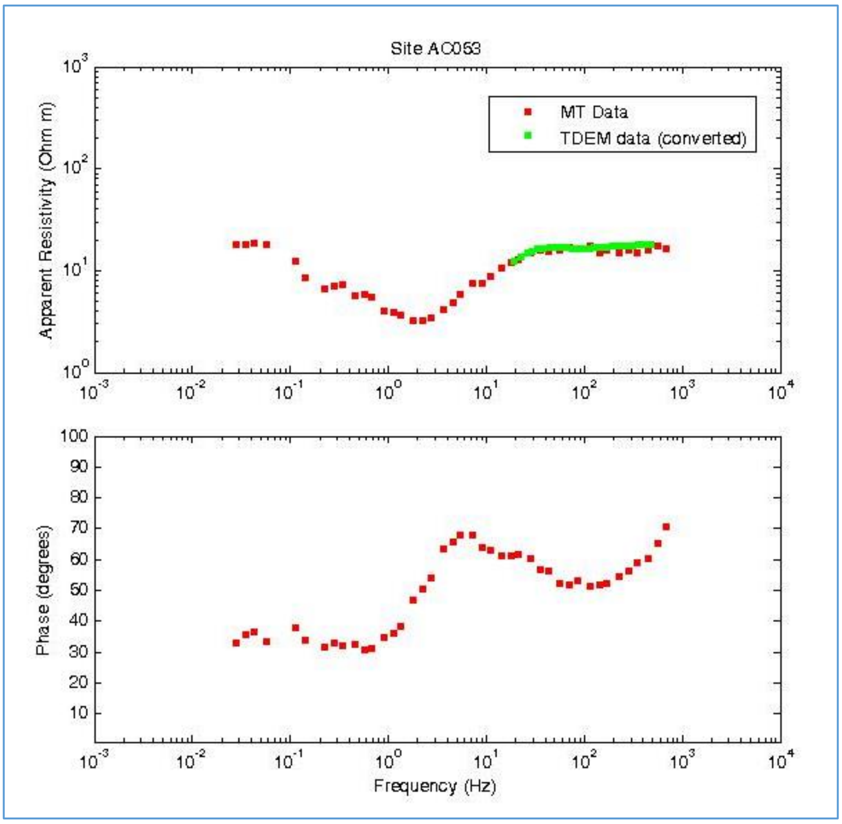

Figure 31: *MT curve and converted TEM curve for the site AC053*

With this approach, we analysed successfully 59 sites, and provided the optimized values of the Static Shift *S* for the XY, YX, components of the MT soundings. Furthermore, we applied the same procedure to the determinant average impedances (in the sense of Berdichevsky and Dmitriev, 1976). The results for the whole dataset are reported in the Annex 1. Here, we show an example from the site AC037, in particular for the XY component. The main settings for the PSO optimization are reported in Table 2.

Table 2: *Main setting for the PSO-Occam optimization (21 layers model) of the AC037 site (XY component).*

JOINT MT/TEM PSO: AC037	
Lower (LB)/Upper boundary (UB)	
Resistivity (Ohm m)	LB=1; UB=1000
Static shift (S)	LB=0.1; UB=10
PSO: settings	
Initial population	300
Particle inertia	0.9
Cognitive attraction	0.5
Social attraction	1.25

Generations (iterations)	100
Trials	25
PSO: Objective function	
a, weight on ρ_a	0.7
b, weight on Φ	0.3
c**, weight on $\rho_a(TEM)$**	1
λ (Lagrangian multiplier)	10^{-3}

We highlight that the optimization procedure is repeated for 25 trials (for the whole dataset) using the same settings to test the repeatability of the results. The resulting a-posteriori distribution is a very useful test for identifying model parameters with scattered distribution that indicate poor quality results, or good quality results with normal distributions. In Figure 32 the optimized values of the Static Shift *S* among the 25 trials for the AC037 sounding is shown in the range of the boundaries used for the procedure (0.1 to 10).

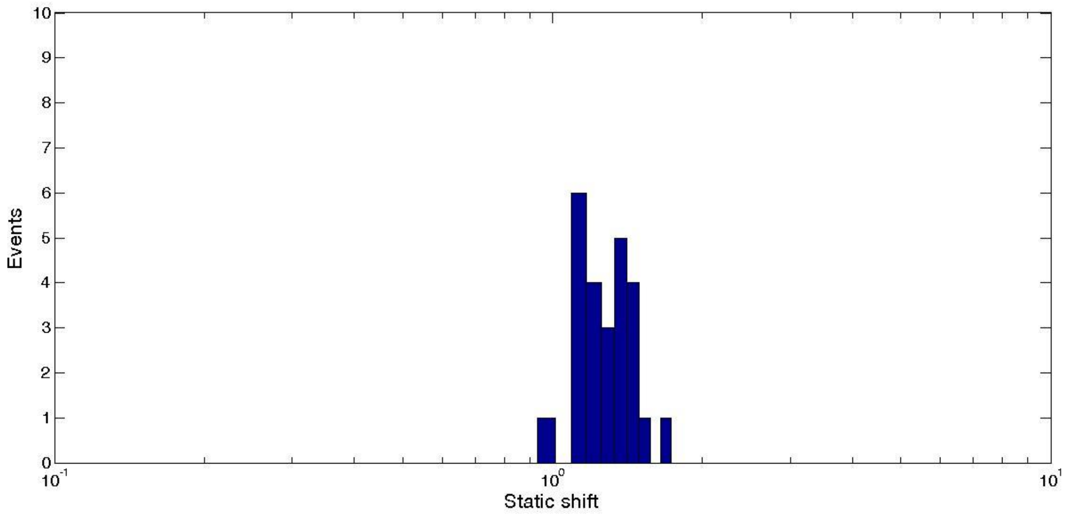

Figure 32: *A posteriori distribution of the optimized parameter S (static shift) among 25 PSO trials on the AC037 MT sounding*

The distribution is log-normal, indicating very good results. The selected static shift value, i.e. 1.362 in this case, is the one from the model with the minimum RMS indicating a MT curve not affected by strong galvanic effects.

Coupled with the optimization of *S*, the procedure implies the optimization of a 1D resistivity model. In Figure 33 is showed the resulting model from the same site AC037.

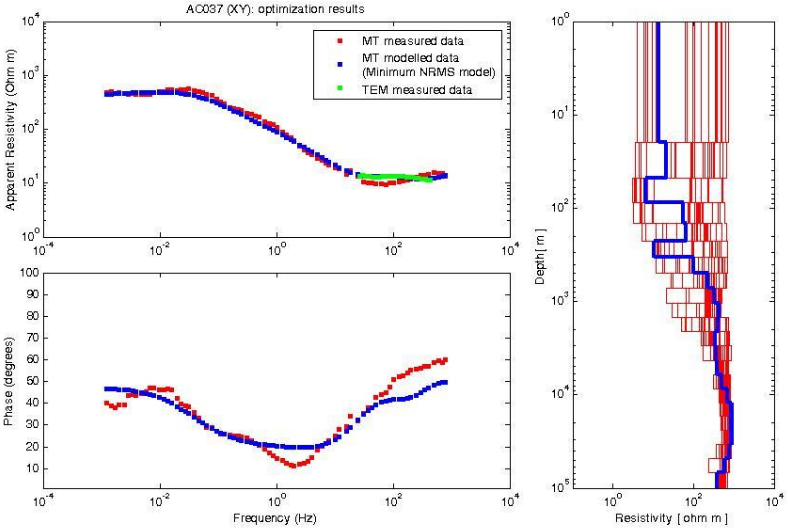

Figure 33: *PSO joint optimization of AC037 MT (XY) and TEM soundings. The resulting 25 models are shown in red, and the minimum normalized RMS model is shown in blue. The theoretical MT data are shown (on the left) for the minimum normalized RMS model and compared with the measured curve.*

In Figure 34 we show an example of MT curve affected by strong galvanic effect, in the AC031 site, for which an optimized value of static shift of 5.426 in the YX component was retrieved.

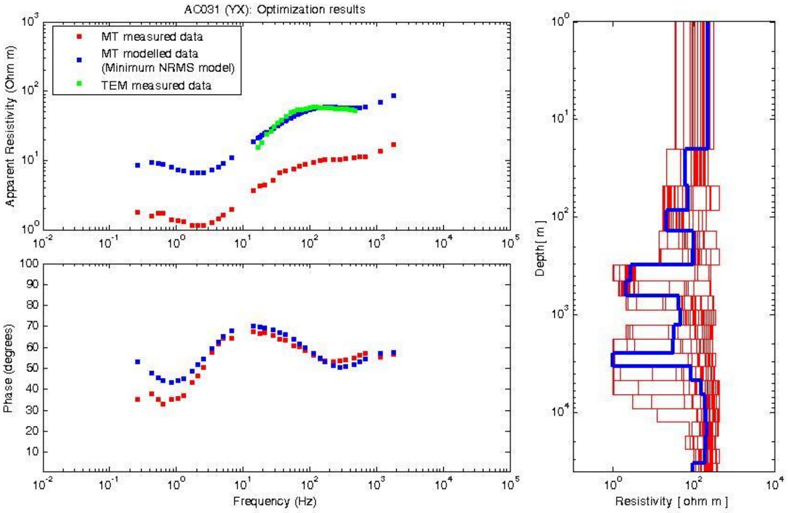

Figure 34: *PSO joint optimization of AC031 MT (YX) and TEM soundings. The resulting 25 models are shown in red, and the minimum normalized RMS model is shown in blue. The theoretical MT data are shown (on the left) for the minimum normalized RMS model and compared with the measured curve.*

The computational time for the joint MT and TEM optimization lasted few minutes.

7.4.2 Results from the single optimization of vertical electrical soundings

This part of the study is aimed at describing the results of an innovative approach to introduce a-priori information during the optimization. For this purpose, we adapted the idea of laterally-constrained inversion of VES data by initializing a small part of the swarm with information coming from the optimization of adjacent VES data along the Profile AA' (Figure 35).

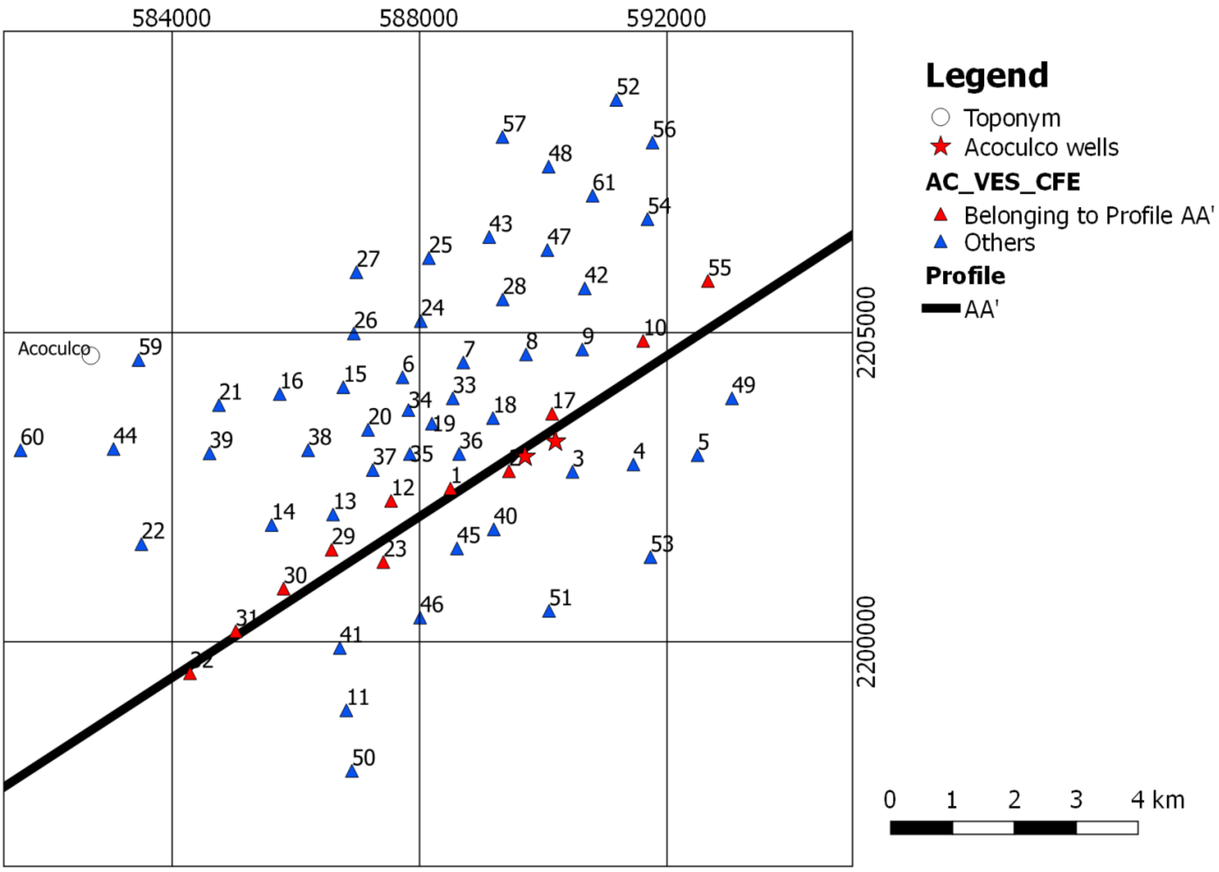

Figure 35: *Location of the Profile AA' and the VES soundings used for the laterally-constrained optimization.*

The Profile AA' corresponds to the geological cross-section built in the frame of the GEMex Project for the 3D geological modelling of the field. Furthermore, the optimization of soundings ACVES02 and ACVES17 has been modelled with a small part of the swarm with information from the deep geothermal wells EAC-2 and EAC-1, in addition to the information from adjacent VES soundings. This approach allows to test external information and their compatibility with the measured data, by influencing the oscillation centre and the direction of the swarm.

The main settings for the optimization of the ACVES17 are provided in Table 3, and the resulting model is shown in Figure 36. The resulting model is also compared with the stratigraphic log from the well EAC-2.

Table 3: *Main setting for the single optimization of the ACVES17 with external information.*

Single VES PSO: ACVES17 with external information	
Lower (LB)/Upper boundary (UB)	
Resistivity (Ohm m)	LB=1; UB=1500
PSO: settings	
Initial population	500
External (a-priori) information	Model from ACVES02 Model from ACVES10 Model from well EAC-2
Number of particles with a-priori information inserted in the swarm	5% of the swarm for each model
Generations (iterations)	150
Trial	1
PSO: Objective function	
λ (Lagrangian multiplier)	10^{-3}

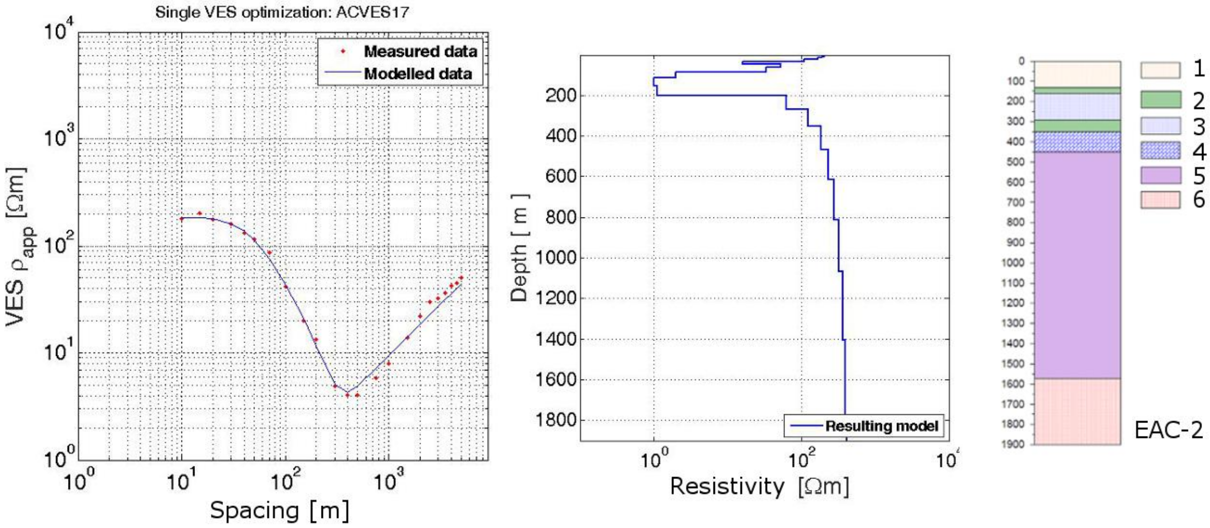

Figure 36: *Resulting model of the ACVES17 with external information. The stratigraphy of the EAC-2 well, as provided from Pulido et al. (2010), is also shown for comparison. Units: 1) Ignimbrite, 2) Andesite, 3) Dacite, 4) Limestone, 5) Hornfels, 6) Granite.*

The resistivity model along the Profile AA' can be of great help for updating and interpreting the geological model of the Acoculco field. The resistivity profile is built from the interpolation of the (laterally-constrained) optimized 1D models of 11 soundings. A script for the interpolation of the optimized models has been implemented in the software package. The resistivity profile is shown in Figure 37.

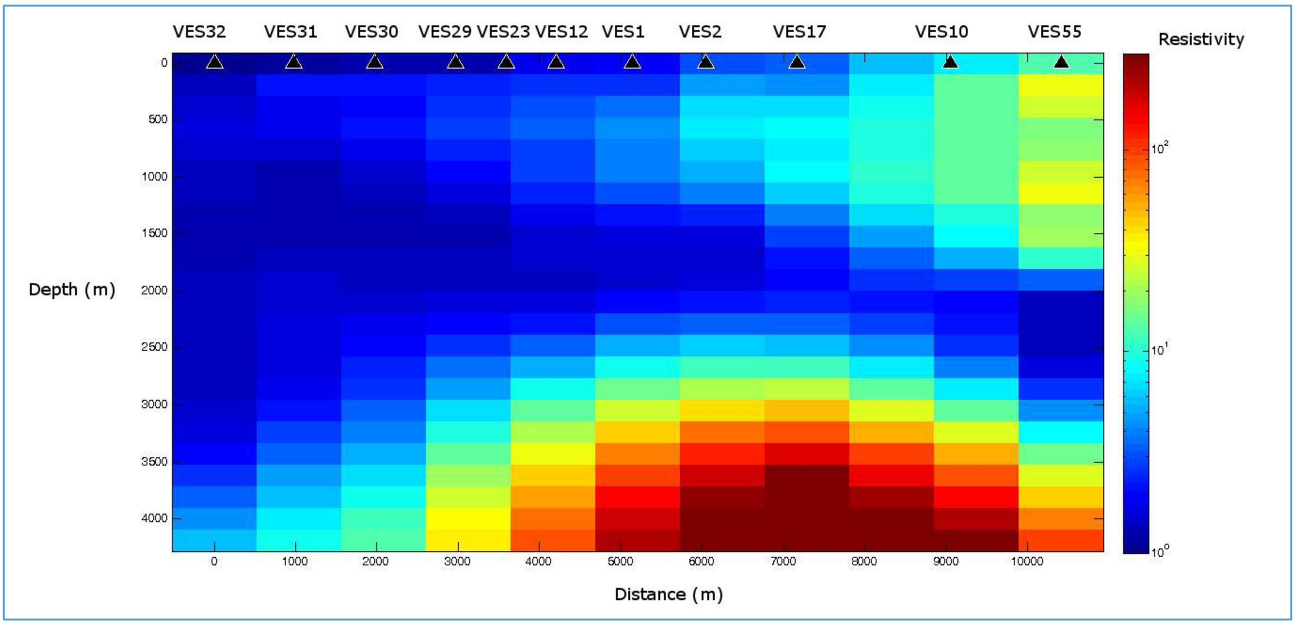

Figure 37: *Interpolated resistivity model along Profile AA' from the laterally-constrained 1D VES sounding models.*

7.4.3 Results from the joint optimization of VES and TEM soundings

The joint optimization of VES and TEM data represented a challenge. Firstly, it should be noted that the optimization is multi-objective with two different minimization functions and two different forward modelling, for VES and TEM data respectively. Consider that the joint MT and TEM optimization exploits only the magnetotelluric forward modelling (for MT and converted TEM data). The multi-objective nature causes very long computational time, due mainly to the longer forward modelling of TEM data with respect to VES one. A single 1D VES forward model lasts 0.08 s (similarly to the 1D MT forward), conversely the TEM forward lasts 0.24 s. In a procedure with thousands of forward models, one order of magnitude of difference means hours of computational time instead of minutes. The PSO joint optimization VES-TEM lasts at least 5-6 hours, depending on the population size and iterations. Furthermore, this joint procedure was not well tested and a sensitivity analysis on several parameters was required. Considering the computational time for each optimization, the correct tuning of the setting parameters represented a challenge. Another important issue to be taken into account is the possibility that TEM and VES soundings measured in the same site provide modelling results that are not compatible, e.g. due to the different sensitivity to conductive and resistive units.

For the study of the Acoculco Caldera, we analysed the VES and TEM datasets from the exploration projects of CFE and the TEM dataset acquired in the GEMex Project. Only 12 sites resulted suitable for the analysis, having high quality VES and TEM data recorded at sufficiently narrow distance. The dataset is showed in Figure 38.

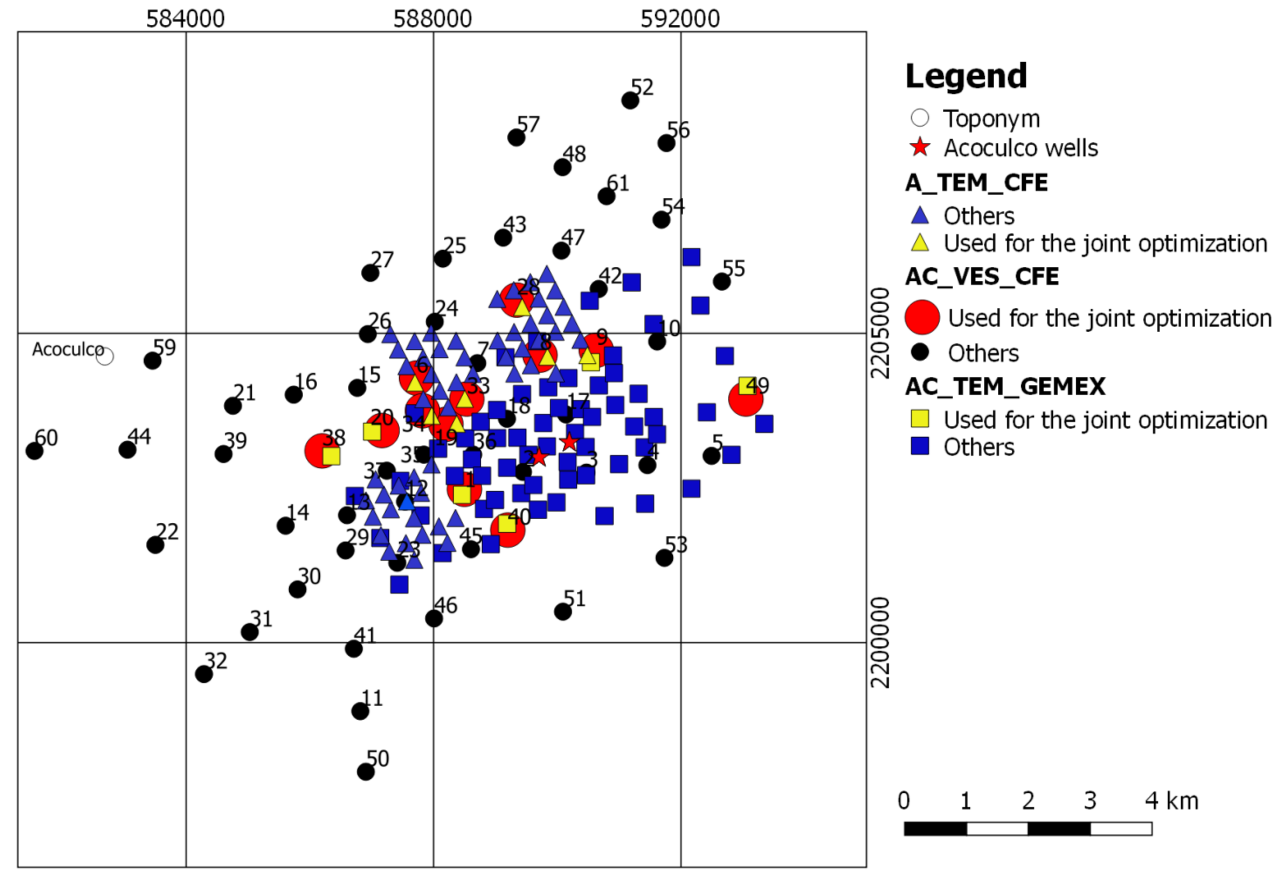

Figure 38: *Location of the VES and TEM soundings analysed by joint optimization.*

The optimization was successfully tested and provided acceptable results for most of the soundings, except for a few cases due to an incompatibility of the datasets. In Figure 39 the results from the sounding ACVES18 and AC015 (TEM) are shown. In Figure 40 the results from the sounding ACVES42 and AC066 (TEM) are shown.

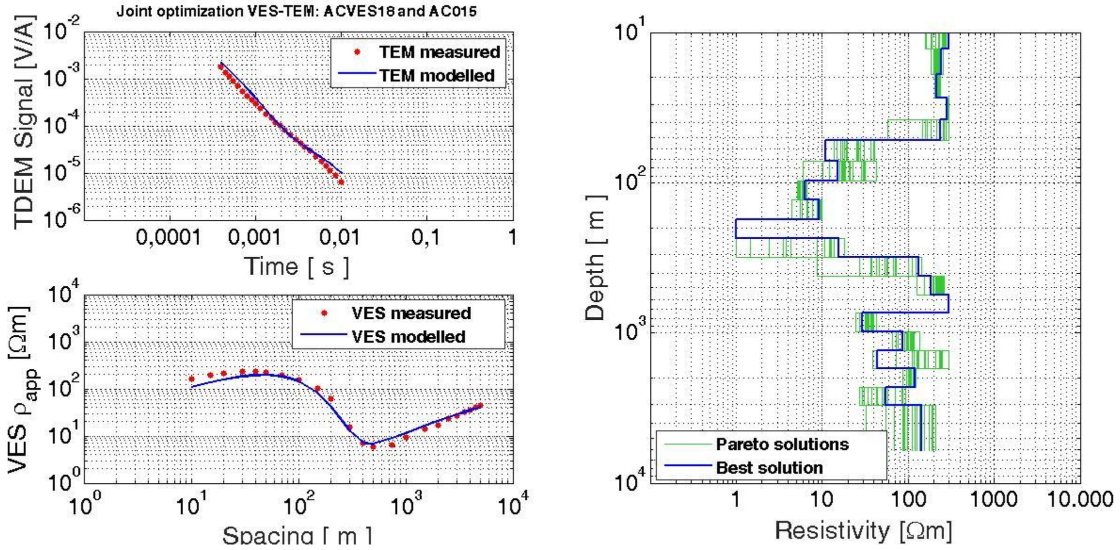

Figure 39: *Resulting resistivity model from the joint optimization of the soundings ACVES18 and AC015.*

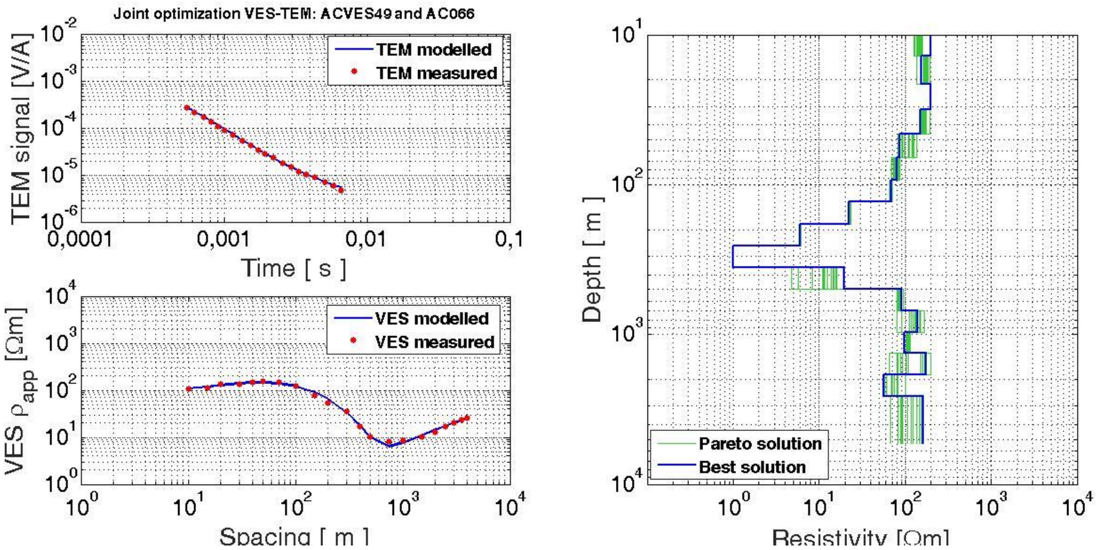

Figure 40: *Resulting resistivity model from the joint optimization of the soundings ACVES49 and AC066.*

We can consider these results as an example of successful optimizations as indicated by the match between modelled and measured VES and TEM data as well as by the match among the solutions belonging to the Pareto Front. The best solution, i.e. the one with the lowest data misfit, is selected from the Pareto Front.

7.5 Conclusion

We have successfully demonstrated the possibility to apply computational intelligence metaheuristics for the geophysical study of geothermal fields. Different approaches have been tested and the related results can be of help for the understanding of a complex system such as the Acoculco geothermal field. The main results of this research are: i) the identification of the static shift of MT curves by means of joint optimization of TEM and MT data (see Annex 1), ii) the computation of a laterally-constrained resistivity profile by means of PSO with external information inserted as part of the swarm in the optimization procedure, iii) the computation of 1D resistivity models from the joint optimization of VES and TEM data.

8 3D inversion of MT data

The 3D inversion of MT data from Los Humeros and Acoculco was performed using the inversion program WSINV3DMT (Siripunvaraporn et al., 2005; Siripunvaraporn and Egbert, 2009). WSINV3DMT uses finite difference forward algorithm and utilizes a formulation of the inverse problem in the data-space rather than in the model-space. This reduces the dimensionality of the problem dramatically and makes 3D inversion of MT data attainable.

Due to non-linearity of the problem the 3D inversion is an iterative minimization process. The choice of initial model can influence the final model. 3D inversion of MT data is a highly underdetermined problem, i.e. the number of unknown resistivity values is much bigger than the number of data values. In the case of Los Humeros, the number of data points is 16800 (100 soundings x 21 periods x 8 real and imaginary tensor elements, see below) but the model has 56144 unknown resistivity values (in the 44 x 44 x 29 blocks, see below) or three times the number of data points. For Acoculco, the number of data points is 5544 (66 soundings x 21 periods x 4 real and imaginary off-diagonal tensor elements, see below) but the model has 80040 unknown resistivity values (in the 46 x 60 x 29 blocks, see below) or fourteen times the number of data points. The inversion therefore, needs to be regularized by imposing constraints on the model (mathematically speaking this means to make the model parameters interdependent in such a way that the number of the truly free parameters is reduced). This is achieved by constraining the model parameters to vary smoothly, often referred to as minimum structure or Occam inversion (Constable et al., 1987). Another way of regularizing is to use reference or "prior" model and constrain the inversion model not to deviate too much from the prior model. Using a prior model offers the possibility of fixing some of the model parameters to a priori known values. WSINV3DMT uses a combination of these regularization methods and minimizes a “penalty function”, which is the weighted sum of: 1) the difference between measured data and calculated response (the data misfit), 2) the roughness of the model, and 3) the deviation from the prior model. Initially, the inversion process quickly adjusts the model to reduce severe misfit of the data. Later, changes that would further reduce the data misfit are rejected because they make the model deviate too much from the prior model.

The user can adjust the smoothing criteria, but not the weight of the deviation from the prior model. This can constrict the iteration from fitting the measured data adequately, especially if a model that deviates considerably from the prior model is required. Running the inversion in steps, where the initial and prior models are updated at each step (the model that gave the best fit in the previous step), can facilitate the processes of fitting the data. That way the limitation of the prior model is gradually relaxed until the data fit can no longer be improved.

The inversion in the case of Los Humeros was performed for the complex elements of the MT impedance tensor, i.e. 8 numbers (4 real and 4 imaginary parts) while for the Acoculco data, the inversion was performed for the complex off-diagonal elements of the MT impedance tensor, i.e. 4 numbers (2 real and 2 imaginary parts). In both cases this was done for all periods of all soundings simultaneously, weighted by their variance. Because resistivity variations can have sharp boundaries, it was decided to apply relatively small smoothing (MODEL_LENGTH_SCALE 4 0.05 0.05 0.05, see Siripunvaraporn et al., 2006).

For the Los Humeros survey area, we also experimented with the following setups:

1. Inverting for the complex off-diagonal elements of the MT impedance tensor with a 400 m width of the grid cells in the densely gridded area
2. Inverting for the complex off-diagonal elements of the MT impdenace tensor with a 200 m width of the grid cells in the densely gridded area

When the width of the grid cells in the densely gridded area was 200 m, the inverse problem grew significantly. With 66 cells in each horizontal direction, the number of model cells is 66 x 66 x 29 = 126324, which is more than two times the number of unknowns than in the case of 400 m cell width in the dense part. As the distance between soundings location was 720 m it was concluded that the 400 m grid in the densest part was the best choice.

If we would choose to invert only for the off-diagonal elements, the number of data points decreases to 8400 (100 soundings x 21 periods x 4 impedance elements). In that case the problem becomes even more underdetermined, with number of model cells almost 7 times higher than the number of unknowns.

From these observations we choose to work with the models that invert for the full-impedance tensor in a 400 m dense grid in the main part of the model.

For Acoculco, however, the average distance between the soundings was 400 m and therefore, it was decided to use only models with 200 m grid in the main part of the model. It was also decided to invert for the off-diagonal elements because the results from the 1D joint inversion of MT/TEM data suggested that the area was characterized by a horizontally layered structure, in which case the diagonal elements of the impedance tensor would be very small.

These speculations show, that it is not trivial to setup a 3D inverse problem for MT data.

8.1 Data preparation

The underlying coordinate system in 3D inversion of MT data is discussed by Tietze and Ritter (2013). Here, the processed MT data have the x-axis in true north. In the 3D inversion the processed data and the model are defined in an internal (local) coordinate system or grid. The measurement grid in Los Humeros was arranged along the true north and east, as the geological structure did not exhibit one preferred direction. Therefore, the MT impedance tensors were not rotated in the case of Los Humeros.

In Acoculco, the measurements were arranged on a grid parallel and perpendicular to the main geological structure. Therefore, the internal coordinate system was taken to have the x-axis in N30°W and consequently the y-axis in N60°E. The MT impedance tensors were rotated by 30° anti-clockwise to the direction of the internal system.

Here, the static shift including the topographic effect, was corrected through joint inversion of TEM and MT data. A 3D inversion of the static shift corrected MT data, where the topography is included in the model would mean correcting twice for the topographic part of the static shift. Therefore, a flat topographic surface was assumed in the 3D inversion.

The 3D inversion was performed for the MT tensor elements that normally contain static shift. By assuming that the static shift is dominantly due to voltage distortion and current channelling including topographic effects, the tensor can be static shift corrected by the equation:

$$\begin{bmatrix} Z^c{}_{xx} & Z^c{}_{xy} \\ Z^c{}_{yx} & Z^c{}_{yy} \end{bmatrix} = \begin{bmatrix} C_x & 0 \\ 0 & C_y \end{bmatrix} \begin{bmatrix} Z_{xx} & Z_{xy} \\ Z_{yx} & Z_{yy} \end{bmatrix} \qquad \text{(3a)}$$

$$C_x = \sqrt{1/S_{xy}} \quad ; \quad C_y = \sqrt{1/S_{yx}} \qquad \text{(3b)}$$

Where, $\mathbf{Z}^c$ is the corrected and $\mathbf{Z}$ the uncorrected tensor, respectively. S_{xy} and S_{yx} are the shift multipliers for the apparent resistivity of the xy and yx polarizations, respectively (Árnason et al., 2010). After the rotation of the soundings to the internal coordinate system, a joint 1D inversion was performed of the apparent resistivity and phase for both xy and yx polarizations and the nearby TEM sounding, to determine the static shift multipliers.

The computational intensity in the inversion is directly proportional to the number of periods to be inverted for. The processed data generally contain 40-70 different periods ranging from about 0.001 s to 1000 s, depending on the quality of the data at different periods. To reduce the computational cost, the static shift corrected tensor was re-sampled at 21 periods equally spaced on log scale. For Acoculco we had four values per decade, from 0.001 s to 200 s and for Los Humeros we had four values per decade, from 0.005 s to 600 s. This choice of periods is a “trade off” between computational cost on one hand and resolution and depth penetration on the other. For physical consistency, the MT tensor must be a smooth function of the logarithm of the period (Weidelt, 1972). The interpolation of the tensor was done with cubic spline using 6 adjacent data points (3 above and 3 below).

Inverting for four periods per decade is considered to give good enough resolution. The period range and the resistivity determine the depth range of exploration. The shorter the period and lower the resistivity, the shallower resistivity structures can be resolved. The longer the period and the higher the resistivity, the deeper structures can be resolved.

8.2 The model grid

The 3D model consists of resistivity cubes in a 3D grid mesh in an internal coordinate system. For Los Humeros, the origin (centre) of the internal coordinate system is approximately at the centre of the area of interest and data coverage and with x-axis positive to the north and the y-axis positive to the east. The mesh has 44 cells in the x and y-directions and 29 vertical grid cells. The grid is dense in the area of interest, with cell space of 400 m. The densely gridded area is 8 km x 8 km. Outside the dense area the grid spacing increases exponentially to the edges at ±135 km in the x- and y-directions. Figure 41 shows a horizontal slice of the central part of the model grid mesh with the location of the MT soundings.

For Acoculco, the origin of the internal coordinate system is approximately at the centre of the area of interest and data coverage, and with x-and y-axis positive towards N30°W and N60°E, respectively. The mesh has 46 and 60 cells in the x and y-directions, respectively, and 29 vertical grid cells. The grid is dense in the area of interest, where the grid cells width is 200 m. The densely gridded area is 4 km x 6.8 km. Outside the dense area the grid spacing increases exponentially to the edges at ±131.9 km and ±133.3 km in the x- and y-directions. Figure 42 shows a horizontal slice of the central part of the model grid mesh with the location of the MT soundings.

In both the survey areas, the vertical grid cells are likewise dense at shallow depth but the spacing increases exponentially with depth until bottom at 160 km. The shallowest layer thicknesses are 35, 35, 50, 50, 75, 75, 100, 100, 140, 140, 200 m etc.

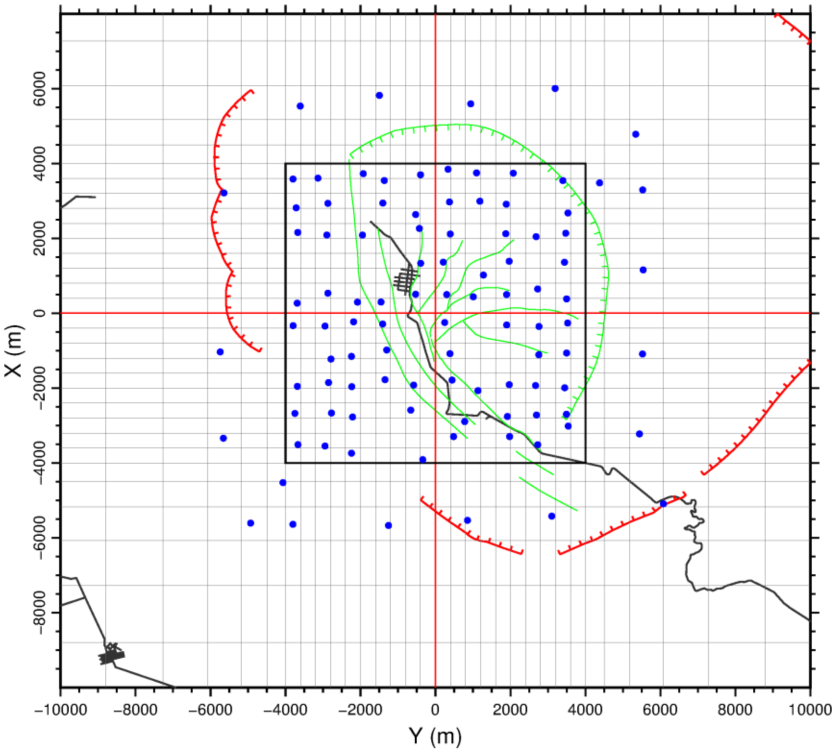

Figure 41: *The model grid for the 3D inversion for the Los Humeros survey area in the internal coordinate system. Blue circles are sounding location, dark gray thick lines are roads and black thin lines denote the model mesh. Red and green hatched lines are the Los Humeros and Los Potreros Calderas, respectively. The green lines are the main faults in the area and the black rectangle outlines the 8 km x 8 km densely gridded survey area. Red lines run along x=0 and y=0.*

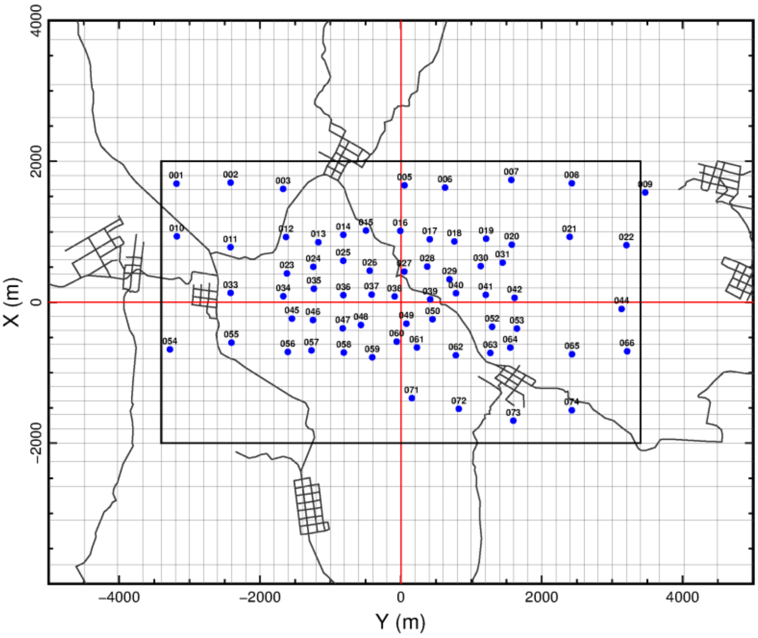

Figure 42: *The model grid for the 3D inversion for the Acoculco survey area in the internal coordinate system. Blue circles are sounding location, dark gray thick lines are roads and black thin lines denote the model mesh. The black rectangle outlines the 4 km x 6.4 km densely gridded survey area. Red lines run along x=0 and y=0.*

8.3 Initial and prior models

As discussed earlier, 3D inversion of MT data is a highly underdetermined problem. The iterative inversion is started from an initial model. To regularize the inversion, a prior model is used to constrain the deviation of the resulting model from the prior model. Consequently, the resulting model may depend on the initial and prior model.

To investigate the influences of the initial model on the resulting model, inversions with four distinct initial models were done: 1) a homogeneous half-space with resistivity 10 Ωm (**H010**) - the inversion only inserts high resistivity where needed, 2) a homogeneous half-space with resistivity 100 Ωm (**H100**) - the inversion only inserts low resistivity where needed, 3) a homogeneous half-space with resistivity 50 Ωm, (**H050**) and 4) a model compiled from joint 1D inversion of individual TEM/MT sounding pairs (**inv1D)**. In all cases the same model was used as initial and prior model.

We initially started with the four initial models for Los Humeros, described above, but chose three of them to run until a small RMS was reached, we chose H010, H050 and inv1d.

A step procedure was used during all the inversion. The inversion was allowed to run for 5 iterations at each step and restarted with the best model from previous step as initial and prior model. This stepwise inversion (and relaxation of the prior model) was continued until the data fit could not be improved any more (3-4 steps).

8.4 The 3D inversion

The inversion program was executed using a parallel processing version of the WSINV3DMT code using the Message Passing Interface (MPI) parallel computing environment (Siripunvaraporn and Egbert, 2009). It was executed on a 32 core computer with 132 GB memory.

The data misfit is defined as the RMS (Root-Mean-Square) of the difference between the measured and calculated values, weighted by the variance of the measured values. The initial and final RMS misfits for the different initial models are summarized in Table 4.

Table 4: *Initial and final RMS for the various starting models for both Los Humeros and Acoculco survey areas.*

Initial model	**Los Humeros**		**Acoculco**	
	Intial RMS	Final RMS	Initial RMS	Final RMS
Homogeneous half-space of 100 Ωm	-	-	36.58	1.66
Homogeneous half-space of 50 Ωm	11.00	1.27	22.21	1.28
Homogeneous half-space of 10 Ωm	20.26	2.31	9.61	1.20
Model compiled from 1D inversion	6.36	1.28	7.13	1.26

8.4.1 Presentation of the 3D resistivity model

Visual presentation of a 3D resistivity model is not straightforward. The final model is presented here in two different ways, i.e. as horizontal and vertical cross-sections through the 3D resistivity model.

Each cell of the model is assigned one resistivity value. The figures presented here, however, show smoothed resistivity between cells. Also, only results in and around the densely gridded area is shown, as the results outside that area do not exhibit reliable structures, since there are not data there to support them.

WSINV3DMT assumes flat topographic surface. This seems to be a limitation, but prior to the inversion, the MT data were corrected for the static shift and this correction removes topographic effects in the data to a large extent because static shift in MT soundings is partly caused by topography (current channelling due to the topography). Before producing the figures showing the 3D inversion results, the resistivity models were elevation corrected, i.e. the depths below each model cell were converted to meters above or below sea level.

8.4.2 Comparison of different initial models

In this section inversion results for different initial models are compared. Based on that, one of them is chosen for each area, which is then analysed as the main resulting model for that area.

Los Humeros

Figures 43, 44 and 45 show examples of the smoothed elevation corrected resistivity maps at 2600 m above sea level, 1400 m above sea, and at 500 m below sea level, for the three starting models for Los Humeros (H010, H050, inv1D).

The model based on H010 is quite different from the ones based on H050 and inv1D, and therefore, not discussed further here.

Commonly, results based on the inv1D model are often different from the others, as the inversion starts out with a certain resistivity structure that is retained throughout the inversion process. In this study, however, it is interesting to note that the results are strikingly similar for the models based on the H050 and inv1D initial models, down to 750 m above sea level (in the top 2000 m) (Figures 43 and 44).

The resistivity model based on the inv1D and H050 initial models do not agree at the intermediate depth range (750 m above sea level to 2500 m below sea level), see Figure 45. The several low-resistivity bubbles observed at this depth-range using the inv1D initial model, are not in ones based on the H010 and H050 initial models, except for the barely visible low-resistivity bubble located just south of the town of Los Humeros.

The resistivity model based on the H050 and inv1D initial models are both good candidates to be the final 3D resistivity model of Los Humeros. We chose the one based on the H050 model because it exhibits a simpler resistivity structure where the two models deviate from one another, thereby using Occam’s razor.

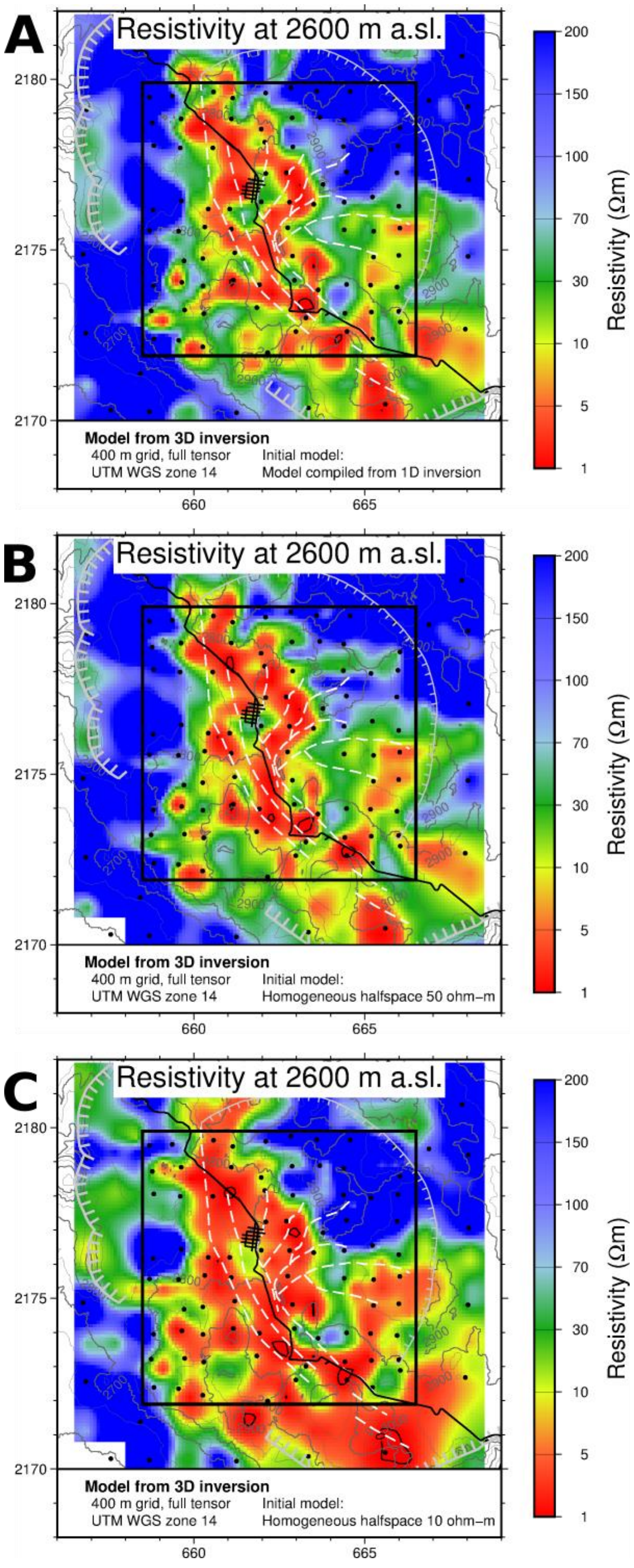

Figure 43: *Horizontal depth-slices at 2600 m above sea level through the 3D resistivity models of Los Humeros. The initial models used were inv1D (**A**), H050 (**B**) and H010 (**C**). The black dots are the MT sites. The black box outlines the densely gridded area of the inversion. Dark gray lines are roads, gray lines are elevation contours, white and gray hatced lines are the Los Potreros and Los Humeros calderas, respectively and white dashed lines are the main faults in the region.*

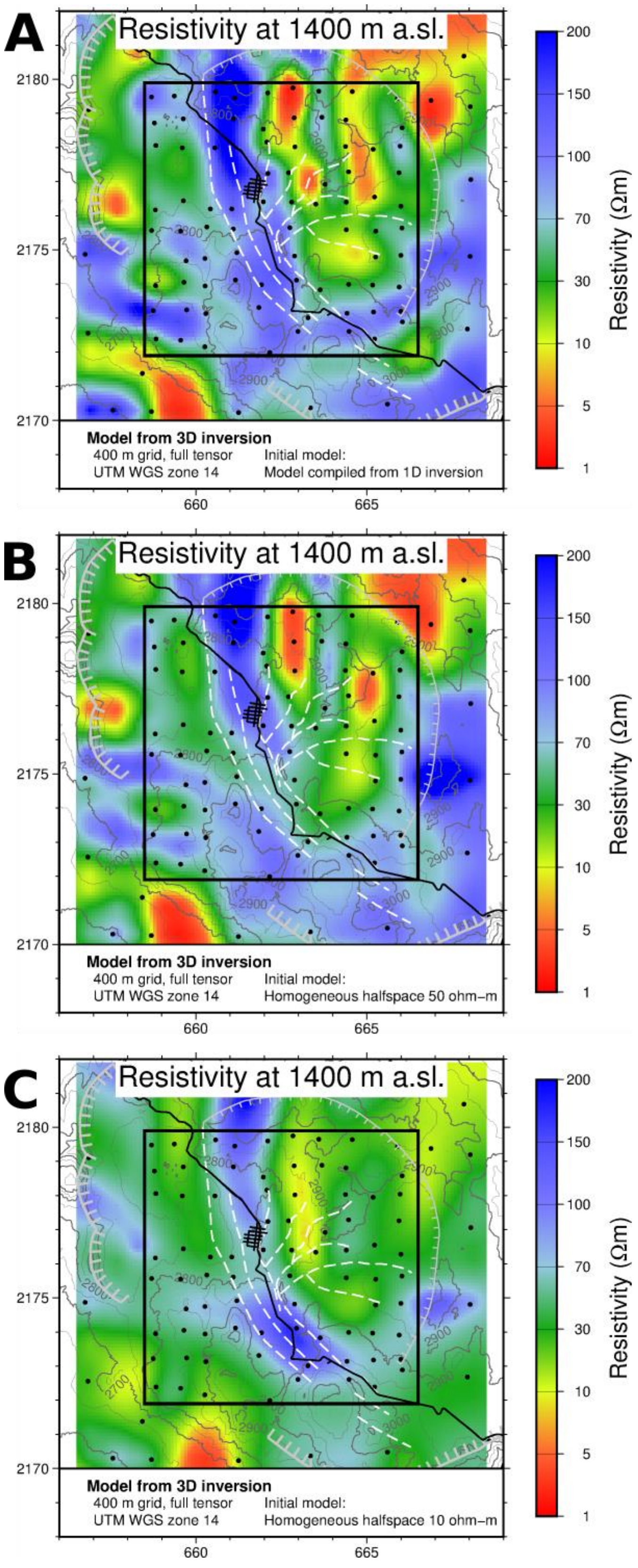

Figure 44: *Horizontal depth-slices at 1400 m above sea level through the 3D resistivity models of Los Humeros. The initial models used were inv1D (**A**), H050 (**B**) and H010 (**C**). The black dots are the MT sites. The black box outlines the densely gridded area of the inversion. Dark gray lines are roads, gray lines are elevation contours, white and gray hatced lines are the Los Potreros and Los Humeros calderas, respectively and white dashed lines are the main faults in the region.*

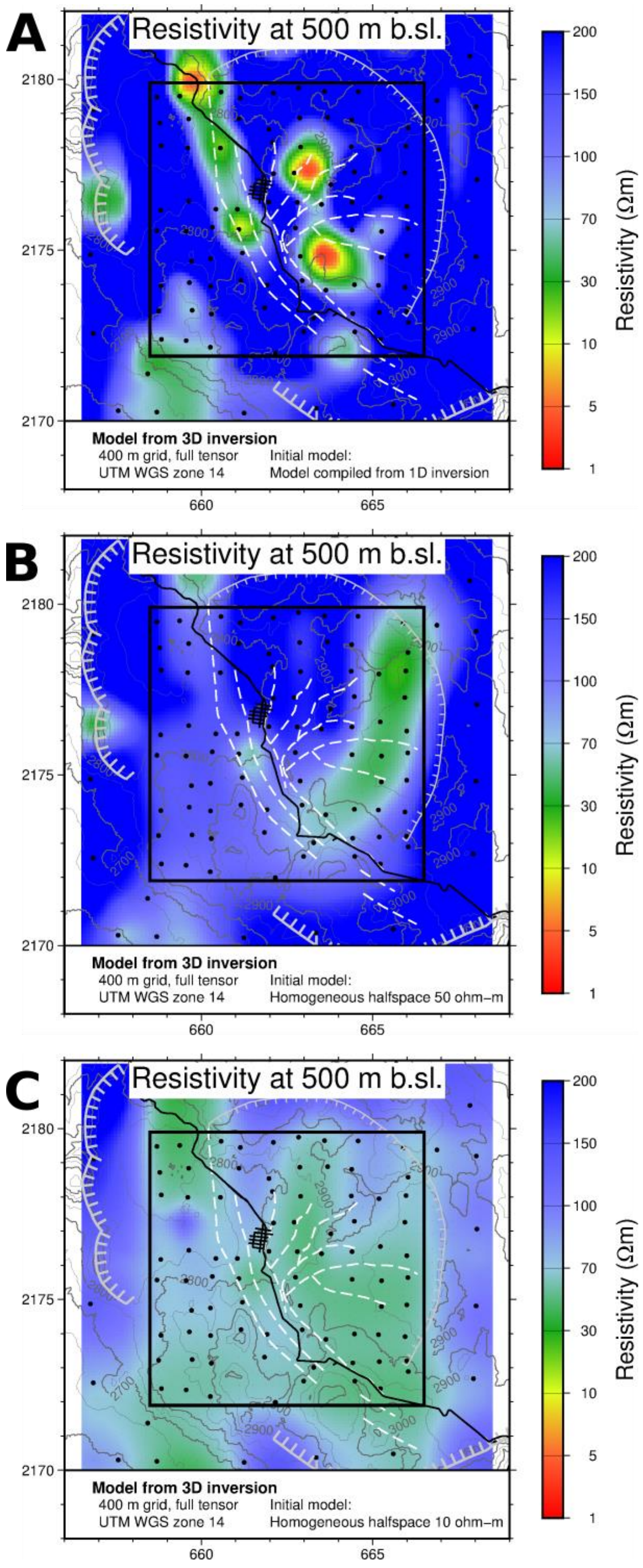

Figure 45: *Horizontal depth-slices at 500 m below sea level through the 3D resistivity models of Los Humeros. The initial models used were inv1D (**A**), H050 (**B**) and H010 (**C**). The black dots are the MT sites. The black box outlines the densely gridded area of the inversion. Dark gray lines are roads, gray lines are elevation contours, white and gray hatced lines are the Los Potreros and Los Humeros calderas, respectively and white dashed lines are the main faults in the region.*

Acoculco

Figures 46-49 show examples of the smoothed elevation corrected resistivity maps at 2700 m above sea level, 2400 m above sea, 1400 m above sea level and at sea level, for the four starting models for Acoculco (H010, H050, H100, inv1D).

It is remarkable how similar the different models are, which can be attributed to the simple resistivity structure in the area, compared to Los Humeros.

The resistive core is very pronounced in all the models at 2400 meters above sea level (Figure 47), striking NW-SE and is located underneath the western EAC well.

The main difference is seen in the model based on the H010 initial model at 2700 meters above sea level (Figure 46A) and at sea level (Figure 49).

The low-resistivity bubble located at the intersection of the major faults in the region (Figure 49) is present in all the models.

For consistency, we chose to analyse the resistivity model based on the H050 initial model, as was done in the case of the Los Humeros study area, noting that we could have chosen the ones from either the inv1D or H100 initial models.

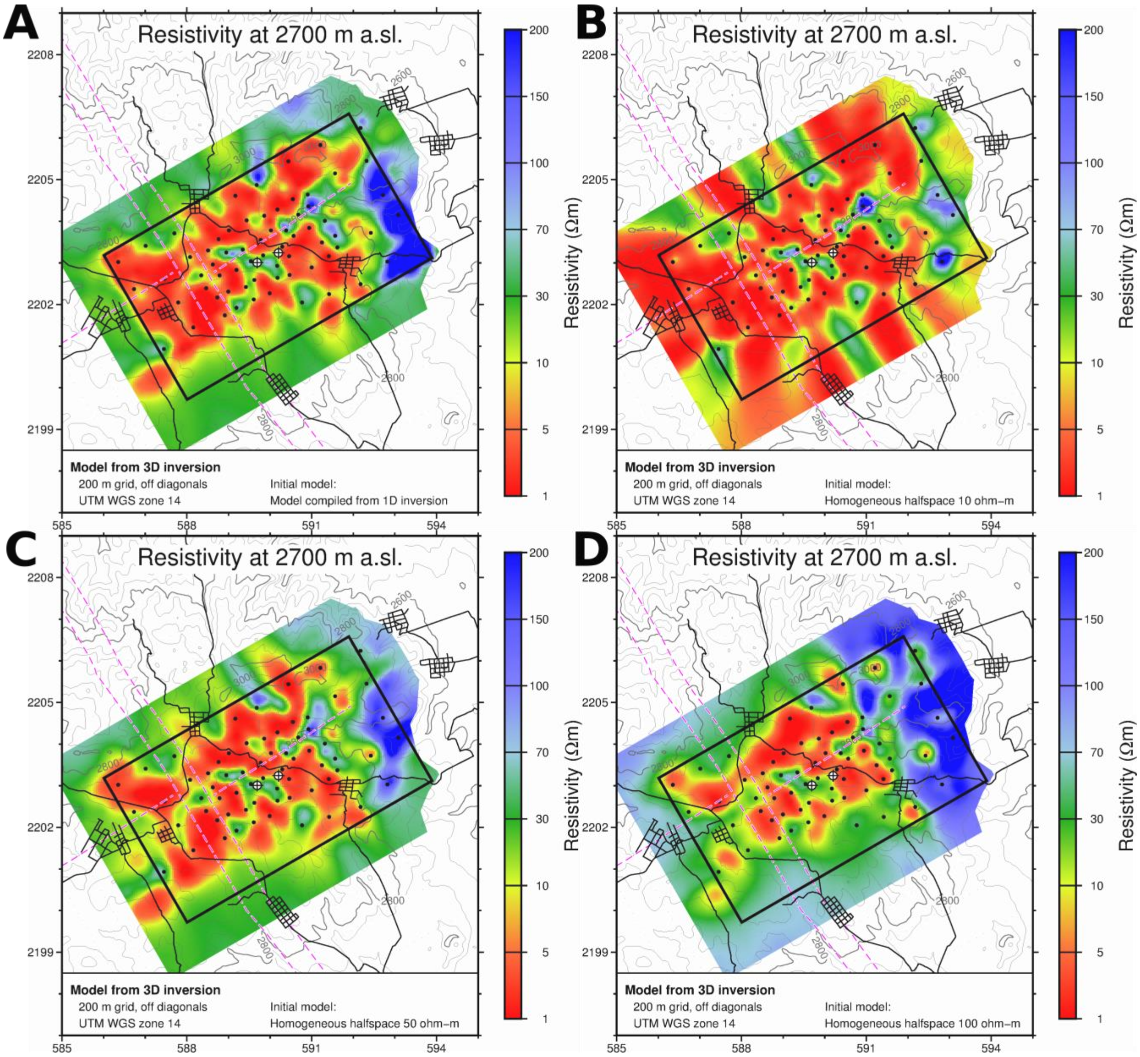

Figure 46: *Horizontal depth-slices at 2700 m above sea level through the 3D resistivity models of Acoculco survey area. The initial models used were inv1D (**A**), H010 (**B**), H050 (**C**) and H010 (**D**). The black dots are the MT sites. The black box outlines the densely gridded area of the inversion. Dark gray lines are roads, gray lines are elevation contours and pink dashed lines are the main faults in the region. The two black crosses on white circles are the EAC wells.*

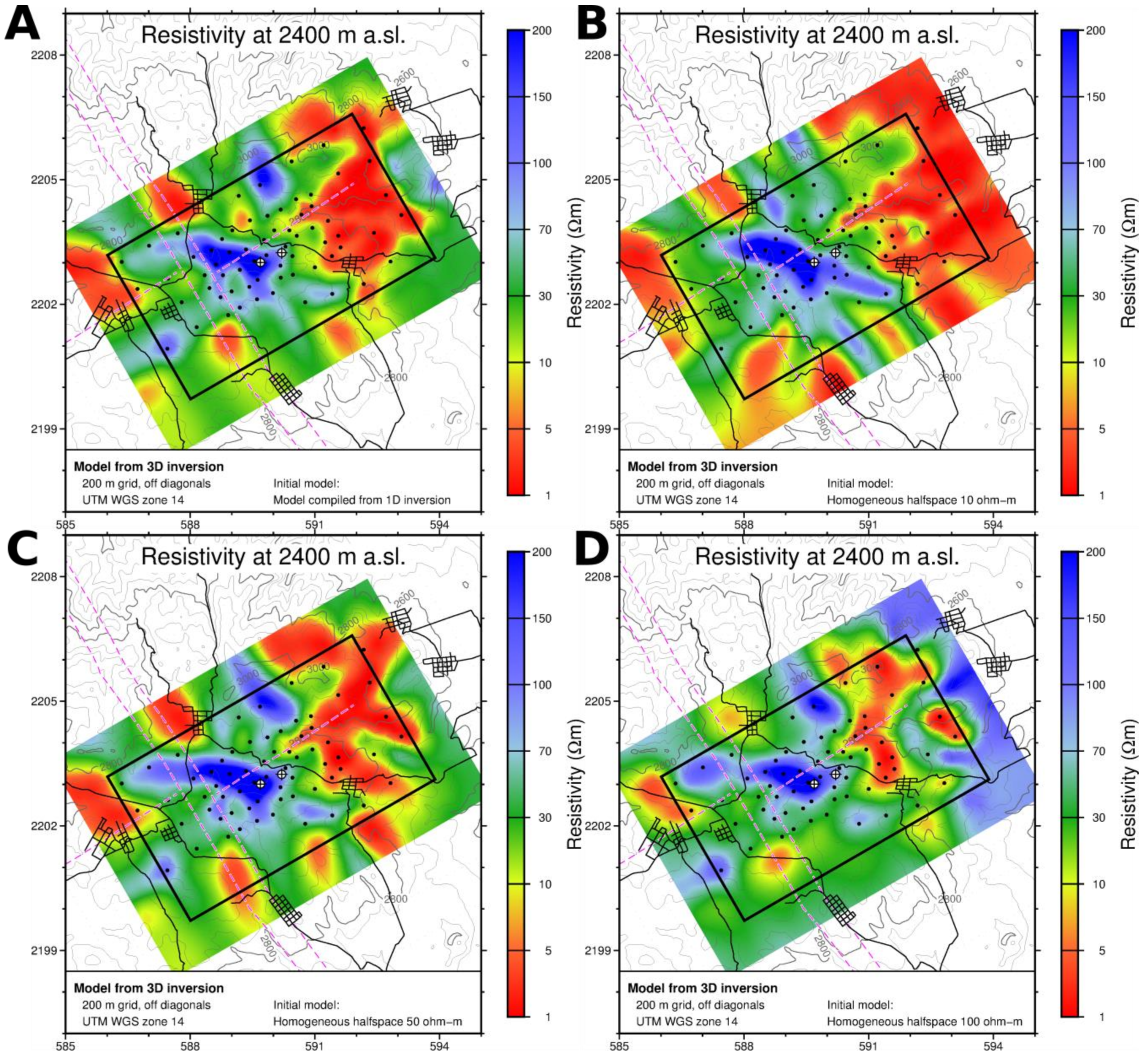

Figure 47: *Horizontal depth-slices at 2400 m above sea level through the 3D resistivity models of Acoculco survey area. The initial models used were inv1D (**A**), H010 (**B**), H050 (**C**) and H010 (**D**). The black dots are the MT sites. The black box outlines the densely gridded area of the inversion. Dark gray lines are roads, gray lines are elevation contours and pink dashed lines are the main faults in the region. The two black crosses on white circles are the EAC wells.*

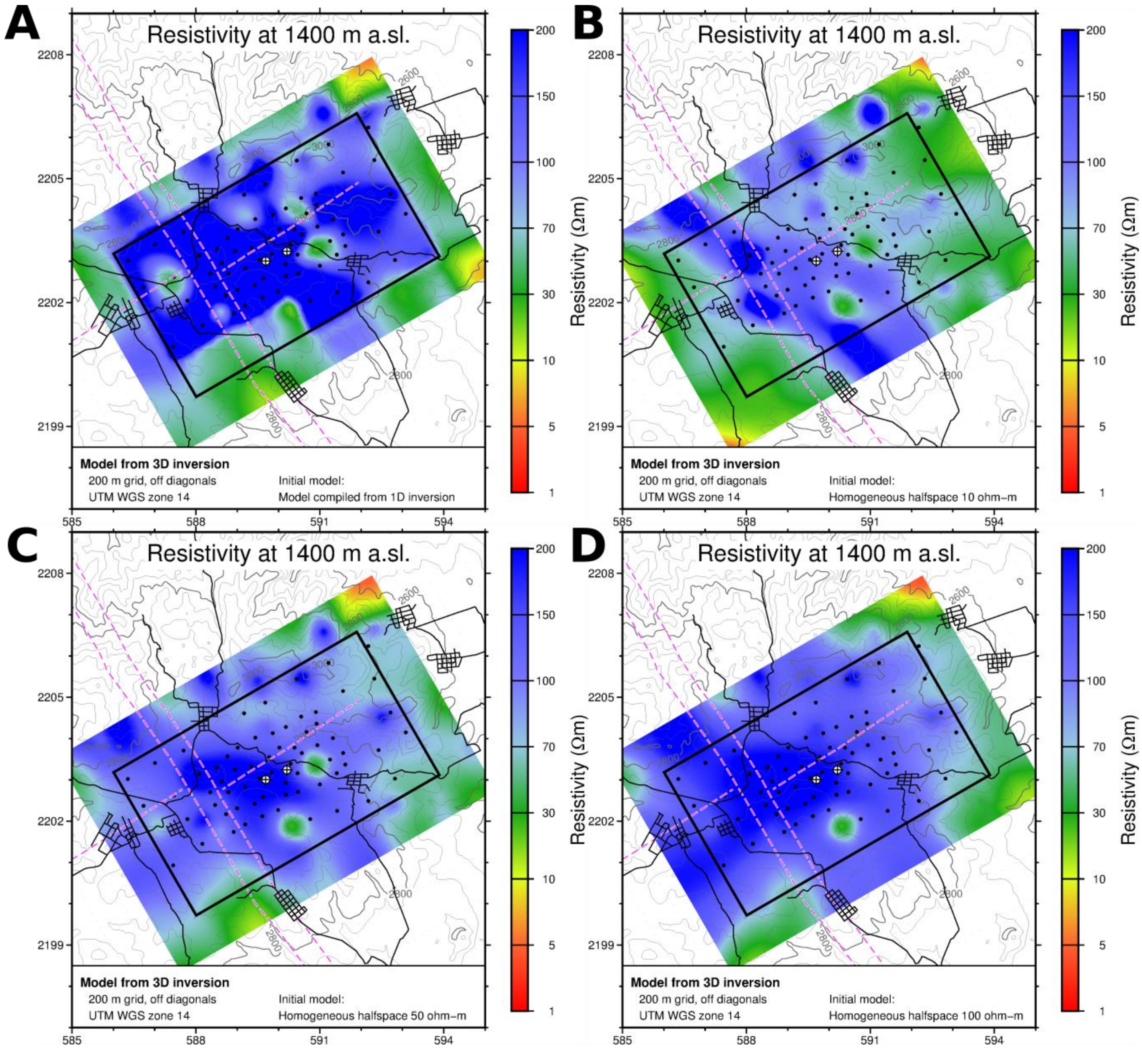

Figure 48: *Horizontal depth-slices at 1400 m above sea level through the 3D resistivity models of Acoculco survey area. The initial models used were inv1D (**A**), H010 (**B**), H050 (**C**) and H010 (**D**). The black dots are the MT sites. The black box outlines the densely gridded area of the inversion. Dark gray lines are roads, gray lines are elevation contours and pink dashed lines are the main faults in the region. The two black crosses on white circles are the EAC wells.*

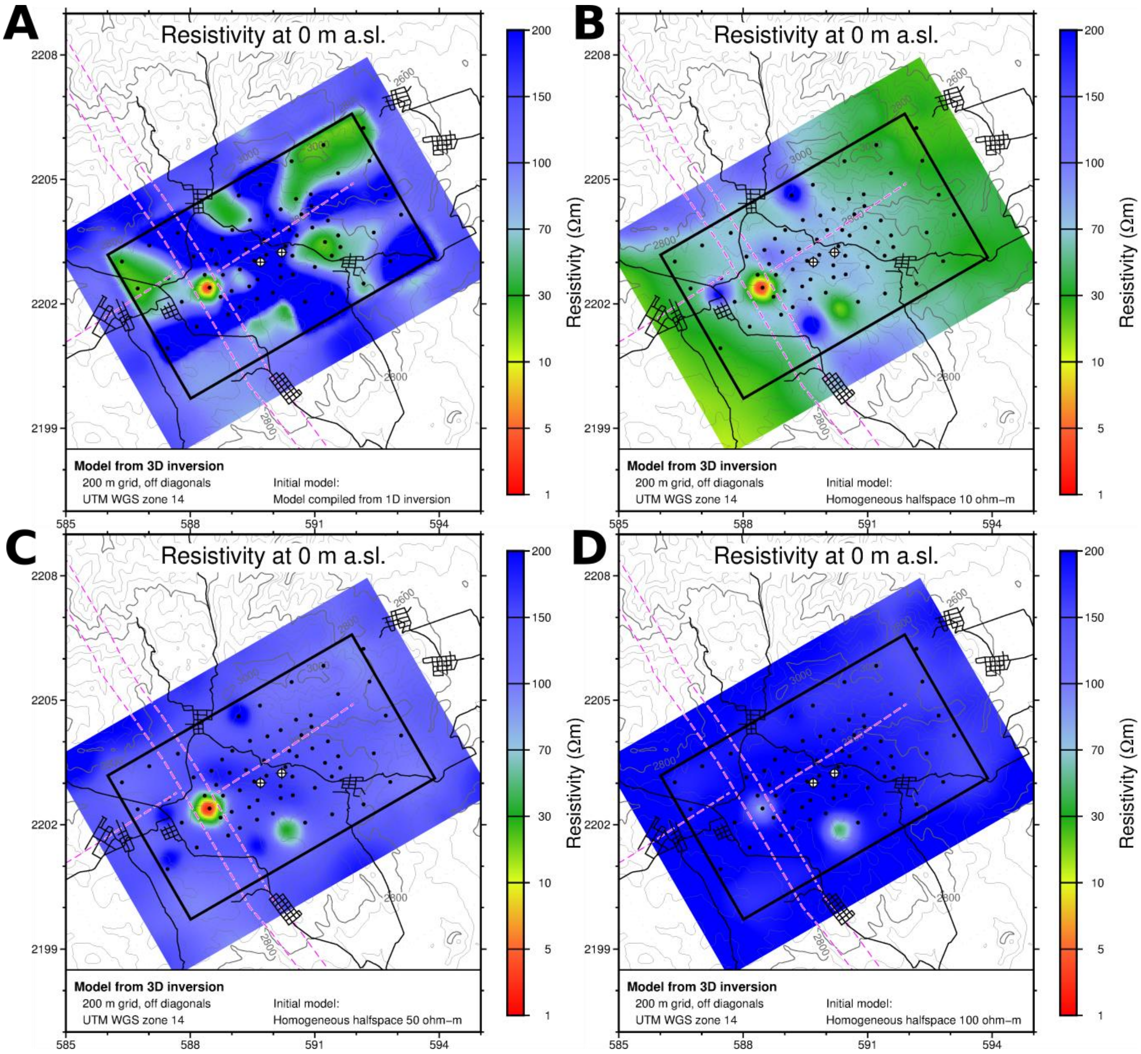

Figure 49: *Horizontal depth-slices at sea level through the 3D resistivity models of Acoculco survey area. The initial models used were inv1D (**A**), H010 (**B**), H050 (**C**) and H010 (**D**). The black dots are the MT sites. The black box outlines the densely gridded area of the inversion. Dark gray lines are roads, gray lines are elevation contours and pink dashed lines are the main faults in the region. The two black crosses on white circles are the EAC wells.*

8.5 Los Humeros: Resistivity model based on 3D inversion of MT data

The resistivity model presented here is based on a homogeneous earth of 50 Ωm initial model.

Figures 50 and 51 show horizontal cross-sections through the final resistivity model at 12 different depths. Figures 52-54 show E-W vertical cross-sections through the final resistivity model down to different depths to enhance different features of the model. Only one N-S lying vertical cross-section through the final resistivity model is shown (Figure 55) because most of the structure has a N-S orientation, which is best observed in the E-W vertical sections. For more cross-sections, see Appendix C.

The resistivity structure of the Los Humeros prospect is very three-dimensional. The conductive cap is shallowest along the main NNW-SSE striking faults in the area (Figure 50A), at 2400 m above sea level (Figure 50B) most of the conductive cap has been cut.

The high-resistive core domes up in two areas. The more pronounced feature stretches along the NNW-SSE faults (Figure 50E, F) rising almost to the surface in the north (Figure 53A) and to 1000 m sea level farther south (Figure 54A). The width of the anomaly at 1400 m above sea level is roughly 2 km (outlined in red in Figure 50E). The western boundary of this anomaly aligns almost perfectly with the westernmost NNW-SSE trending fault, throughout the survey area (Figures 50E, F and 51A-D). The fault, therefore, seems to fence off the resistive core the west.

The somewhat less up-doming feature of the high-resistive core lies to the east of the more pronounced feature (see the eastern feature in Figure 50E, F). It stretches N-S and lies in between two low-resistivity blocks (Figures 52A and 53A). It is overlain by more than 1 km of high-resistive material (Figures 52A and 53A) and the top of the high-resistive core is consistently at 1 km above sea level.

At 5000 meters below sea level a layer of intermediate resistivity is present. This layer reaches to shallower depths following the shape of the Los Potreros caldera (Figure 51 A-C).

Just south of the town of Los Humeros, a deep circular low-resistivity anomaly is present (Figure 51 D, E). This anomaly is also seen in E-W lying vertical cross-sections (Figure 54 B, C) and in the N-S lying vertical cross-section (Figure 55 B, C). One can speculate if the anomaly is an artefact from the inversion, but we note that the anomaly was also present when using the inv1D initial model (Figure 45B). Also, the location of the anomaly is where two fault directions intersect, making it a perfect place for increased permeability.

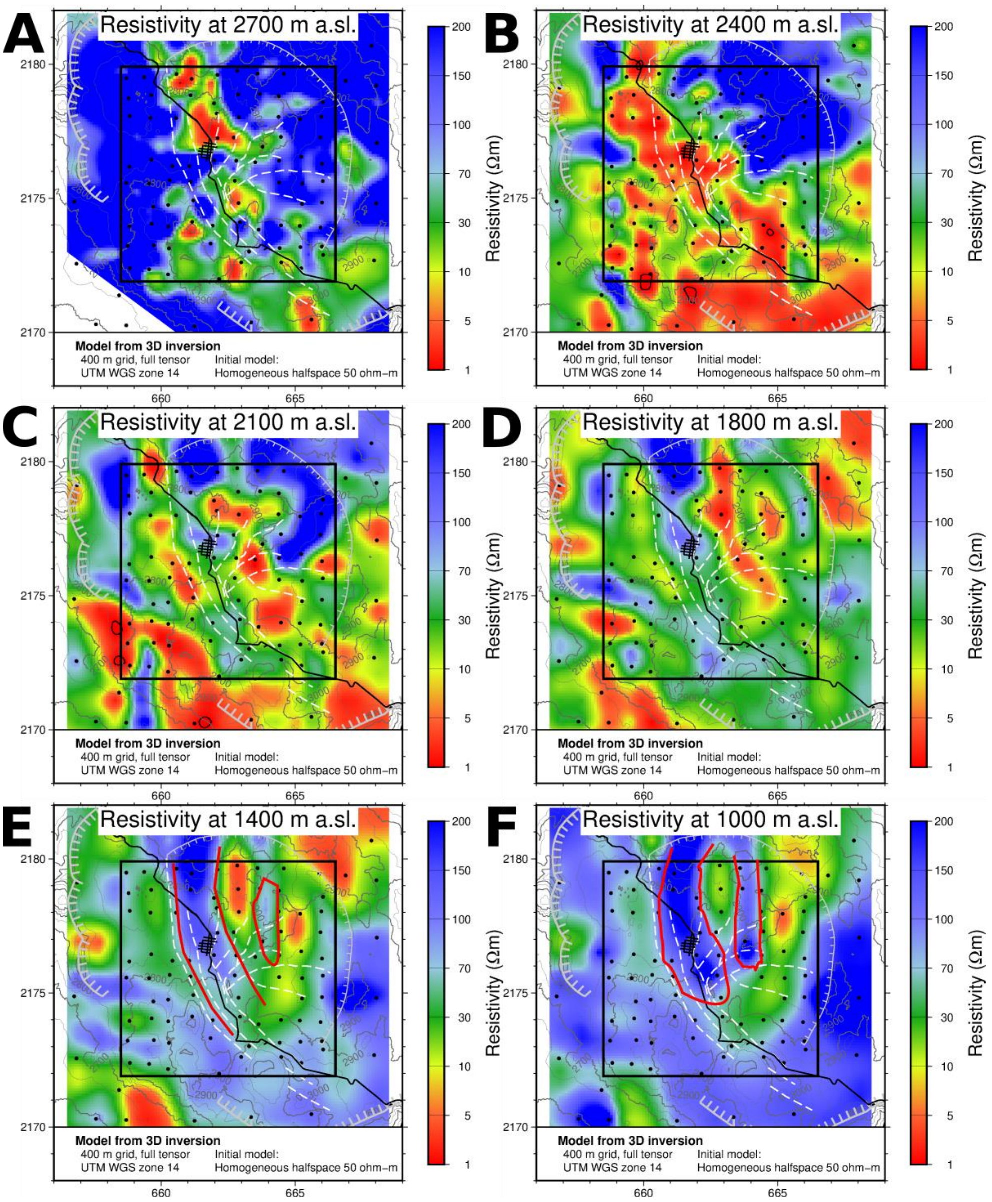

Figure 50: *Horizontal cross-sections through the final resistivity model based on the H050 initial model at 2700 m above sea level (**A**),2400 m above sea level (**B**), 2100 m above sea level (**C**), 1800 m above sea level (**D**), 1400 m above sea level (**E**) ,and 1000 m above sea level (**F**). The black dots are the MT sites. Black box shows the location of the densely gridded area in the 3D inversion. Thick and thin gray hatched lines are the Los Humeros and Los Potreros Calderas, respectively, black circles are sounding locations, white dashed lines are main faults in the area and black lines are roads. Dark gray elevation contour lines every 50 meters. Red lines in E and F outline up-doming areas seen in vertical cross-sections in Figure 53.*

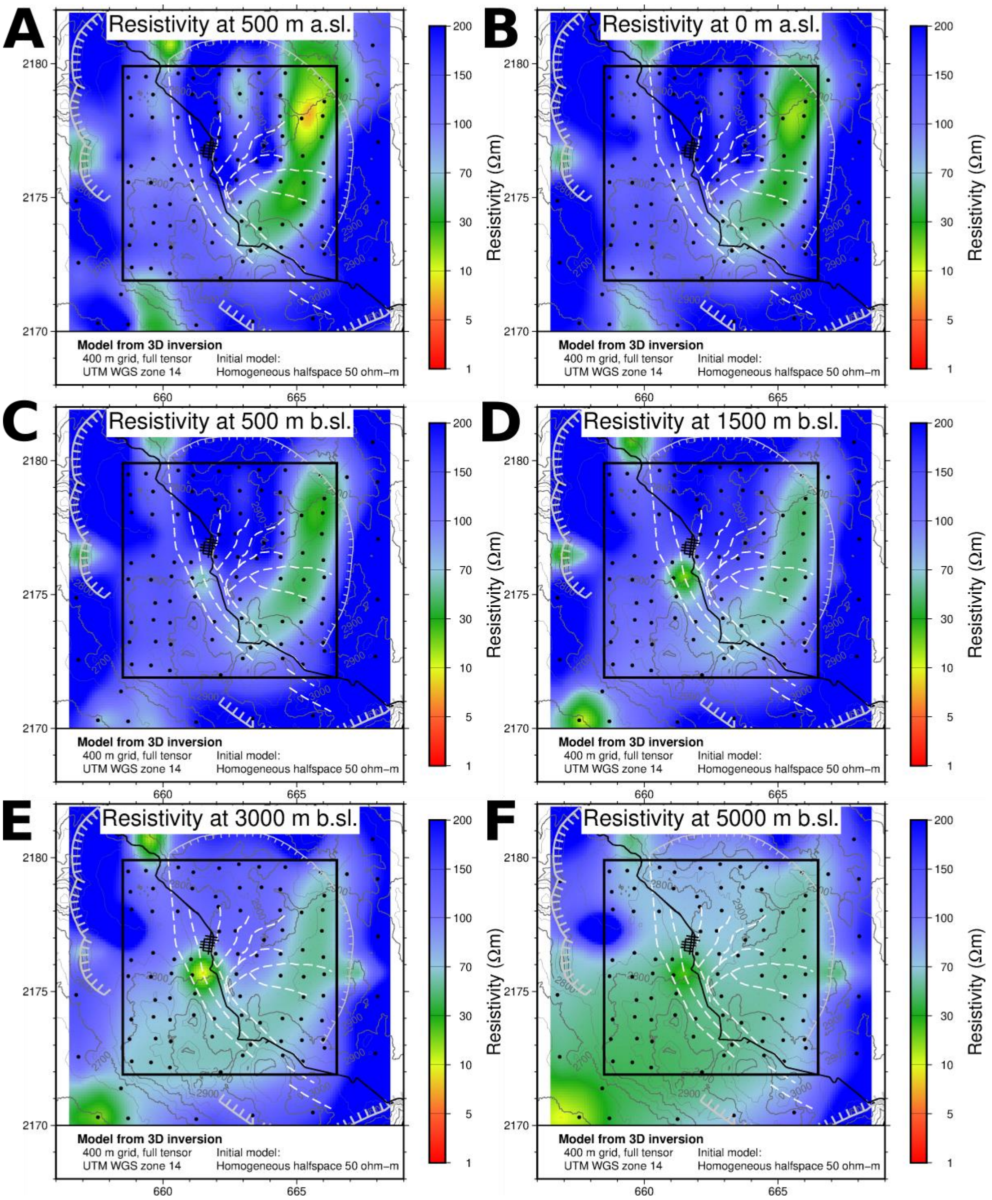

Figure 51: *Horizontal cross-sections through the final resistivity model based on the H050 initial model at 500 m above sea level (**A**), sea level (**B**), 500 m below sea level (**C**), 1500 m below sea level (**D**), 3000 m below sea level (**E**), and 5000 m below sea level (**F**). The black dots are the MT sites. Black box shows the location of the densely gridded area in the 3D inversion. Thick and thin gray hatched lines are the Los Humeros and Los Potreros Calderas, respectively, black circles are sounding locations, white dashed lines are main faults in the area and black lines are roads. Dark gray elevation contour lines every 50 meters.*

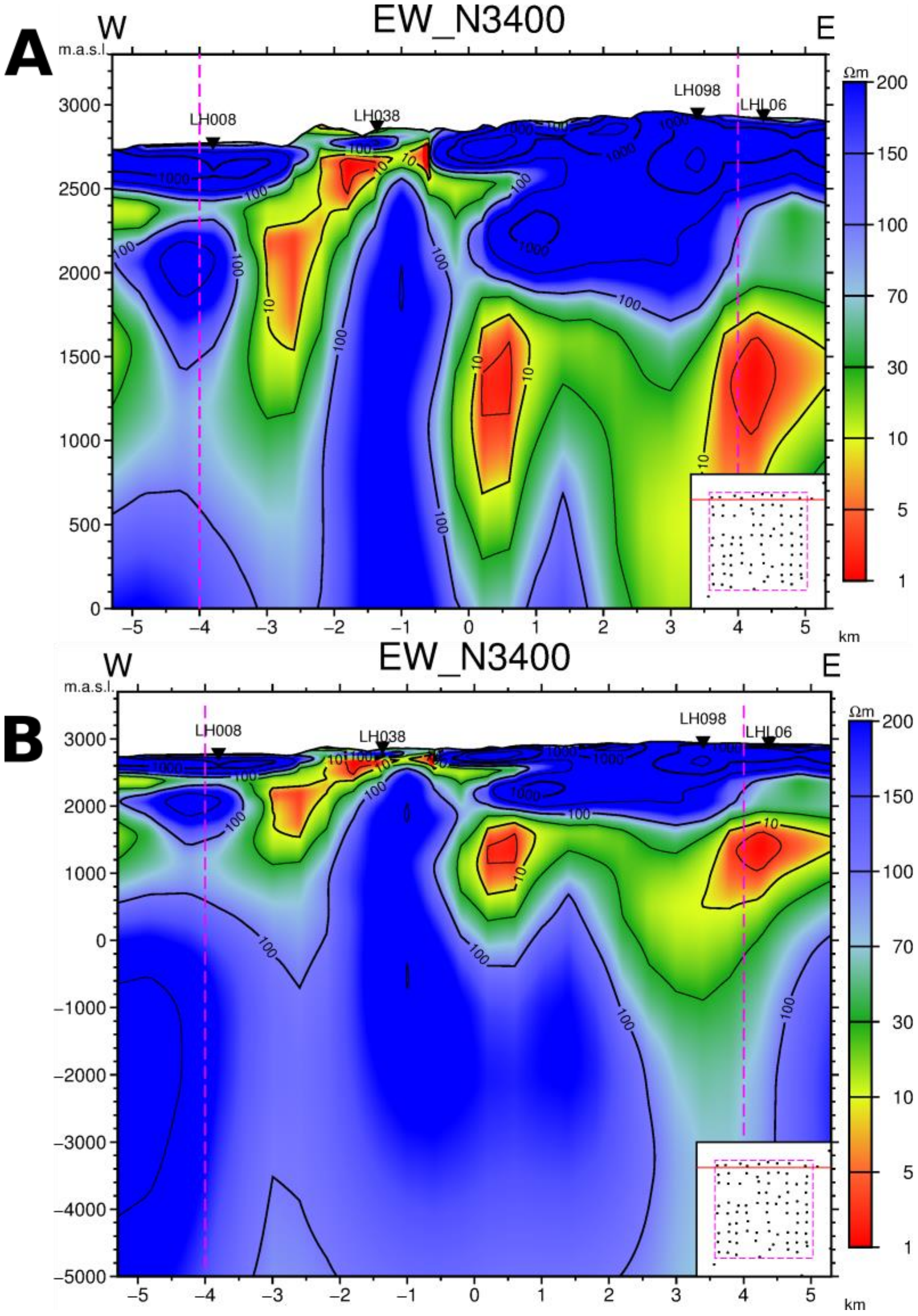

Figure 52: *West-east lying vertical cross-section at N3400 through the final resistivity model based on the H050 initial model of the Los Humeros area down to sea level (**A**) and 5000 meters below sea level (**B**). Dashed pink lines show where the densely gridded area ends. Sounding locations are shown as triangles at the surface with the sounding names. Small inlet in the bottom right corner: Location of the cross-section is shown as a red line. The black dots are sounding locations and pink dashed lines are the outlines of the densely gridded area.*

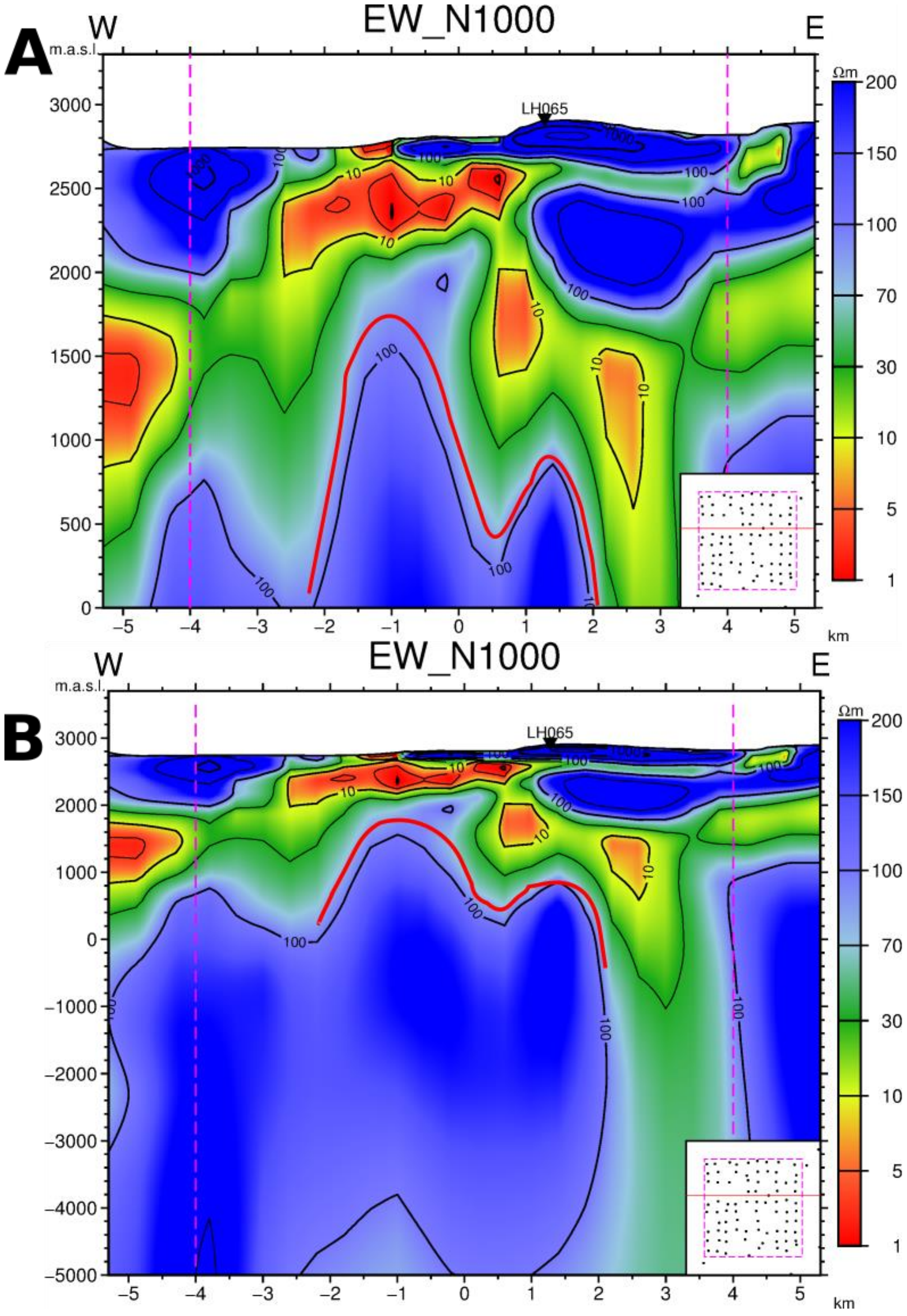

Figure 53: *West-east lying vertical cross-section at N1000 through the final resistivity model based on the H050 initial model of the Los Humeros area down to sea level (**A**) and 5000 m below sea level (**B**). Dashed pink lines show where the densely gridded area ends. Sounding locations are shown as triangles at the surface with the sounding names. Small inlet in the bottom right corner: Location of the cross-section is shown as a red line. The black dots are sounding locations and pink dashed lines are the outlines of the densely gridded area.*

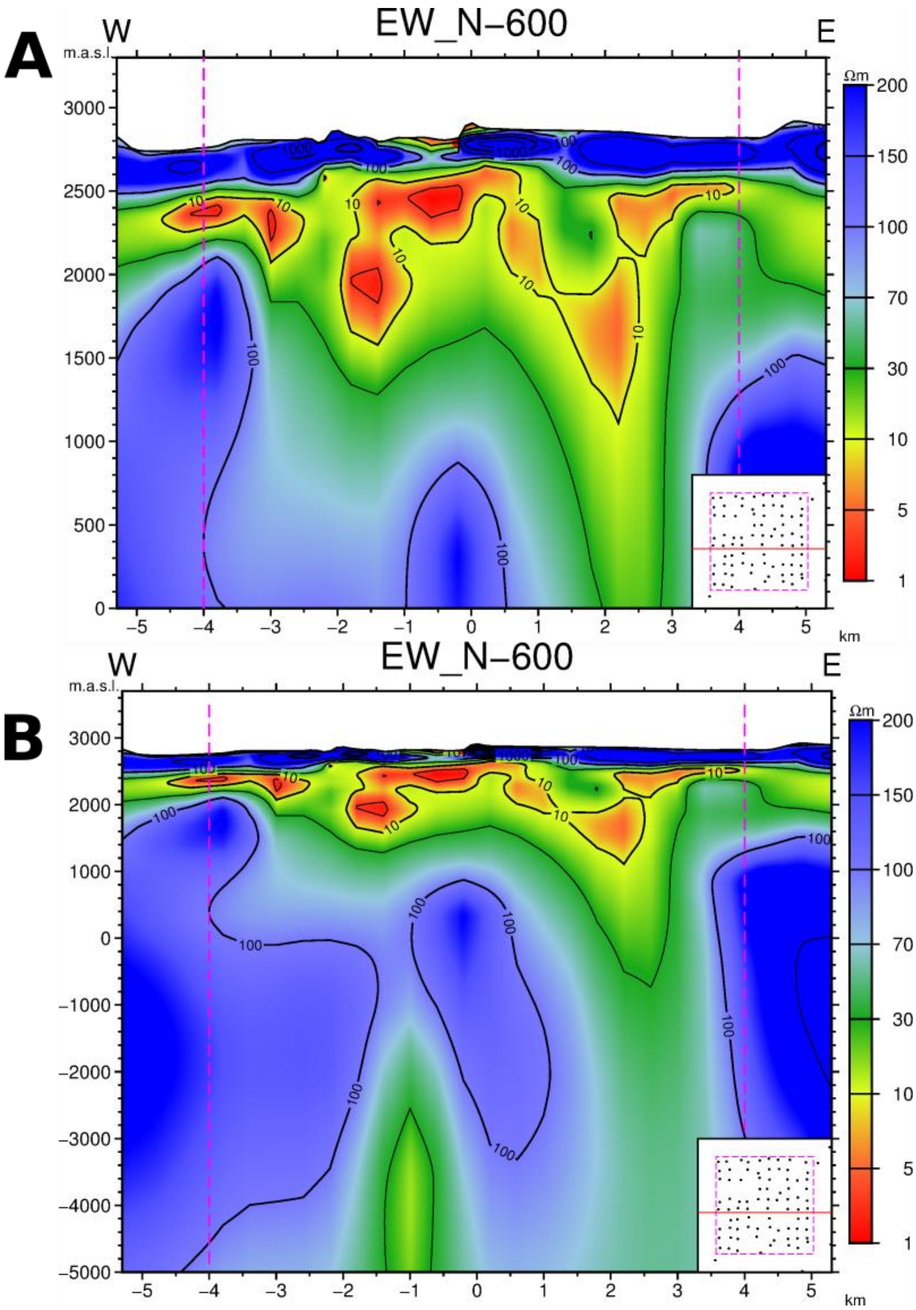

Figure 54: *West-east lying vertical cross-section at N-600 through the final resistivity model based on the H050 initial model of the Los Humeros area down to sea level (**A**) and 5000 m below sea level (**B**). Dashed pink lines show where the densely gridded area ends. Sounding locations are shown as triangles at the surface with the sounding names. Small inlet in the bottom right corner: Location of the cross-section is shown as a red line. The black dots are sounding locations and pink dashed lines are the outlines of the densely gridded area.*

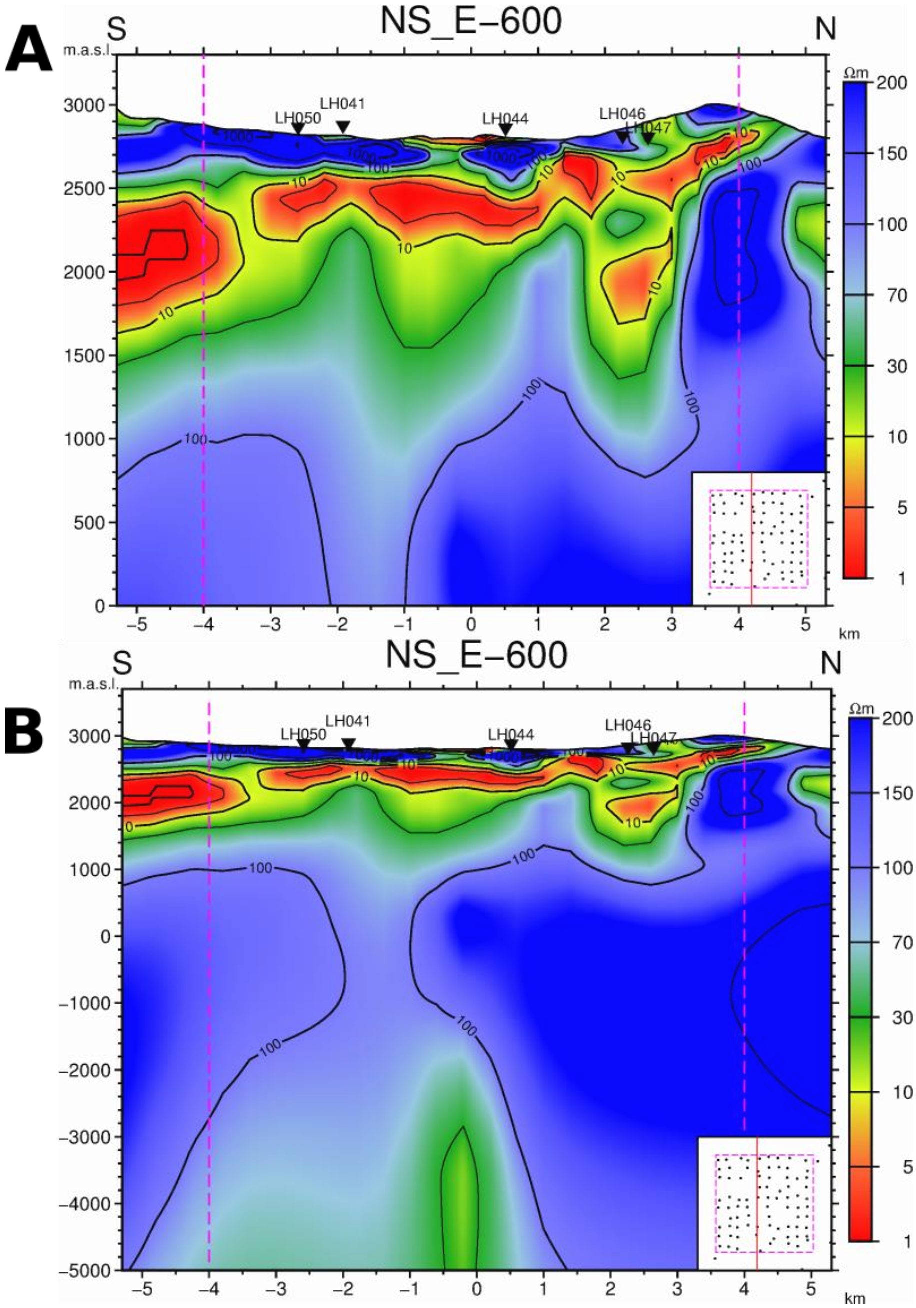

Figure 55: *South-north vertical cross-section at E-600 through the final resistivity model based on the H050 initial model of the Los Humeros area down to sea level (**A**) and 5000 m below sea level (**B**). Dashed pink lines show where the densely gridded area ends. Sounding locations are shown as triangles at the surface with the sounding names. Small inlet in the bottom right corner: Location of the cross-section is shown as a red line. The black dots are sounding locations and pink dashed liens are the outlines of the densely gridded area.*

8.6 Acoculco: Resistivity model based on 3D inversion of MT data

The resistivity model presented here is based on a homogeneous earth of 50 Ωm initial model.

Figure 56 shows horizontal cross-sections through the final resistivity model at 6 different depths. Figure 57 shows E-W lying vertical cross-sections through the final resistivity model down to sea level. For more cross-sections, see Appendix D. Data were limited to periods shorter than 10 s in most cases, and therefore, we focus on the depth range from surface down to sea level.

The resistivity structure of Acoculco is characterized by horizontal layers in most of the survey area. At 2700 m above sea level (Figure 56A) the conductive cap is present and at 2400 m below sea level (Figure 56B); the resistive core is present in the area close to the western EAC well. The zone of the resistive core exhibits a WNW-ESE orientation (Figure 56B, C).

A white dashed line, at 2400 and 2000 m above sea level (Figure 56B, C), marks the transition seen in the strike analyses and the 1D resistivity model of Acoculco. The area to the east of the transition zone exhibits a 1D structure while the area to the west has a more 3D resistivity structure.

The resistive core has one very prominent up-doming feature (Figure 57) and is shallowest at 400-600 m below the surface, close to sounding 37 (Figure 57 B), which is located close to the western EAC well.

One peculiar feature is observed at the intersection of the main fault zones in the area at a depth of 500 m above sea level down to 4000 m below sea level. This feature is observed in all the models (Figure 49) and is unusually confined. Apparently, the data require this feature in the models for a good fit but should still be interpreted cautiously.

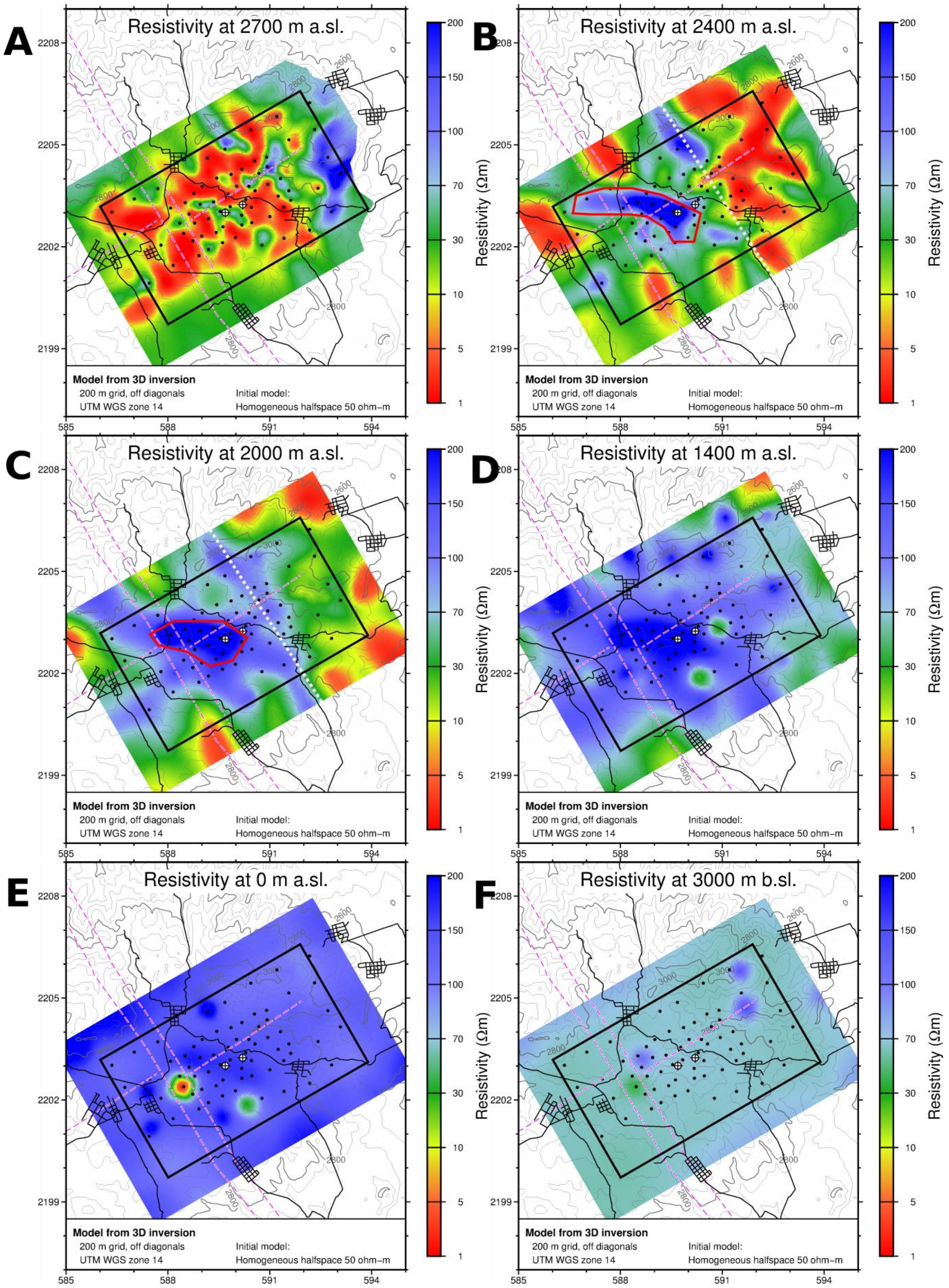

Figure 56: *Horizontal cross-sections through the final 3D model based on the H050 initial model of the Acoculco survey area at 2700 meters above sea level (**A**), 2400 meters above sea level (**B**), 2000 meters above sea level (**C**), 1400 meters above sea level (**D**), sea level (**E**), and at 3000 meters below sea level (**F**). The black dots are the MT sites. Black box outlines the densely gridded area black circles are sounding locations, pink lines are main fault lines in the area, gray lines are elevation contours, and dark gray lines are roads. Black crosses on a white circle are the locations of the two EAC wells.*

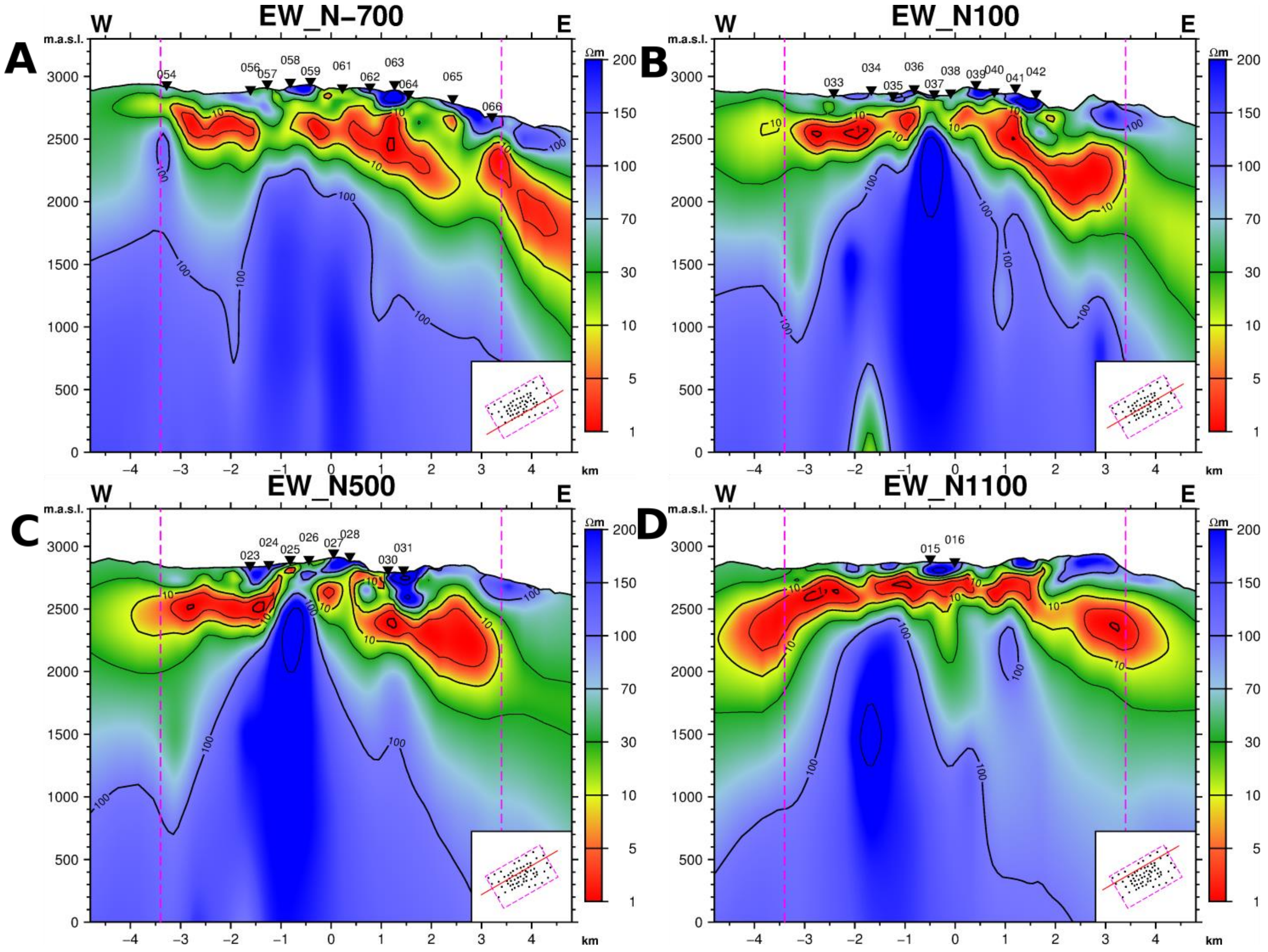

Figure 57: *West-east lying vertical cross-sections through the final resistivity model based on the H050 initial model for the Acoculco area plotted down to sea level. Pink dashed vertical lines are the boundaries of the densely gridded area. Black triangles at the surface are the station locations along with their names. Small inlet in the bottom right corner: Location of the cross-section is shown as a red line. The black dots are sounding locations and pink dashed lines are the outlines of the densely gridded area.*

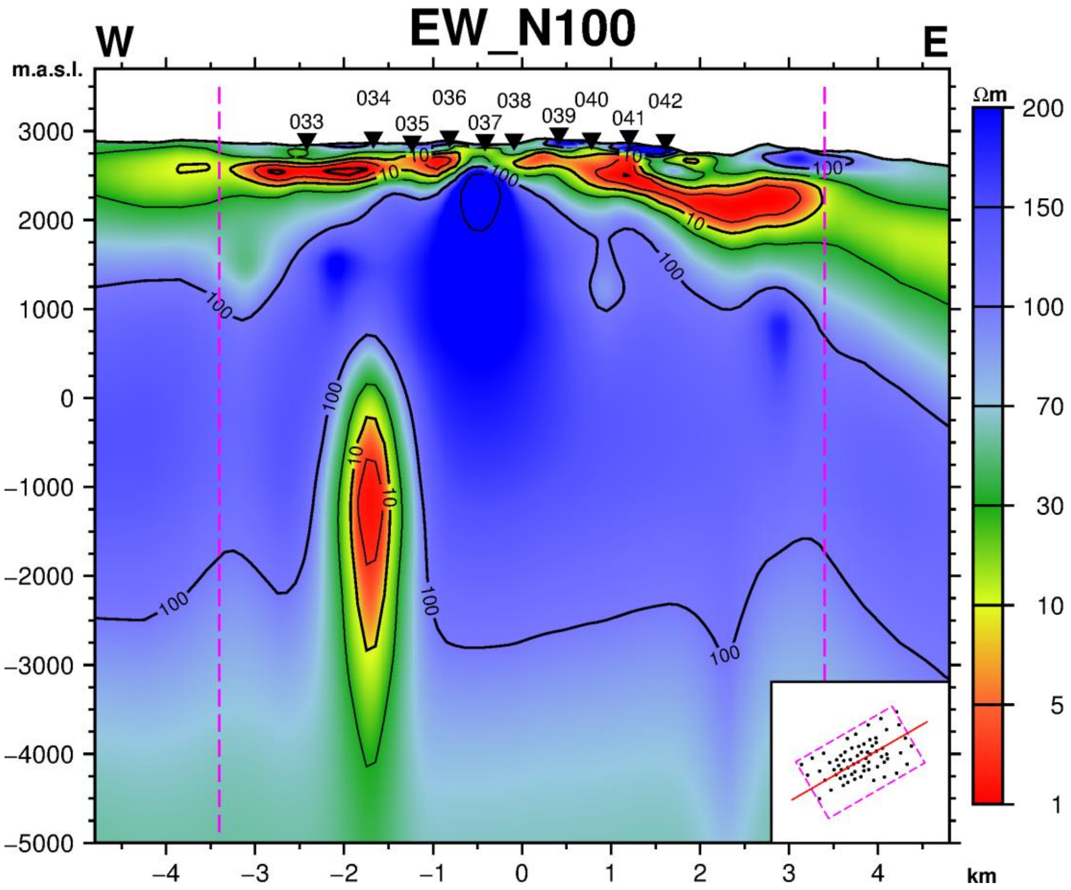

Figure 58: *West-east lying vertical cross-section through the final resistivity model based on the H050 initial model for the Acoculco survey area. Pink dashed vertical lines are the boundaries of the densely gridded area. Black triangles at the surface are the station locations along with their names. Small inlet in the bottom right corner: Location of the cross-section is shown as a red line. The black dots are sounding locations and pink dashed lines are the outlines of the densely gridded area.*

8.7 Conclusion

The final models based on 3D inversion of the MT data from the Los Humeros and Acoculco survey areas have been calculated and presented.

Upon comparing the results based on different initial models for the Los Humeros area we chose a model calculated from an initial model consisting of a homogeneous earth with 50 Ωm. The main resistivity structure follows the NNW-SSE striking faults in the region and the outlines of the Los Potreros caldera. Two up-doming features were identified. The western one, striking NNW-SSE, was more pronounced, compared to the N-S oriented eastern one. A deep lying intermediate-resistivity bubble is observed at the junction of two main fault orientations in the region. An intermediate-resistivity body seems to follow the outlines of the eastern part of the Los Potreros caldera.

For Acoculco we chose a model calculated from an initial model consisting of a homogeneous earth with 50 Ωm, although all the different tests using different initial models resulted in a similar model. The main feature in the Acoculco area was a shallow lying resistive core, located underneath the western EAC well and stretching towards the NW. Also, a low-resistivity body, located 500 m above sea level down to 4000 m below sea level, was observed. The body was confined, and it is unknown whether this is an artefact or a real feature. As the longest MT data periods acquired in the Acoculco area where relatively short (1-10 s in most cases), practically no structures were resolved at depths below sea level.

9 Resistivity model of the Krafla and Reykjanes geothermal fields

Iceland is the home to many high-temperature geothermal fields, including Krafla, NE-Iceland and Reykjanes, SW-Iceland (Figure 59). The Reykjanes high-temperature geothermal field is located on the tip of the oblique spreading Reykjanes Peninsula and is the point in Iceland where the mid-ocean ridge becomes sub-areal. Krafla is a central volcano located in the Northern Volcanic Rift zone. The high-temperature geothermal system takes it name from the volcano. The installed capacity at Reykjanes and Krafla geothermal power stations is 100 MWe and 60 MWe, respectively.

Recently, two deep wells were drilled in Iceland, as a part of the Iceland Deep Drilling Project (IDDP). The first one in Krafla, drilled in 2008-2009 and the second one in Reykjanes, drilled in 2016-2017. The aim with the IDDP wells is to drill deep, where hydrothermal fluid in supercritical conditions is found.

Experience from the two IDDP sites can be applied to other superhot geothermal systems to a certain extent. Every system is different but the similarities between the different superhot geothermal systems are also striking. They all exhibit a resistive-core, that domes up at the center of the field, overlain by a conductive cap. The geometry is, of course, variable from one field to another. Therefore, one can apply the general knowledge gained from the previously drilled deep wells without expecting exactly the same results or behavior in a different system, where deep drilling is planned.

As a part of this project, the resistivity models of the Krafla and Reykjanes geothermal fields have been revisited in light of IDDP well 1 and 2. The resistivity structure of the two Icelandic superhot systems are compared to the one in Los Humeros.

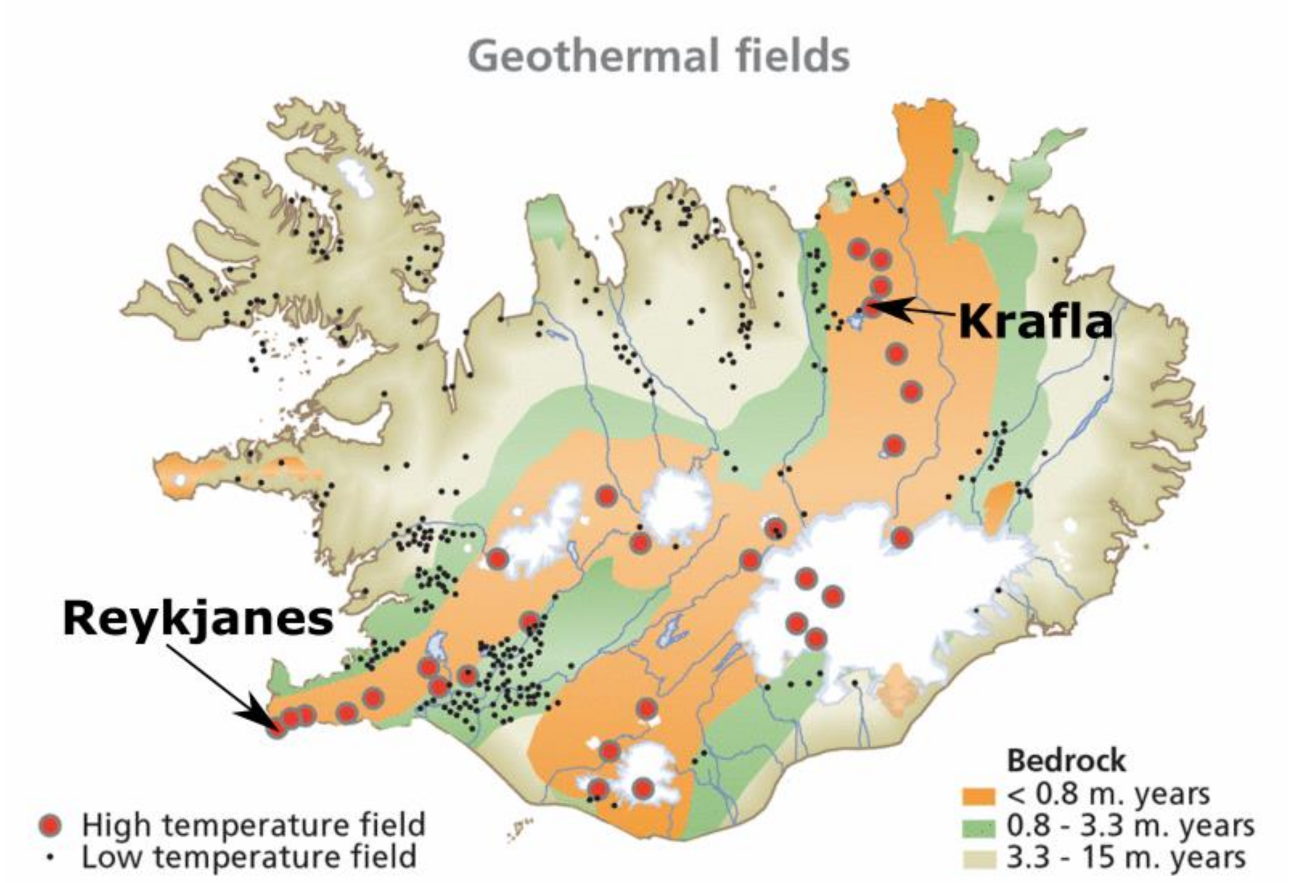

Figure 59: *High- and low temperature fields in Iceland in relation to the rift zones and the geology of Iceland. Locations of Krafla and Reykjanes geothermal fields are indicated. Map from www.nea.is.*

9.1 Resistivity model of the Reykjanes geothermal field

The geothermal system in Reykjanes is young, as it is situated on the Reykjanes Peninsula, where no caldera-forming central volcanoes are located.

The most recent resistivity model of the Reykjanes high-temperature field was published by Karlsdóttir et al. (2018). In the resistivity model of the Reykjanes high-temperature field a very confined system is revealed. A conductive cap underlain by a high resistive core reflects the thermal alteration of the rock (Figure 60).

The resistivity structure is controlled by the tectonics in the region. Figure 60 shows a horizontal cross-section through the resistivity model of the Reykjanes geothermal field. The system is elongated in a SW-NE direction, which is the main fault direction in the area. Elongated low-resistivity ridges are observed at the tip of the peninsula, that are offset to the NW, via a likely left-lateral transform fault (black box in Figure 60).

Within the bounds of the low-resistivity ridges is a resistive core, the main reservoir structure of the Reykjanes geothermal system. By the description given here, the lateral extent of the system is 2 km SW-NE and 1 km NW-SE.

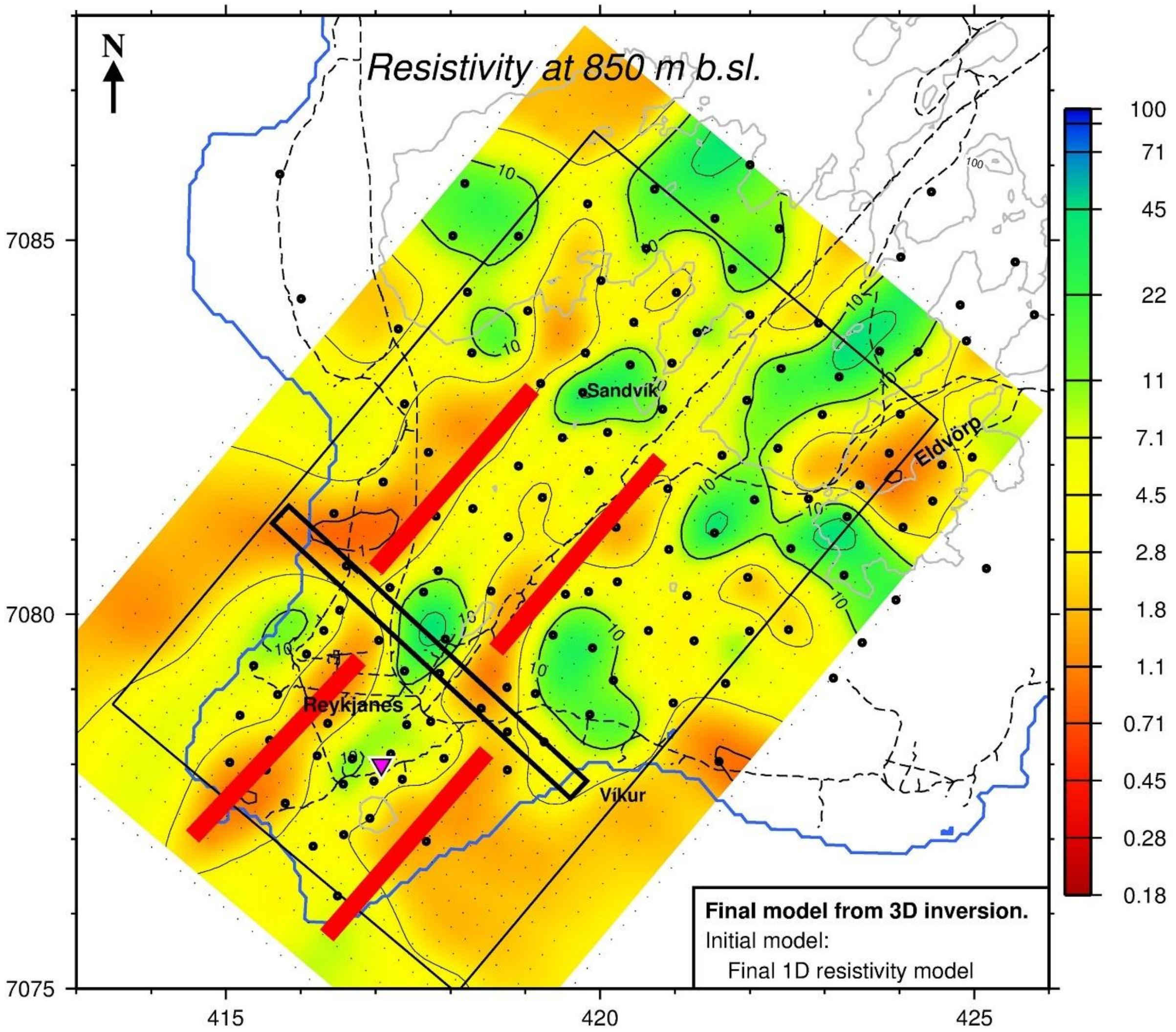

Figure 60 : *A horizontal cross-section through the resistivity structure in the Reykjanes geothermal area, after Karlsdóttir et al. (2018). Gunnuhver hot spring is marked with a purple triangle. The two red lines in the southwest, denote low-resistivity anomalies and mark the boundaries of the Reykjanes system. In between the two red lines is the resistive core of the system. The black, unfilled, box marks a possible NW-SE fracture zone, that possibly closes the system off to the NE. Blue line is the coast line and black dashed lines are roads. Black circles are sounding sites and elevation contours are gray thin lines.*

Figure 61 shows two vertical cross-sections through the geothermal system in Reykjanes. The top of resistive core lies at the center of the area, giving rise to an up-doming feature of the resistive-core. The alteration in the wells agrees well with the resistivity structure of the area. Smectite alteration zones in the wells coincide with the conductive cap and the resistive chlorite-epidote alteration zones are in the more resistive parts of the cross-section.

Figure 62 shows a horizontal cross-section through the resistivity model of Reykjanes at 5000 meters below sea level. The low-resistivity column seen in the vertical cross-sections (Figure 61B, C) is seen as a circular feature, just north of Gunnuhver (pink triangle). The low-resistivity feature coincides with an aseismic zone, that Karlsdóttir et al. (2018) interpreted as a fracture zone with higher temperature and/or permeability within the geothermal system.

The location of the IDDP-2 well and its well-path is shown (Figure 61 A). Red stars in the vertical cross-sections show the location where the IDDP-2 well intersects them (Figure 61 B, C).

The IDDP-2 well was drilled down to almost 4600 meters, reaching a temperature of 426°C (Figure 63). It was drilled into the low-resistivity column underneath the high-resistive core. Here, we note the importance of seismic data in joint interpretation of the system, as the resolution of the resistivity data diminishes largely in areas where conductive bodies are located close to the surface and screen off the deep-lying bodies.

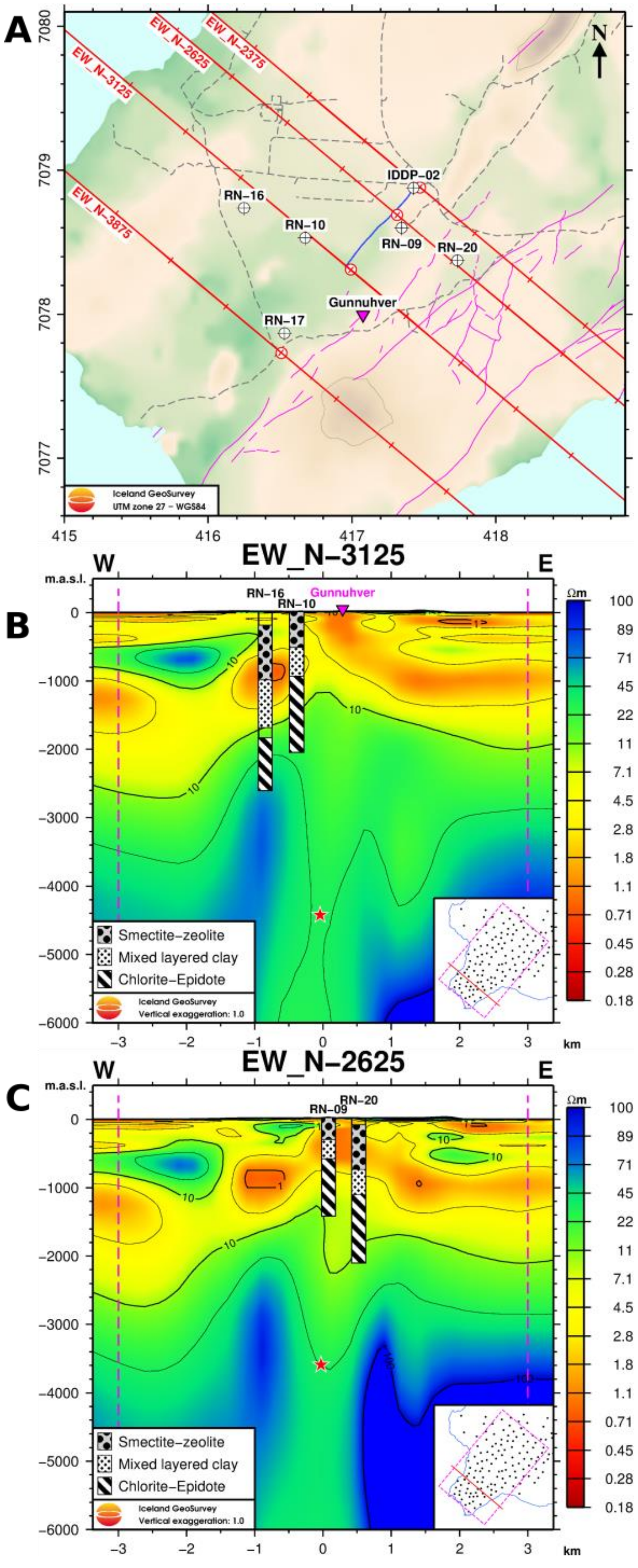

Figure 61: *Vertical cross-sections through the resistivity model at the Reykjanes geothermal field (B, C) and a location map of the cross-sections.* ***A.*** *Location of vertical wells in the geothermal area (white circles with black crosses) and the well-path for IDDP-2 (blue line). Red lines denote the location of the cross-sections.* ***B. and C.*** *Vertical cross-section down to 6000 meters below sea level. Red star marks the location where the IDDP-2 well cuts through the cross-section. Wells and their alteration minerology is also displayed. All images are from Karlsdóttir et al. (2018).*

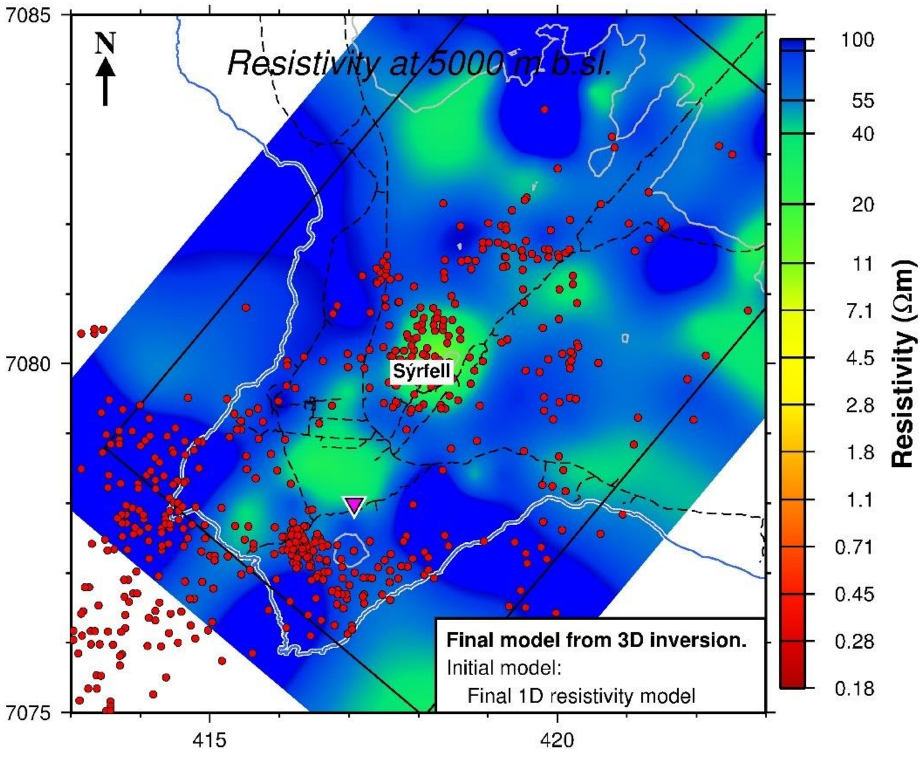

Figure 62: *Deeper parts of the Reykjanes geothermal field (from Karlsdóttir et al. (2018)) as seen in a horizontal cross-section at 5000 meters below sea level. Red circles are earthquakes at 4.5-5.5 km depth from January 2013 to July 2016, revealing an aseismic zone in the center of the system. The low-resistivity column from Figure 61 is seen north of Gunnuhver (purple triangle).*

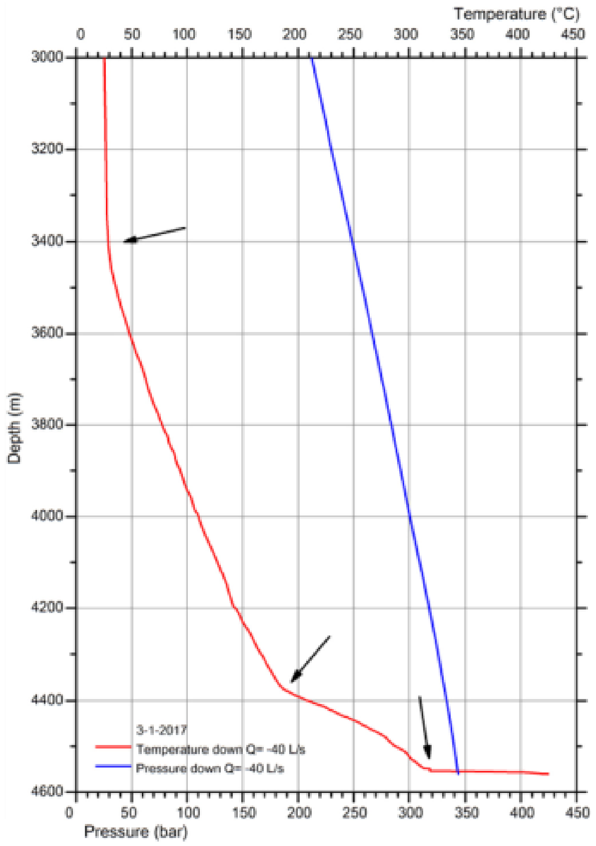

Figure 63: *Temperature (red curve) and pressure (blue curve) in the IDDP-2 well (from Friðleifsson et al. (2018)).*

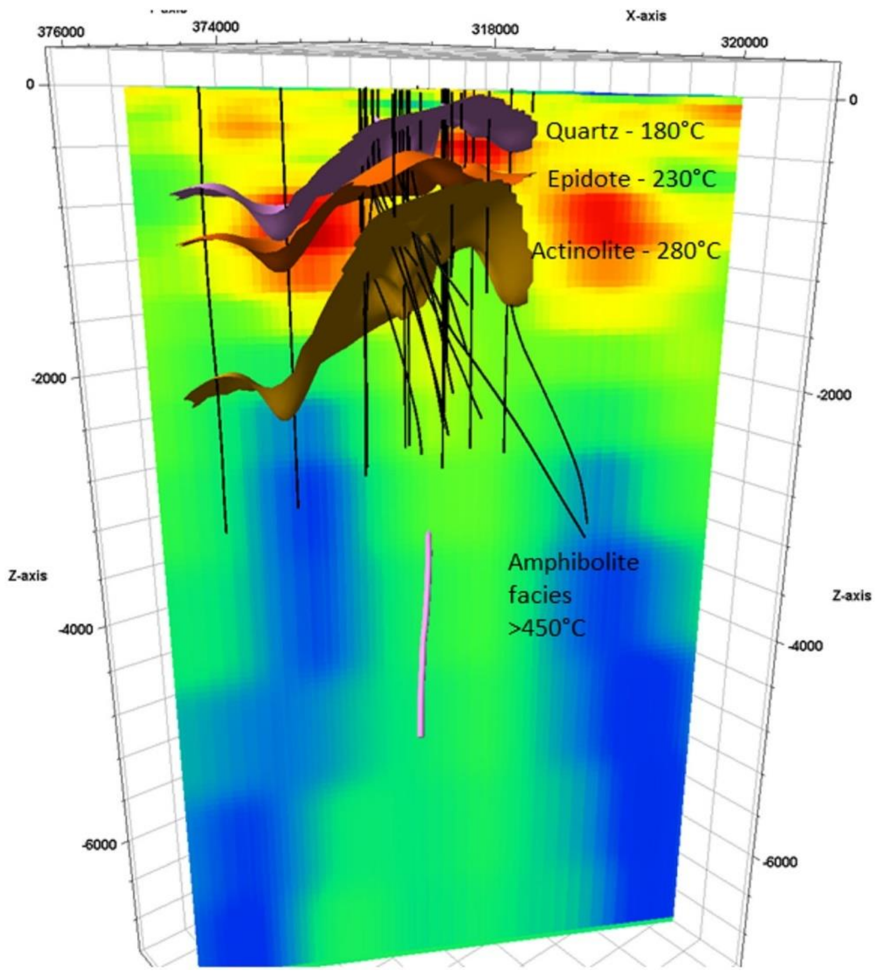

Figure 64 *Wells in the Reykjanes geothermal field in relation to the resistivity structure of the region. Purple well is the IDDP-2 well. Warm and cold colors are low-and high resistivity values, respectively. Surfaces interpolated between wells based on the first appearance of hydrothermal quartz (purple), epidote (orange) and actinolite (brown) are shown and have the minimum depths within the center of the well field. Figure taken from Friðleifsson et al. (2018).*

9.2 **Resistivity model of the Krafla geothermal field**

The Krafla central volcano has a caldera, though which the fissure swarms, associated with the central volcano, run. The dominant strike direction is SSW-NNE, faults and fissures that are cross cut by a transform graben-oriented WNW-ESE (Figure 65).

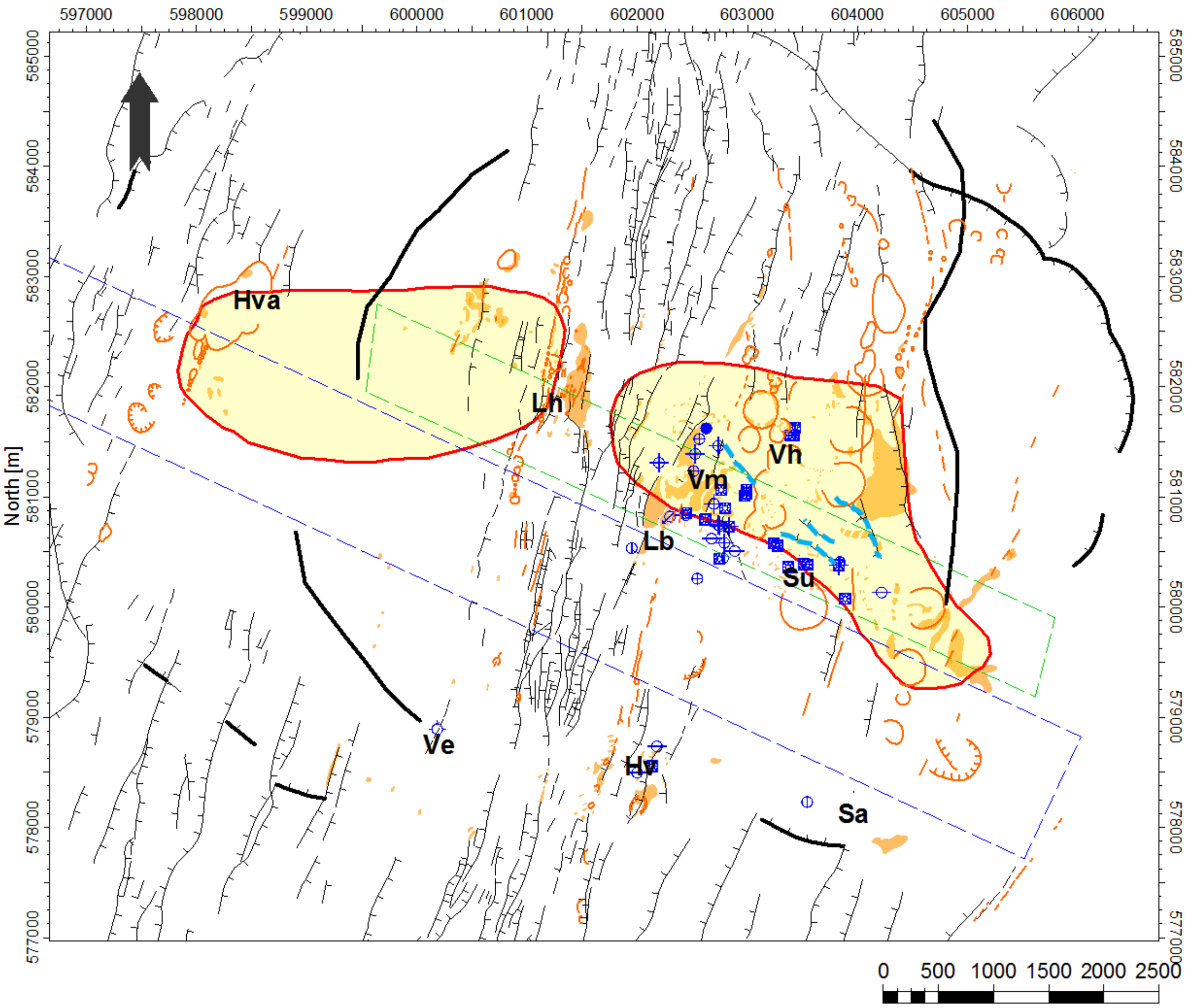

Figure 65: *Geologial structure of the Krafla geothermal area. Light blue dashed lines show the NNW-SSW to WNW-ESE trending faults and fissures as well as the magma chamber. Dark blue dashed lines show the inferred transform graben mapped by Árnason et al. (2011) and green dashed lines represent parallel resistivity high. Yellow shaded areas are S-wave shadows (Einarsson, 1978). The sub-areas are labelled as abbreviations on the map: Hvannstóð (Hva), Leirhnjúkur (Lh), Vesturhlíðar (Vh), Vítismór (Vm), Leirbotnar (Lb), Suðurhlíðar (Su), Vestursvæði (Ve), Hvíthólar (Hv), Sandabotnar (Sa). Black lines mark outer and inner calderas and blue points mark well tops. Figure from Thorsteinsdóttir et al. (2018).*

Figures 66 and 67 show the resistivity structure in Krafla, from two studies, Rosenkjær et al. (2015) in Figure 66 and from Gasperikova et al. (2015) in Figure 67. The WNW-ESE graben is seen in gravity data and a high resistivity anomaly, also trending WNE-ESE, is located just north of the graben (Figure 65,66). The location of the vertical IDDP-1 well was in between Vítismóar (Vm) and Vesturhálsar (Vh).

The well was drilled down to 2.1 km when it hit rhyolitic magma at 900-1000°C (Friðleifsson, 2015). The well was not cemented, as had been done in Hawaii when they drilled to magma (Stolper et al., 2009), but allowed to heat up. Figure 68 shows temperature measurements in the IDDP-1 well at different days of heating, reaching 350°C. After two months of heating the wellhead temperature was 450°C.

The site selection for IDDP-1 was based on various data, including results from 1D joint inversion of MT and TEM data (Friðleifsson, 2014), as no 3D inversion was available at that time. Figure 69 shows a horizontal cross-section at 4000 meters below sea level through a model based on 1D join inversion of TEM/MT data (Árnason, 2011). Two low-resistive bodies, east and west of the NNW-SSE fissure swarm that cross-cuts the caldera, were interpreted to be either magma bodies or the boundary to the brittle/ductile transition. These two bodies rise up to 2.5-3 km below sea level. These two low-resistivity bodies are also seen in a more recent 3D inversion of MT data (Figure 66, lower left panel) from Rosenkjær et al., (2015). The IDDP-1 target was the eastern low-resistivity anomaly (Friðleifsson, 2014) and the plan was to drill to 4500 meters below sea level.

It is wort noting that other data such as seismic, geological and data from drill-holes were also considered when deciding the location for the IDDP-1 well (Friðleifsson et al., 2014). Needless to say, the IDDP-1 did not reach 4500 m as it hit rhyolitic magma at 2100 m.

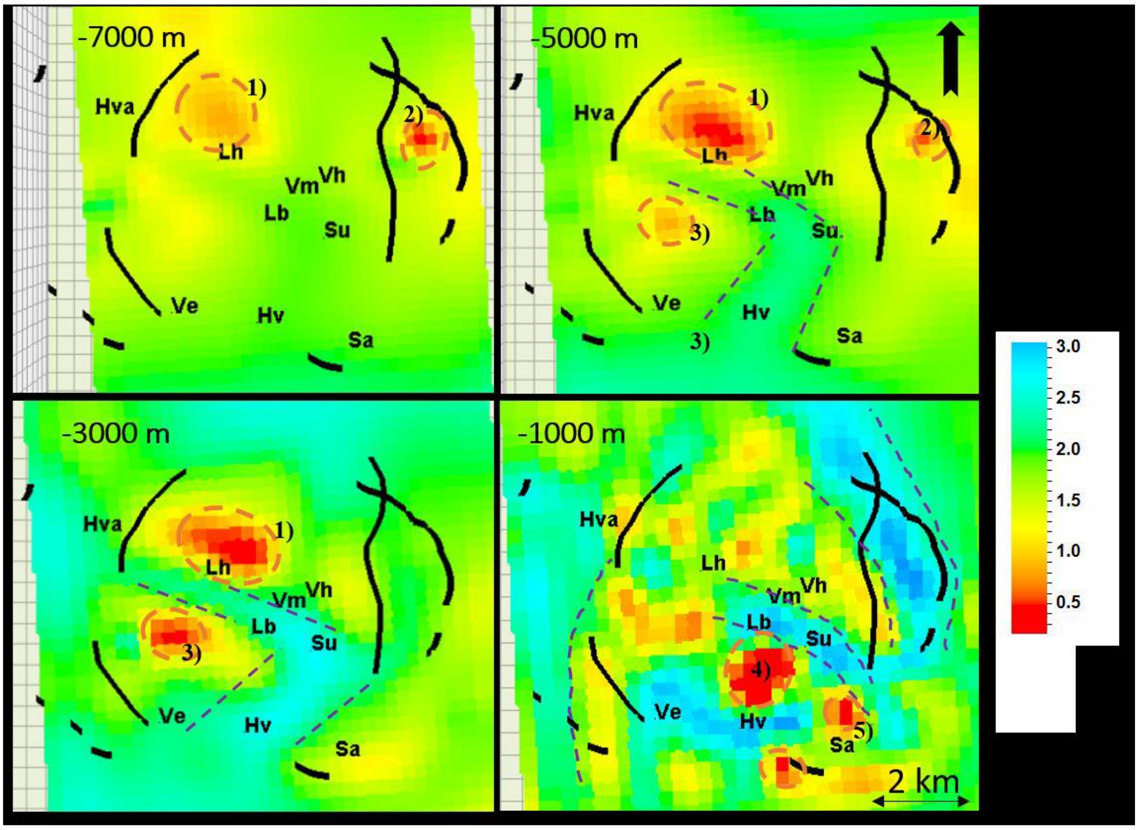

Figure 66: *Horizontal cross-sections through the resistivity model of Krafla (after Rosenkjær, 2015). Location of the IDDP-1 well is in between Vm (Vítismóar) and Vesturhálsar (Vh).*

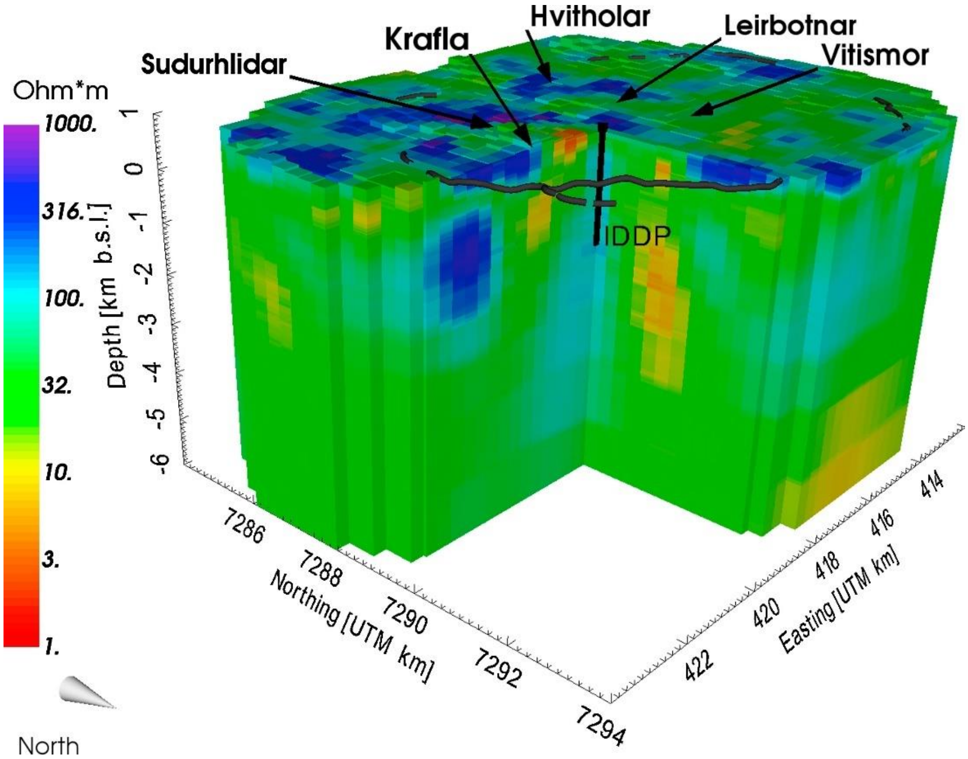

Figure 67: *Resistivity structure of the Krafla geothermal field as presented by Gasperikova et al., (2015). The IDDP-1 well is in the center of the block.*

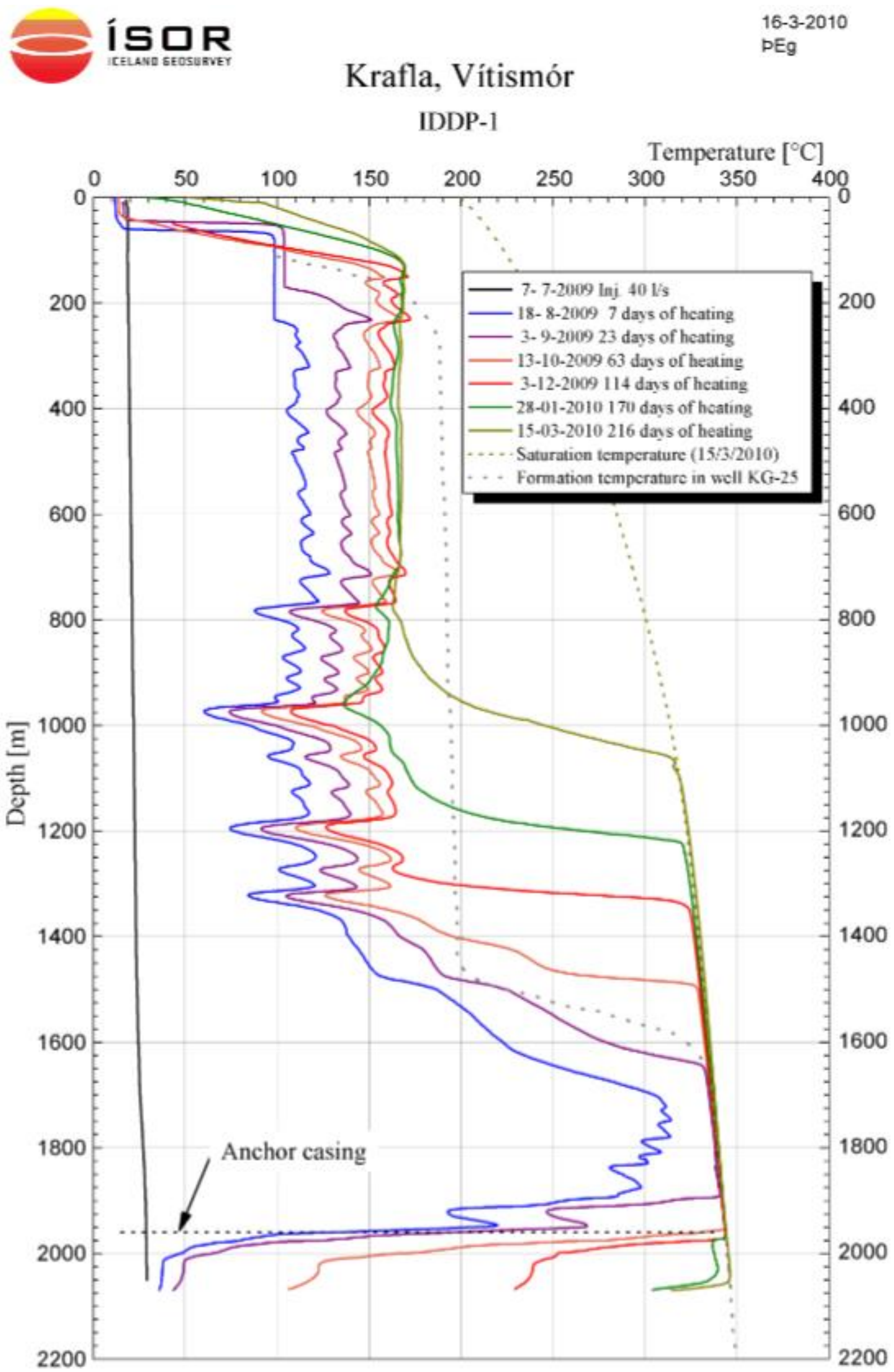

Figure 68 *Temperature profile from IDDP-1. Figure from Friðleifsson et al. (2015).*

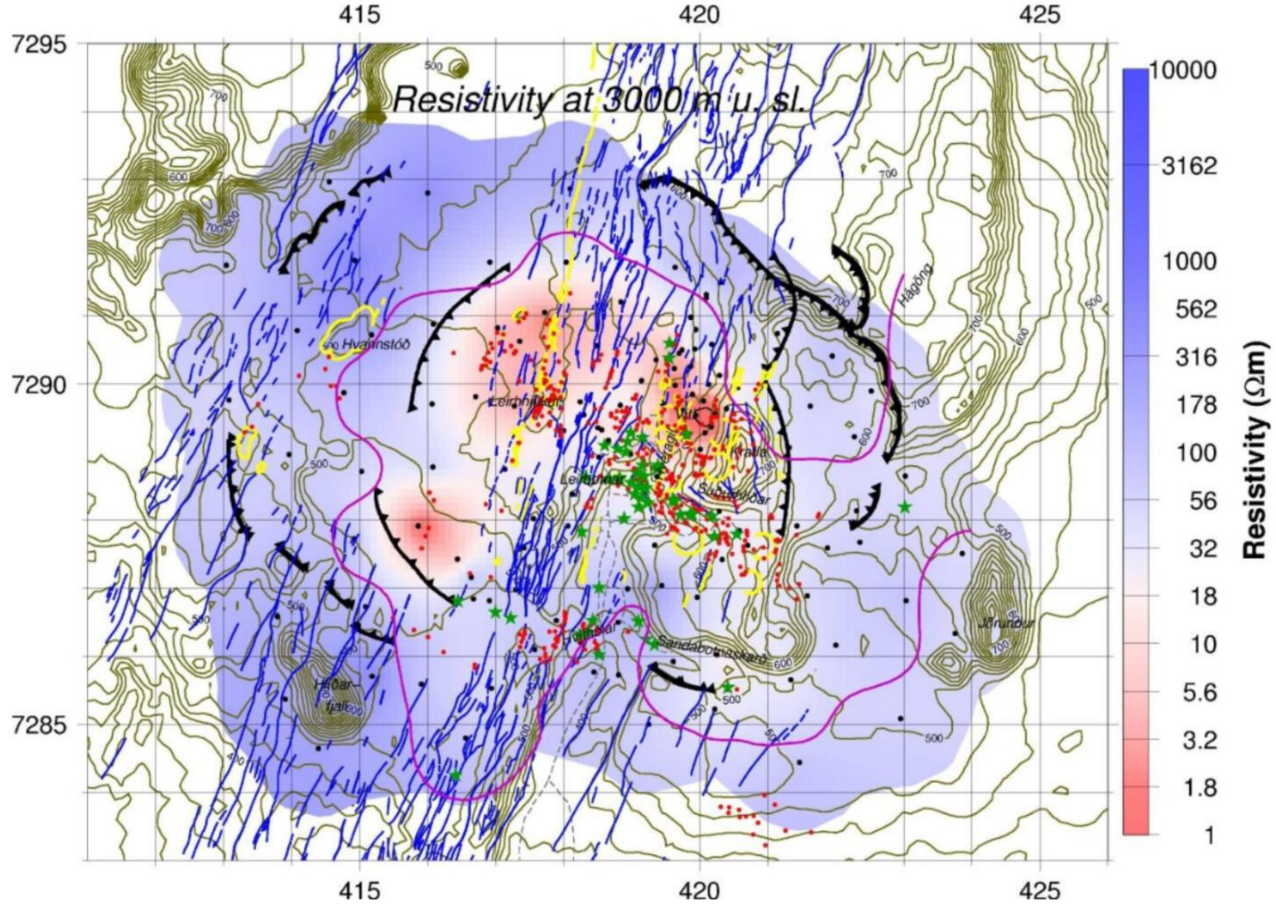

Figure 69: *Horizontal cross-section at 3000 meters below sea level based on 1D joint inversion of MT/TEM data (Árnason et al., 2011). The two low-resistivity bodies to the east and west of the fissure swarm intersecting Krafla were interpreted as molten magma.*

9.3 Superhot geothermal systems in Iceland and Mexico – a comparison

Here, we discuss the similarities and difference between the superhot geothermal systems in Iceland and Mexico. Acoculco was considered to be an EGS site, and the MT/TEM survey was designed to cover the area around the two existing wells in the area. Los Humeros, on the other hand, is a superhot geothermal system, and the MT/TEM survey was designed to understand that system better.

Superhot geothermal systems in volcanic regions have the similar resistivity structure. Permeability and heat give rise to alteration in clay minerals. The clay minerals have a distinct resistivity signature, which makes resistivity methods so valuable in geothermal prospecting in volcanic regions.

The alteration mineral chlorite forms at 220-230°C and has a resistive signature. Smectites form at a lower temperature than chlorite, 150-220°C, and they are very conductive. So, in a location where high temperature and permeability are found, the resistivity structure of the system will be characterized by a low-resistivity (smectite) layer that curves up underneath the main zone of hot water rising up. Underneath the smectites there will be a zone where chlorite is formed, at higher temperature, and therefore that zone will be resistive. The resistive zone (referred to as the resistive core) will also bulge up where the main upflow of hot water is.

This general feature is found in all three areas, Los Humeros, Reykjanes and Krafla. In Reykjanes, the resistive core is slightly elongated in the main fault strike in the region (NE-SW) and it is confined by a transform zone to the north. In Krafla, the structure is complex. In Figure 67 we can see that the resistive core domes up underneath the IDDP-2, but at 3 km depth a restistive structure trending WNW-ESE is present (Figure 69). In Los Humeros, two resistive cores that dome up, are found. The more pronounced one is bouned by a fault to the east and follows the main fault strike in the area and the other one, less pronouned, has a N-S orientation to it.

Los Humeros and Krafla have more similarities than Los Humeros and Reykjanes in that they are both central volcanoes with one or more calderas. At central volcanos scilicic (more evolved) magmas are often found. These have a lower melting temperature, and therefore, it is more likely to drill into a magma body there than at i.e. Reykjanes, where the system is basaltic.

In Krafla, a deeper more conductive layer domes up in two locations. The two up-doming features lie in the north part of the caldera on either side of a NNW-SSE trending fissure swarm running through the caldera. These are bounded by the fissureswarm, the aldera and a transverse structure WNE-ESE, intersecting the caldera (Figure 69). In Reykjanes, a circular column of lower-resistivity, is observed (Figure 62). In Los Humeros, a zone of lower-resistivity structure is found at the intersection of two fault structures, and an elongated structure, that runs along the eastern side of the Los Potreros caldera is present.

The two IDDP wells were targeting low-resistivity structures that had been imaged through 1D or 3D inversion of MT data. We note that, at a depth larger than a few kilometers, the resolution of MT data in superhot geothermal systems, where a low-resistivity cap screens off the signal, is poor. Therefore, it is of great importance to incorporate other data, such as seismic data and gravity data, to jointly interpret deeper structures such systems.

10 Acknowledgement

We thank CFE for providing the VES and TEM data for the study of the Acoculco Caldera. We thank Prof. Alberto Godio and the PhD candidate Francesca Pace of the Politecnico di Torino for the precious work in the frame of the scientific collaboration with CNR-IGG. For Chapter 7 the high-performance computational resources were provided by the Institute of Geosciences and Earth Resources CNR-IGG of Pisa.

11 References

Arzate, J., Corbo-Camargo, F., Carrasco-Núñez, G., Hernández, J., & Yutsis, V., 2018. The Los Humeros (Mexico) geothermal field model deduced from new geophysical and geological data. *Geothermics*, *71*, 200-211.

Árnason, K., 2006a. *TemX short manual.* ÍSOR – Iceland GeoSurvey, Reykjavík, internal report, 17 pp.

Árnason, K., 2006b. TEMTD a program for 1D inversion of TEM and MT data. Short manual. ISOR internal report, 17 pp.

Árnason, K., Eysteinsson, H., & Hersir, G. P., 2010. Joint 1D inversion of TEM and MT data and 3D inversion of MT data in the Hengill area, SW Iceland. *Geothermics*, *39*(1), 13-34.

Árnason, K., Vilhjálmsson, A., and Björnsdóttir, Þ. (2011). A study of the Krafla volcano using gravity micro earthquake and MT data, *KenGen, Lake Naivasha, Kenya, November 2-17, 2007*, 14 pp.

Árnason, K., 2015. The static shift problem in MT soundings. Proceedings of the World Geothermal Congress 2015, Melbourne, Australia; 2015 (12 pp).

Caldwell, T.G., Bibby, H.M., Brown, C., 2004. The magnetotelluric phase tensor. *Geophys. J. Int. 158*, 457–469.

Chave, A.D., Thomson, D.J., 2004. Bounded influence magnetotelluric response function estimation. *Geophys. J. Int. 157,* 988–1006.

Constable, C.S., Parker, R.L., Constable, C.G., 1987. Occam's inversion: a practical algorithm for generating smooth models from electromagnetic sounding data. *Geophysics 52*, 289-300.

Egbert, G., Booker, J., 1986. Robust estimation of geomagnetic transfer functions. Geophys. J. Int. 87, 173–194.

Einarsson, P., 1978. S-wave Shadows in the Krafla Caldera in NE-Iceland, Evidence for a Magma Chamber in the Crust. *Bull. Volcanol 43,* 187-195.

Ekinci, Y.L. & Demirci, A., 2008. A Damped Least-Squares Inversion Program for the Interpretation of Schlumberger Sounding Curves. *Journal of Applied Sciences,* **8**, 4070-4078.

Engelbrecht, A. P., 2007, Computational intelligence, an introduction: John Wiley & Sons.

Friðleifsson, G. Ó., Ármannsson, H., Guðmundsson, Á., Árnason, K., Mortensen, A. K., Pálsson, B., & Einarsson, G. M., 2014. Site selection for the well IDDP-1 at Krafla. *Geothermics*, *49*, 9-15

Friðleifsson, G. O., Pálsson, B., Albertsson, A. L., Stefánsson, B., Gunnlaugsson, E., Ketilsson, J., & Gíslason, P., 2015. IDDP-1 drilled into magma—World's first magma-EGS system created. In *World Geothermal Congress* (pp. 19-25).

Friðleifsson, G. Ó., Elders, W. A., Zierenberg, R. A., Fowler, A. P., Weisenberger, T. B., Mesfin, K. G. and others, 2018. The Iceland Deep Drilling Project at Reykjanes: Drilling into the root zone of a black smoker analog. *J. Vol. Geotherm. Res.*

Gamble, T. D., Goubau, W. M., & Clarke, J., 1979. Magnetotellurics with a remote magnetic reference. *Geophysics*, *44*(1), 53-68.

Gasperikova, E., Rosenkjaer, G. K., Arnason, K., Newman, G. A., & Lindsey, N. J., 2015. Resistivity characterization of the Krafla and Hengill geothermal fields through 3D MT inverse modeling. *Geothermics*, *57*, 246-257.

GEOTEM, 2015. Prospectando el valor de Mexico. Edicion de Aniversario.

Godio, A. and Santilano, A. 2018. On the optimization of electromagnetic geophysical data: application of the PSO algorithm. *J. App. Geophys. 148,* 163-174.

Held, S., Schill, E., Pavez, M., Díaz, D., Muñoz, G., Morata, D., Kohl, T., 2016. Resistivity distribution from mid-crustal conductor to near-surface across the 1200 km long Liquiñe-Ofqui Fault System, southern Chile. *Geophys. J. Int. 207.*

Hersir, G.P. and Benediktsdóttir, Á., 2018. *GEMex WP5. Reports on Resistivity Surveys in Los Humeros and Acoculco, Mexico, and Workshops on Geophysical Studies.* Iceland GeoSurvey, report, ÍSOR-2018/086, 22 pp + Appendix.

Ingeman-Nielsen, T. and Baumgartner, F., 2006. CR1Dmod: A Matlab program to model 1D complex resistivity effects in electrical and electromagnetic surveys. *Comp. Geosci., 32*, 1411–1419.

Jones, A. G., 1988. Static shift of magnetotelluric data and its removal in a sedimentary basin environment. *Geophysics, 53*, 967–978.

Jones, A. G., 2012. Distortion of magnetotelluric data: Its identification and removal, in A. D. Chave and A. G. Jones, eds., The magnetotelluric method, theory and practice: Cambridge University Press, 219-302.

Karlsdóttir, R., Vilhjálmsson, A. M., Guðnason, E. Á., 2018. Three dimensional inversion of magnetotelluric (MT) resistivity data from Reykjanes high temperature field in SW Iceland. *J. Vol. Geotherm. Res.*

López-Hernández, A., García-Estrada, G., Aguirre-Díaz, G., González-Partida, E., Palma-Guzmán, H., Quijano-León, J.L., 2009. Hydrothermal activity in the Tulancingo–Acoculco Caldera Complex, central Mexico: Exploratory studies. *Geothermics, 38*, 279-293.

Marti, A., Queralt, P., Jones, A.G., Ledo, J., 2005. Improving Bahr’s invariant parameters using the WAL approach. *Geophys. J. Int., 163*, 38–41.

Pace, F., Godio, A., Santilano, A., Comina, C. Under Review. Joint optimization of geophysical data using multi-objective swarm intelligence. Geophys. J. Int.

Pace, F., Santilano, A. & Godio, A., 2018. Pareto-optimal Multi-Objective Particle Swarm Optimization of vertical electrical sounding and time-domain electromagnetic data, in *Proceedings of 24th European Meeting of Environmental and Engineering Geophysics*, European Association of Geoscientists and Engineers.

Park, S. K. and Livelybrook, D. W., 1989. Quantitative interpretation of rotationally invariant parameters in magnetotellurics. *Geophysics, 54*, 1483–1490.

Pethick, A., and B. Harris, 2015. 1D magnetotelluric forward modelling Web App: 24th International Geophysical Conference and Exhibition Perth, ASEG-PESA, Extended Abstracts, 1–4.

Pulido, C.L., Armenta, M.F., Silva, G.R., 2010. Characterization of the Acoculco geothermal zone as a HDR system. GRC Transaction, Vol 34, 2010.

Rosenkjaer, G. K., Gasperikova, E., Newman, G. A., Árnason, K., and Lindsey, N. J., 2015. Comparison of 3D MT inversions for geothermal exploration: Case studies for Krafla and Hengill geothermal systems in Iceland. *Geothermics 57*, 258-274.

Santilano, A., Godio, A., Manzella, A. 2018. Particle swarm optimization for simultaneous analysis of magnetotelluric and time-domain electromagnetic data. *Geophysics, 83* (3), E151-E159.

SEG, 1991. MT/EMAP data interchange standard.Society of Exploration Geophysicists, 112 p.

Sen, M. K., and P. L. Stoffa, 2013, Global optimization methods in geophysical inversion: Elsevier.

Sims, W. E., and F. X. Bostick, 1969, Methods of magnetotelluric analysis: Technical report 58, University of Texas, Electrical Geophysics Research Laboratory.

Siripunvaraporn, W., Egbert, G., Lenbury, Y. and Uyeshima, M., 2005. Three-dimensional magnetotelluric inversion: data-space method. *Phys. Earth Planet. Int.*, *150*, no. 1, 3–14.

Siripunvaraporn,W. and Egbert, G., 2009. WSINV3DMT: Vertical magnetic field transfer function inversion and parallel implementation. *Phys. Earth Planet. Int.*, *173*, no. 3, 317–329.

Spies, B.R. and Eggers, D.E., 1986. The use and misuse of apparent resistivity in electromagnetic methods. Geophysics, 51 (7), 1462-1471.

Sternberg, B. K., Washburne, J. C., & Pellerin, L., 1988. Correction for the static shift in magnetotellurics using transient electromagnetic soundings. *Geophysics*, *53*(11), 1459-1468.

Stolper, E. M., DePaolo, D. J., & Thomas, D. M., 2009. Deep drilling into a mantle plume volcano: The Hawaii Scientific Drilling Project. *Scientific Drilling*, *7*, 4-14.

Szarka, L., 1987. Geophysical aspects of man-made electromagnetic noise in the earth-A review. *Surv. Geophys. 9*, 287–318.

Thorsteinsdóttir, U., Blischke, A., Hersir, G.P., and Helgadóttir, H.M., 2018. 3D Geological Static Field model of the Krafla Geothermal Area, NE Iceland: constructing a workflow. Iceland GeoSurvey, report, ÍSOR-2017/059, 105 pp

Tietze, K., & Ritter, O., 2013. Three-dimensional magnetotelluric inversion in practice—the electrical conductivity structure of the San Andreas Fault in Central California. *Geophys. J. Int.*, *195*(1), 130-147.

Appendix A

Report on geophysical surveys in Los Humeros in November 2017

This report was originally uploaded on the VRE in December 2017.

Gylfi Páll Hersir and Ásdís Benediktsdóttir from ÍSOR arrived in Mexico on Friday, November the 17th and met with Claudia Arango. They both left the day after with Pepe and Emiliano from UNAM for Acoculco to set up the remote reference station with two colleagues from UMSNH (the MT unit came from UMSNH). The station was kept running during the whole survey period and was taken care of by the two colleagues from UMSNH. The four left for Los Humeros in the afternoon and stayed there until Monday the 27th when Gylfi and Ásdís left for Mexico City and back to Iceland the day after. Sebastian from KIT joined us in the field for two days and Nadine from KIT came on the 26th and will stay as a part of the resistivity crew until December the 9th. Sebastian, who came to Los Humeros on the 23rd of November, spent 2 days with the gravity group and left for Europe on the 27th. Maximiliano from KIT came with Nadine on the 26th and will work with the gravity group. On Monday the 27th, Gylfi, Ásdís, Sebastian and Claudia met in Mexico City and discussed the survey campaign, the processing work and interpretation – minutes from the meeting will be made available on the VRE. After Sebastian had left to catch his plane to Europe, the remaining three discussed the eventually forthcoming resistivity campaign in Acoculco.

TEM data were collected in Los Humeros using a TerraTEM unit from UNAM and MT data using 4 Metronix units (owned by UNAM, Cisese and UMSNH). Data collection started in Los Humeros on Sunday the 19th of November. When we left, 26 MT and TEM soundings had been acquired out of the 140 planned in Los Humeros. The survey will pause on December the 16th - hoping to have measured close to 90 sounding pairs by that time. The plan is to finish the MT/TEM survey in Los Humeros with a 2 weeks campaign at the end of January 2018. The location of the 2018 resistivity measurements will be based on a preliminary processing of the data (finished at the end of December) and a preliminary 1D joint inversion model of the two data sets – done before mid-January. The final processing of the 2017 MT data will be accomplished in January 2018. We plan to have the 1D resistivity model for Los Humeros ready, say - by the second half of March. The 3D model a couple of months later. This of course is only an educational guess work and should be regarded as such!

Collection of the resistivity data in Los Humeros is going well and done professionally by our Mexican partners from UNAM, Cisese and UMSNH. The main problem we face is the noise originating from the power plant and the power lines plus the cultural noise coming from different electrical sources. It will be a challenge to minmize the effect of the noise and increase the signal to noise ratio through the processing work. TEM data are fine and not a problem. However, we have collected MT data close to both the power plant and power lines and acquired useable data – many of them of high quality. The resistivity data already collected show that the campaign has the potential to be a successful one, resulting in a reasonable resistivity model of Los Humeros area.

During the survey campaign we stayed in Cafe Negro in Perote town (20 minutes drive from Los Humeros) where we got breakfast. We had lunch at a private home in Perote – Mexican food at its best. All facilities were excellent during our stay. CFE (Cecilia) was oriented about our work well in advance and we communicated with CFE every day and got a walkie talkie in the mornings which was delivered after work. A geophysicist (Rafael) from CFE joined us in the survey for one day. CFE will be contacted this week by Claudia to receive an orientation about the progress of our work.

The gravity survey began at the same time as the resistivity survey but faced several problems in the beginning, both regarding gravity and GPS. These problems have now been solved and the campaign is on track since November 25th. Around 50 points have already been measured and the crew expects to measure about 15 points per day. The plan is to measure around 390 gravity points – they will pause on the 15th of December.

In Los Humeros 45 seismic stations have been deployed – 43 from EU and 2 from the Mexican side. The first round of downloading the data has already begun and will be finalised next week – including data from the two recent big earthquakes; the first one 700 km away of 8.2 and the second one 200 km away of 7.1. We still do not have access to data from the 5 seismic stations run by CFE. Regarding the active seismic data from the four profiles – raw data from one of the profiles have already been digitized by UNAM – ready to be delivered and we hope the other three will be digitized before the end of the year by UNAM (they had problems with the digitizer).

Figure 70 :*Setting up an MT station in Los Humeros*

.

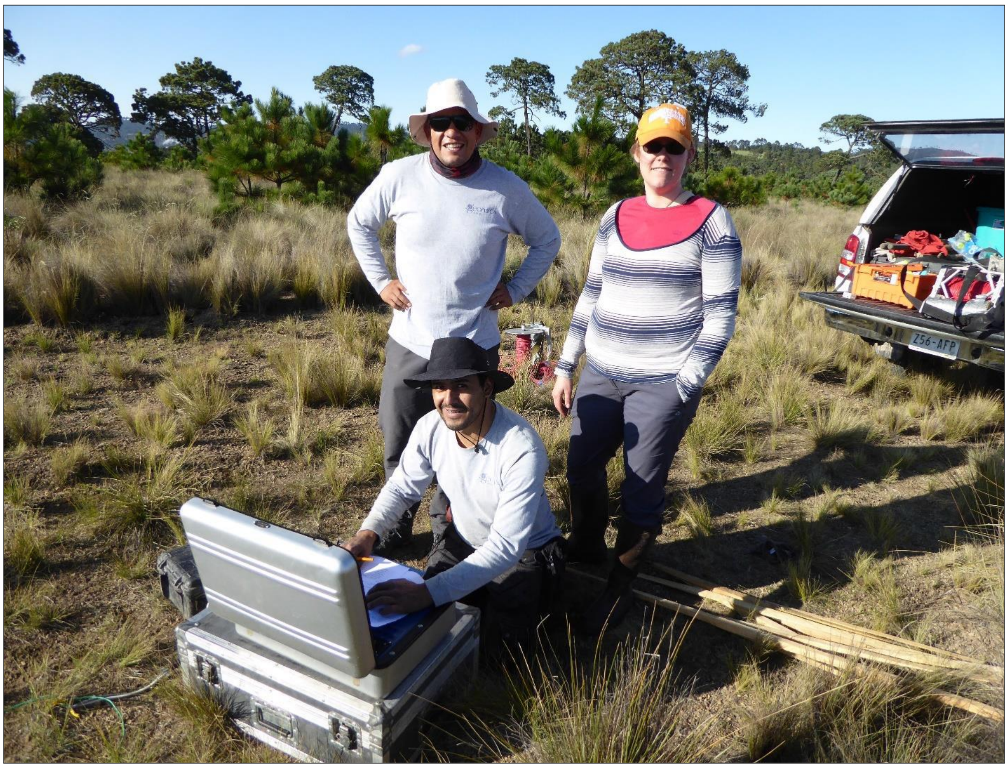

Figure 71: *Measuring TEM in Los Humeros: Pepe, Emiliano and Ásdís.*

Figure 72: *The resistivity survey crew in Los Humeros.*

Report on a workshop within GEMex, WP5.1 and 5.3, in Mexico City and the consequent start of the resistivity survey in Acoculco in early May 2018

This report was originally uploaded on the VRE in May 2018.

Gylfi and Ásdís from ÍSOR (Iceland GeoSurvey) arrived in Mexico City on the 1st of May and met with Claudia Arango from UNAM to finalize the agenda for a two-day workshop, organised by the European and Mexican consortium on EM and gravity data processing held at Instituto de Geofísica, UNAM, Mexico City on May 2nd and 3rd. The following agenda was adopted:

Table 5: *The agenda for a two-day workshop, organised by the European and Mexican consortium on EM and gravity data processing.*

May 2; time:	Topic
9:30	Introduction to the workshop (Claudia)
	Introduction to gravity prospecting in geothermal exploration (Gylfi)
	Gravity in Los Humeros – Regional approach (Jonathan)
	Gravity in Los Humeros – Local approach (Jonathan)
	Gravity in Acoculco – Acquisition plan and processing (Omar and Natalia)
11:30 -12:00	Coffee break
	Introduction to resistivity of rocks in geothermal exploration (Gylfi)
	Introduction to basic theory of TDEM (Gylfi)
14:00– 15:00	Lunch break
	The Los Humeros resistivity campaign – data acquisition, first and second phase - data coverage (Pepe)
	First impression of data quality - do we need more MT? (Isaí)
16:00 – 16:30	Coffee break
	TDEM data acquisition and processing (Pepe and Ásdís)
	Introduction to basic theory of MT (Gylfi)
	MT processing – Impedance tensor estimation using BIRRP (UNAM approach) (Abraham and Isaí)
end 18:00	MT processing – Impedance tensor estimation using BIRRP (CICESE approach) (Talia)
May 3; time:	Topic
9:30	Discussion on optimal MT and TDEM processing sequence (all)
	Quadratic solution for the 2-D magnetotelluric impedance tensor distorted by 3-D electro-galvanic effects (José Manuel Romo)
11:00 – 11:30	Coffee break
	Geothermal alteration in Los Humeros (Georgina Izquierdo)
	The geology of Los Humeros (Gerardo Carrasco)
	The article in Geothermics: The Los Humeros geothermal field model deduced from new geophysical and geological data (Gerardo Carrasco and Fernando Corbo)
	1D joint inversion of MT and TEM data; an introduction to ÍSOR‘s temtd inversion code – OCCAM inversion vs blocky models (Ásdís)
	Preliminary results from the first phase of the field survey in Los Humeros (Ásdís)
	On 3D inversion of the MT data – ÍSOR’s practice and UNAM´s plan for ModEM (Ásdís and Claudia)
14:00 – 15:00	Lunch break
	Summary and timeline (Gylfi and Claudia, J.M. Romo)
End 18:00	The forthcoming campaign in Acoculco (Claudia)

The workshop was attended by 16 people. It included several introductory talks on the subjects and a review of what has already been achieved regarding resistivity and gravity field work. Overview talks on the geology and geothermal alteration in Los Humeros were given by Gerardo Carrasco, Fernando Corbo and Geogina Izquierdo. The processing and interpretation of the data were discussed lively back and forth and finally the important part: What to do with the data, what are the next steps and timelines – summarized below:

- Workshop in Ensanada on MT data processing in mid-June (UNAM & CICESE)
- Finalizing the processing of the MT data – end of July – both Los Humeros and Acoculco (UNAM, CICESE, KIT)
- Strike analysis, phase tensor analysis (inversion) – mid-August (KIT, ÍSOR)
- 1D inversion of both fields – mid-October prior to the Morelía meeting (18-20 of October) (ÍSOR & UNAM) + probabilistic methods (CNR) – Workshop on October 17th in Mexico City.
- 2D inversion both fields – mid-November (CICESE)
- 3D inversion of both fields - December (preliminary version) (ÍSOR & UNAM/CICESE)

This means that resistivity models based on 1D inversion for both Los Humeros and Acoculco will be available in mid-October and presented at a special workshop to be held on October 15th in Mexico City prior to GEMex's 3rd General Assembly in Morelia on October 16th to the 18th. These models will serve as input models for several Work packages in GEMex. The models based on 3D inversion of the data will be available towards the end of this year and could then be replaced by the ones based on 1D inversion.

Figure 73: *Claudia Arango introducing the workshop.*

Figure 74: *Gylfi describing some aspect of the resistivity of rocks.*

Figure 75: *José Manuel Romo ending his talk on quadratic solution of the 2D magnetotelluric impedance tensor – demonstrated in several languages.*

Figure 76 : *From the workshop – some of the audience.*

Figure 77: *Georgina Izquierdo speaking on geothermal alteration in Los Humeros.*

Figure 78: *Gerardo Carrasco explaining the geology of Los Humeros.*

Figure 79: *Ásdís talking about the first resistivity results from Los Humeros.*

Gravity and MT data acquisition in Los Humeros – the second phase - was finalized a couple of days prior to the workshop in Mexico City, including the long profile. The figure below shows the location of all the gravity and MT sites in Los Humeros. It only remains to measure TEM at some of the sites – will be done this summer.

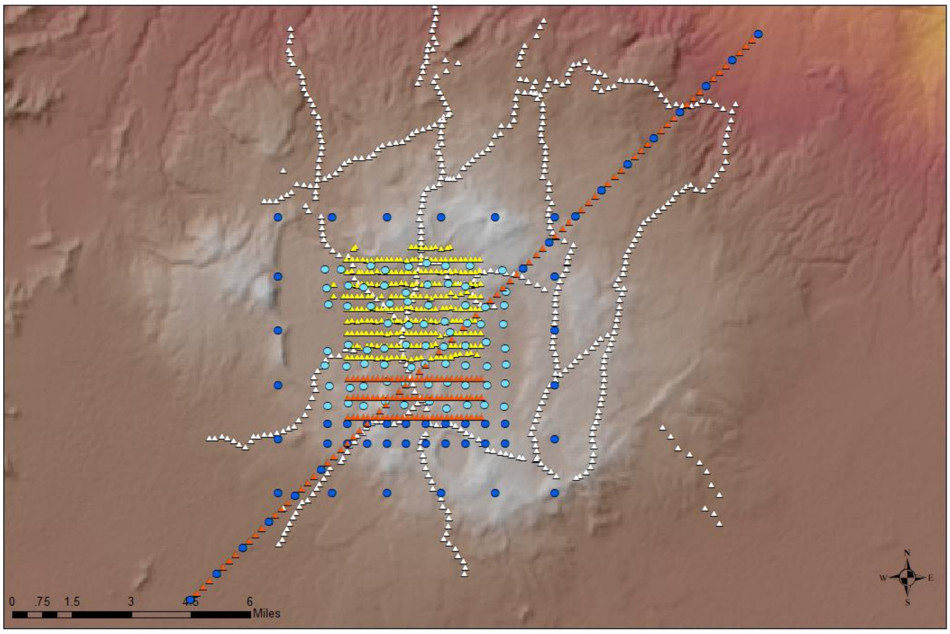

Figure 80: *Gravity and MT campaign in Los Humeros: Cyan dots: MT since late 2017; blue dots: MT sites since April 2018; yellow filled triangles: Gravity sites since late 2017; red filled triangles on the long profile: Gravity sites since April/May 2018*.

Right after the workshop - early morning of the 4th of May - some of us went to Los Humeros to deploy the MT remote reference station while the rest of the MT team went to Acoculco (the town Cruz Colorada) and hired two guards for keeping an eye on the MT equipment while collecting data during the whole survey period. The MT team working in the Acoculco area stayed in the town of Chignahuapan at a very fine guesthouse, Cabañas La Mision, where breakfast and dinner were served as well as pack lunch – excellent and warm place to stay in and fine food!

The day after, on the 5th of May, we attended a meeting with the locals in Cruz Colorada to discuss the project and what we are doing (see picture below) – attended by around 50 persons, mostly elderly men. Claudia gave an excellent talk and replied to some questions. The locals were positive towards what we are doing although some negative issues had been raised before the meeting and confusion was ongoing, who we are and if we are a part of company (Canadian, I think) exploiting mineral resources from the locals, silver and gold – this was only a few months before the elections in Mexico by the way. This rumor was corrected and no objections were raised against our work. Later other municipalities (San Francisco Terrerillos and Jonuco Pedernales) gave their permission as well to our work but the last one, Cuautelolulco did not give us permission – even threatened to damage the equipment. It seems that there is a lot of disinformation regarding the project in the area and a poor coordination among the different WPs. This is something to think about.

Figure 81: *From the meeting in Cruz Colorada with the locals.*

The MT field work went amazingly well – finding good spots was easier than expected and the Mexican MT crew did a fine job; effective, hardworking; nice and intelligent people, pleasure to work with. MT acquisition was finished in late May. See figure below (red and pink dots sites not measured). TEM still remains to be done.

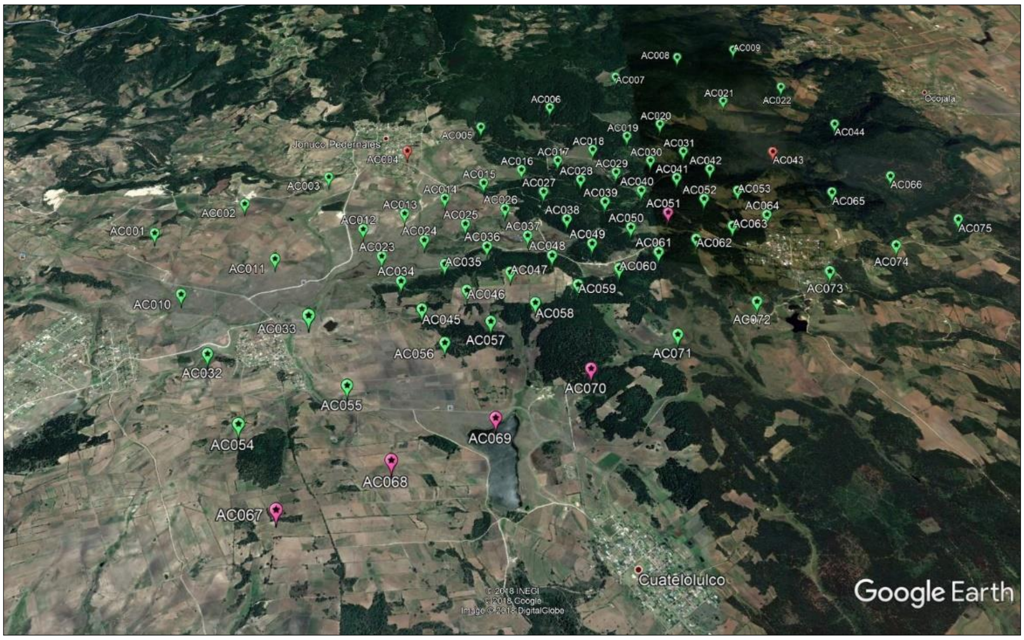

Figure 82: *Resistivity sites in Acoculco.*

Figure 83: *Setting up an MT station close to the wells in the Acoculco prospect.*

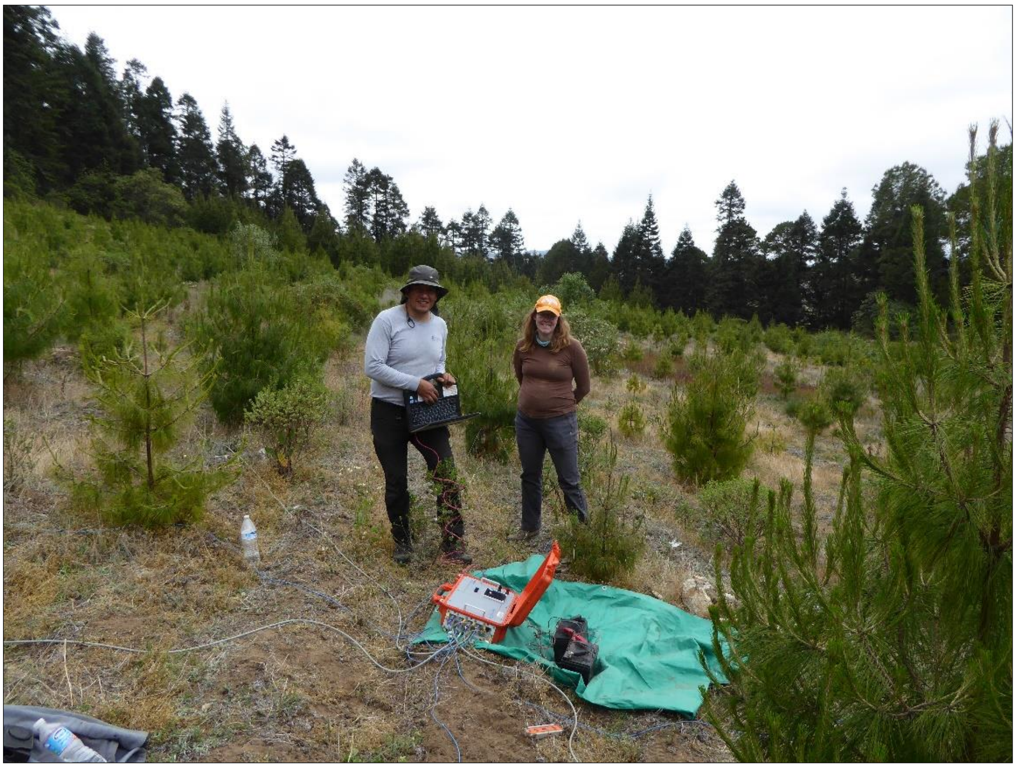

Figure 84: *Fun during MT data acquisition in the Acoculco prospect area - Pepe and Ásdís.*

Gravity field work in Acoculco was finalized in early May, see figure below.

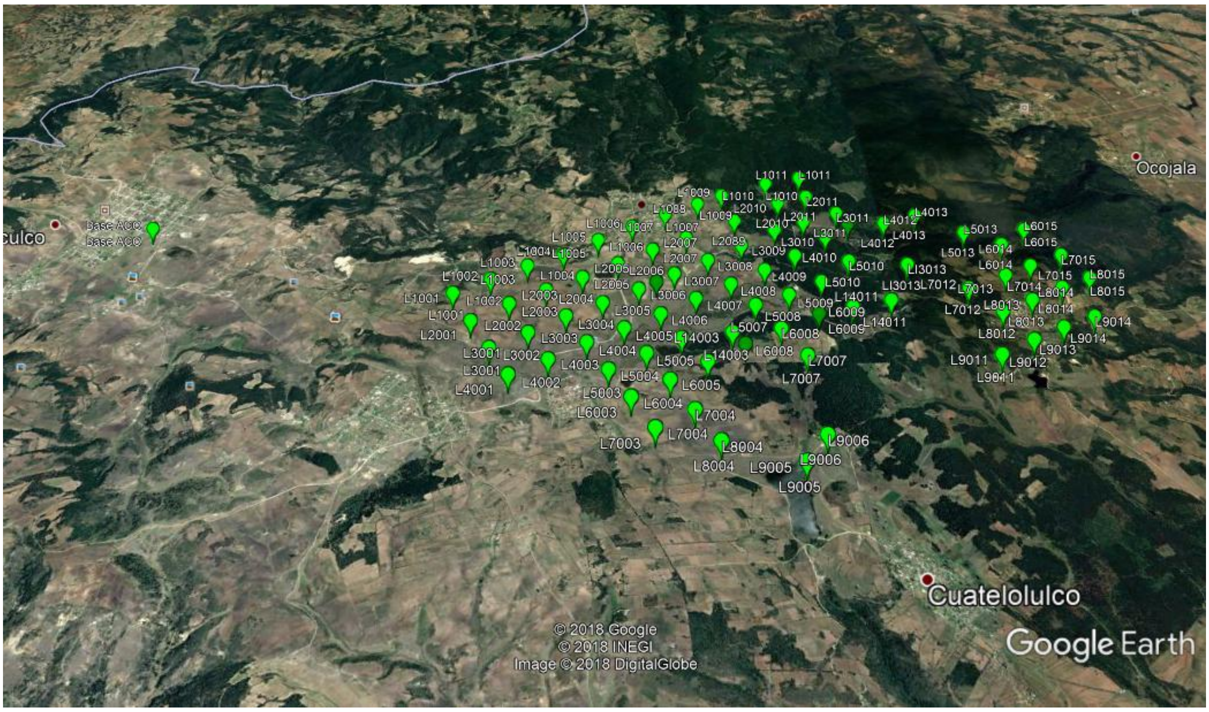

Figure 85: *Location of gravity stations in Acoculco.*

Finally this: A total of 15 micro-seismic stations have already been deployed in the Acoculco area and begun collecting data.

Workshop in Mexico City on October 17th 2018

The status of the work and perspectives are shown in Table 2.

Table 6: *The agenda for a workshop within WP5 – Status of the work and perspectives - organised by the European and Mexican consortium in Mexico City on October 17th 2018.*

GEMex: Workshop within WP5 Status of the work and perspectives October 17th 2018, Mexico City Program	
Auditorio Monges López – Instituto de Geofísica, UNAM	
09:00 – 09:10	**Introduction to the workshop and the program of the day** *Claudia & Gylfi*
09:10 – 09:30	**The resistivity campaign in Los Humeros and Acoculco and the processing of the data - an overview of the survey and problems encountered** *Thalia & Pepe*
09:30 – 9:50	**Results of 1D inversion of TEM and MT data from Los Humeros - the 1D resistivity model**

	Ásdís
9:50 – 10:10	**Results of 1D inversion of TEM and MT data from Acoculco - the 1D resistivity model** *Gylfi*
10:10 – 10:30	**Phase tensor analysis (both fields); comparing results from KIT and ÍSOR** *Ásdís & Gylfi*
10:30 – 10:45	**Rho+/- apparent resistivity and phase curves (invariant approach)** *José Manuel & Thalia*
10:45 – 11:35	**Summary and discussion: How to continue - geothermal significance of the resistivity models - 3D inversion – how to continue** *All WP5.1*
11:35 – 11:45	**Status of the 5.3.1 Task: Heat flow measurements** *Rosa María*
11:45 – 12:15	**Coffee break**
12:15 – 12:35	**On the general advancement and the global results, both areas** *Philippe & Marco Calò*
12:35 – 12:55	**The highlights on the seismic results** *Philippe & Marco Calò*
12:55 – 13:10	**Regional approach - gravity/magnetics** *Marco Pérez*
13:10 – 13:25	**Bouguer gravity map from Los Humeros** *Natalia*
13:25 – 13:40	**Bouguer gravity map from Acoculco** *Natalia*
13:40 – 14:30	**Lunch break**
14:30 – 14:45	**Joint/constrained inversion/interpretation** *Luis Alonso*
14:45 – 15:00	**Conclusion of the day – the perspectives** *Claudia & Gylfi*

Appendix B

In this appendix cross-sections through the 1D resistivity models in Los Humeros (Figures 86-97) and Acoculco (Figures 98-99) are presented.

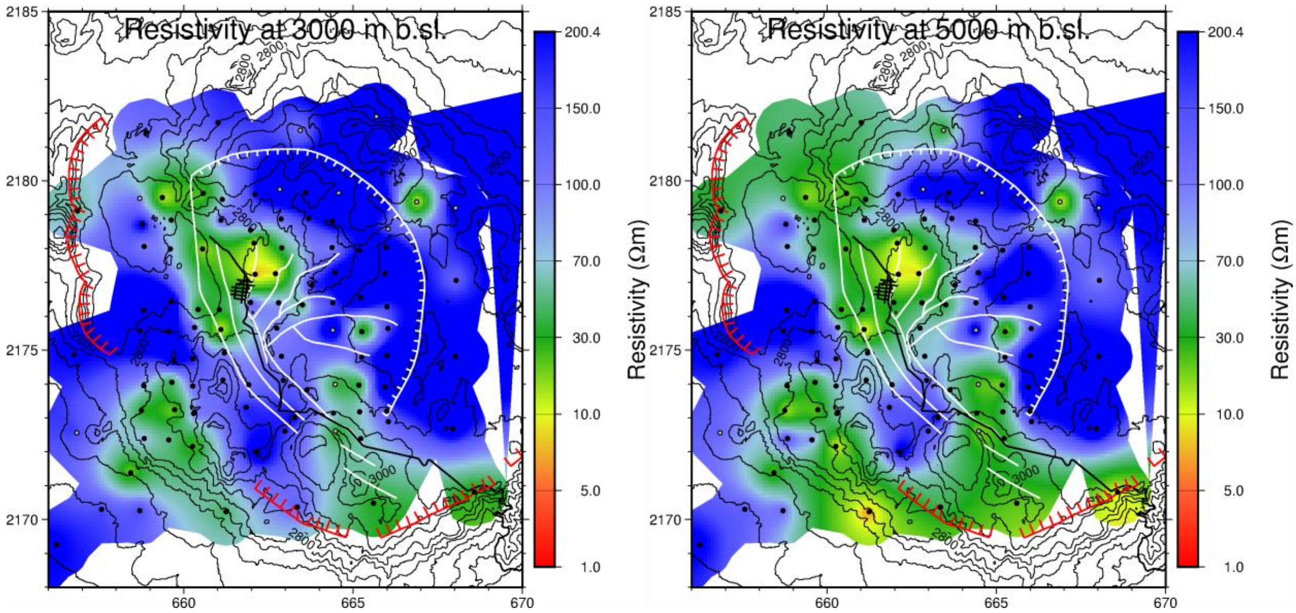

Figure 86 Horizontal cross-section through the 1D resistivity model of Los Humeros at 3000 meters below sea level (**left panel**) and 5000 meters below sea level (**right panel**). Features are described in the legend of Figure 19.

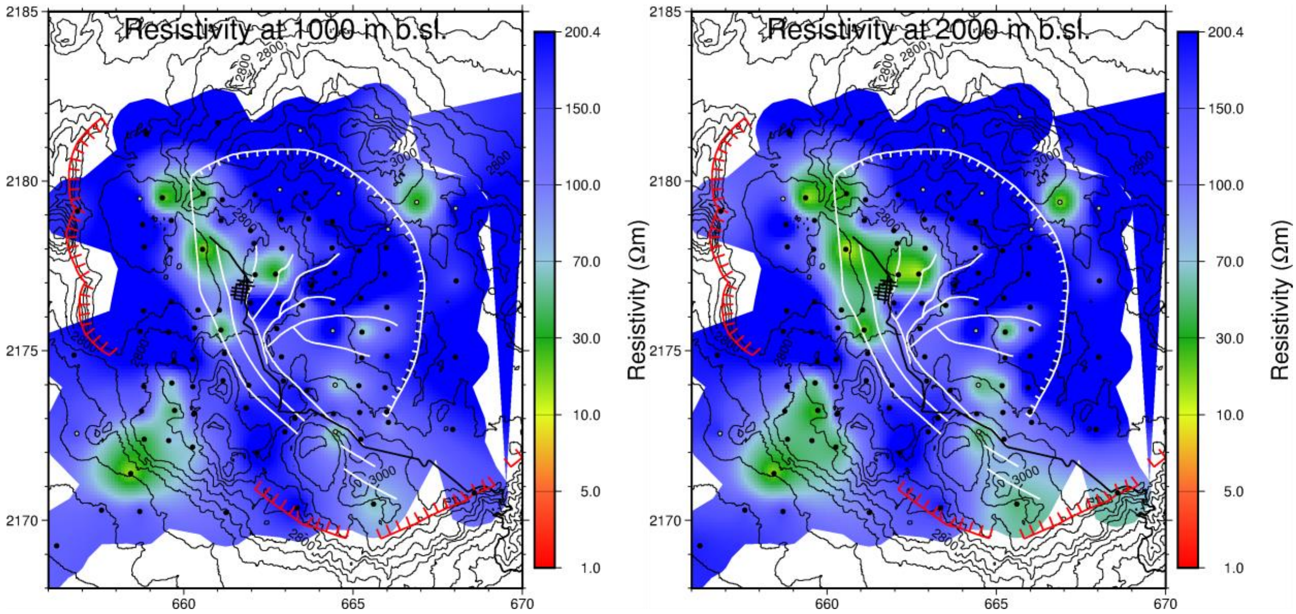

Figure 87: *Horizontal cross-section through the 1D resistivity model of Los Humeros at 1000 meters below sea level (**left panel**) and 2000 meters below sea level (**right panel**). Features are described in the legend of Figure 19.*

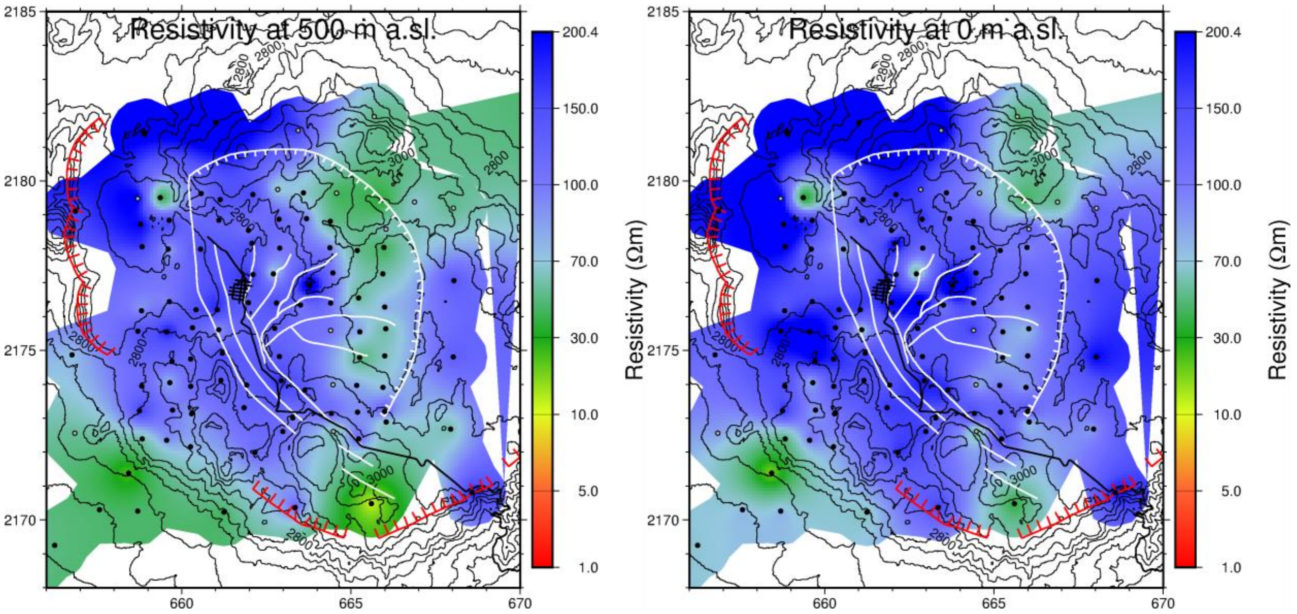

Figure 88 *Horizontal cross-section through the 1D resistivity model of Los Humeros at 500 meters above sea level (**left panel**) and at sea level (**right panel**). Features are described in the legend of Figure 19.*

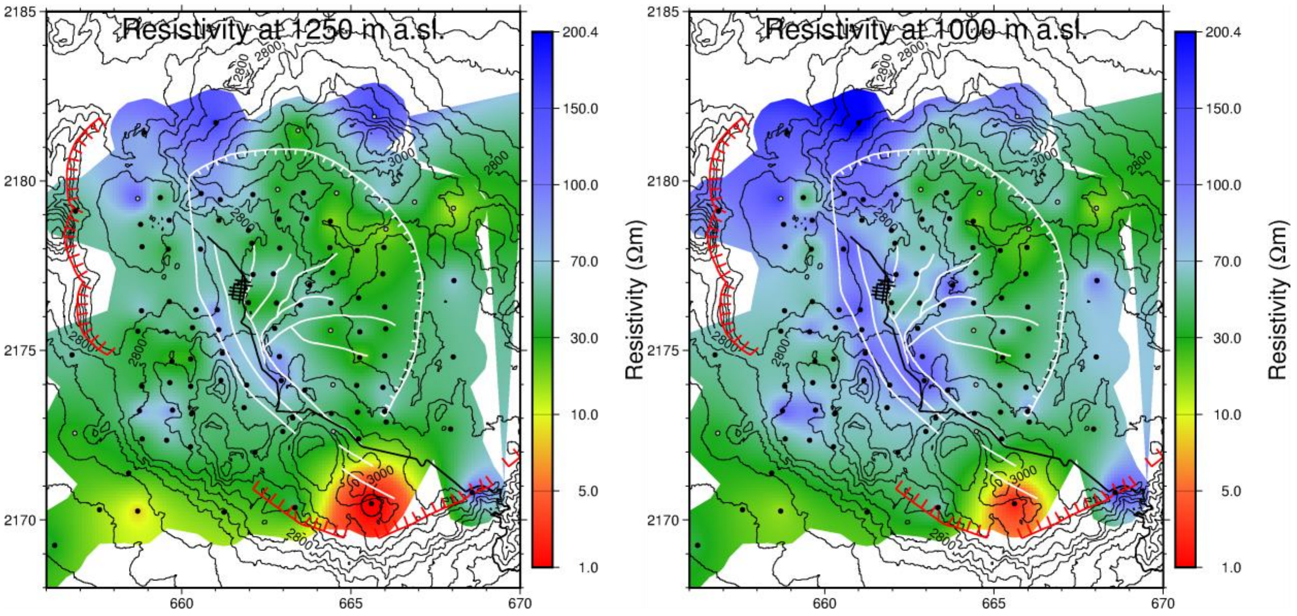

Figure 89 *Horizontal cross-section through the 1D resistivity model of Los Humeros at 1250 meters above sea level (**left panel**) and at 1000 meters above sea level (**right panel**). Features are described in the legend of Figure 19.*

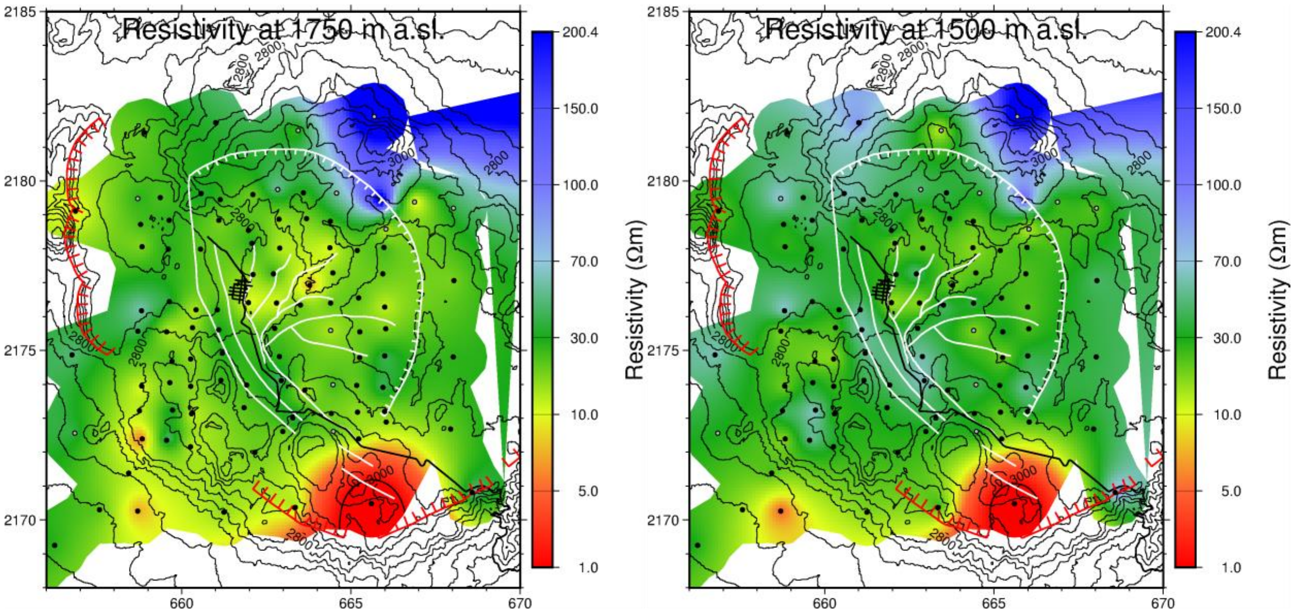

Figure 90: *Horizontal cross-section through the 1D resistivity model of Los Humeros at 1750 meters above sea level (**left panel**) and at 1500 meters above sea level (**right panel**). Features are described in the legend of Figure 19.*

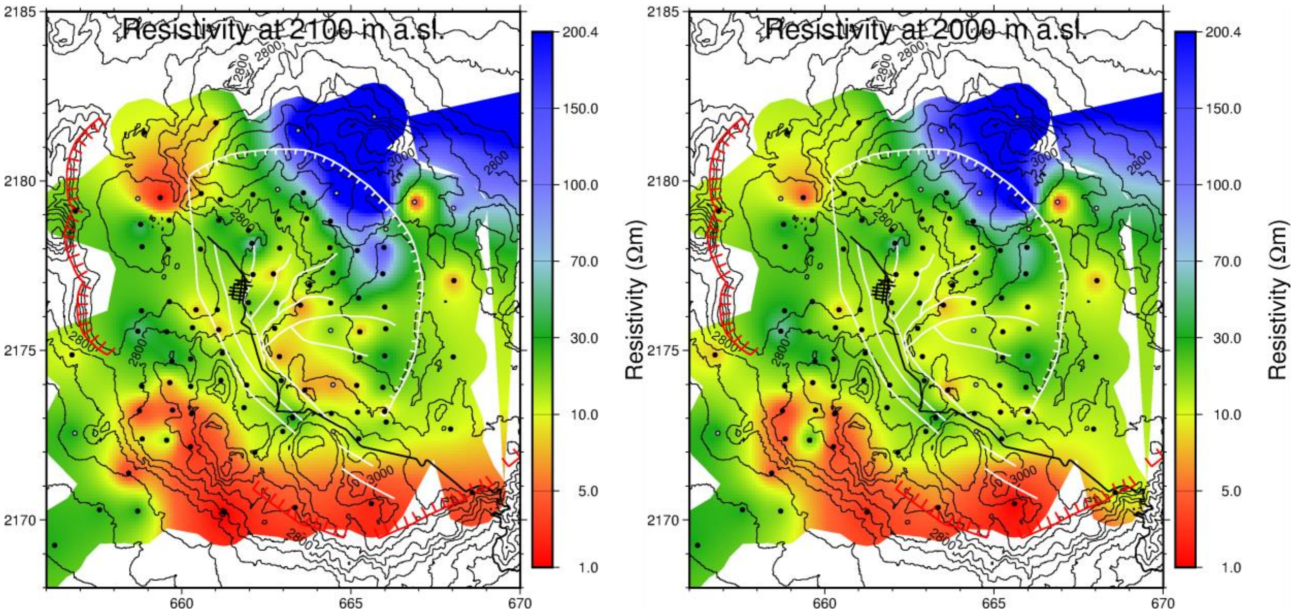

Figure 91: *Horizontal cross-section through the 1D resistivity model of Los Humeros at 2100 meters above sea level (**left panel**) and at 2000 meters above sea level (**right panel**). Features are described in the legend of Figure 19.*

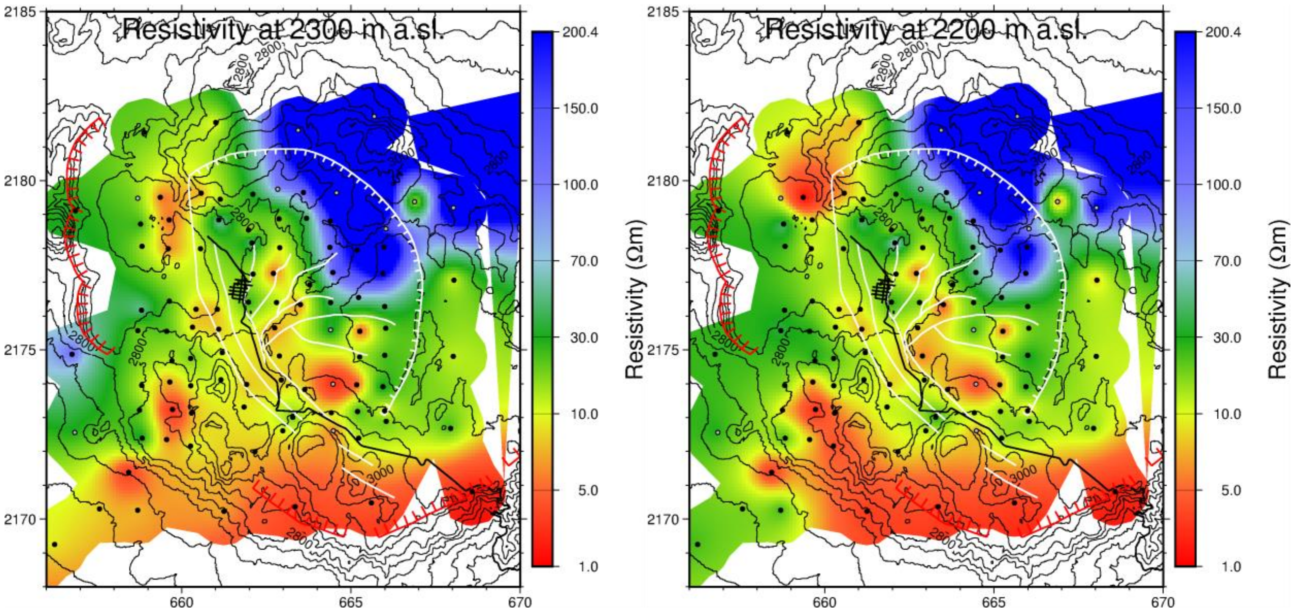

Figure 92: *Horizontal cross-section through the 1D resistivity model of Los Humeros at 2300 meters above sea level (**left panel**) and at 2200 meters above sea level (**right panel**). Features are described in the legend of Figure 19.*

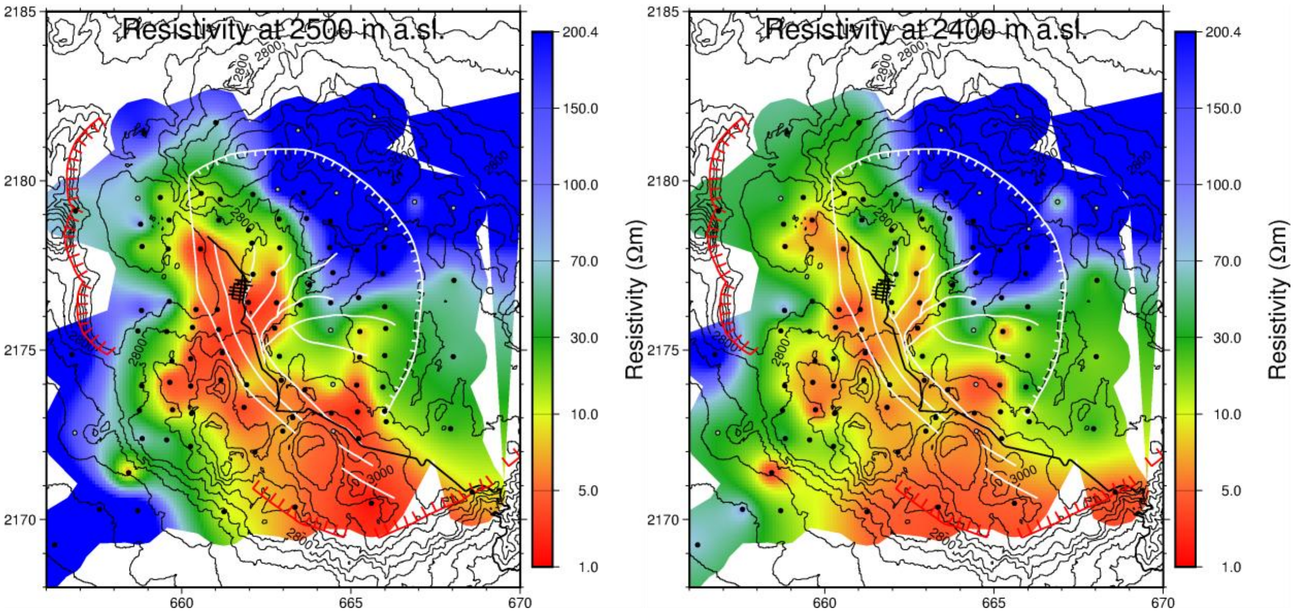

Figure 93: *Horizontal cross-section through the 1D resistivity model of Los Humeros at 2500 meters above sea level (**left panel**) and at 2400 meters above sea level (**right panel**). Features are described in the legend of Figure 19.*

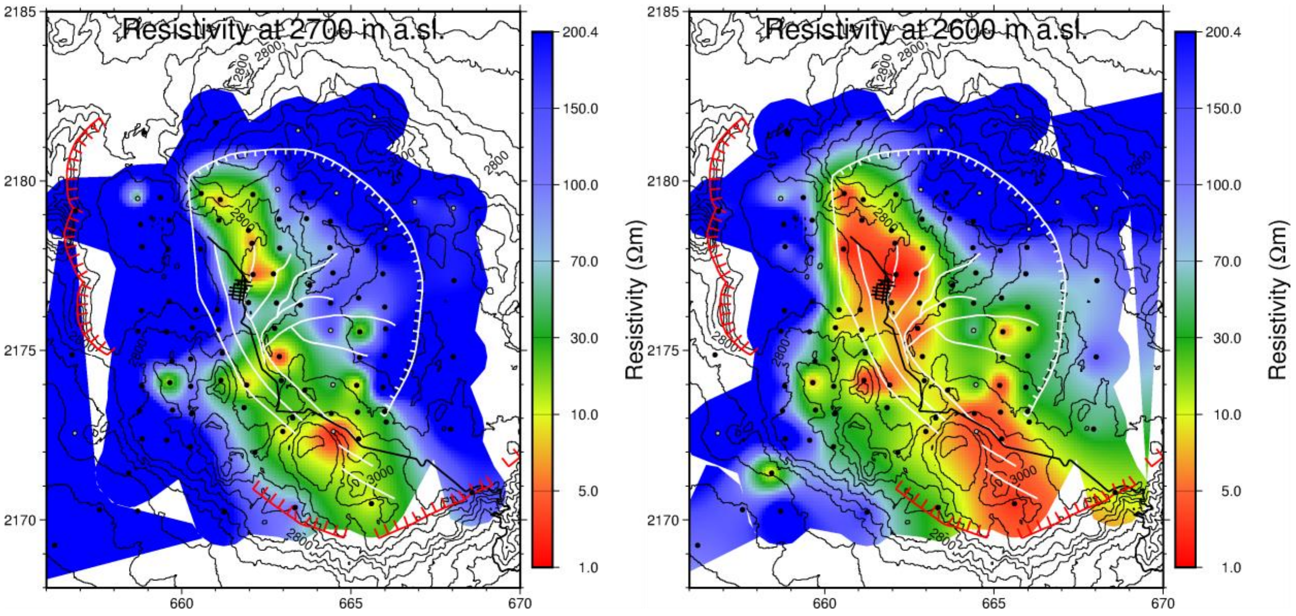

Figure 94: *Horizontal cross-section through the 1D resistivity model of Los Humeros at 2700 meters above sea level (**left panel**) and at 2600 meters above sea level (**right panel**). Features are described in the legend of Figure 19.*

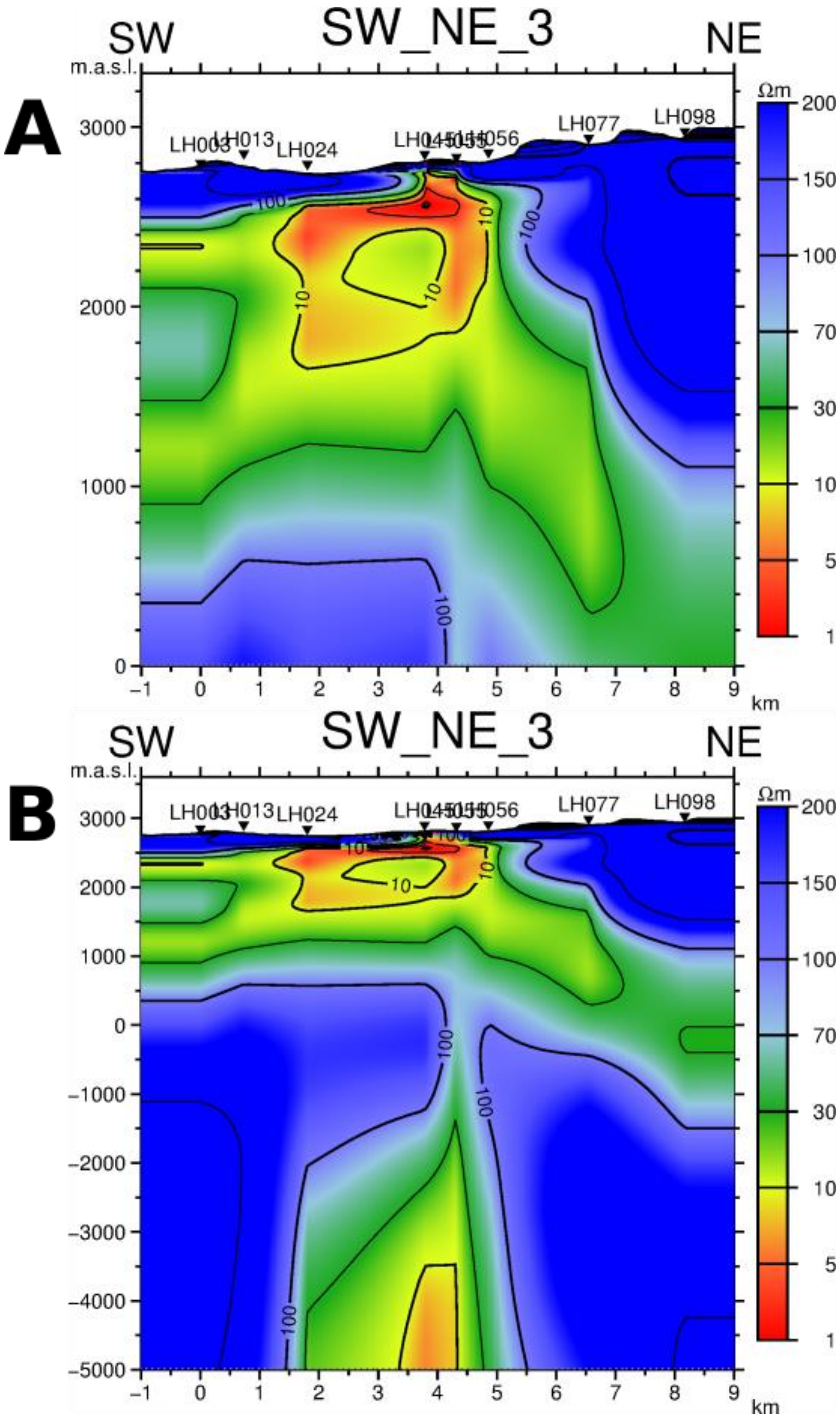

Figure 95: *Vertical cross-section through the 1D resistivity model of Los Humeros down to sea level (**A**) and 5000 meters below sea level (**B**). Triangles at the surface are the sounding locations along with the names. Location of the profile is shown in Figure 19 as P3.*

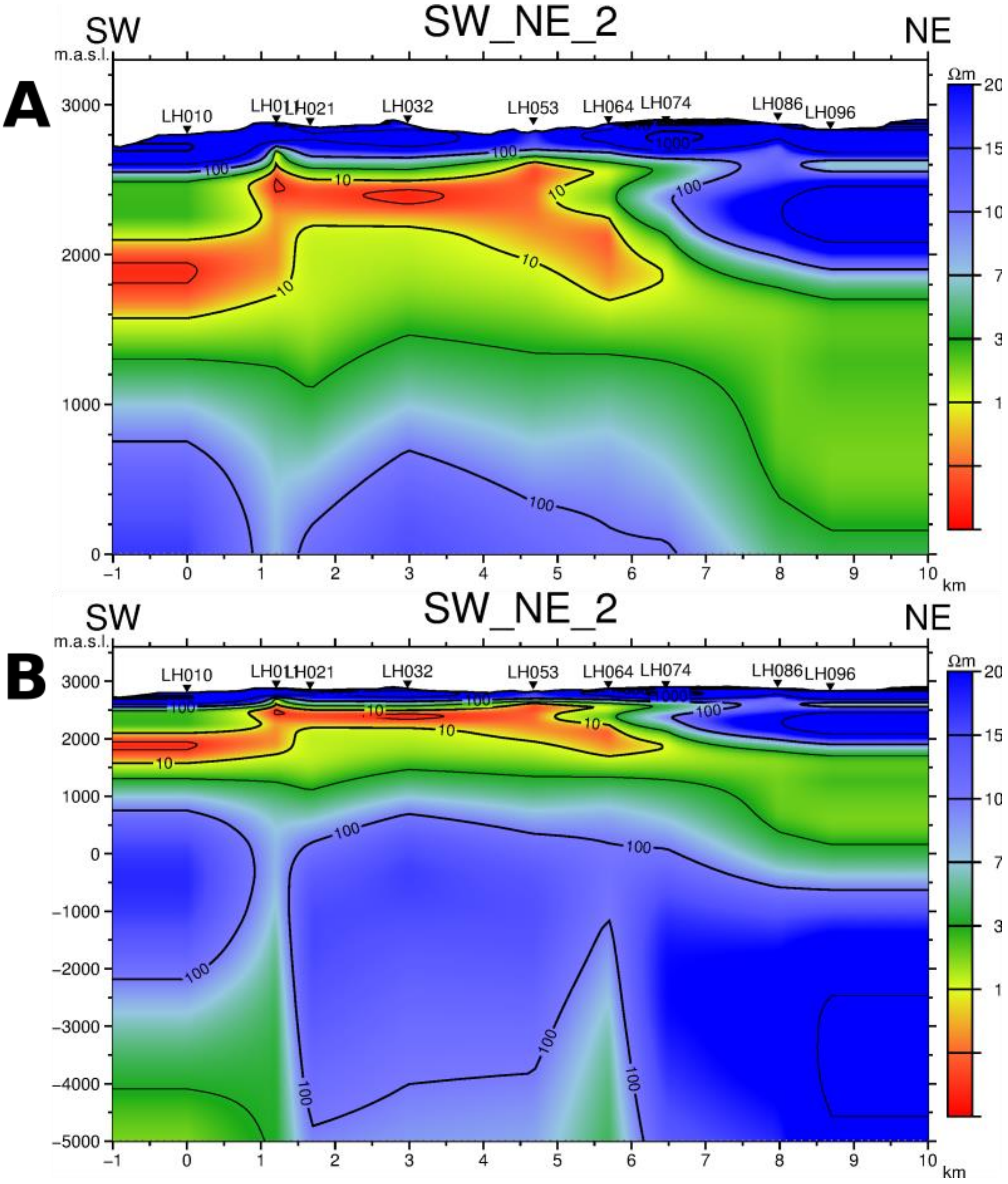

Figure 96: *Vertical cross-section through the 1D resistivity model of Los Humeros down to sea level (**A**) and 5000 meters below sea level (**B**). Triangles at the surface are the sounding locations along with the names. Location of the profile is shown in Figure 19 as P2.*

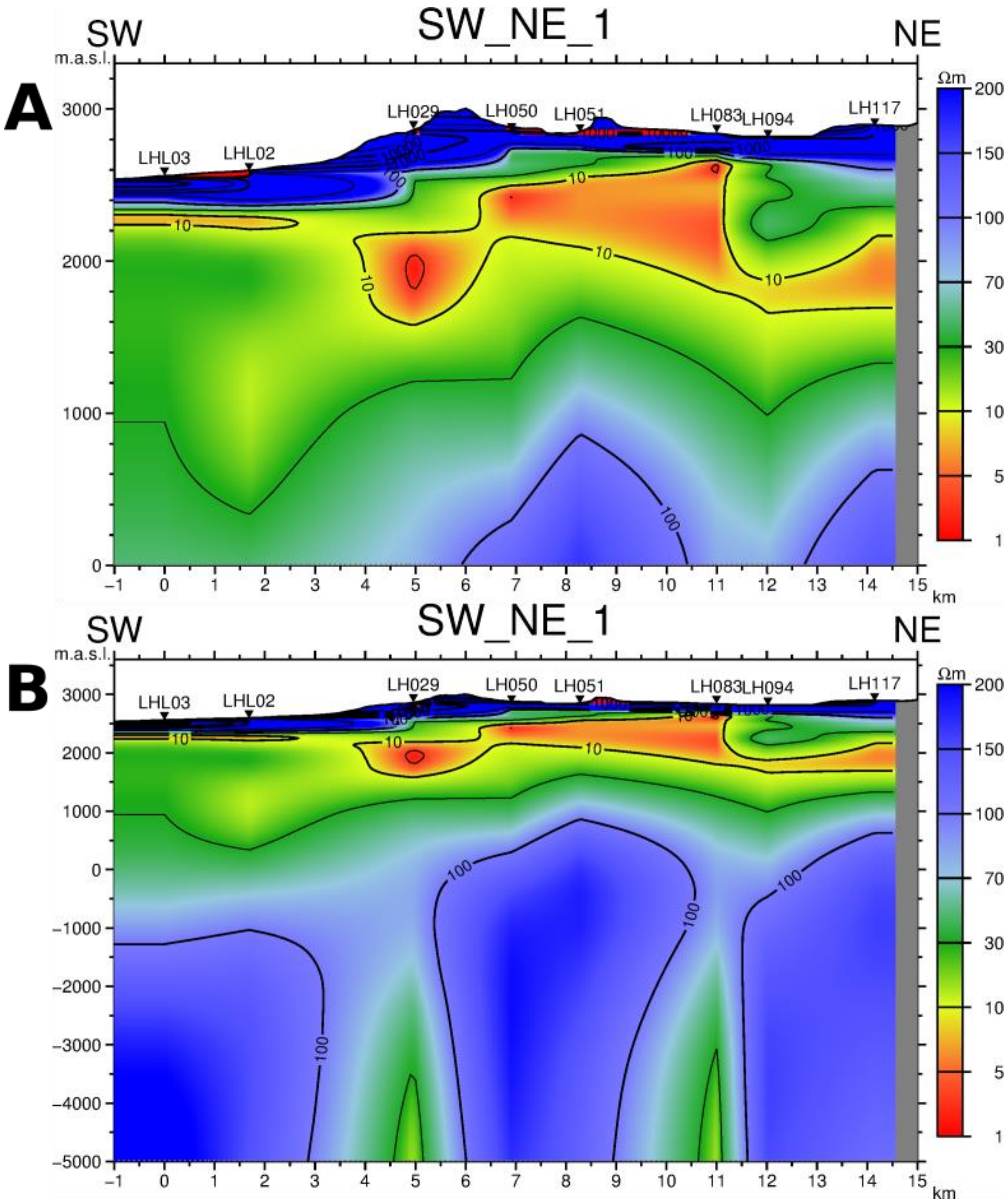

Figure 97: *Vertical cross-section through the 1D resistivity model of Los Humeros down to sea level (**A**) and 5000 meters below sea level (**B**). Triangles at the surface are the sounding locations along with the names. Location of the profile is shown in Figure 19 as P1.*

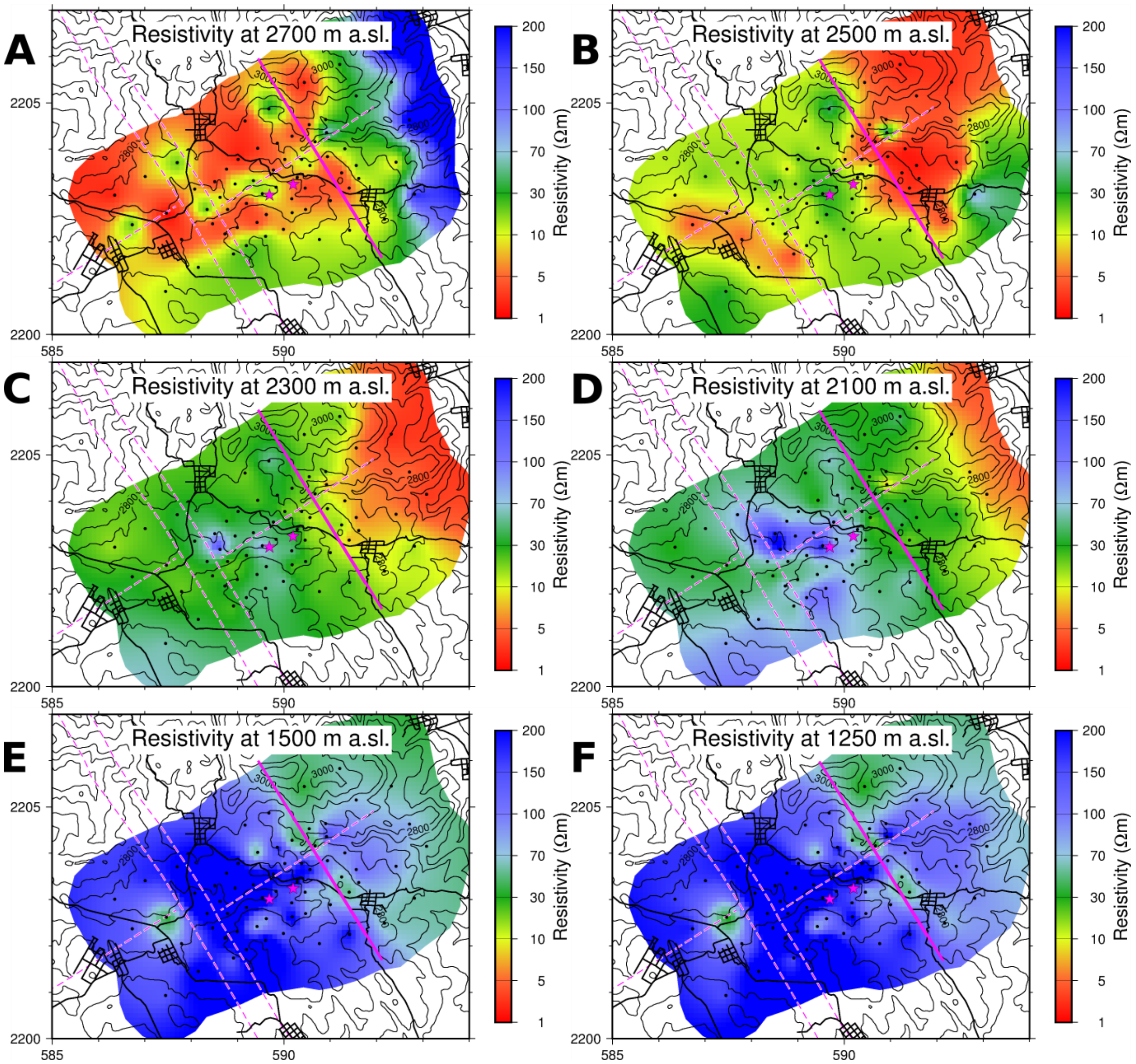

Figure 98: *Horizontal cross-sections through the 1D model of the Acoculco area at 2700 meters above sea level (**A**), 2500 meters above sea level (**B**), 2300 meters above sea level (**C**), 2100 meters above sea level (**D**), 1500 meters above sea level and (**E**) and 1250 meters above sea level (**F**). Thick black lines are roads, thin black lines are elevation contours every 50 meters. Pink starts are the locations of the EAC wells, dashed pink lines are major fault lines and thick pink line is the discontinuity as observed from the resistivity data.*

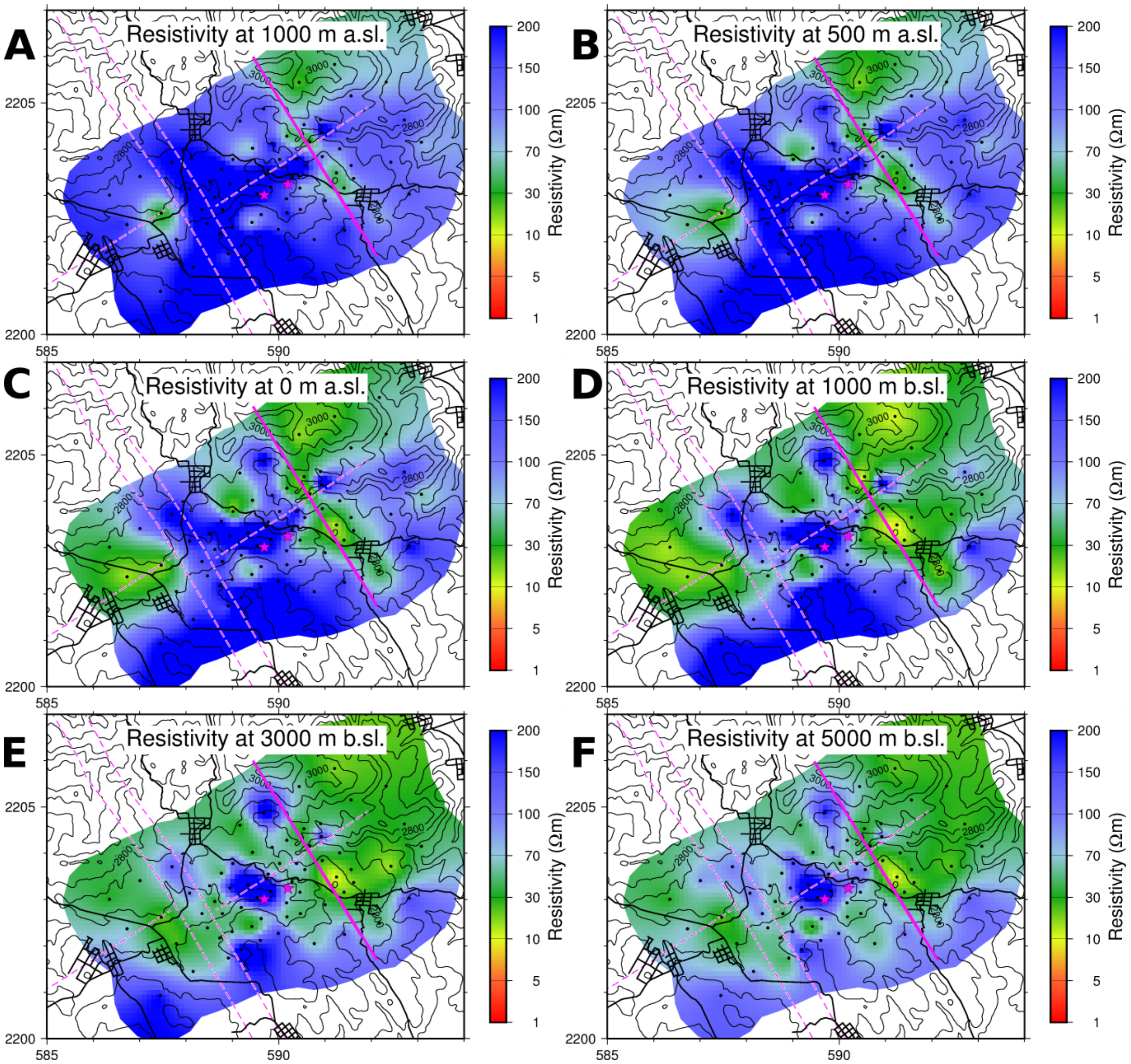

Figure 99: *Horizontal cross-sections through the 1D model of the Acoculco area at 1000 meters above sea level (**A**), 500 meters above sea level (**B**), at sea level (**C**), 1000 meters below sea level (**D**), 3000 meters below sea level and (**E**) and 5000 meters below sea level (**F**). Thick black lines are roads, thin black lines are elevation contours every 50 meters. Pink starts are the locations of the EAC wells, dashed pink lines are major fault lines and thick pink line is the discontinuity as observed from the resistivity data.*

Appendix C

In this appendix horizontal and vertical cross-sections though the final three dimensional resistivity model in Los Humers survey area, are presented.

Vertical cross-sections (Figures 100-109) are down to sea level (upper panel in each figure) and down to 5000 meters below sea level (lower panel of each figure), every 800 meters. The location of the cross-section is indicated as a red line in the small inlet in the lower-right corner of each figure. In the small inlet the black circles are sounding locations and dashed pink rectangle is the outline of the densely gridded area. In each vertical cross-section the limits of the densely gridded area is represented by pink dashed vertical lines. Station locations are indicated on the surface with black triangles and with the station names above. The vertical cross-sections are ordered from north to south. We only show west-east cross-sections as they are oriented approximately perpendicular to the main structures in the area.

The horizontal slices (Figure 110-111) are at depths, indicated in the header of each figure. Thick and thin hatched gray lines are the Los Humeros and Los Potreros calderas, respectively. Dashed white lines are main faults in the region and dark gray lines are elevation contours every 50 meters. Black rectangular box shows the outline of the densely gridded area and black lines are roads. Black circles are sounding locations.

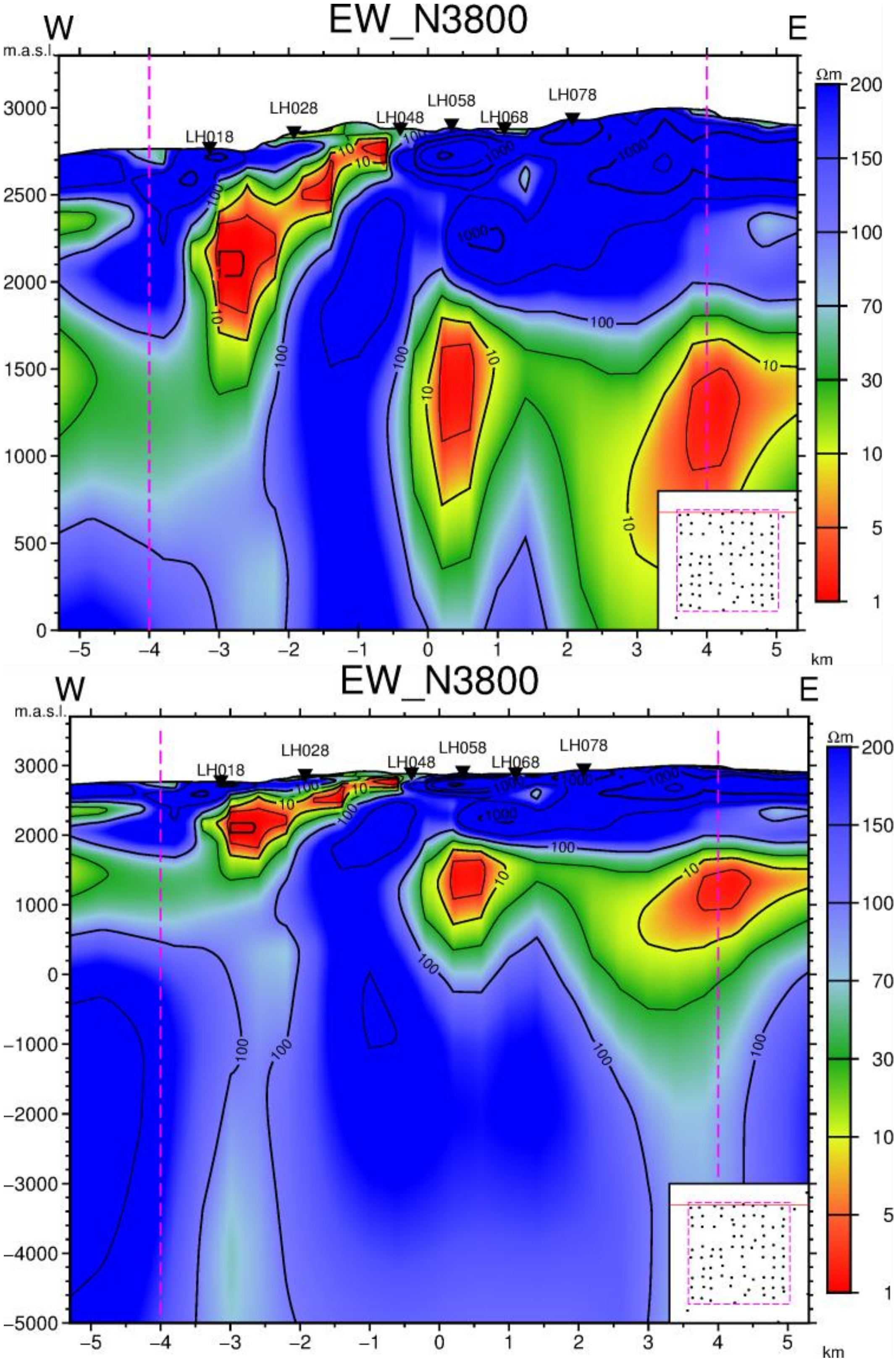

Figure 100: *Vertical cross-section through the final resistivity model of Los Humeros. See Appendix C for figure details.*

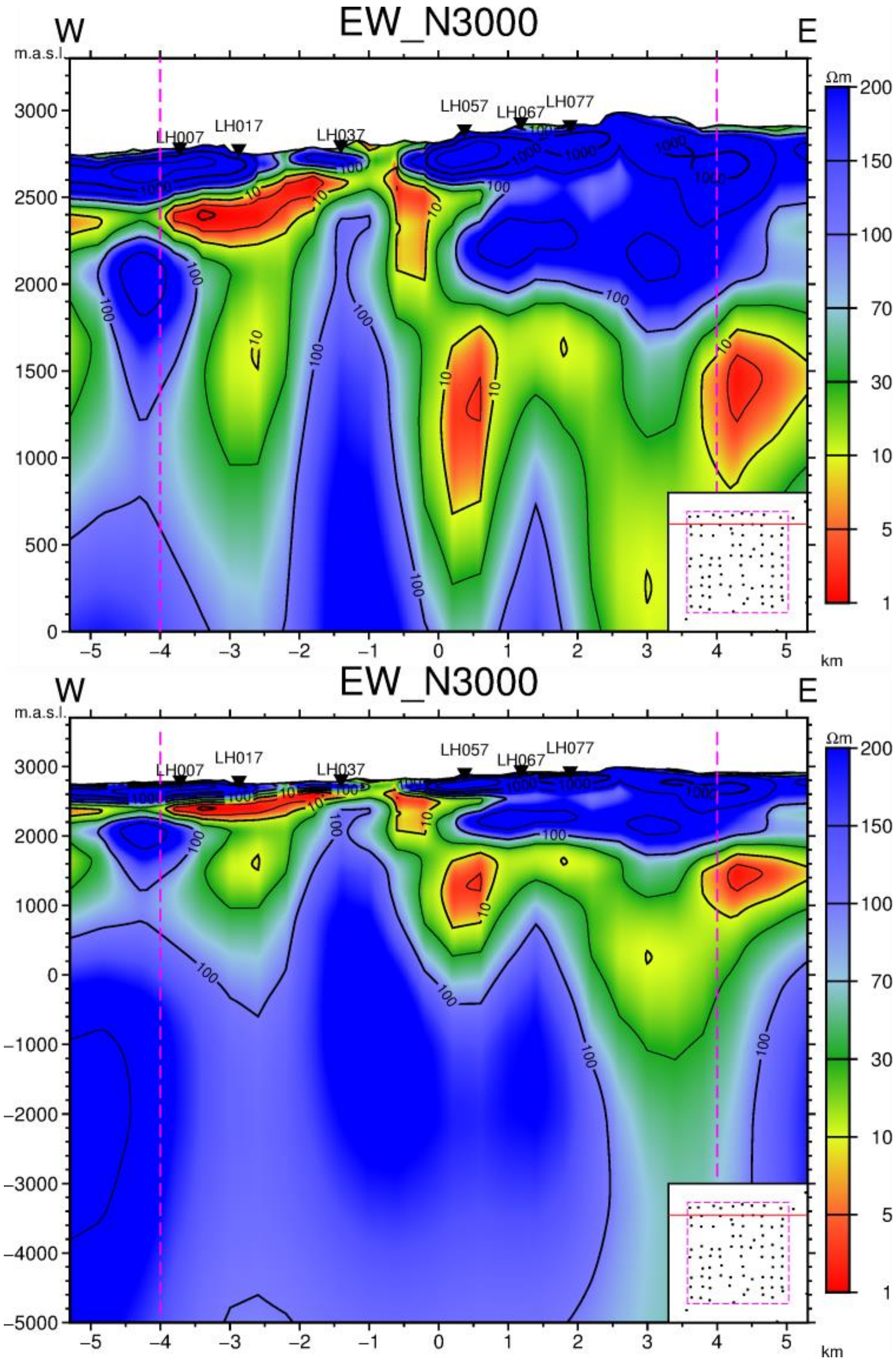

Figure 101: *Vertical cross-section through the final resistivity model of Los Humeros. See Appendix C for figure details.*

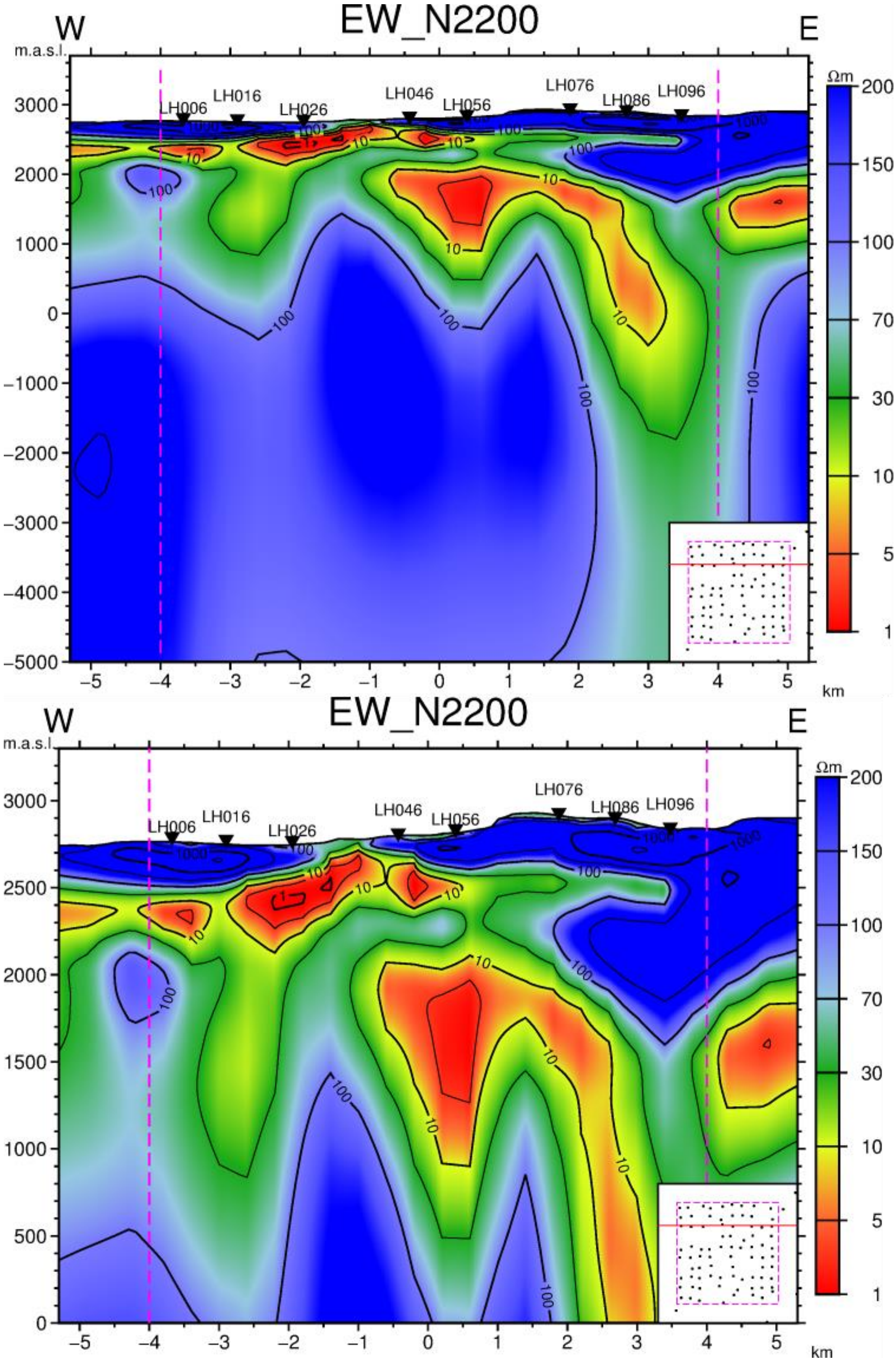

Figure 102: *Vertical cross-section through the final resistivity model of Los Humeros. See Appendix C for figure details.*

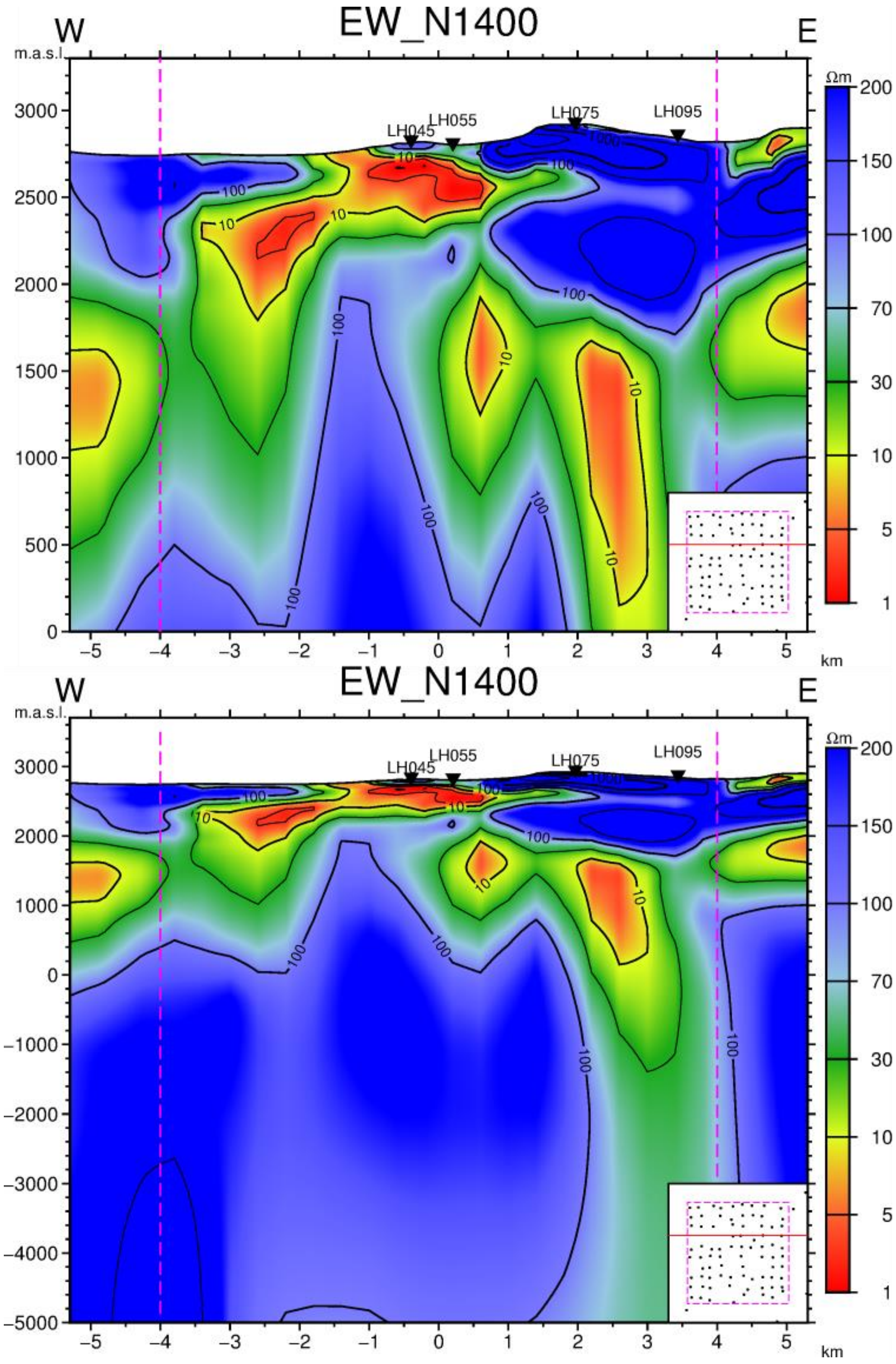

Figure 103: *Vertical cross-section through the final resistivity model of Los Humeros. See Appendix C for figure details.*

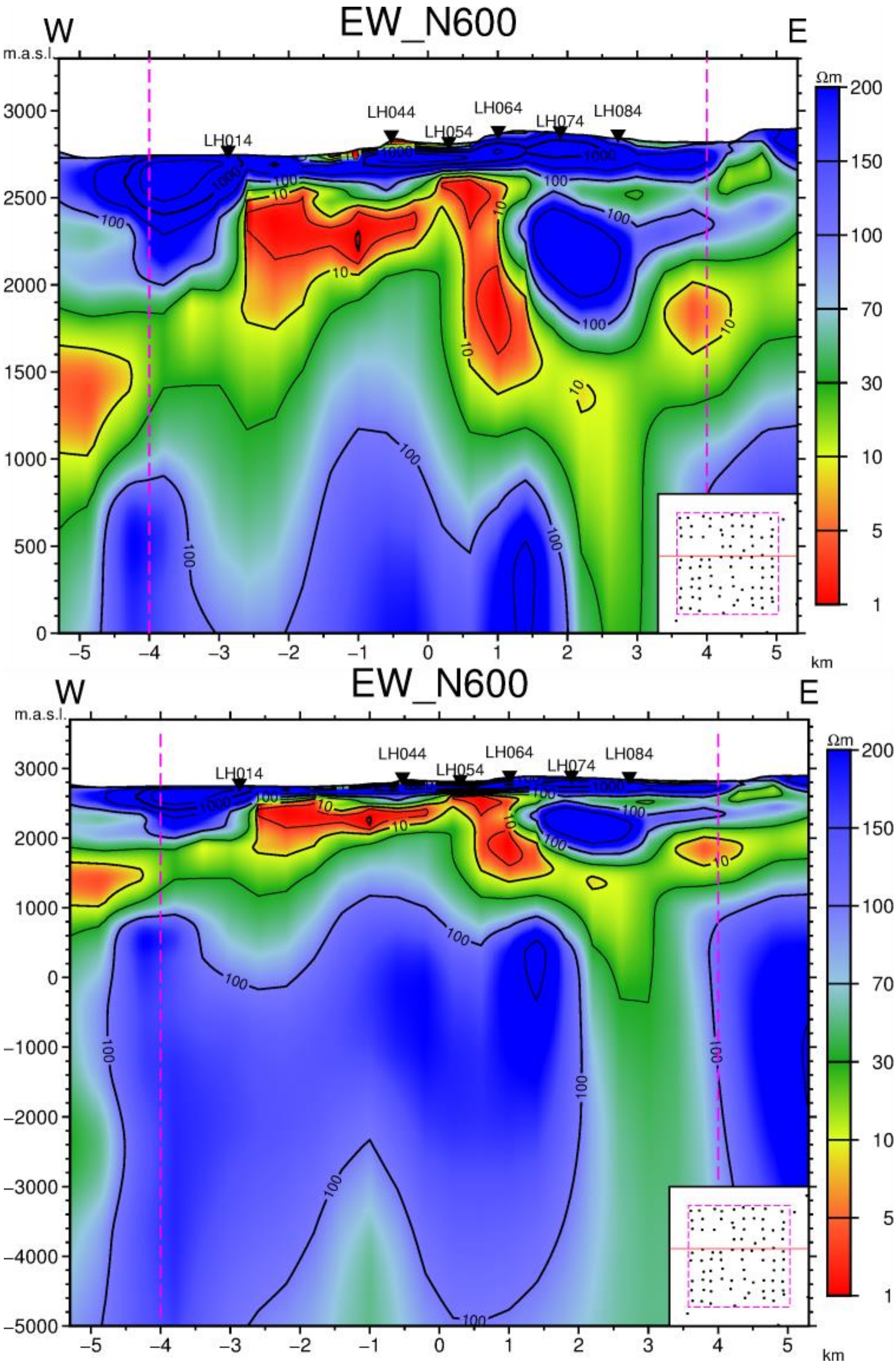

Figure 104: *Vertical cross-section through the final resistivity model of Los Humeros. See Appendix C for figure details.*

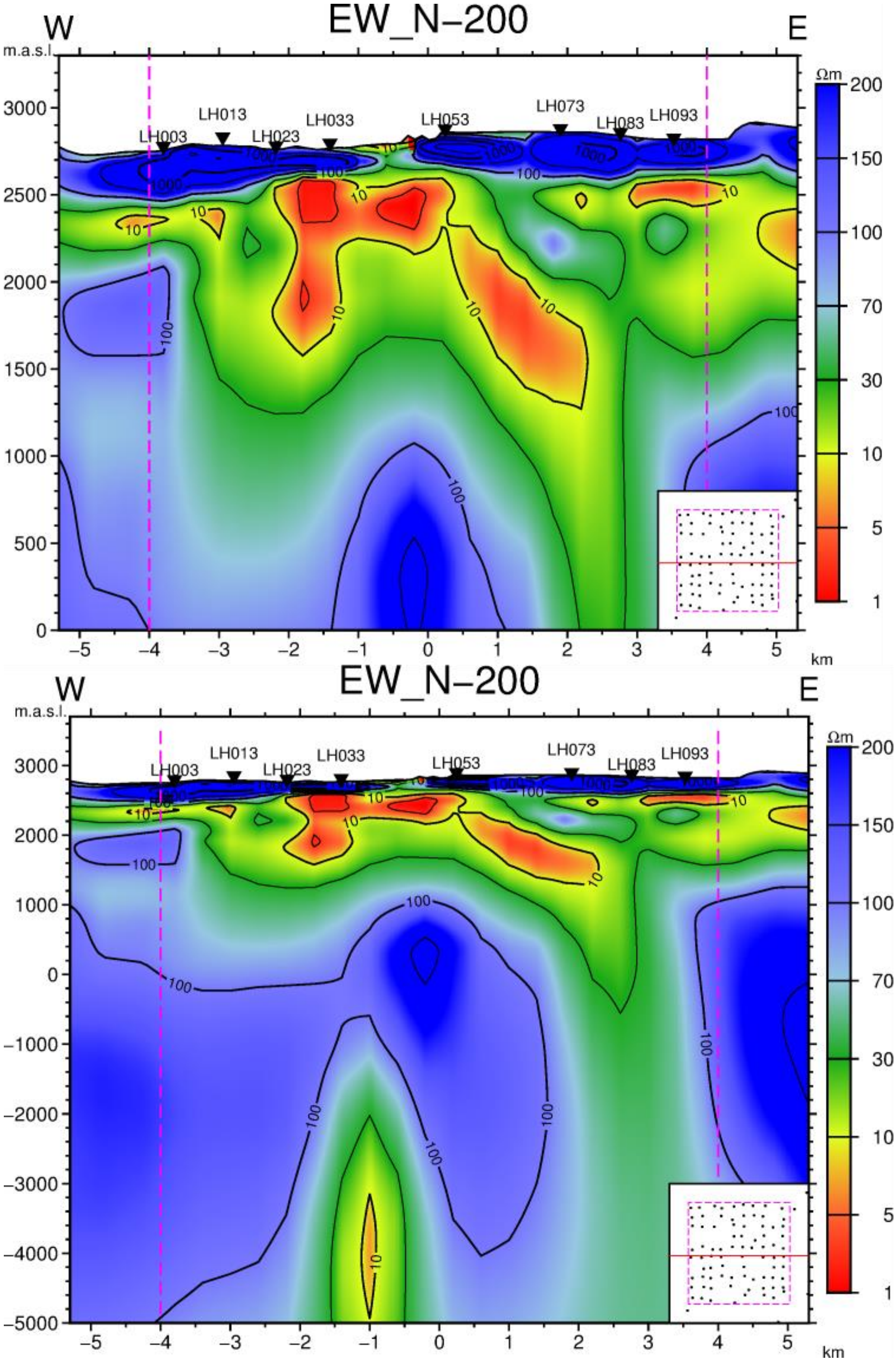

Figure 105: *Vertical cross-section through the final resistivity model of Los Humeros. See Appendix C for figure details.*

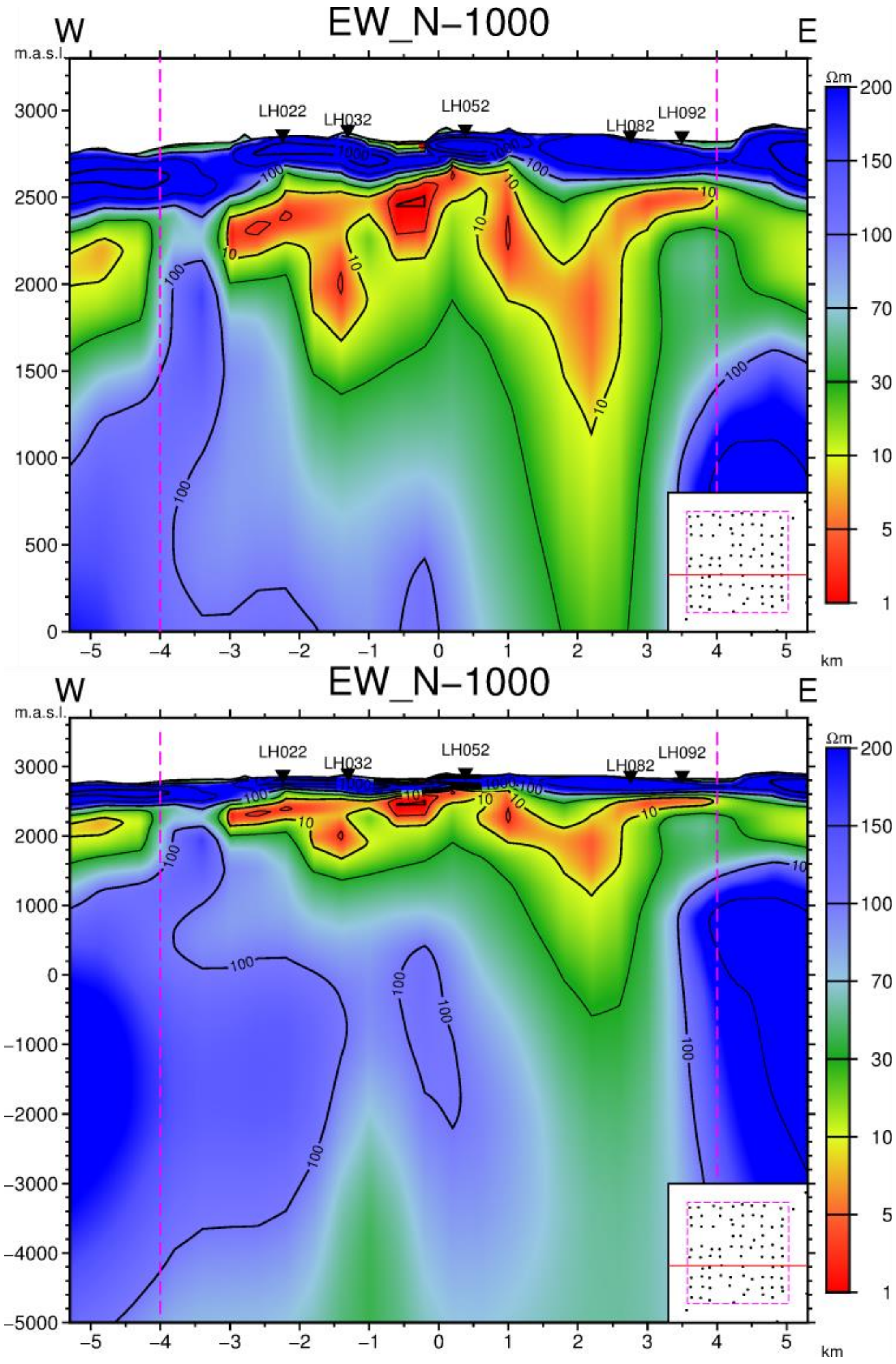

Figure 106: *Vertical cross-section through the final resistivity model of Los Humeros. See Appendix C for figure details.*

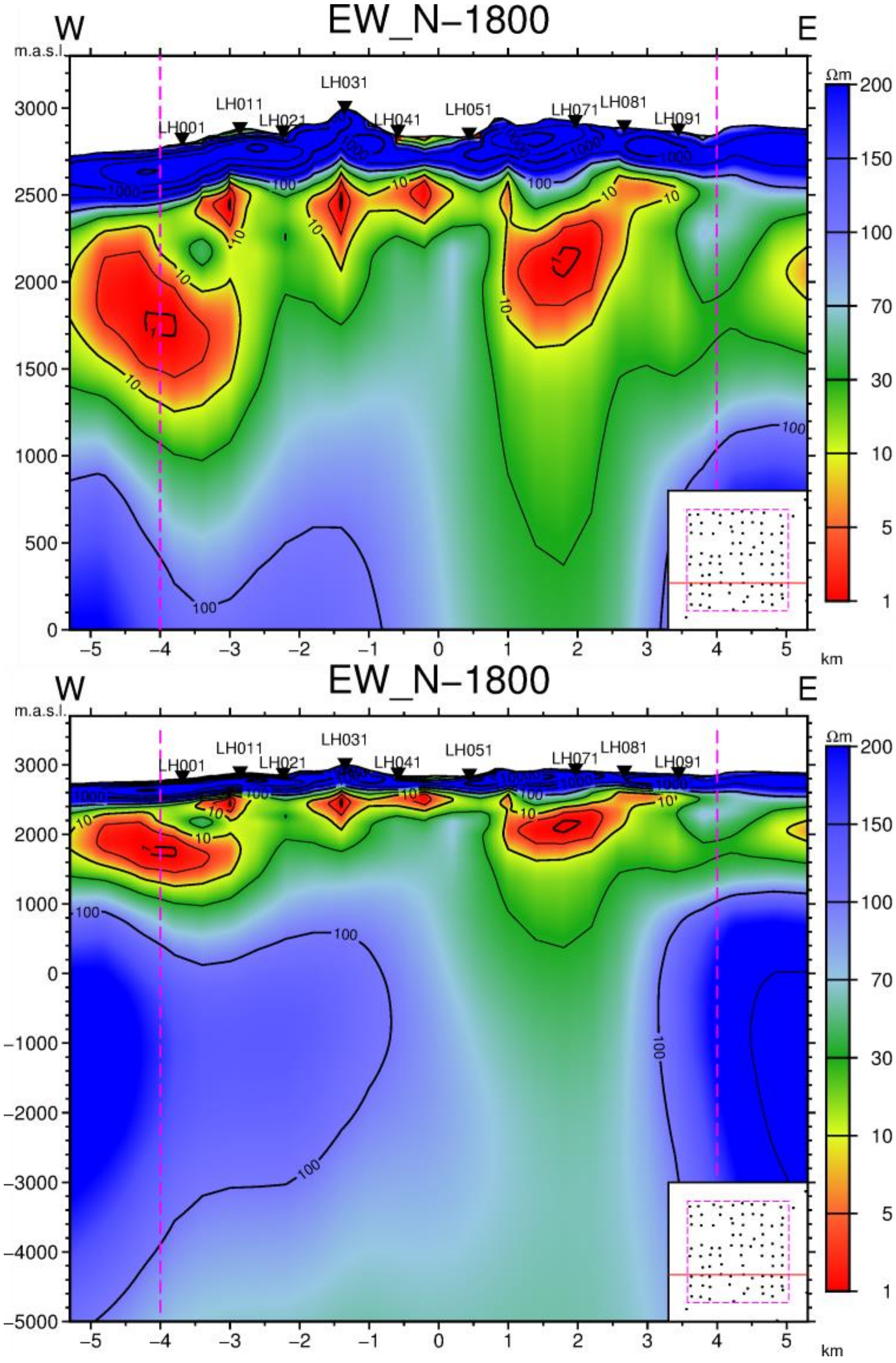

Figure 107: *Vertical cross-section through the final resistivity model of Los Humeros. See Appendix C for figure details.*

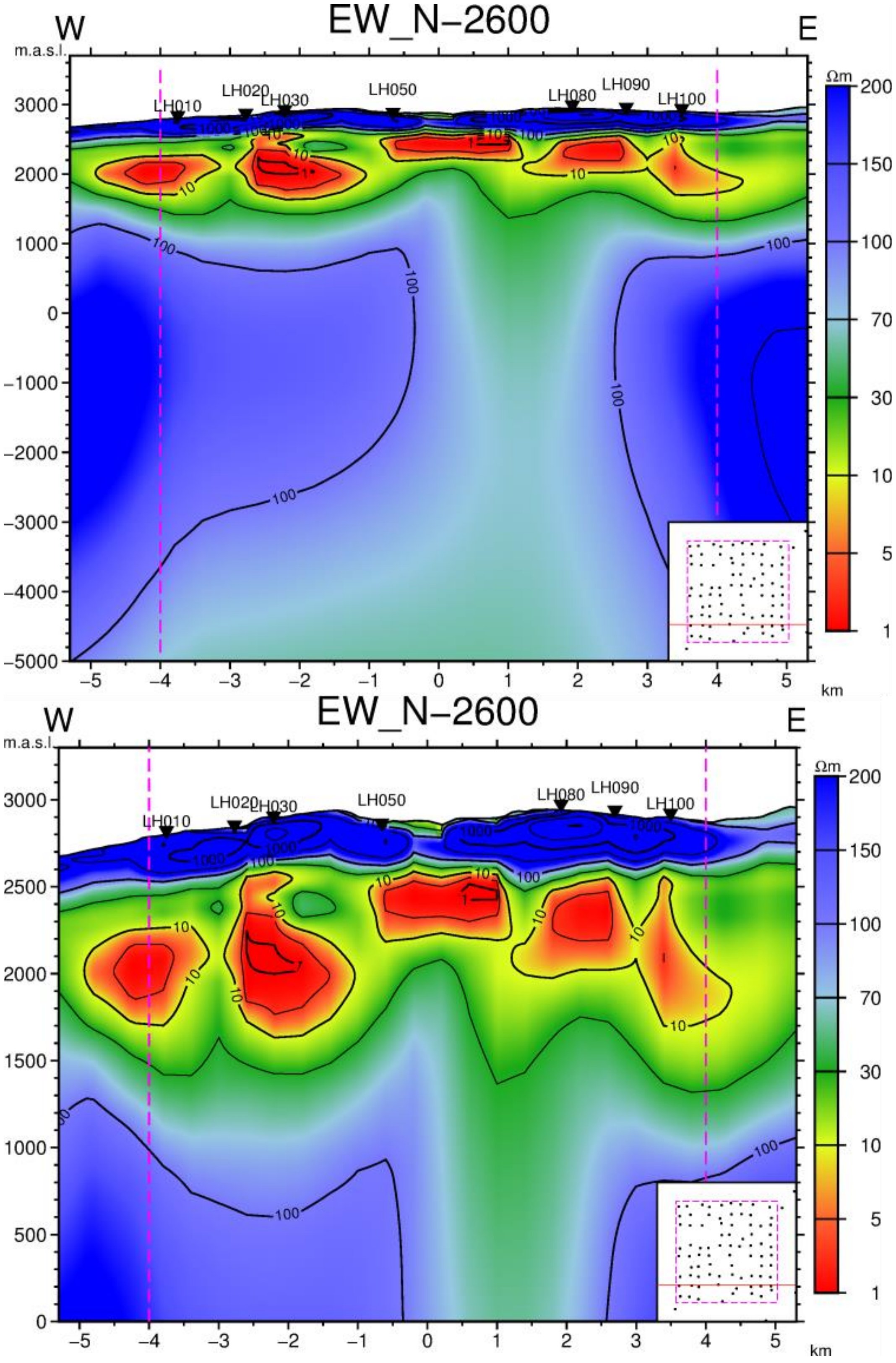

Figure 108: *Vertical cross-section through the final resistivity model of Los Humeros. See Appendix C for figure details.*

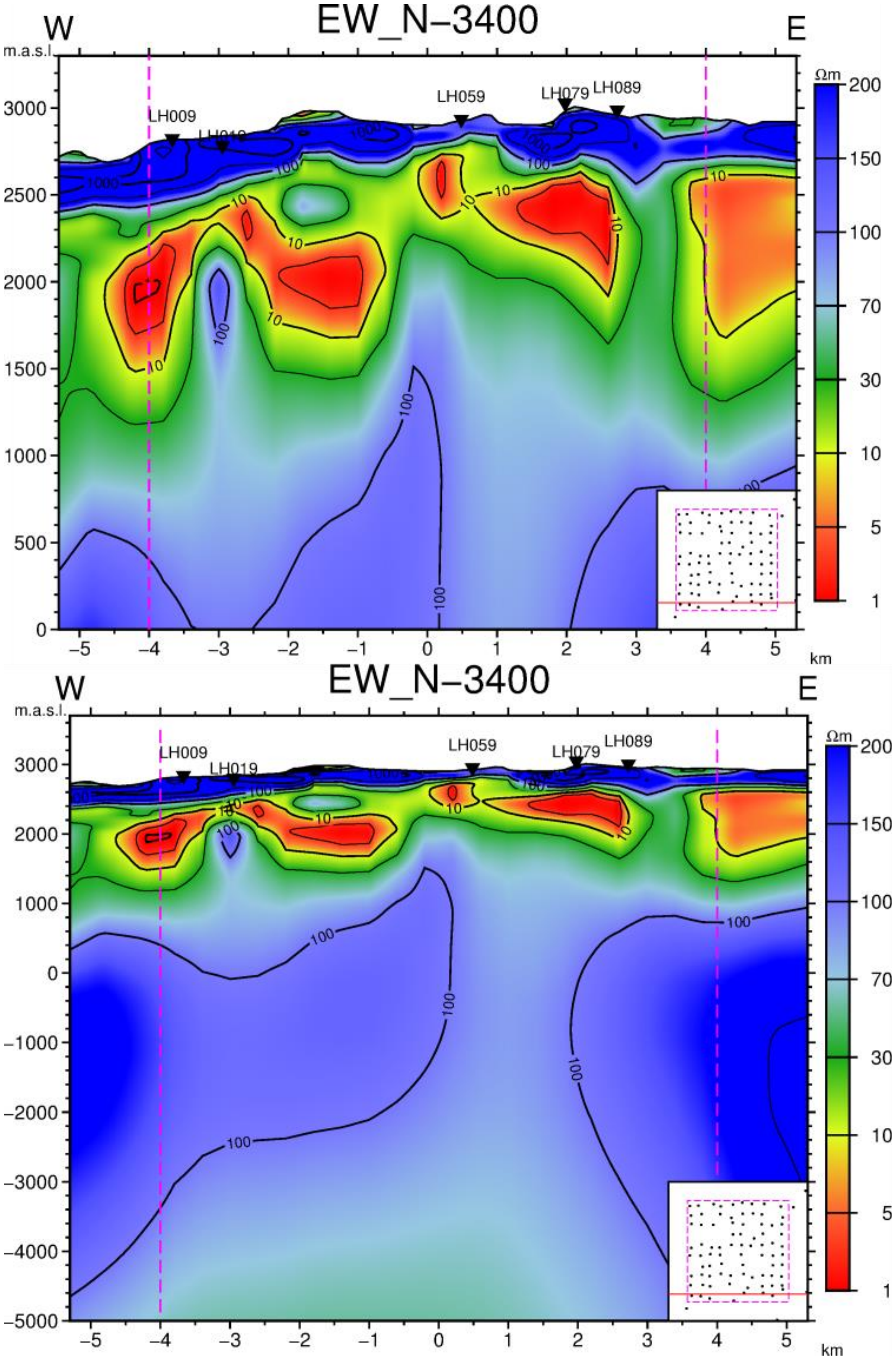

Figure 109: *Vertical cross-section through the final resistivity model of Los Humeros. See Appendix C for figure details.*

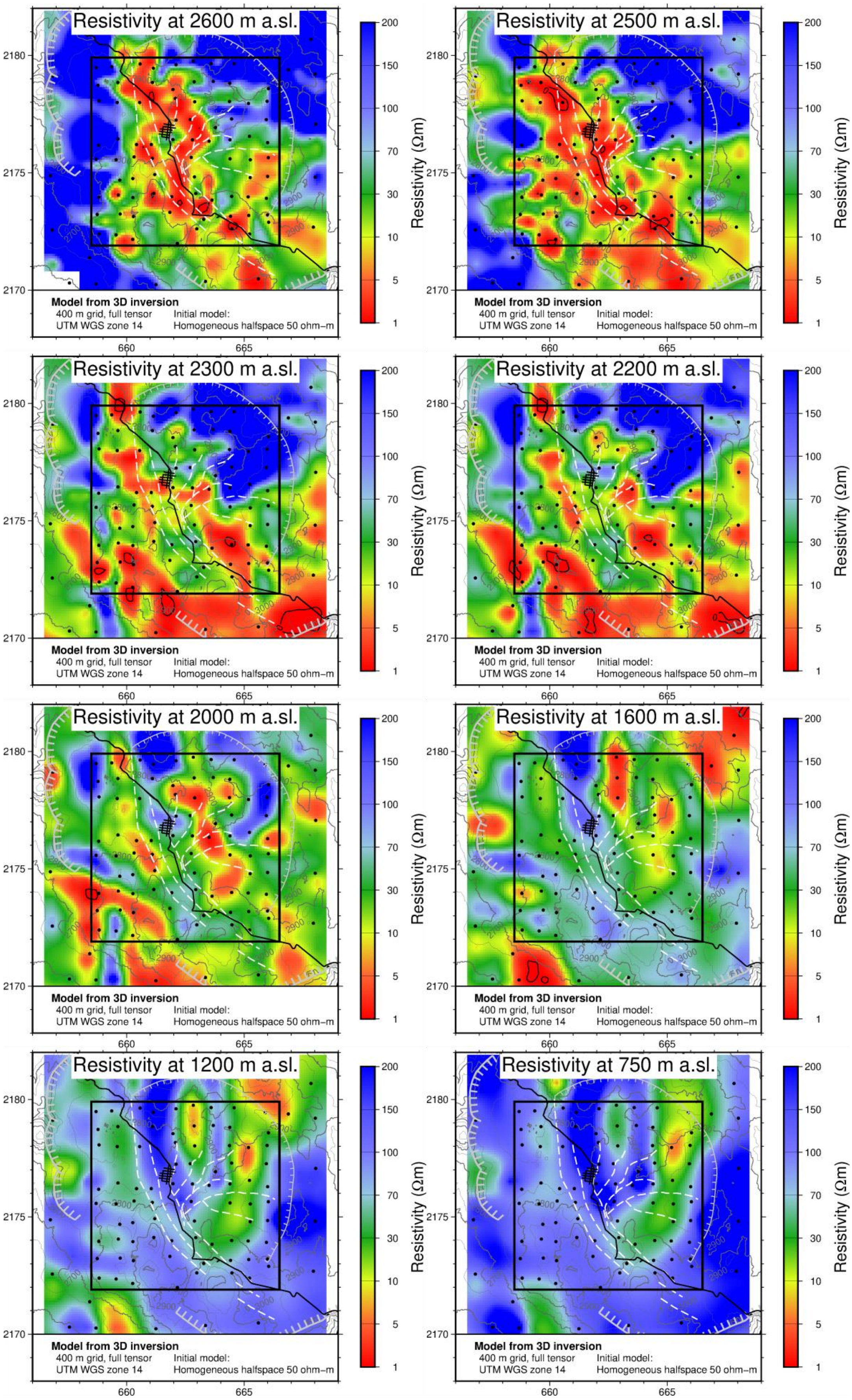

Figure 110: *Horizontal cross-sections through the final resistivity model of Los Humeros. See Appendix C for figure details.*

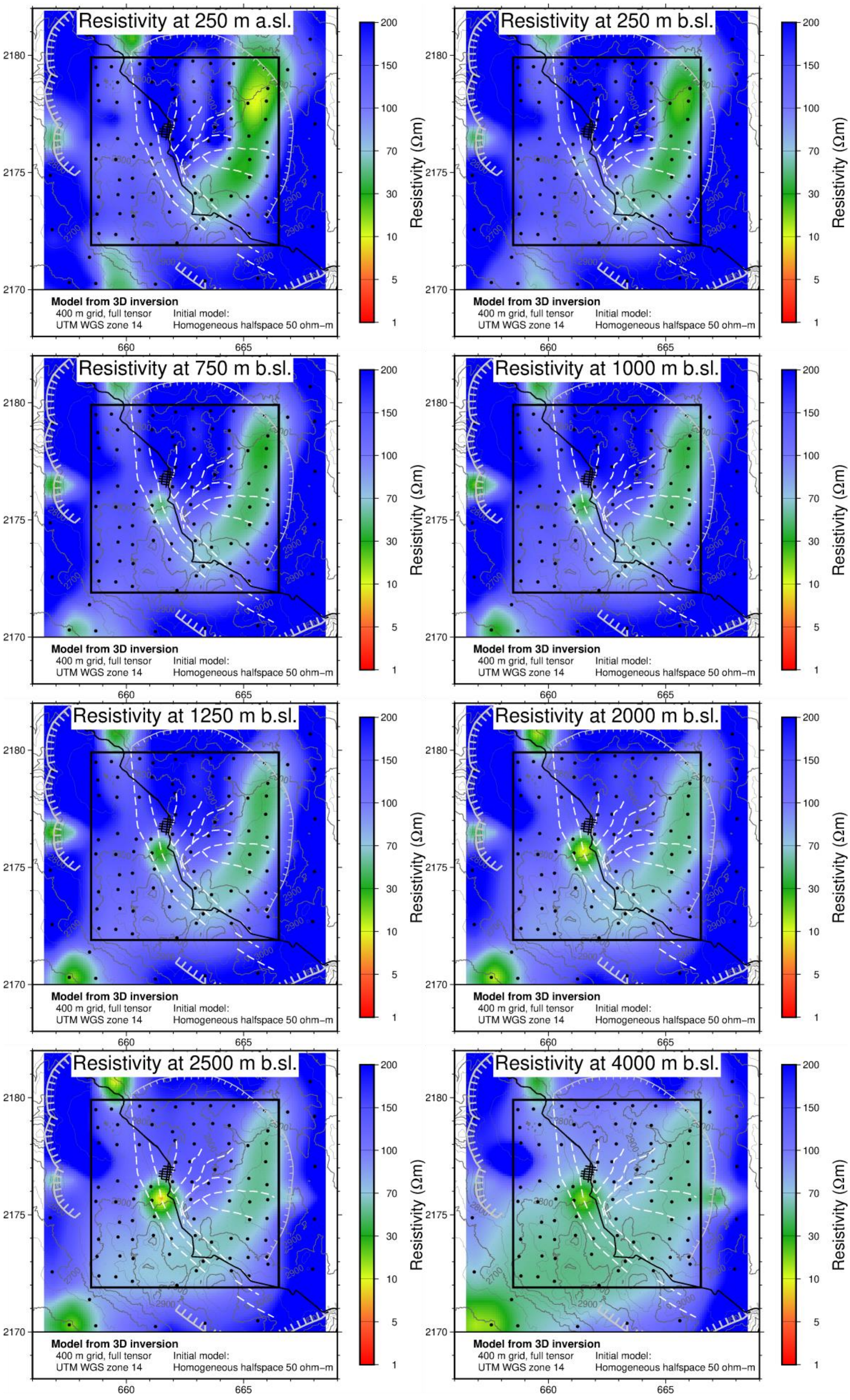

Figure 111: *Horizontal cross-sections through the final resistivity model of Los Humeros. See Appendix C for figure details*

Appendix D

In this appendix horizontal and vertical cross-sections though the final three dimensional resistivity model in the Acoculco survey area, are presented.

Vertical cross-sections (Figures 112-129) are shown down to sea level (upper panel of all figures) and down to 5000 meters below sea level (bottom panel for all figures), every 400 meters in the southwest-northeast direction and every 600 meters in the northwest-southeast direction. The location of the cross-section is indicated as a red line in the small inlet in the lower-right corner of each figure. In the small inlet the black circles are sounding locations and dashed pink rectangle is the outline of the densely gridded area. In each vertical cross-section the limits of the densely gridded area is represented by pink dashed vertical lines. Station locations are indicated on the surface with black triangles and with the station names above. The vertical cross-sections are ordered from northwest to southeast and then from southwest to northeast.

Horizontal slices (Figures 129-131) are at depths, indicated in the header of each figure. Dashed pink lines are the main faults in the region and dark gray lines are elevation contours every 50 meters. Black rectangular box shows the outline of the densely gridded area and black lines are roads. Black circles are sounding locations. The two EAC wells are shown as black crosses on top of a white circle.

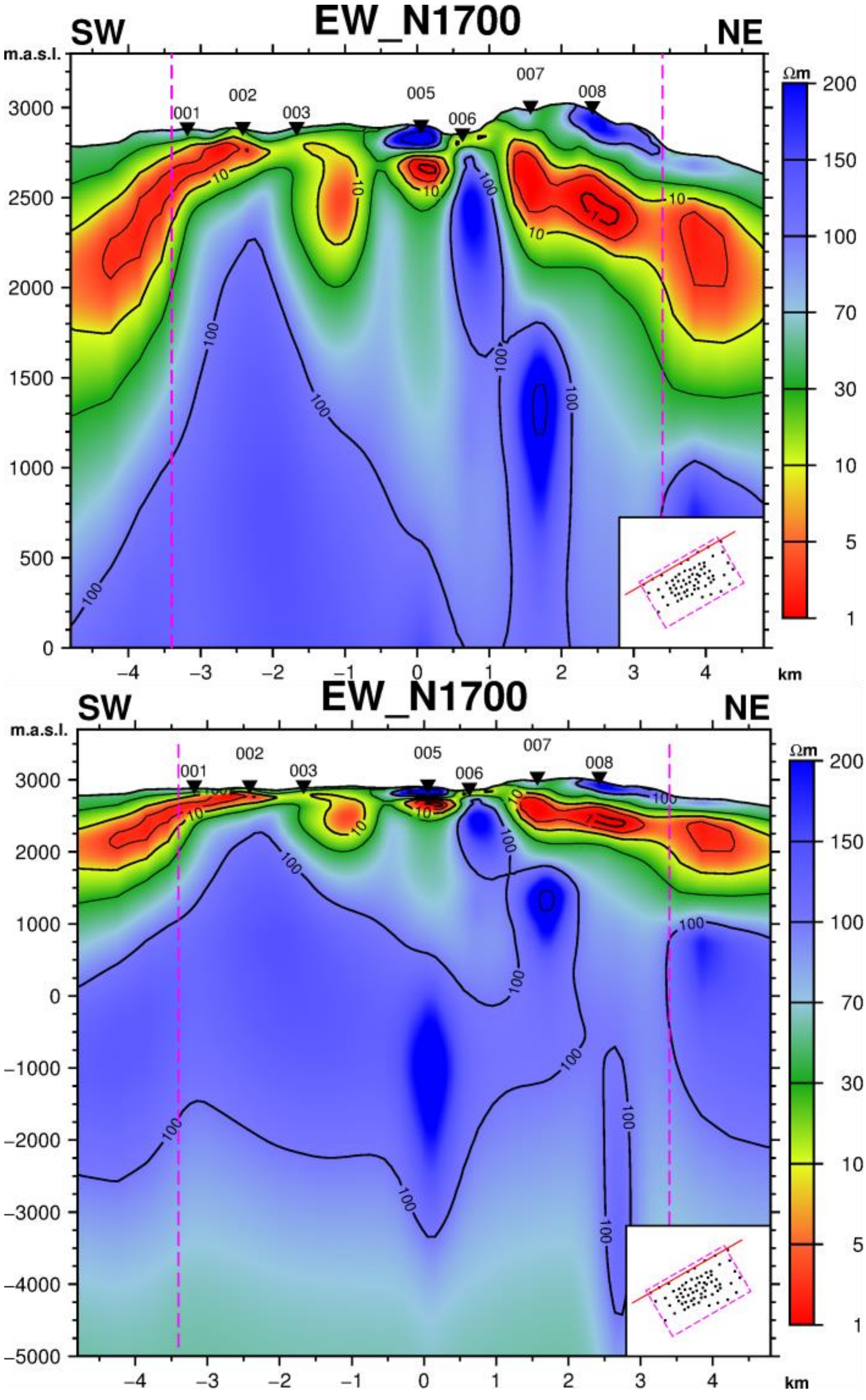

Figure 112: *Vertical cross-section through the final resistivity model of the Acoculco survey area. See Appendix D for figure details.*

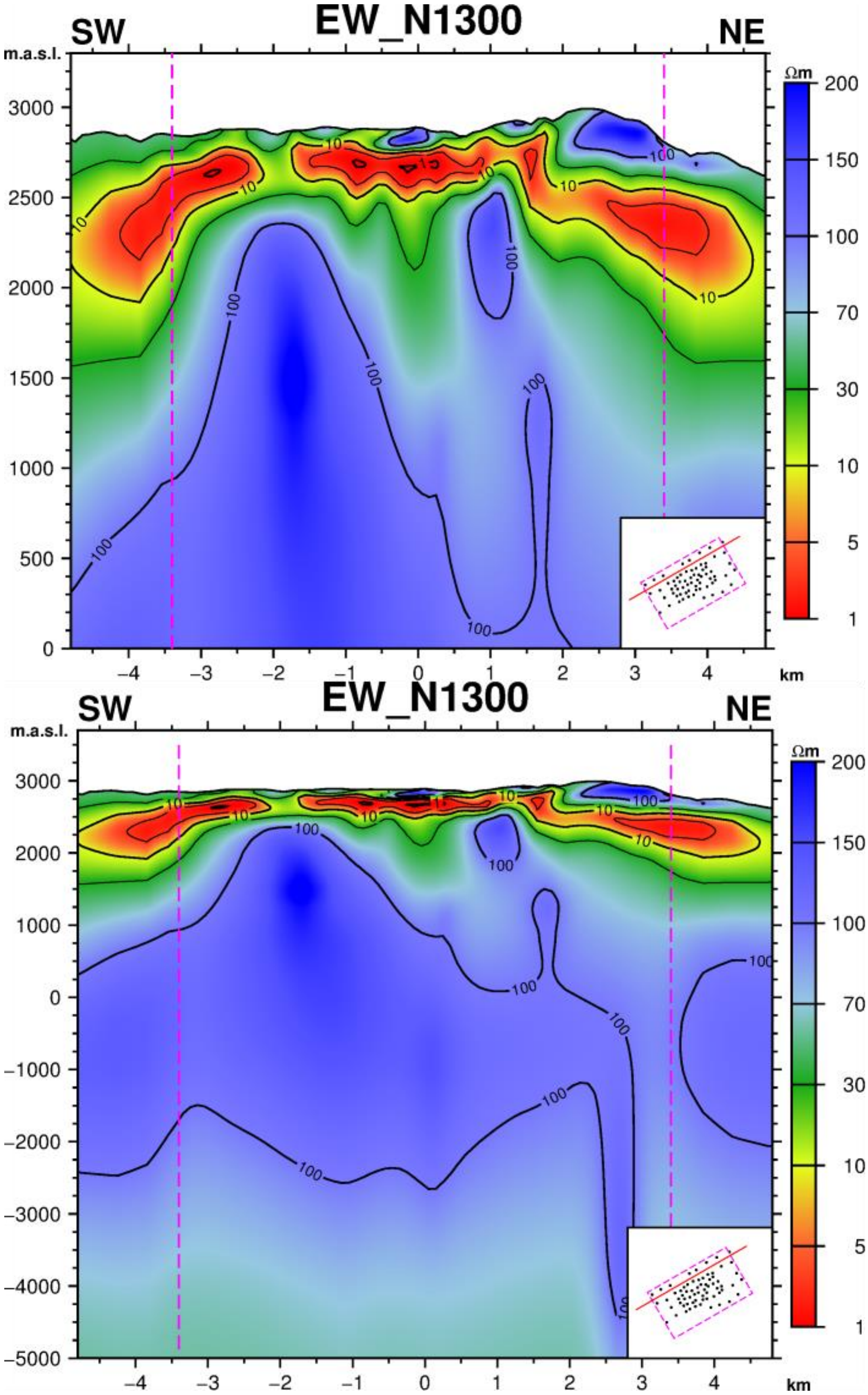

Figure 113: *Vertical cross-section through the final resistivity model of the Acoculco survey area. See Appendix D for figure details.*

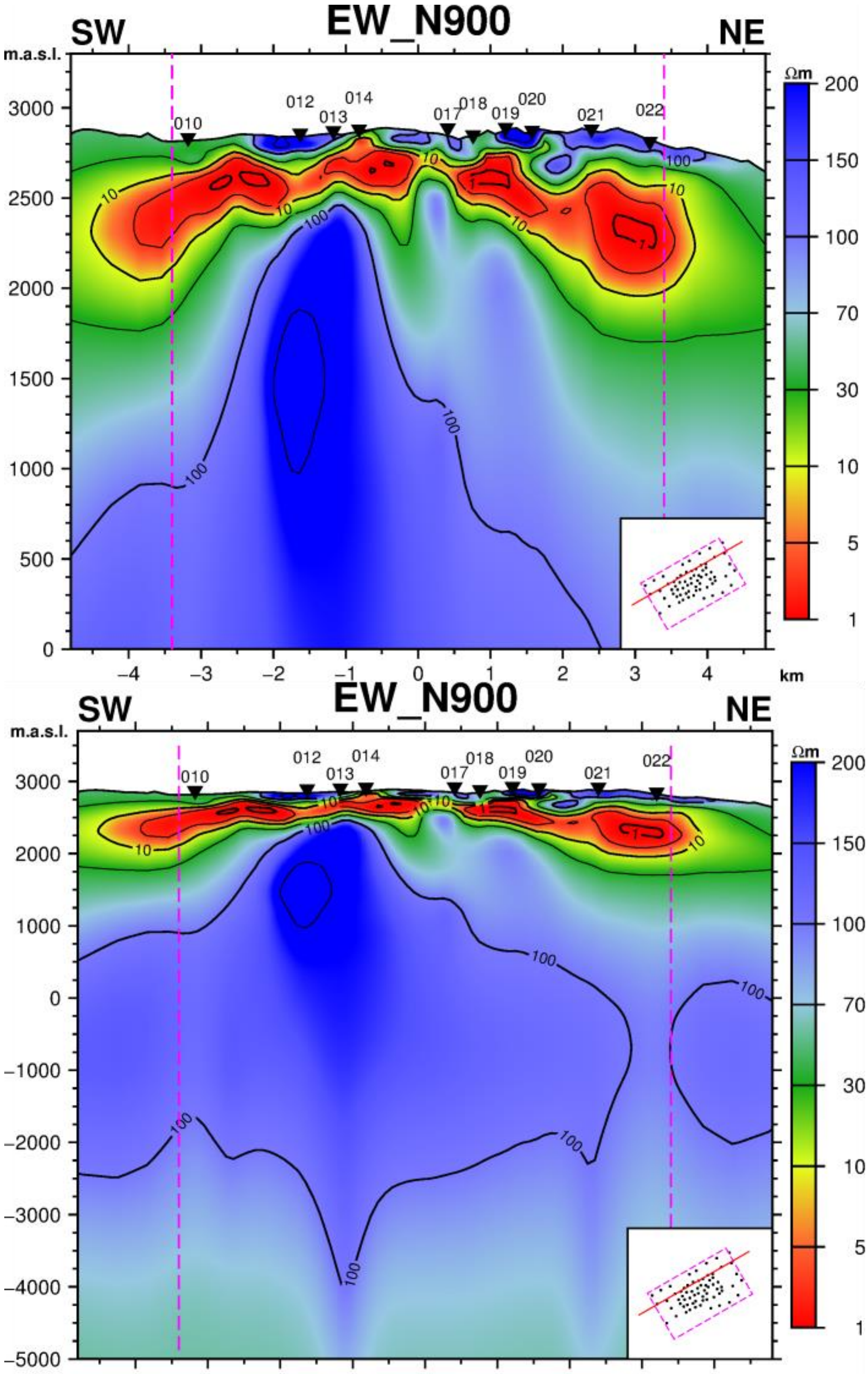

Figure 114: *Vertical cross-section through the final resistivity model of the Acoculco survey area. See Appendix D for figure details.*

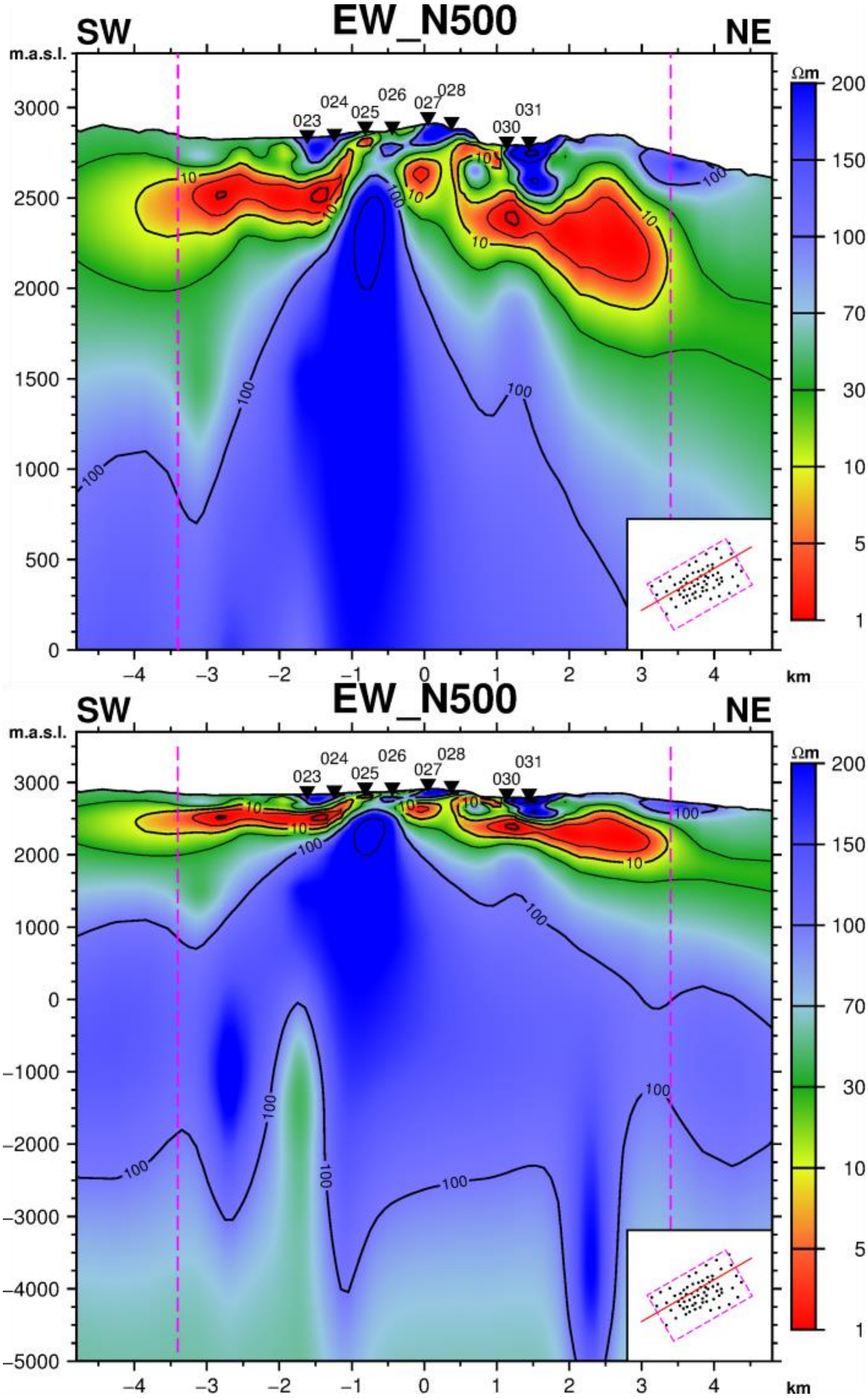

Figure 115: *Vertical cross-section through the final resistivity model of the Acoculco survey area. See Appendix D for figure details.*

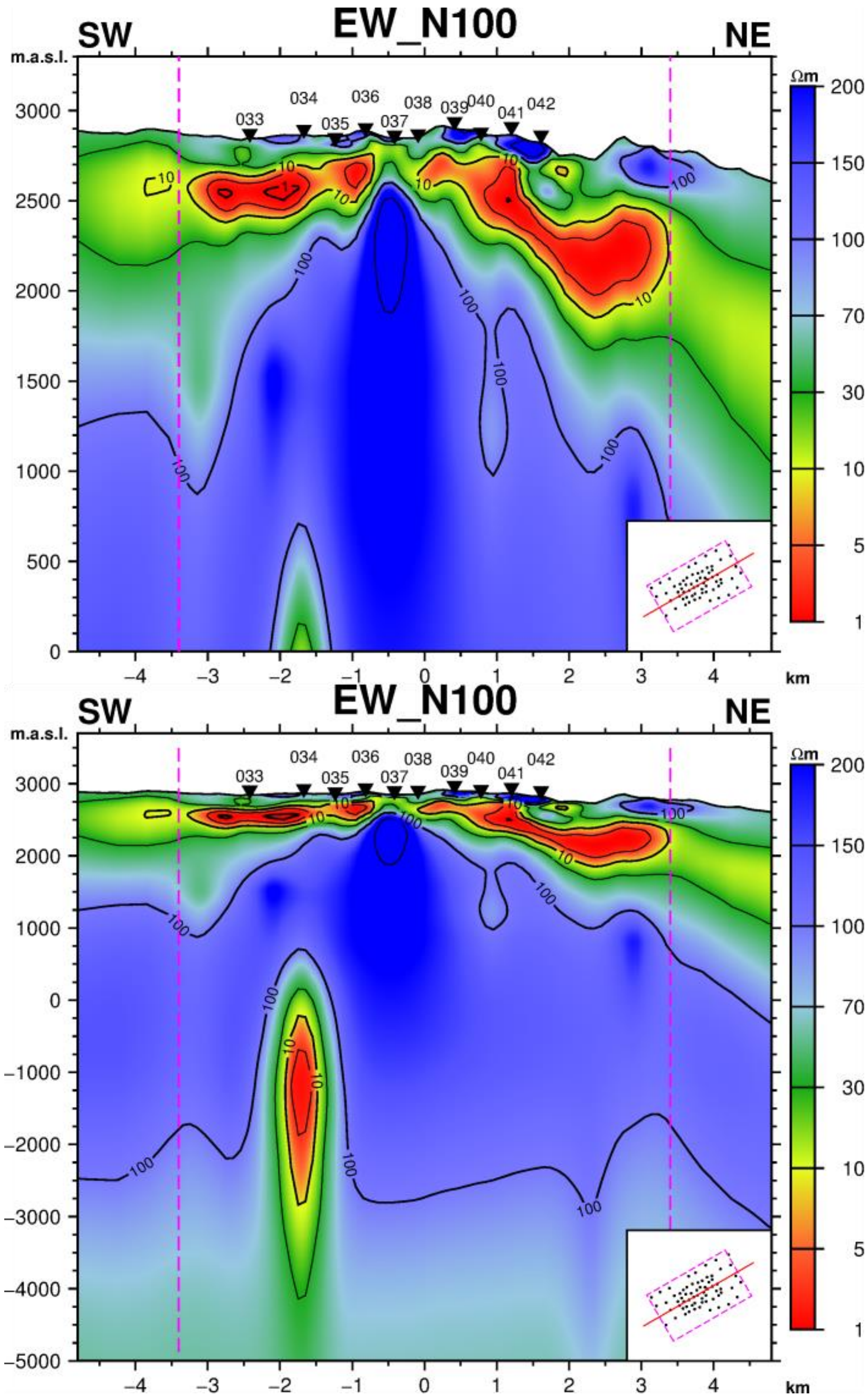

Figure 116: *Vertical cross-section through the final resistivity model of the Acoculco survey area. See Appendix D for figure details.*

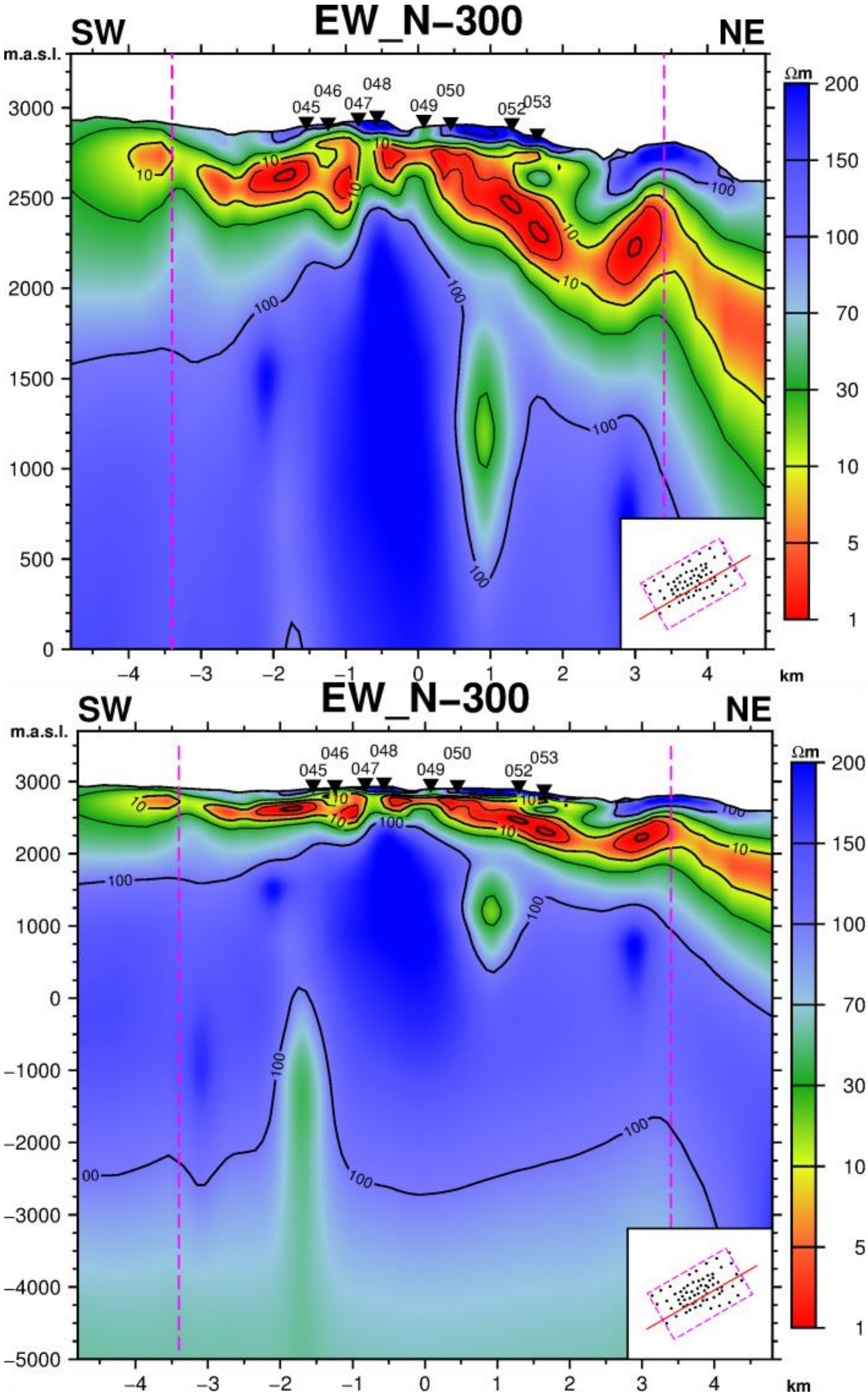

Figure 117: *Vertical cross-section through the final resistivity model of the Acoculco survey area. See Appendix D for figure details.*

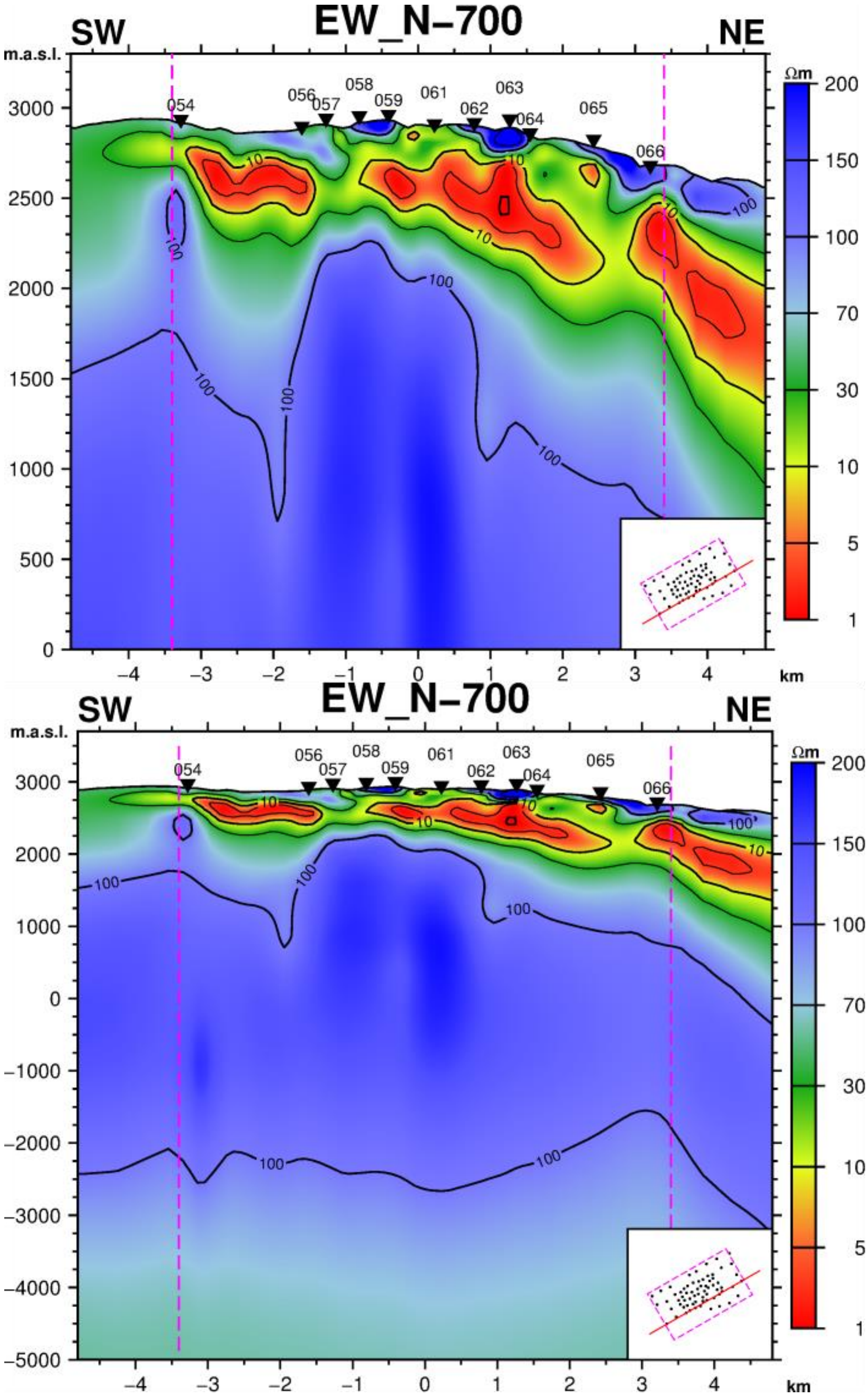

Figure 118: *Vertical cross-section through the final resistivity model of the Acoculco survey area. See Appendix D for figure details.*

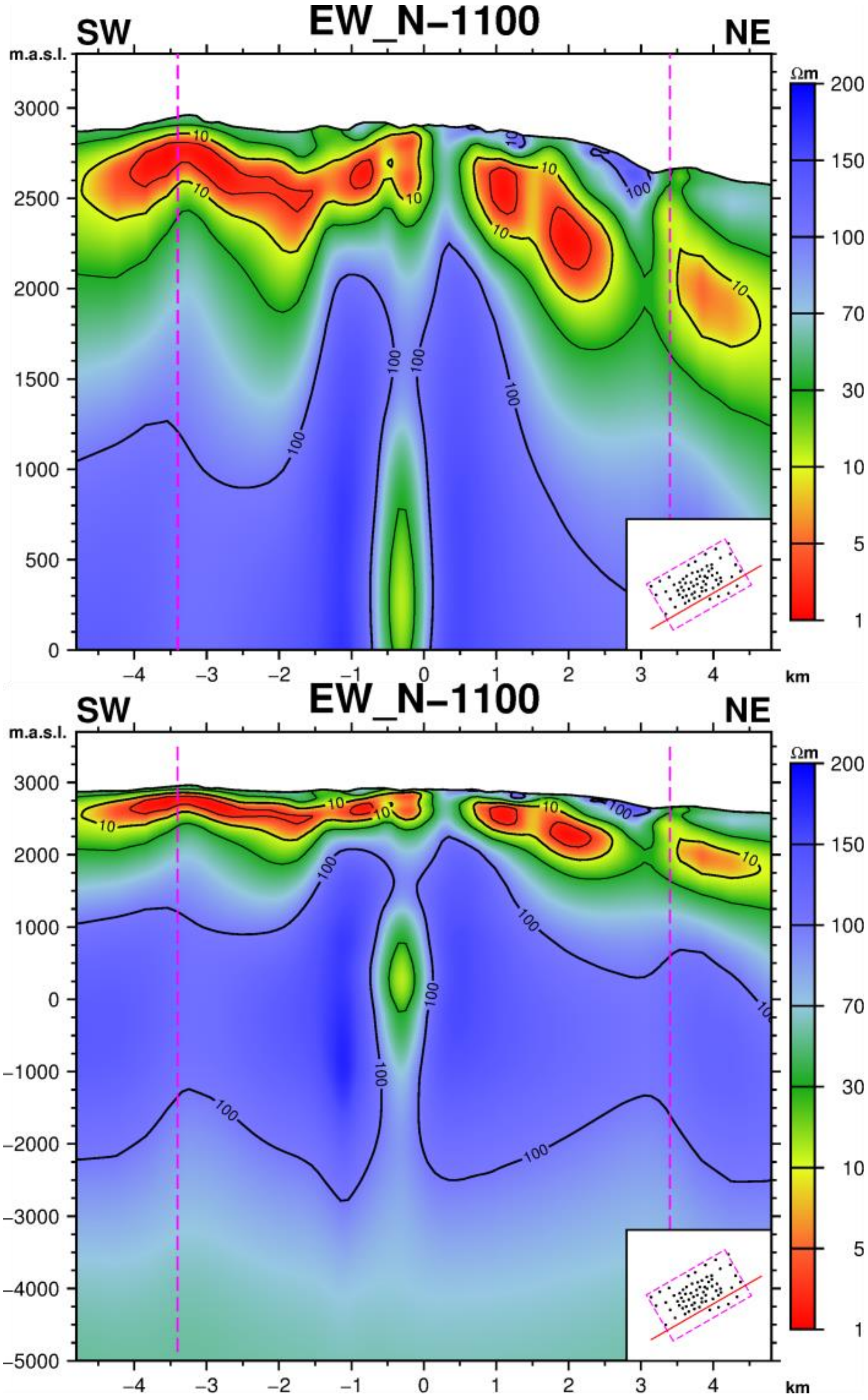

Figure 119: *Vertical cross-section through the final resistivity model of the Acoculco survey area. See Appendix D for figure details.*

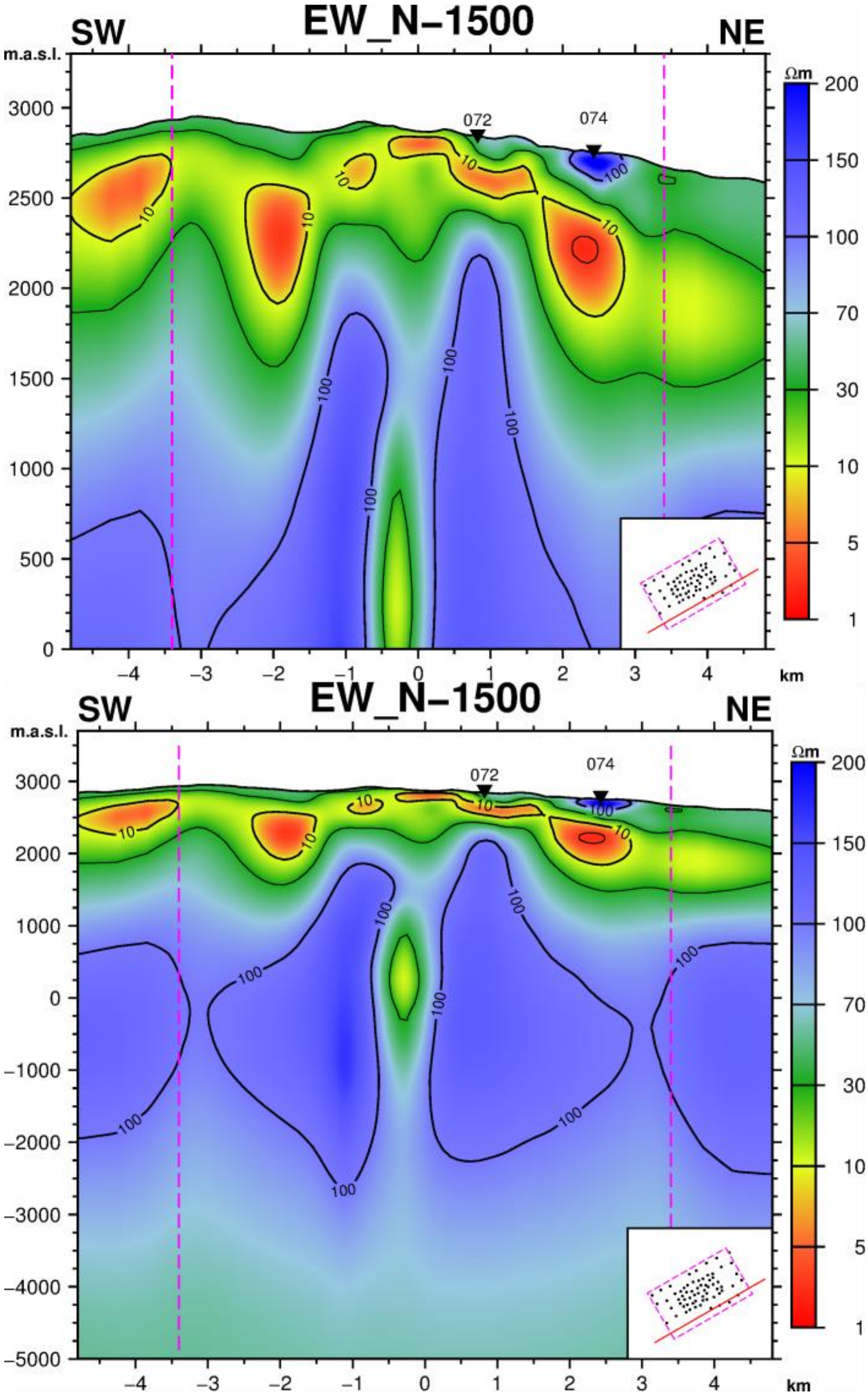

Figure 120: *Vertical cross-section through the final resistivity model of the Acoculco survey area. See Appendix D for figure details.*

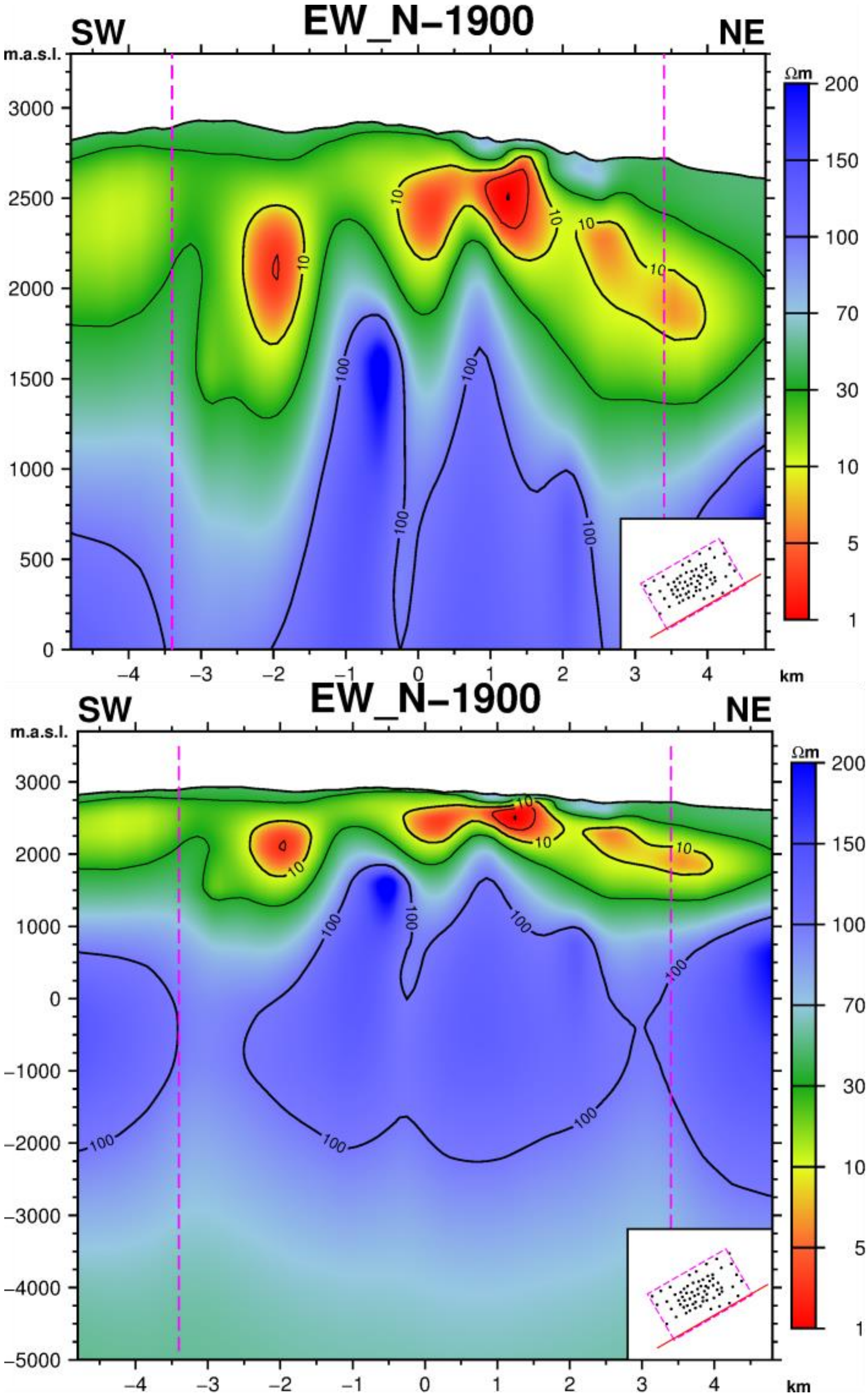

Figure 121: *Vertical cross-section through the final resistivity model of the Acoculco survey area. See Appendix D for figure details.*

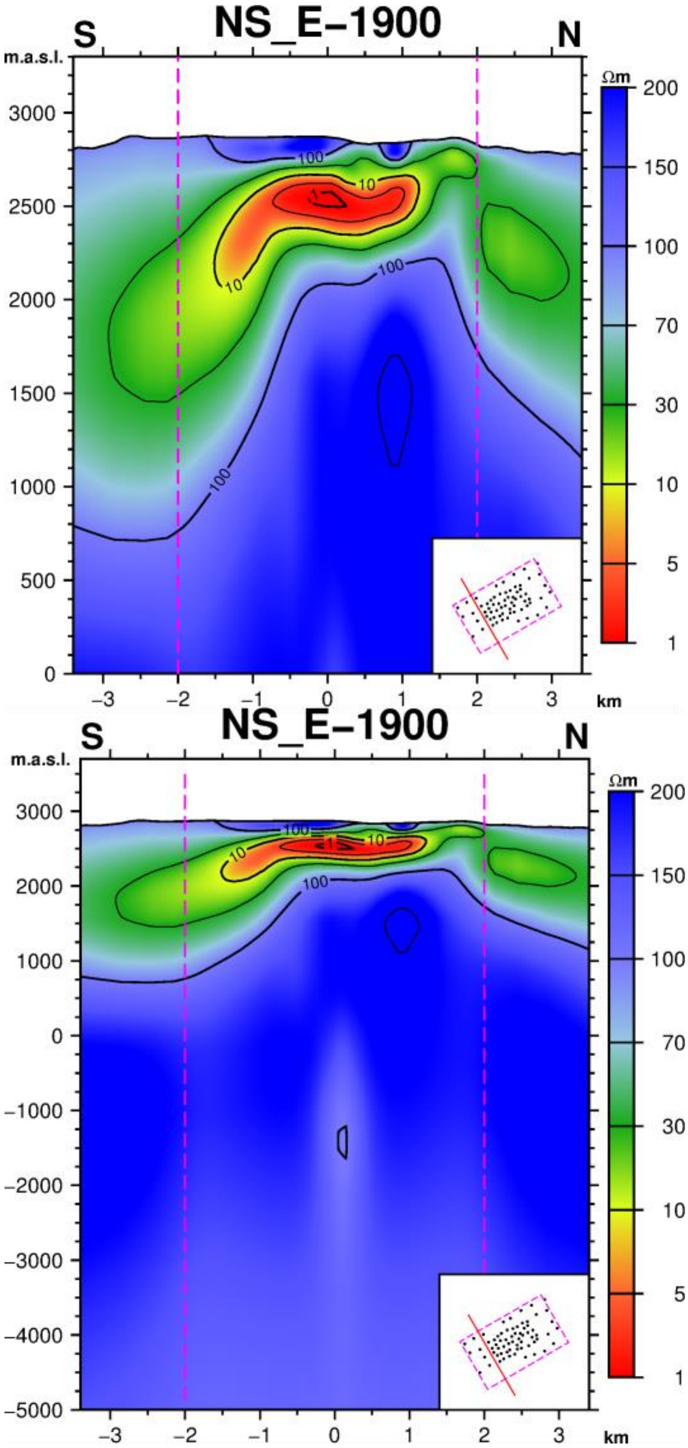

Figure 122: *Vertical cross-section through the final resistivity model of the Acoculco survey area. See Appendix D for figure details.*

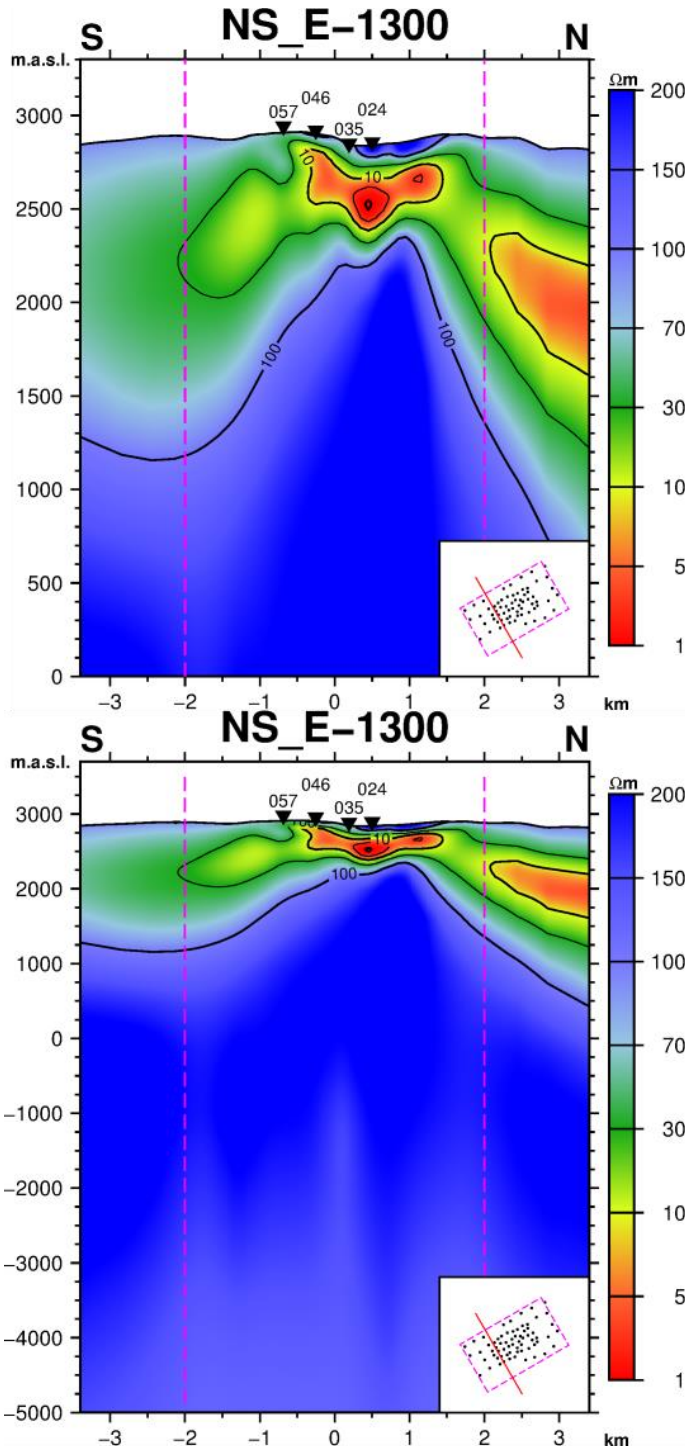

Figure 123: *Vertical cross-section through the final resistivity model of the Acoculco survey area. See Appendix D for figure details.*

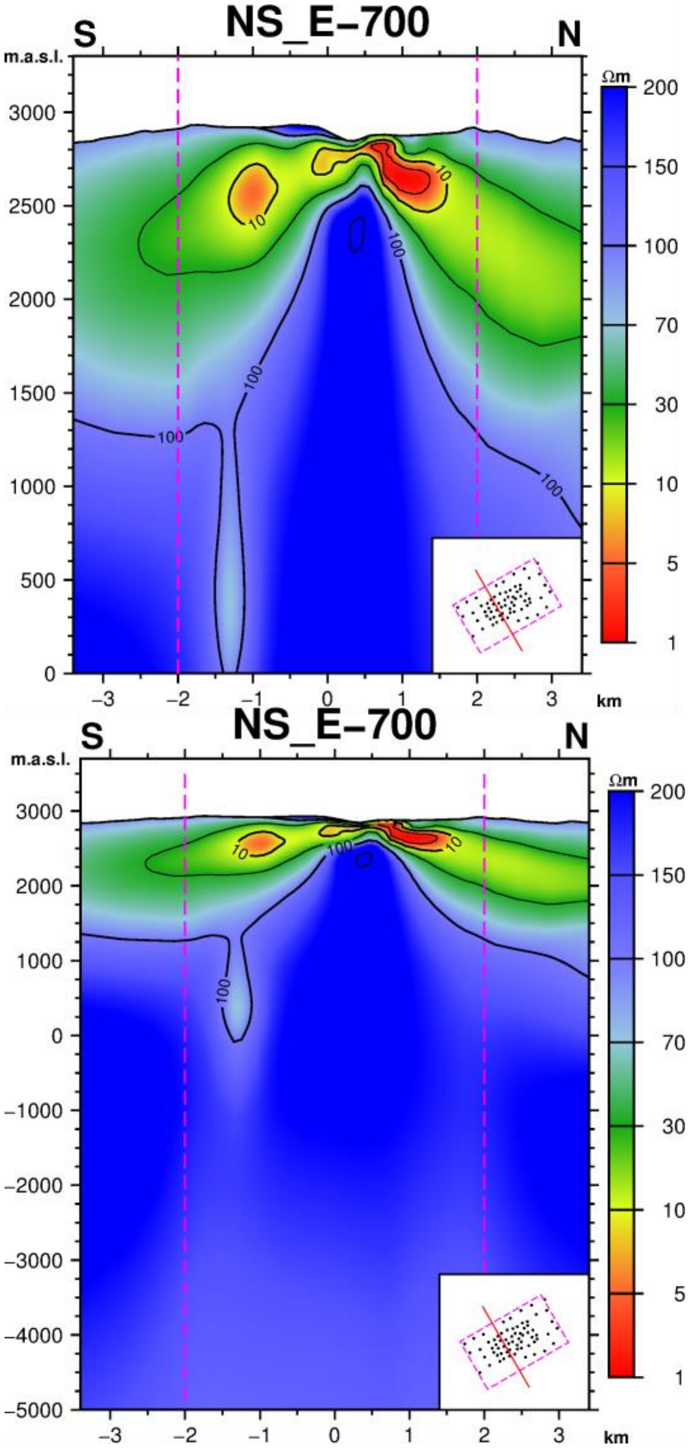

Figure 124: *Vertical cross-section through the final resistivity model of the Acoculco survey area. See Appendix D for figure details.*

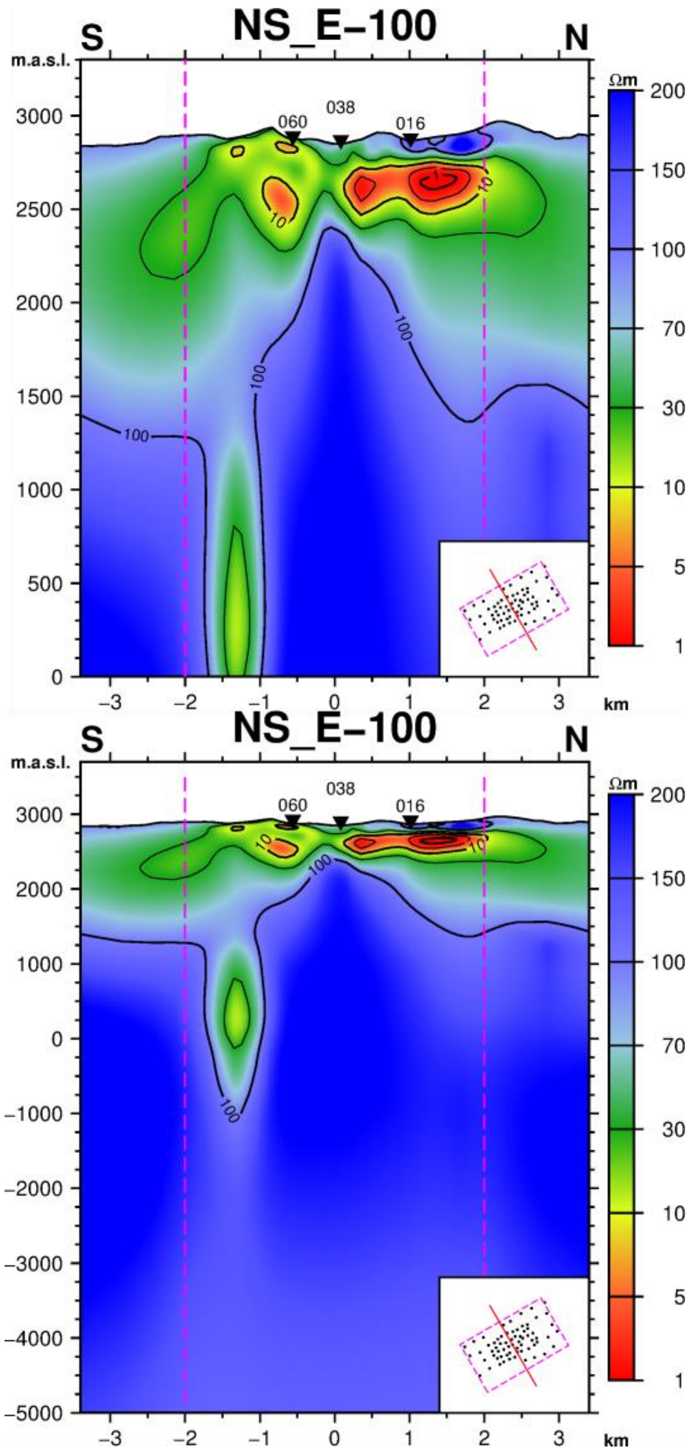

Figure 125: *Vertical cross-section through the final resistivity model of the Acoculco survey area. See Appendix D for figure details.*

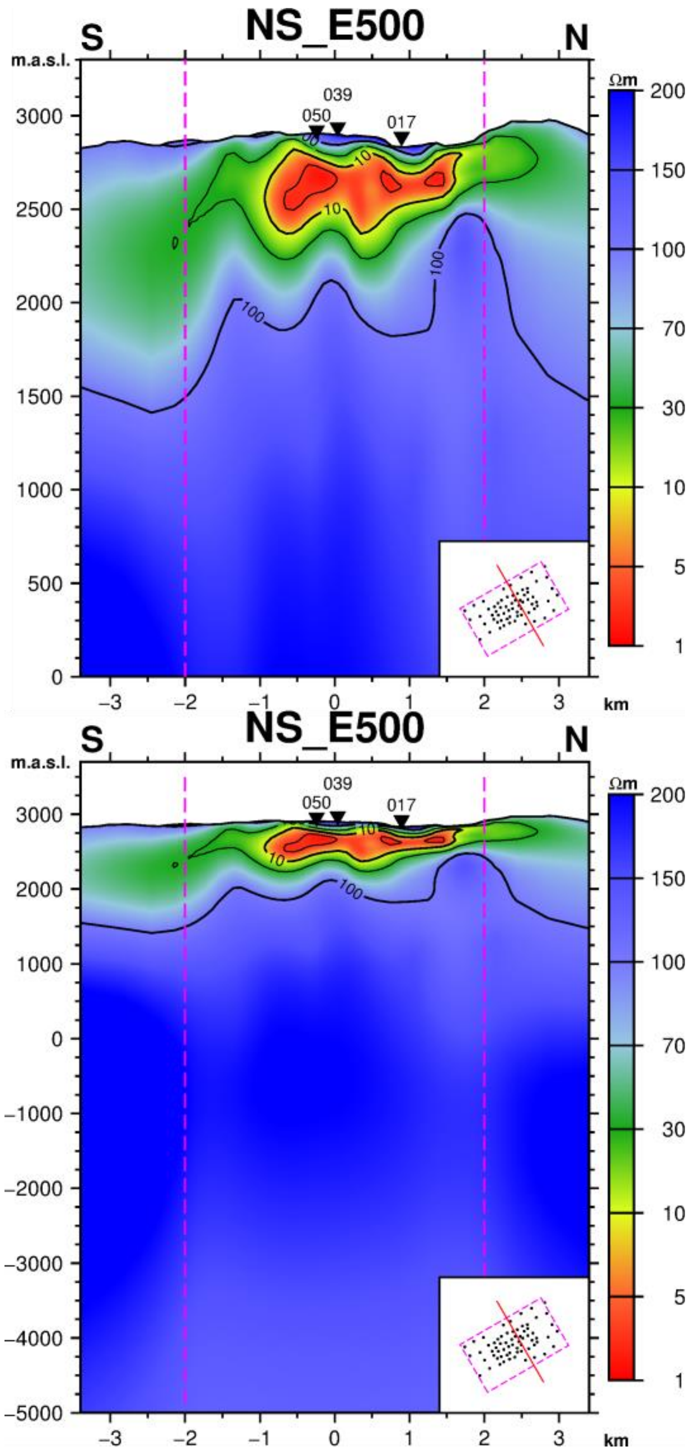

Figure 126: *Vertical cross-section through the final resistivity model of the Acoculco survey area. See Appendix D for figure details.*

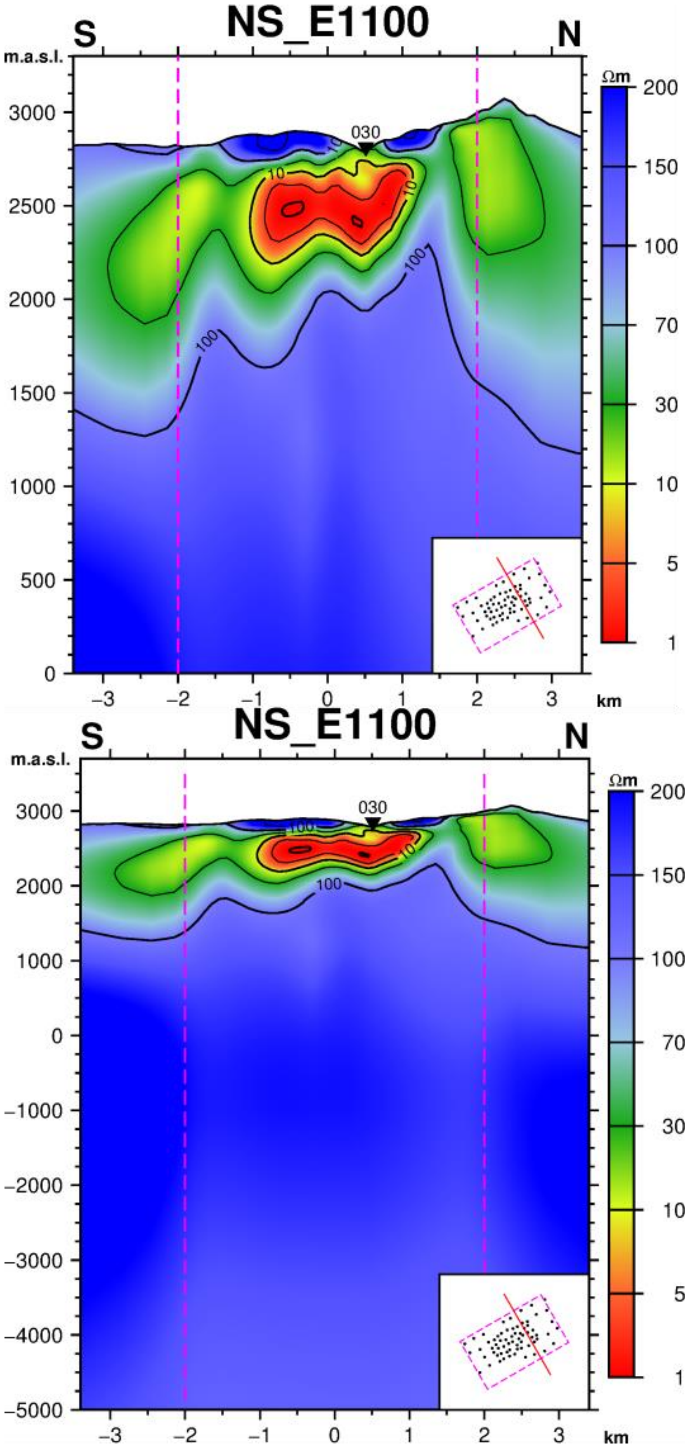

Figure 127: *Vertical cross-section through the final resistivity model of the Acoculco survey area. See Appendix D for figure details.*

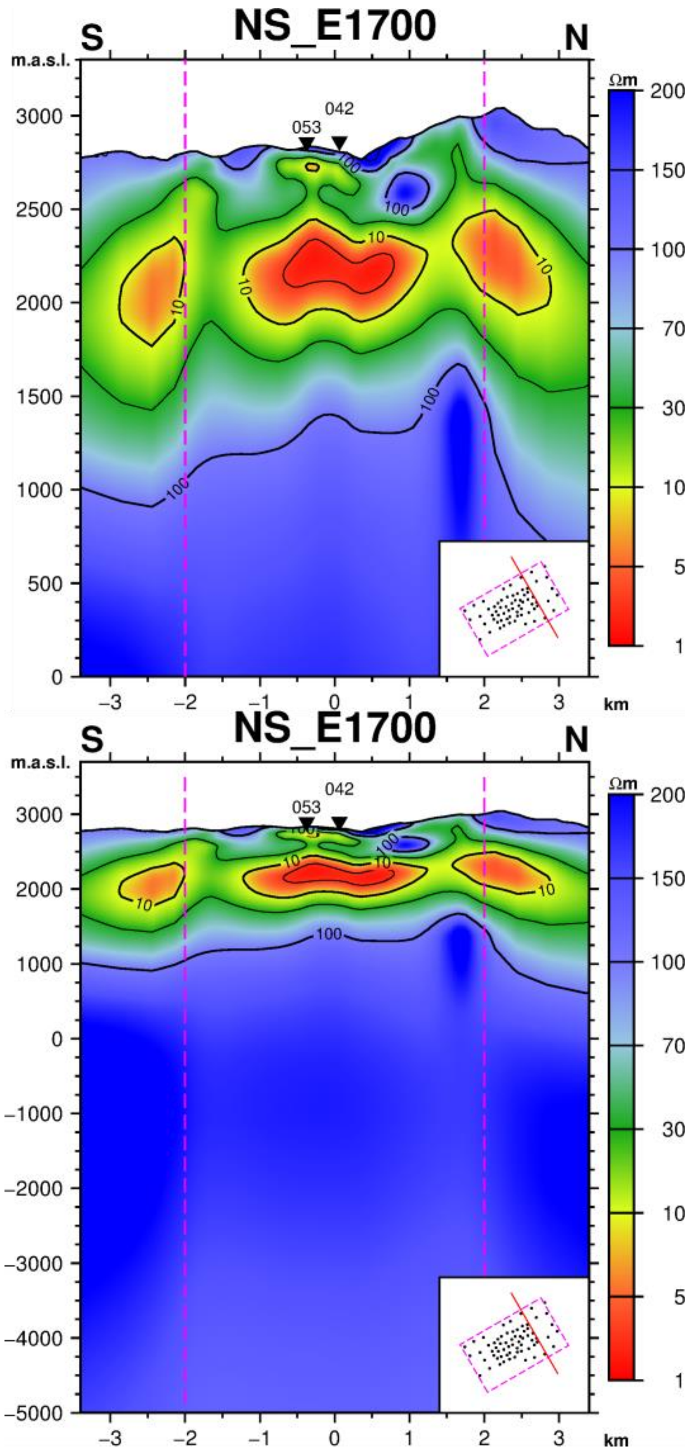

Figure 128: *Vertical cross-section through the final resistivity model of the Acoculco survey area. See Appendix D for figure details.*

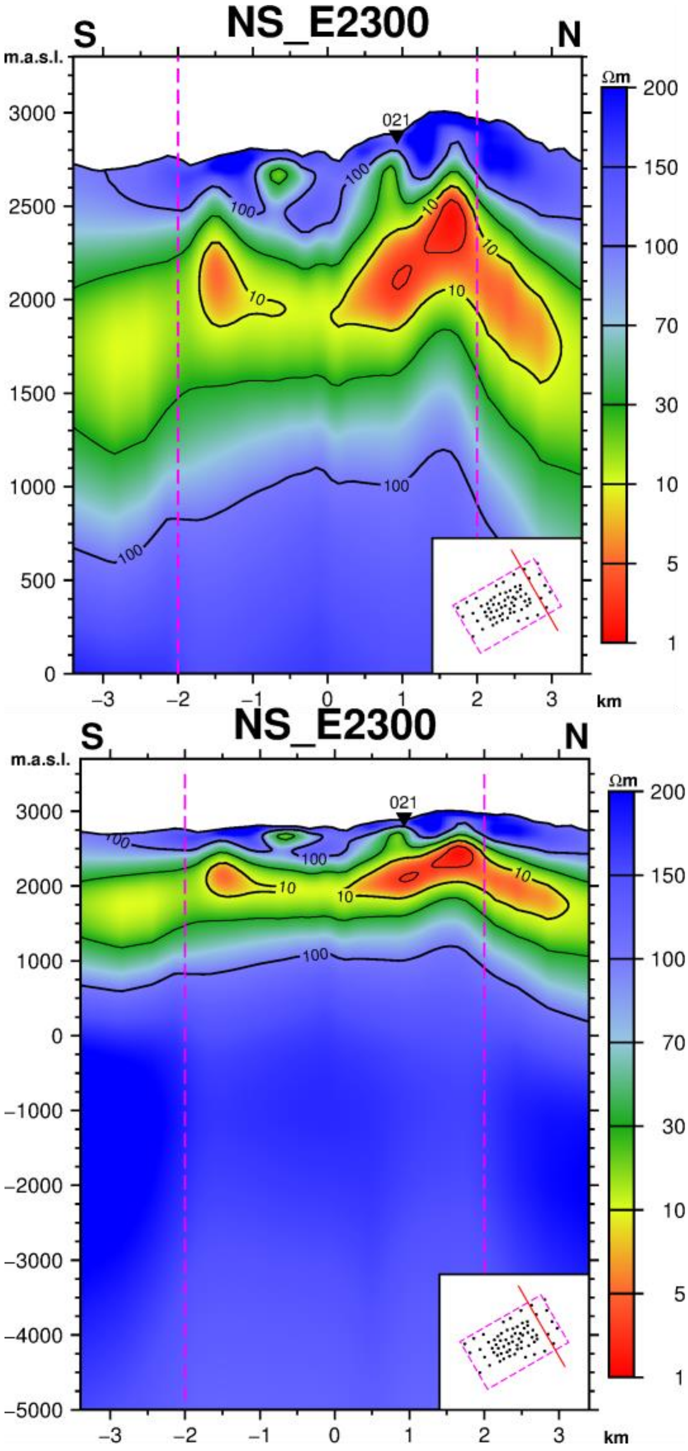

Figure 129: *Vertical cross-section through the final resistivity model of the Acoculco survey area. See Appendix D for figure details.*

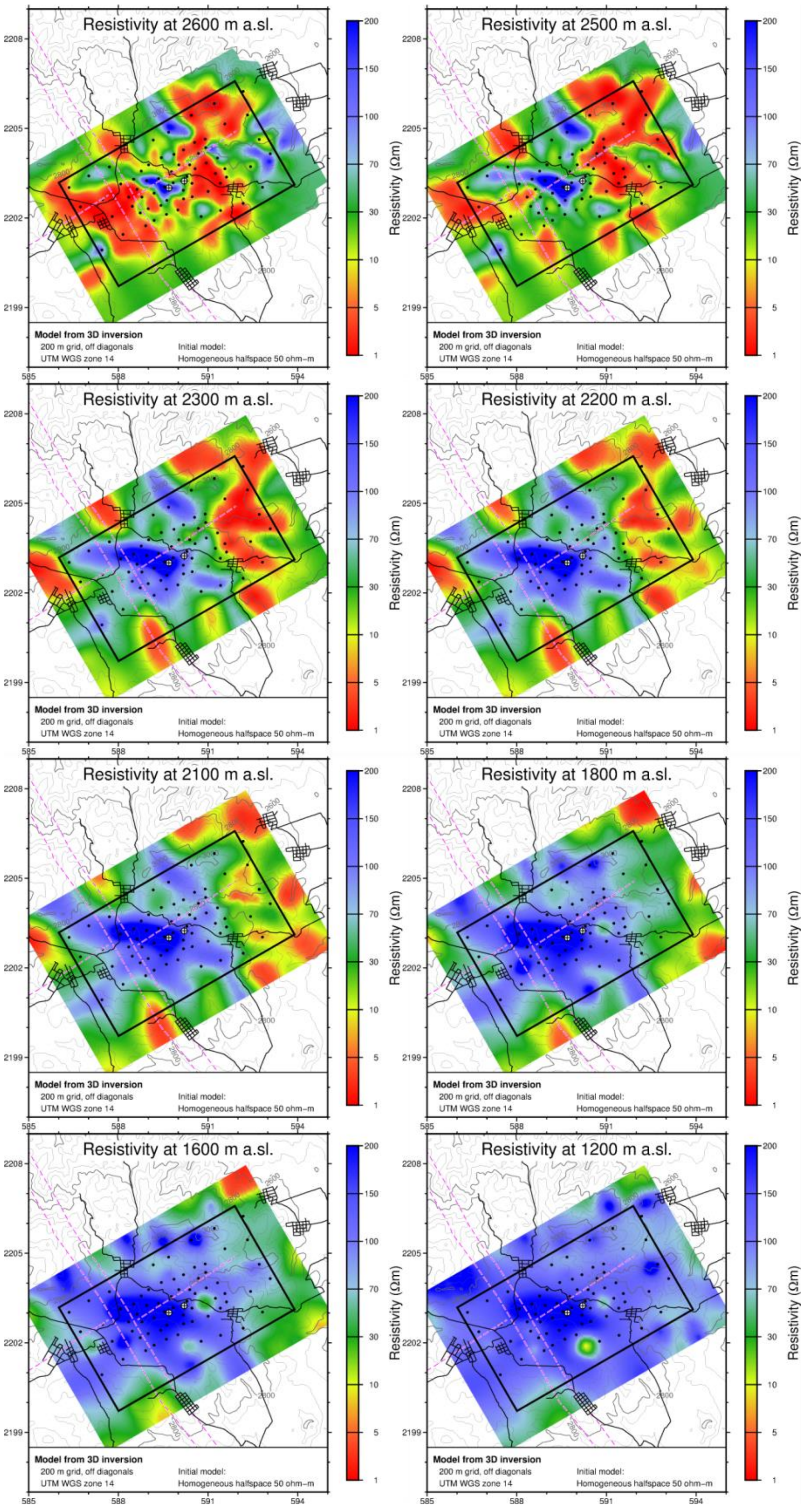

Resistivity at 2600 m a.sl.

Resistivity at 2500 m a.sl.

Resistivity at 2300 m a.sl.

Resistivity at 2200 m a.sl.

Resistivity at 2100 m a.sl.

Resistivity at 1800 m a.sl.

Resistivity at 1600 m a.sl.

Resistivity at 1200 m a.sl.

Figure 130: *Horizontal cross-sections through the final resistivity model of the Acoculco area. See Appendix D for figure details*

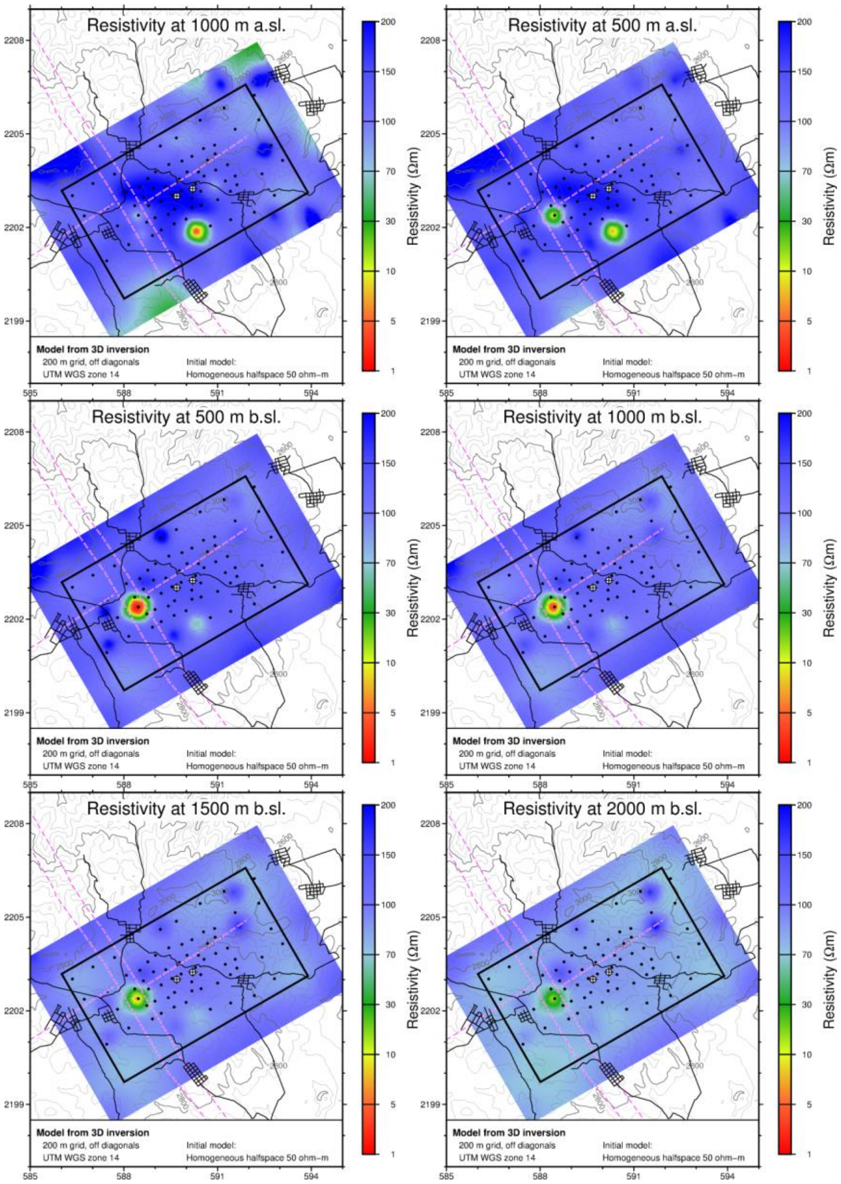

Figure 131: *Horizontal cross-sections through the final resistivity model of the Acoculco area. See Appendix D for figure details.*

Coordination Office, GEMex project

Helmholtz-Zentrum Potsdam
Deutsches GeoForschungsZentrum

Telegrafenberg, 14473 Potsdam

Germany